Synthesis of aerogels, nanocomposites and lightweight silica aerogel superinsulation nanocomposites by ambient pressure drying method

by

Khalil Thabit Hassan

A thesis presented for the degree of

Doctor of Philosophy

School of Engineering

Newcastle University, UK

July 2019

Abstract

This thesis mainly investigates the improvement of the new ambient pressure approach used to synthesise aerogels by using a solvent comprising of sodium bicarbonate and water instead of a low surface tension solvent. Firstly, to improve the efficiency of thermal insulation, the sodium bicarbonate approach is utilised to synthesise cost effective ceramic blanket silica aerogels (CBSA) and short ceramic fibres silica aerogel composites (CSSA).

To reduce the manufacturing cost and scalable of silica aerogels, we propose applying the sodium bicarbonate approach to synthesis silica aerogels from sodium silicate (water glass) precursor. In addition, the approach is used to synthesise alumina-based aerogel (dawsonite-sodium aluminium carbonate hydroxide) from Aluminium sec-butoxide precursor (ASB).

To mimic the structure and thickness of the wings of the damselfly, which was the main source of inspiration for this study, multi-layered silica aerogel films with a thickness of 0.3 mm were synthesised using the bicarbonate approach.

Finally, wavy nickel nanowires (NiNWs) were synthesise and immobilised on mesoporous silica (SiO_2) aerogels by the sol-gel method. In addition, nickel nanoparticles (NiNPs) were immobilised in silica aerogels to do a comparative study between the catalytic activity of immobilised NiNWs and NiNPs in silica aerogels for CO_2 hydration reaction (CHR) in gaseous phase. Dynamic vapour sorption (DVS) analysis is used for that purpose. The analysis is performed at levels of 50% CO_2 and 50% H_2O vapour for SiO_2 aerogels, immobilised nickel nanoparticles (NiNPs) on silica aerogels and NiNWs-SiO_2 aerogels composites.

Transmission electron microscopy (TEM), scanning electron microscopy (SEM), X-ray diffraction (XRD), uniaxial compression test, Brunauer-Emmett-Teller (BET) and Barrett-Joyner-Halenda (BJH) methods are used to characterise the synthesised materials.

ACKNOWLEDGEMENTS

Firstly, all praises to Allah to help me in completing this thesis. I would like to express my extreme gratefulness to my Supervisor Dr. Lidija Šiller (Professor in Nanoscale Science, School of Engineering, Newcastle University, UK) for her professional guidance, motivation and thoughtful advice during my PhD. Her advice encouraged me to be creative and to think deeper. I have enjoyed working with her and she has helped me learn many techniques under her supervision.

I would also like to thank the Higher Committee for Education Development in Iraq (HCED) for a PhD scholarship.

I would also like to thank my lab mates especially Dr. Xiao Han for their help during my research.

I owe my deepest gratitude and special words of thanks to the partner of my life my wife Maryam Alrawe, without her continuous support, I cannot finish my work.

My deepest gratitude goes to my beloved parents. Your contribution in my life made it more comfortable and my loss is more bearable.

Finally, yet importantly, as it would be impossible to thank them as they deserved, I would like to dedicate my work to the spirit of my father (Thabit Al-Fityan), my aunt (Naseemah Al-Fityan) and my uncle (Husham Al-Fityan) who all passed away during my studying journey, my mother, my sisters, my wife and my children.

Contents

List of Figures

List of tables

Abbreviations

APD	Ambient pressure drying
APTES	3-aminopropyltriethoxysilane
ASB	Aluminum sec-butoxide
BET	Brunauer-Emmett-Teller
BJH	Barrett-Joyner-Halenda
BSEs	Backscattered electrons
CBSA	Ceramic blanket-silica aerogel composites
CHR	Carbon dioxide hydration reaction
CFB	Ceramic fibre blanket
CeB_6	Cerium hexaboride
CSF	Ceramic short fibres
CSSA	Short fibres reinforced-aerogel composites
DI	Deionised water
DMF	N, N–dimethylformamide
DVS	Dynamic vapour sorption
E-T	Everhart-Thornley detector
EtOH	Ethanol
FEGs	Field emission guns
HDI	Hexamethylene diisocyanate
HVAC	Heating, ventilation and air conditioning
IUPAC	International Union of Pure and Applied Chemistry
LaB_6	Lanthanum hexaboride
LST	Low surface tension
MTES	Methyltriethoxysilane
MTMS	Methyltrimethoxysilane
NA	Numerical aperture
NiNPs	Nickel nanoparticles
NiNWs	Nickel nanowires

PEI	Poly(ethyleneimine) solution
PTES	Propyltriethoxysilane
R-value	Thermal resistance
SEM	Scanning electron microscopy
SEs	Secondary electrons
TEM	Transmission electron microscopy
TEOS	Tetraethyl orthosilicate
TEPA	Tetraethylenepentamine
TMCS	Chlorotrimethylsilane
TMOS	Tetramethyl orthosilicate
TPS	Transient Plane source
U-value	Thermal transmittance
VIPs	Vacuum insulation panels
XRD	X-ray powder diffraction

Chapter 1 General background and literature review

This chapter is an introduction and brief review on silica aerogel synthesis techniques including the common drying processes that is used to synthesise aerogels, reinforcement techniques utilised for enhancing mechanical properties and recent industrial applications of aerogels. This chapter also outlines main aims of this thesis.

1.1 Introduction

Aerogel is a fascinating nanostructed material which is synthesised by replacing the solvent, present within the pores of a gel, with air. This substitution can be done such that the structure of the gel is retained (Zhang *et al.*, 2017). Historically, gels have been known about and used since the beginning of human civilization. In comparison with gels, the history of aerogels started at the beginning of the 20th century after some scientists proposed the capability of replacing the liquid inside the gel's pores with air. The first successful attempt to synthesise silica aerogel was carried out by Steven Kistler at Stanford University in 1931 using a supercritical drying method (Wan *et al.*, 2018). Aerogels can be classified in different ways. They can be classified as monoliths, powders and films according to their appearance or they could be classified as inorganic, organic and hybrid aerogels according to their composition (Stergar and Maver, 2016). The open cell porous structure gives silica aerogel excellent heat insulation performance. Due to their unique properties such as high porosity, small pore size (2 to 50 nm) and a low solid conductivity of the silica skeleton, silica aerogels are considered among the best insulators. In addition to having the lowest measured thermal conductivity of any material, silica aerogel offers a promising opportunity to produce a non-flammable insulation which is inert, transparent to solar light and strongly blocks infrared thermal radiation (Rolison and Dunn, 2001). At room temperature, silica aerogels have a very low thermal conductivity, even lower than the thermal conductivity of air (25 mW/m K); the values can be as low as between 0.005-0.02 W/m K (Kistler, 1931; Lu *et al.*, 1992; Rolison and Dunn, 2001; Sorensen *et al.*, 2006; Hayase *et al.*, 2014; Jiang *et al.*, 2017a; Liu *et al.*, 2017).

In addition to their superinsulation properties, a tremendous amount of studies have been carried out to investigate the capability for efficient use of silica aerogels in different applications such as humidity sensors (Wang *et al.*, 2005), gas sensors (Yamada *et al.*, 2002), supercapacitors (Kim and Popov, 2002), drug delivery (Rajanna *et al.*, 2015), CO_2 capture (Lin and Kuo, 2016), catalyst supporters, acoustic insulators (Feng *et al.*, 2016) and as heat storage

devices (Ulker *et al.*, 2013; Maleki *et al.*, 2014b). A brief of different applications of aerogels are presented in the diagram seen in Figure 1. 1

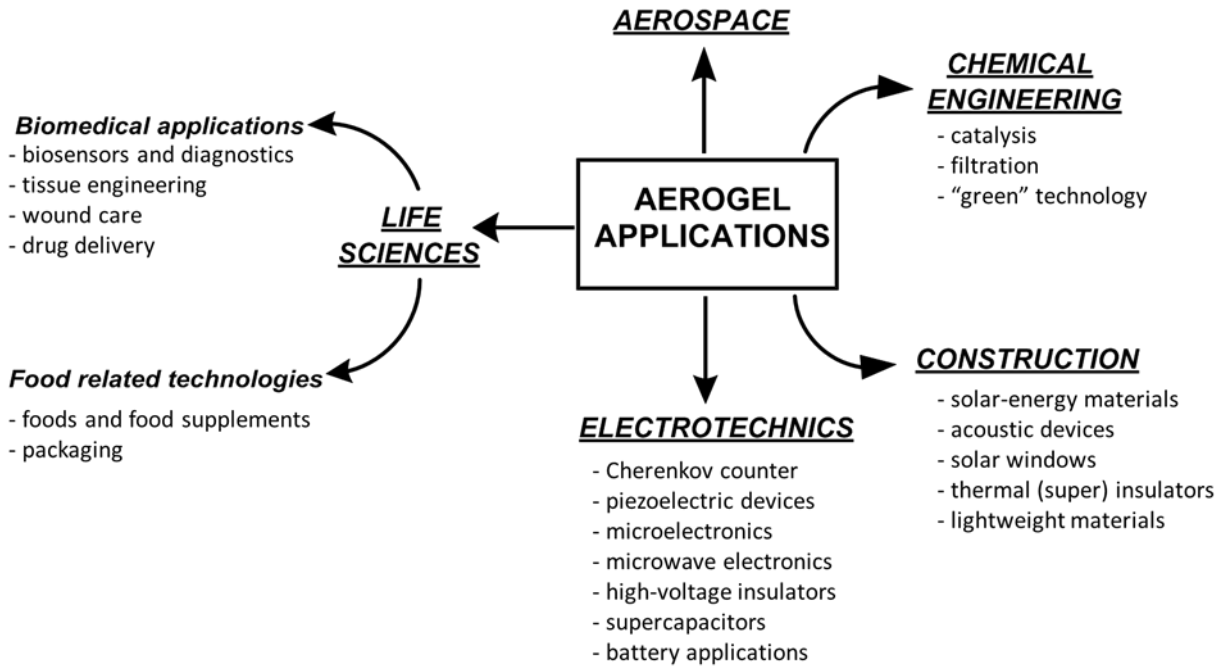

Figure 1. 1 Current aerogels applications (Stergar and Maver, 2016).

The recent increase of industrial applications for aerogel in sectors such as thermal insulation for aerospace, building or any application which requires high surface area and porosity is reflected by the pronounced increase of scientific research and publications infield of aerogels in the recent years (Maleki, 2016). Figure 1. 2 illustrates the growth in scientific publications on aerogels over the last three decades.

More recently, publications have been focusing on producing new fascinating types of aerogels, employing new applications for aerogels and improving upon the production of aerogels in an attempt to reduce the manufacturing time. Despite the wide range of applications, the inherited poor mechanical properties and fragility are the reasons behind the drawback in commercialization of silica aerogels. The poor strength under compression is reported so far in literature (Yang *et al.*, 2011). Therefore, several attempts have been carried out to enhance the strength of silica aerogel networks to improve the material's mechanical properties (Leventis *et al.*, 2002). One effective method for enhancing mechanical properties is achieved by recruiting secondary materials such as fibres. For example; xonotlite, nonwoven fibres and ceramic or carbon fibre were utilized for that purpose (Deng *et al.*, 1998; Yang *et al.*, 2011).

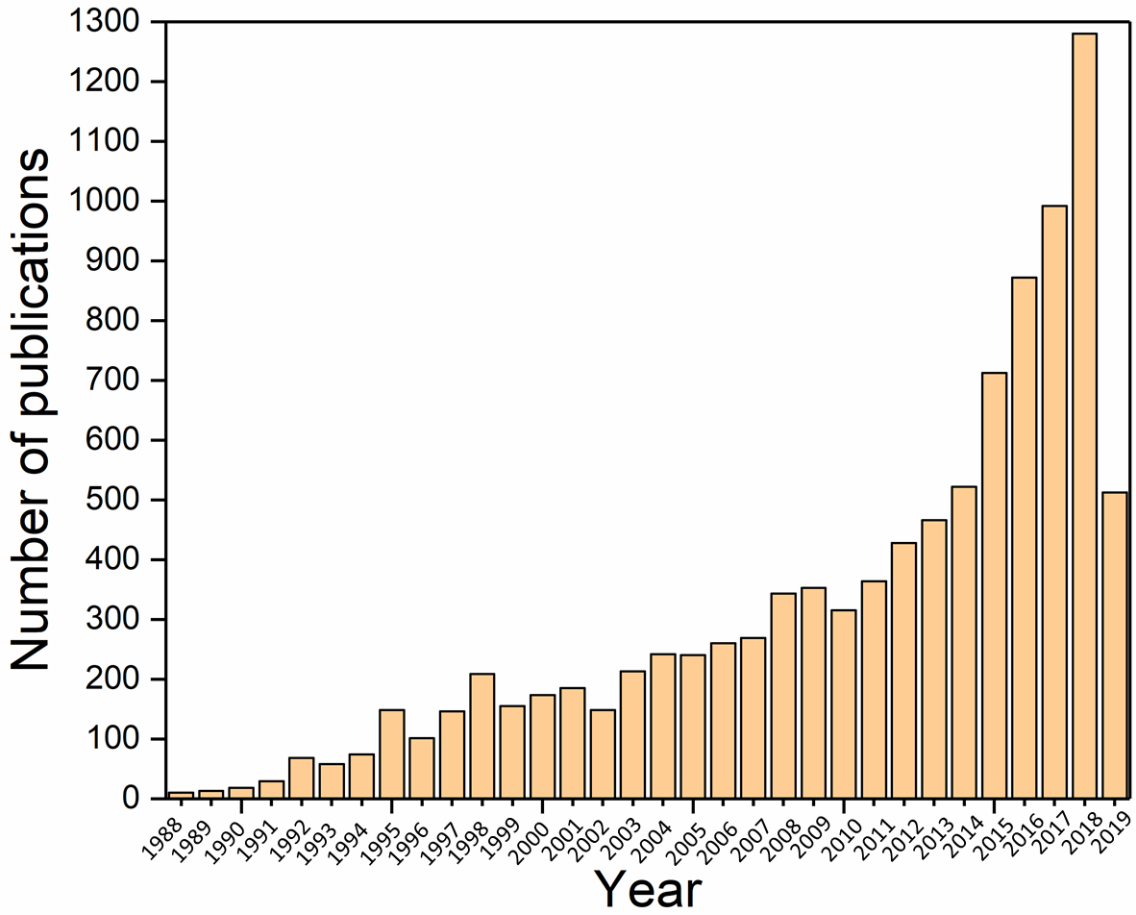

Figure 1. 2. Total number of publications by year for the last 30 years that contains "aerogel" in their content (web of Science, date of search/ 28th May 2019).

Generally, silica aerogel synthesis takes place in three main stages: gelation (transition of sol into gel), ageing (enhancing the mechanical properties of the gel) and drying (replacing the solvent inside pores with air at a certain temperature and pressure). In gelation, a sol- gel method is used to prepare the silica gel. A gel of nanostructured network is formed via polymerization process in a liquid reaction medium. Silica precursor delivers the siloxane bridges (≡Si–O–Si≡) between the Si atoms. After gelation, the gel needs to be aged before the final stage of drying. The most common precursor which is used for the synthesis of silica aerogels is Tetraethyl orthosilicate (TEOS). The drying process of the gel can be utilized by one of three common methods: freeze drying, ambient pressure drying and supercritical drying; these methods will be discussed in more detail later in this chapter. Figure 1. 3 illustrates the general steps for the synthesis of aerogel.

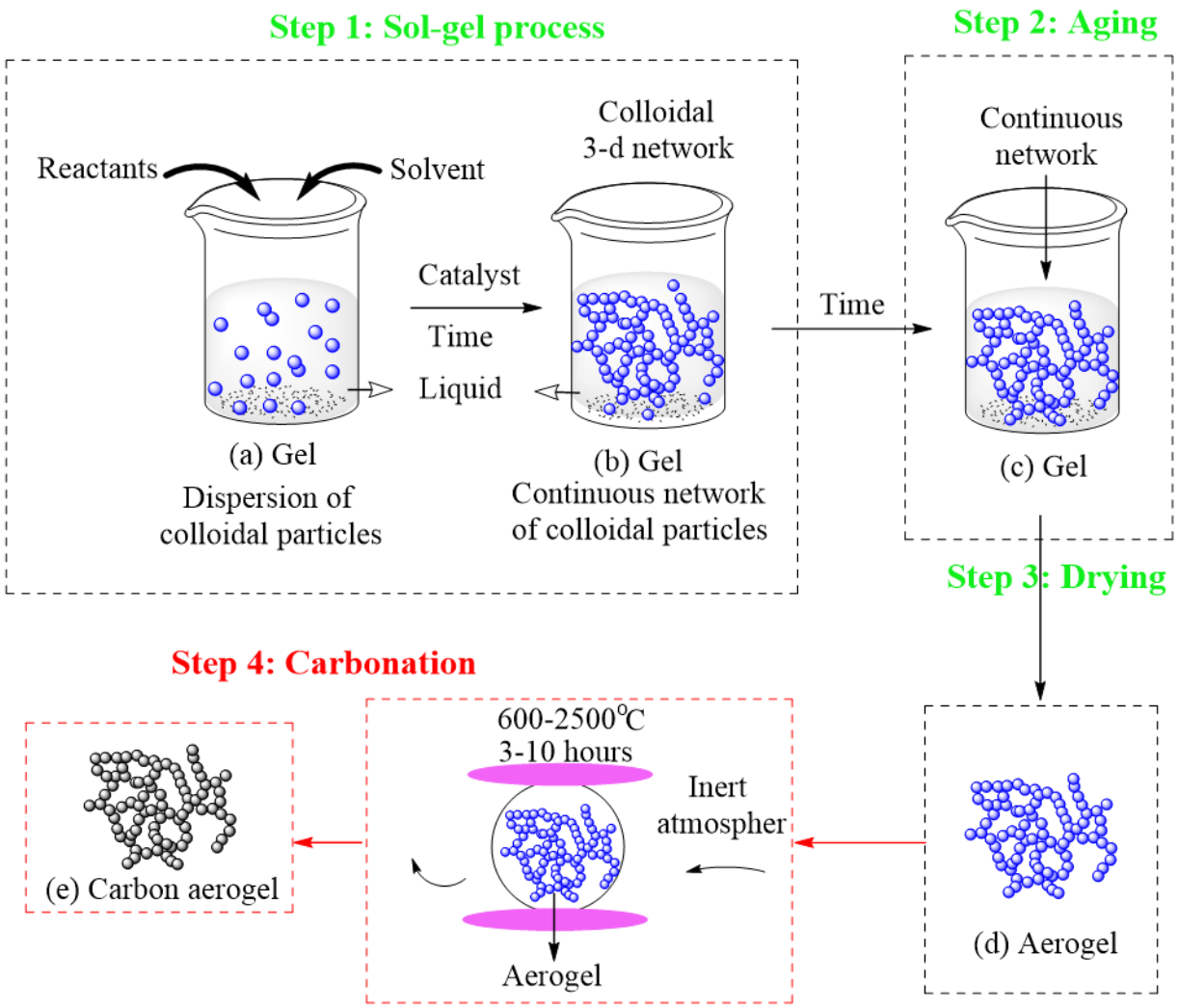

Figure 1. 3 general stages of aerogels synthesis. Step 4 is only for carbon-based aerogels (Zuo *et al.*, 2015).

The recent research on aerogels are focusing on three main branches. First is concerned on developing ambient pressure drying method to reduce the production cost and use cheaper precursors such as water glass. Where the second is about enhancing the strength and fragility of the silica aerogel structure, which can be achieved by either modifying the microstructure through hybridization or by reinforcing the material with inorganic or organic substances. The final category focuses on the introduction of silica aerogel into other materials such as polymers, insulation materials or encapsulating structures (Dourbash *et al.*, 2017). Figure 1. 4 presents the core research about silica aerogels (Dourbash *et al.*, 2017).

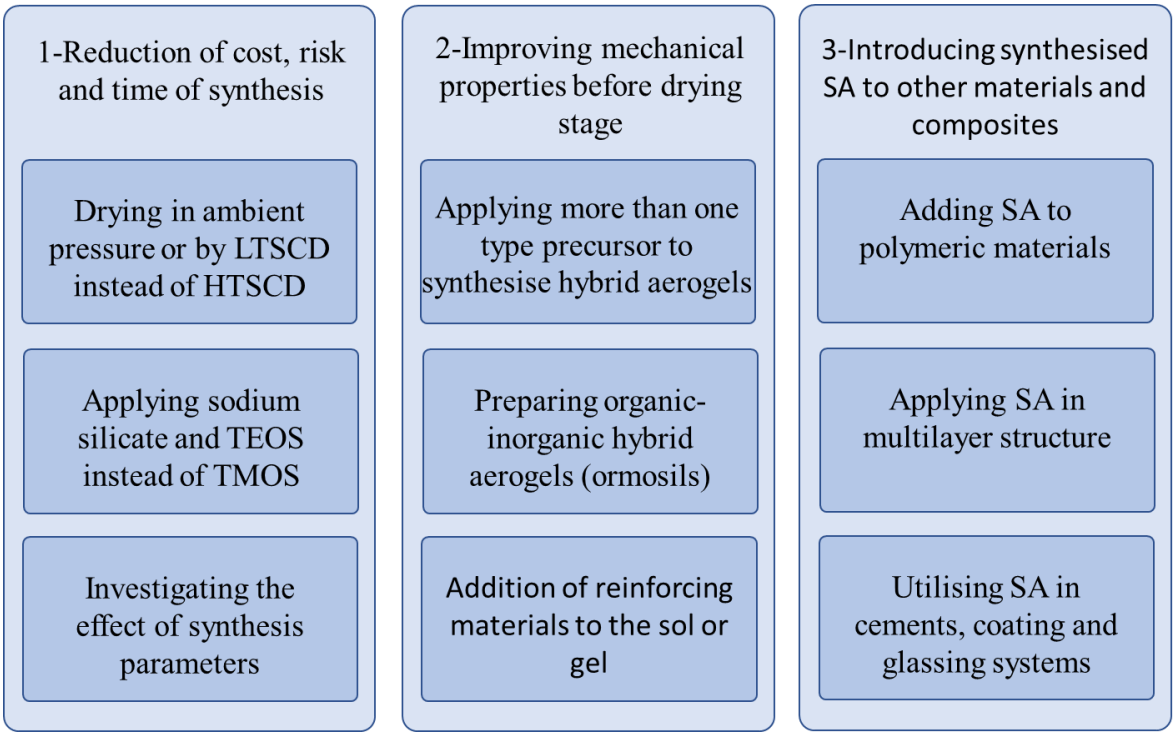

Figure 1. 4 Core silica aerogels research topics (Dourbash *et al.*, 2017).

1.2 Sol-gel process

Sol-gel is the process by which most aerogels are synthesised from different precursors. Sol can be described as a colloidal solution of primary particles or monomers. In general, the sol consists of a mixture of starting precursor, water, solvent and catalyst (Maleki, 2016). The structure of the gel is formed after successive reactions and reverses of hydrolysis and condensation. Hydrolysis is the process by which the nucleophilic attack of water leads to replacement of alkoxide groups by hydroxyl groups. While condensation is the process of forming M-O-M bonds between two species of M-OH (where M is a metal element) or M-OH and M-OR (OR is an alkoxide group). The process releases water or alcohol molecules, respectively (Wan *et al.*, 2018).

Metal oxide sol-gel process from alkoxide precursors can be described through three reactions of formation the polymeric M-O-M bonds as illustrated in Figure 1. 5 (Brinker, 1988; Maleki, 2016).

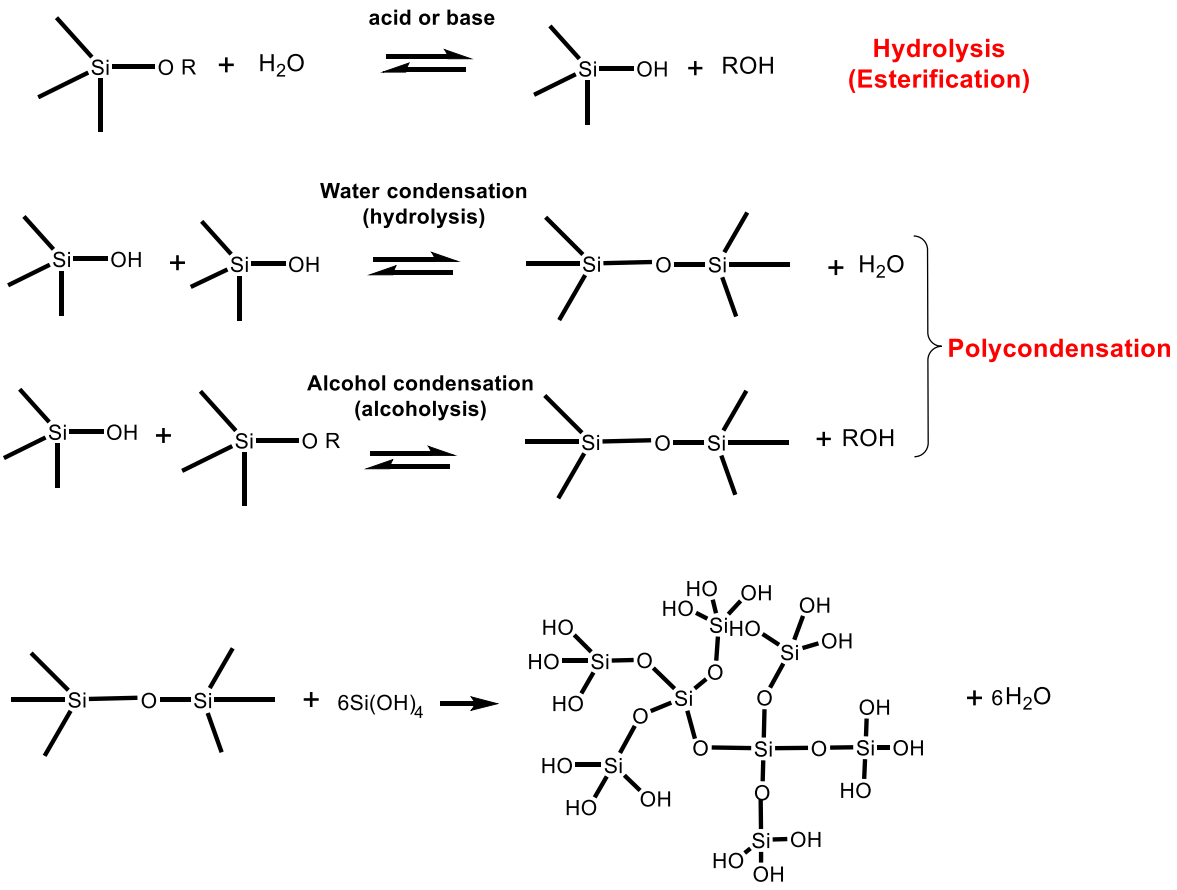

Figure 1. 5. Sol-gel reaction for an alkoxysilane (Maleki, 2016).

Many parameters may influence a sol-gel process. Those parameters are the pH of the solution, temperature, precursor activity and the water / precursor ratio. In addition, the rate of hydrolysis and condensation reactions can be controlled by adding some catalysts, (Brinker, 1988; Gurav *et al.*, 2010), varying the molar ratio or the type of catalyst that is employed to control the hydrolysis and condensation rates as well as the time of gelation.

The silica precursor could be either sodium silicate (water glass) or alkoxides. The most common alkoxides, which are used as a silica precursor, are tetraethyl orthosilicate (TEOS), methyltrimethoxysilane (MTMS) and tetramethyl orthosilicate (TMOS) (Zhang *et al.*, 2004; Bhagat *et al.*, 2007; He *et al.*, 2009). From commercial perspective, water glass is the cheapest and promised precursor for silica aerogel production , however, it requires several treatments, such as ionic exchange to remove Na+ ions, in addition to a huge consumption of expensive solvents for surface modification (Shi *et al.*, 2006).

One of the biggest advantages of the sol-gel process is the ability to amend the molecular or the nanoscale structure of the aerogel by incorporating an extra phase or chemical groups such as alkoxide organofunctions or additives and nanoparticles in the porous network (Maleki, 2016).

1.3 Ageing

During gelation, silica gel for instance, primary particles are linked together to form the necklace structure of silica gel. However, at that stage the linking among those particles are quite weak and there is a need for enhancement (Iswar *et al.*, 2017). Therefore, several attempts were conducted to enhance the strength of the necklace structure of the gel. Haereid *et al.* (1995) applied heating treatment (hot water) on the wet gel to enhance the mechanical properties of the silica aerogel. The enhanced strength of the wet gel backbone, when heat treatment is utilised, was attributed to the effect of Ostwald ripening process (Reichenauer, 2004). Ageing is also strengthening the structure of the gel and minimising the shrinking of the gel during drying. The ageing process provides additional time for the reaction of some reactive species and unreactive monomers inside the pores with solvent that are not finished during gelation step. The ageing process is carried out by soaking the gel in a proper solvent (such as a mixture of water and ethanol (Einarsrud *et al.*, 2001) or mother solvent (He *et al.*, 2009)) for a period from several hours to days. For instance, using water as the ageing solvent promotes dissolution and reprecipitation of silica species into the contact points of particles (see Figure 1. 6 which illustrates Ostwald ripening on the gel); while ageing with mother solvent provides more hydrolysis and condensation reaction which will increase the strength of the gel (He *et al.*, 2009). In addition, the ageing process could be controlled by many parameters such as temperature, pH and time (Maleki, 2016).

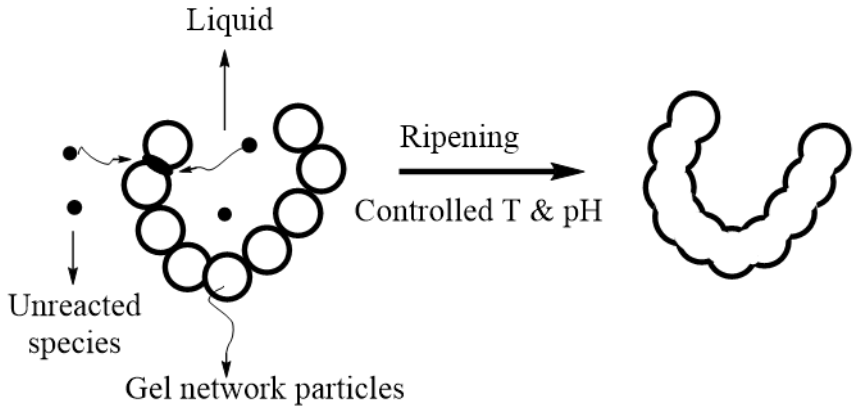

Figure 1. 6. Ostwald ripening process on gel nanoparticles during ageing (Maleki, 2016).

1.4 Drying

The aim of the drying process is to obtain aerogels with the original porous structure of gels. The main parameter that affects drying of gels is the presence of capillary forces inside pores, which cause the gel's shrinkage. As a result of shrinking, chemical groups in the internal surface

of the pores react with each other (if the walls of pores are shrunk enough to touch each other) and cause the collapse of the aerogel structure (Schwertfeger F., 1998). Before discussing the main drying methods, it is important to explain the capillary forces which arise at the solid-liquid-vapour interface inside the pores.

Capillary

The big challenge for any drying method of aerogels is overcoming the generated capillary forces. The smaller radius of the pores becomes, the higher the hydrostatic pressure is or the higher the liquid column inside the pores will be. To calculate the capillary pressure inside the pores (see Figure 1. 7), Young- Laplace equation is used to balance the static forces

$$2\pi r\gamma cos\theta = \pi r^2 h\rho g$$

$$2h\rho g = p_r = 2\frac{\gamma cos\theta}{r} \qquad (1.1)$$

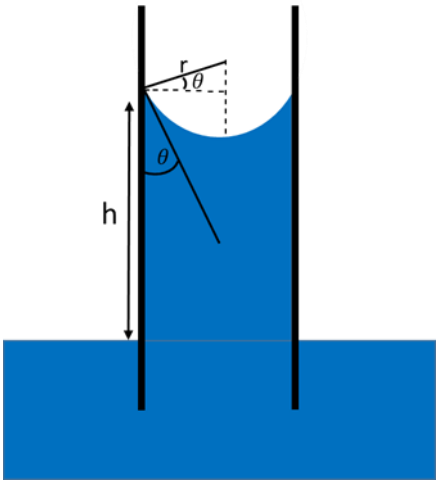

Figure 1. 7. Diagram of a capillary to demonstrate measurements used in the Young-Laplace equation.

where, r is the radius of the pore, γ is the surface tension, θ is the contact angle, h is the height of liquid column, ρ is liquid density and p_r is the interfacial pressure. Since the pore diameter is measured in nanometres, the hydrostatic pressure inside pores is very high; therefore, the particles will compact on each other under the effect of surface tension and the meniscus. Consequently, the collapse occurs due to the porous structure especially if the gel has very fine pores (Gurav *et al.*, 2010). In addition, the surface of the wet gel is terminated by either hydroxyl (OH) or alkoxy (OR) groups and these groups could react and yield ≡SiO−O−Si≡ bonds during drying. This will create an irreversible shrinking and produce high density silica xerogels (>0.5 g/m) (Rao *et al.*, 2001).

Freeze drying method

This is an easy and cost effective drying method which depends on bypassing the triple point as shown in Figure 1. 8 (Aegerter *et al.*, 2011). Generally, the obtained material from this drying method is called cryogel (maximum porosity of 80%). In this drying method, the process is going around the liquid- gas boundary and the solvent inside the pores is frozen and then extracted via sublimation under vacuum (Blaszczynski *et al.*, 2013; Maleki *et al.*, 2014a; Maleki, 2016). The porous structure of aerogels that are produced by the freeze drying method is dependent on the rate of freezing. Small pore size aerogel is obtained when fast freezing rates are applied while slow rates produce large pore size aerogels (Kumar *et al.*, 2018).

However, this drying method has not proven to produce monolithic aerogels. Products are either cracked pieces or powder, where the ice inside the pores leads to the filling of the porous structure. The process also needs solvent exchange with low expansion coefficient solvents (such as hexane, toluene and THF) (Aegerter *et al.*, 2011; Maleki, 2016).

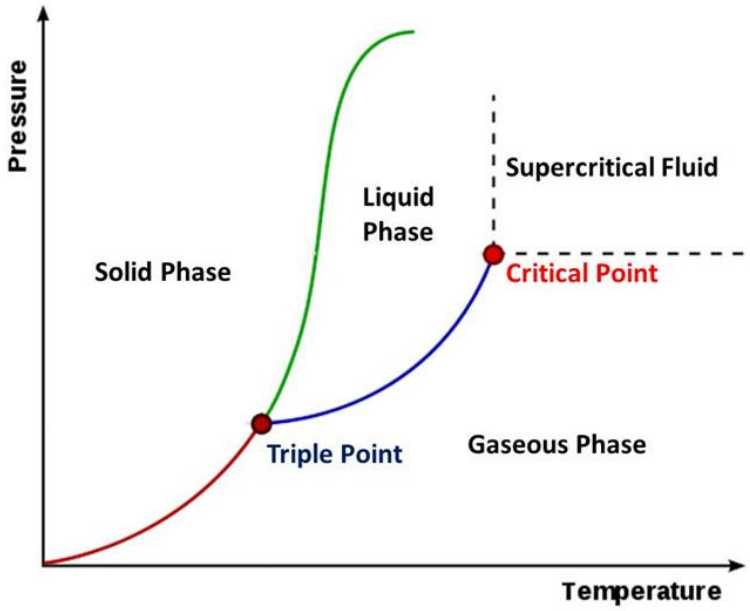

Figure 1. 8. Supercritical drying method phase diagram (Aegerter *et al.*, 2011).

Supercritical drying method

To maintain the porous structure during drying of the gel and to produce high quality silica aerogels, a supercritical drying method is utilised to avoid the effect of capillary forces, which is the main cause for the destruction of the porous structure. When Kistler and Charles 1931 have successfully developed a drying method to replace the liquid inside pores of gels by the air without collapsing the porous structure of the gel, soon after that they have synthesised SiO_2

aerogel with density of only 0.02 g/cm^3 (Kistler, 1931). Then they synthesised alumina, stannic oxide, nickel tartrate, tungstic oxide, agar, gelatine and cellulose aerogels. Kistler utilised autoclave to elevate the temperature of the gel, which was already impregnated in liquid, above the critical temperature of that liquid and to maintain the pressure over the vapour pressure. The evaporation of the liquid occurs without the collapsing of the aerogel network due to the absence of a liquid-vapour meniscus caused by traditional drying methods (Kistler, 1931; Aegerter *et al.*, 2011).

As mentioned earlier, the supercritical drying method is designed to overcome the capillary forces. To explain that, at a specific point, critical point in Figure 1. 8, the liquid inside the pores behave as a supercritical fluid. At that stage, each molecule moves freely due to the absence of the surface tension and forming of liquid-vapour interfaces. Therefore, there is no presence of capillary forces at the pore's walls and the drying occurs without the collapse of the aerogel structure (Smith *et al.*, 1995).

The supercritical drying method is performed with either organic solvent or by solvent exchange with CO_2. Figure 1. 9 illustrates the autoclave that is used in the supercritical drying method (Gurav *et al.*, 2010). A super critical drying method is called a hot process if an organic solvent is used for drying because it is carried out at high pressure and temperature. In general, alcohol is the most commonly used solvent in this process. Using ethanol or methanol for drying requires the temperature and the pressure of the autoclave to be set to the critical values of 243oC and 7.9 MPa, respectively (Gurav *et al.*, 2010; Aegerter *et al.*, 2011).

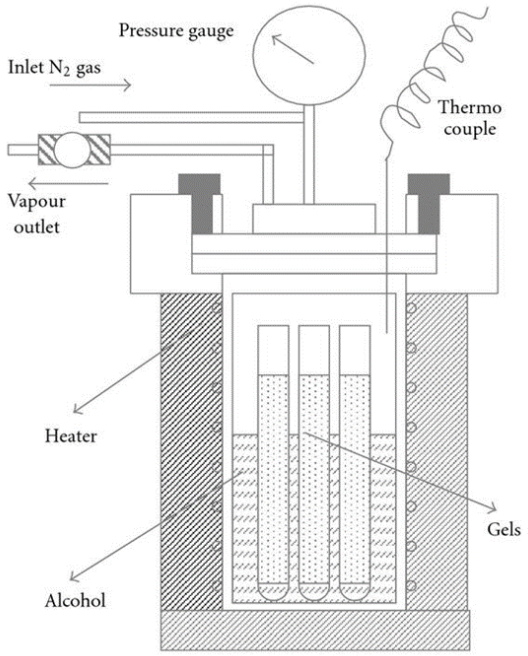

Figure 1. 9 Schematic representation of supercritical drying autoclave (Gurav *et al.*, 2010).

On the other hand, the cold process is carried out by exchanging the solvent with CO_2 during the drying process. The critical point for carbon dioxide is (31.1 ºC at 7.39 MPa) (Blaszczynski *et al.*, 2013). The lower temperature for the cold supercritical drying makes that process cheaper and preferable to produce monolithic aerogels compared with the hot process (Blaszczynski *et al.*, 2013). Table 1. 1 shows the critical temperature and pressure for some commonly used solvents in the supercritical drying method (Sone *et al.*, 2013).

Table 1. 1. Critical conditions of commonly used solvents (Sone *et al.*, 2013).

Fluid	Critical Temperature (K)	Critical Pressure (MPa)
CO_2	304.1	7.39
NH_3	405.5	11.35
H_2O	647.3	22.12
n-Pentane	469.7	3.37
Toluene	591.8	4.10

Ambient pressure drying method

The supercritical drying method is typically used for commercial production of monolithic aerogels. However, this drying method has some commercial restrictions which limit the scaling up. Such restrictions demand special equipment (special kinds of autoclaves) and involve some special safety and cost issues related to operation at high pressures and temperatures (Sarawade *et al.*, 2010; Smitha *et al.*, 2011; Bangi *et al.*, 2012; Mazraeh-shahi *et al.*, 2013; Toivonen *et al.*, 2015). After Prakash *et al.* (1995) introduced synthesis of silica aerogels by ambient pressure drying method (APD), which is much safer and less expensive, the process has been developed to be an alternative method for commercial production of silica aerogels. APD includes aging and many solvent exchange stages in order to strengthen and to modify the silica gel surface before drying. From the Young Laplace equation, see Eq. 1.1, in order to prevent the pore from collapsing, the pressure inside the pores can be decreased via reducing the surface tension inside the pores. Furthermore, the gel needs surface modifications before the drying as the gel without modifications experience an irreversible shrinking and cracking because of the capillary pressure. Surface modification of silica network occurs

through modifying hydroxyl groups with non-polar methyl groups usually from silanes (Rao *et al.*, 2001; Smitha *et al.*, 2011; Shao *et al.*, 2013). Typically, trimethylchlorosilane (TMCS) is used for surface modification of silica gel. Eq. (1.2), (1.3) and Figure 1. 10 show the reactions on surface between TMCS and hydroxyl groups. In addition, TMCS reacts with water inside pores simultaneously.

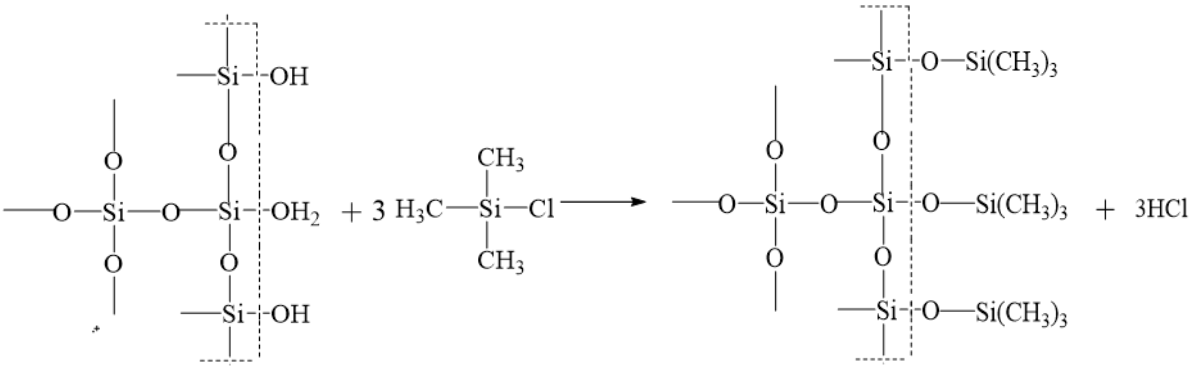

Silica alcogel TMCS Modified silica gel (1.2)

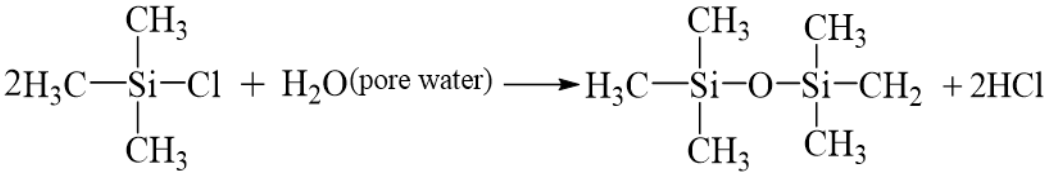

(1.3)

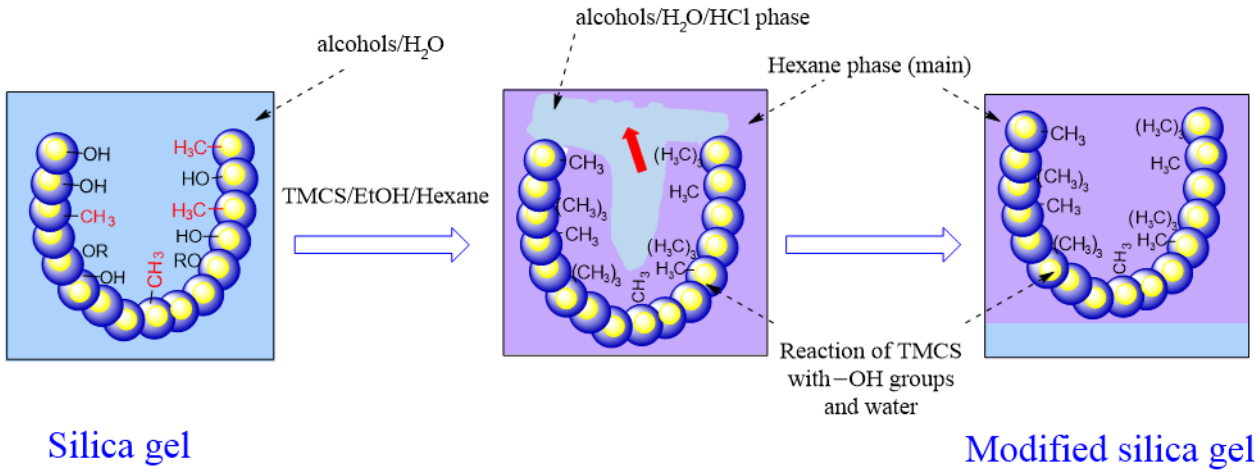

Figure 1. 10. The mechanism of surface modification and solvent exchange (Shao *et al.*, 2013).

However, this method requires multi-steps of solvent exchange and surface modification in order to preserve the porous network (Sarawade *et al.*, 2011). Although using low cost sodium silicate precursor will reduce the manufacturing cost of silica aerogels synthesised via APD, the production cost of silica aerogels using APD is still high. Furthermore, APD produces a large amount of chemical waste (Gurav *et al.*, 2009).

Bicarbonate based ambient pressure drying method

Recently, Han and Šiller (2015) developed a new ambient pressure drying approach by reducing the solvent exchange and surface modification process that in turn reduces the cost for synthesising silica aerogels. The novel ambient pressure drying approach uses sodium bicarbonate solution instead of organic low surface tension solvents in conventional ambient pressure drying method, in order to generate CO_2 gas in the pores of the wet-gel before drying at a certain temperature. The approach is inspired from the life cycle of a damselfly and more specifically from the drying process of their wings. The process generates CO_2 inside the pores during gel stage prior to drying. Therefore, instead of reducing the capillary pressure by undertaking surface modification and solvent exchange in APD, combination of TMCS and sodium bicarbonate solution generates CO_2 gas without surface modification. The formed CO_2 is trapped inside the wet gel that generates pressure (CO_2 bubbles) are found opposing to the capillary pressure. The pressure, which is formed by CO_2 generation, prevents collapsing of the wet gel structure during ambient pressure drying. The dried aerogel has hydrophilic properties. The diagram in Figure 1. 11 illustrates the difference between APD using an organic low-surface-tension (LST) solvent and APD using inorganic sodium bicarbonate solution (Han and Šiller, 2015; Han *et al.*, 2018).

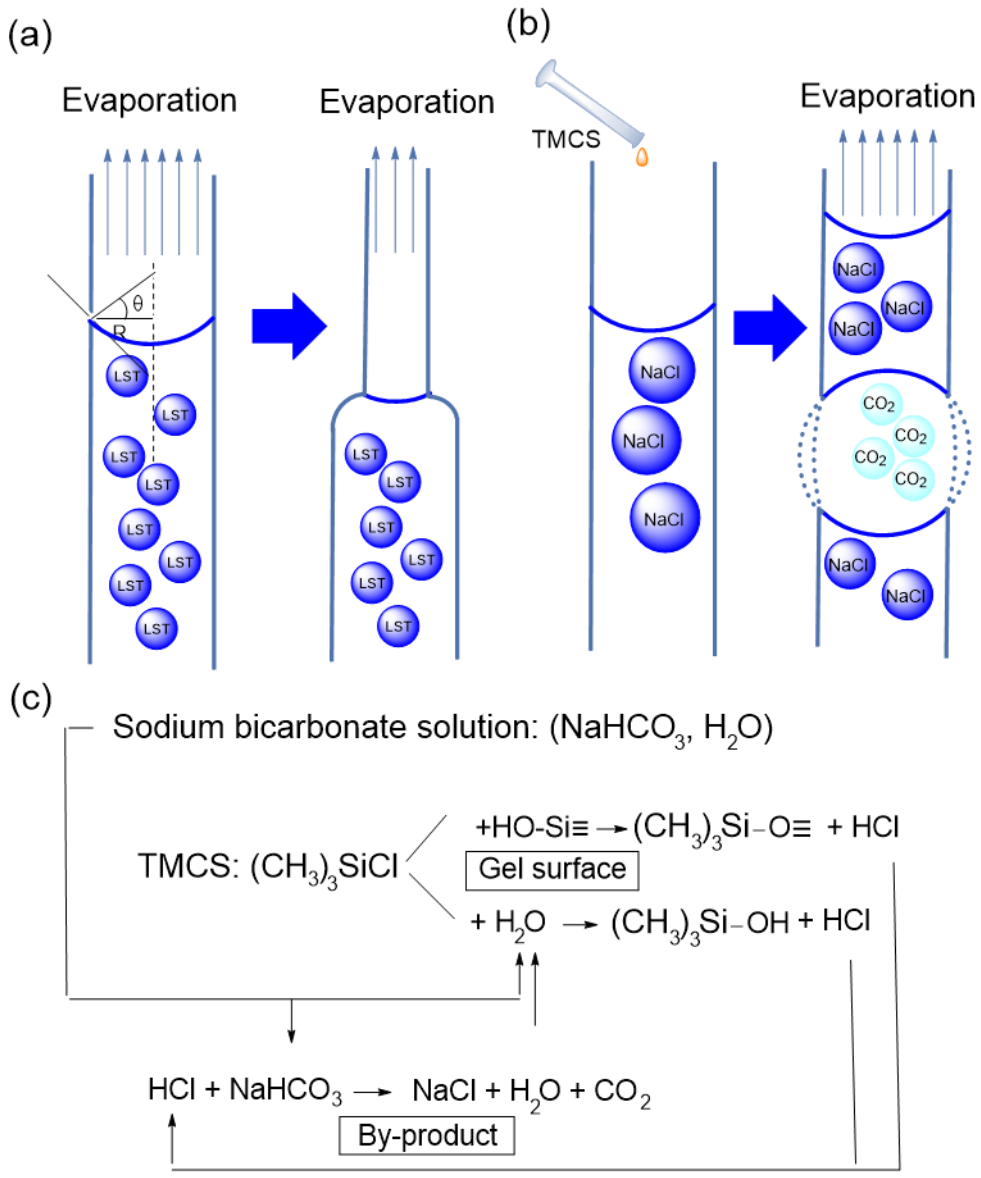

Figure 1. 11. A schematic comparison between ambient pressure drying methods for aerogels. (a) conventional APD using an organic low surface tension (LST) solvent. (b) APD using inorganic sodium bicarbonate solution. (c) A proposed net-chemical-reaction route in the sodium bicarbonate solution APD method with TMCS ($(CH_3)_3SiCl$) (Han *et al.*, 2018).

1.5 Mechanical reinforcement of silica aerogels

The inherited properties of brittleness, low compressive strength and overall low mechanical properties of aerogels are the main barriers for the commercialisation of aerogels (Chen *et al.*, 2012). A great effort is dedicated by researchers to improve mechanical properties of silica aerogels (Leventis, 2007). Three outlined challenges could limit the industrialisation of silica aerogels which are: brittleness, high manufacturing cost and instability in moist atmospheres. Therefore, further optimisation of the manufacturing cost and mechanical properties of aerogels will ensure their use as thermal or acoustic insulators (Meador *et al.*, 2005).

Many strategies are used to overcome the associated drawbacks of the weakness and brittleness of silica aerogels. Here is a short description of some common reinforcing strategies.

Hybridisation

The strengthening of silica aerogels can be achieved through hybridisation. (Yim *et al.*, 2002). Modifying the internal surface of the pores to be hydrophobic rather than hydrophilic via emerging organic functional groups improves the resistance of silica gel against shrinking and water (Hayase *et al.*, 2011). Hybridisation is carried out by co-gelation of silicon alkoxide like TEOS with trifunctional organosilane precursors such as methyltrimethoxysilane (MTMS) and methyltriethoxysilane (MTES). The obtained flexibility and elastic properties of silica aerogels are achieved by hybridisation that comes from obtaining the organosilane compounds when one silicon atom has a non-hydrolysable group. Hybrid aerogels were intensively studied in literature in order to improve the mechanical and hydrophobicity properties of aerogels.

Hegde and Rao (2007) investigated the change in flexibility of hybrid silica aerogels with the change in molar ratio of MeOH/MTMS. The molar ratio of MTMS: MeOH: acidic water: basic water was 1:35:3.97:3.97, respectively which gives the best elastic and hydrophobic properties to silica aerogels.

Pan *et al.* (2017) used a freeze-drying method for the synthesis of a hybrid silica aerogels from MTMS and water glass precursors aiming to enhance the mechanical performance, maintain the mesoporous structure and produce a suitable low thermal conductivity material for thermal insulation application.

Employing inorganic functional groups could also enhance the mechanical properties and provide elastic recovery properties for silica aerogels. Ehgartner *et al.* (2017) produced flexible silica aerogels using MTMS precursor and organic functional alkoxysilanes via drying by supercritical extraction with CO_2. The synthesised aerogels were found to have a good elastic recovery of up to 60% under uniaxial compression test.

Polymer cross-linking

Introducing crosslinking polymers into silica backbone is a common way to improve the mechanical strength of the silica aerogels (Lamy-Mendes *et al.*, 2018). Resulting composites have unique properties from both organic and inorganic materials (Randall *et al.*, 2011; Maleki *et al.*, 2014a). Chemically, polymer-aerogels composites can be classified into two classes. Class I which can be described as a physical mixing in which both polymer and silica network phases are completely independent from each other and bonded via van der Waals forces or

hydrogen bonding. While in class II there are covalent bonds between the components (Sanchez and Ribot, 1994; Capadona *et al.*, 2006). The most notable examples of class I is the physical dissolving of biomolecules or organic dyes with inorganic precursor such as TEOS or TOMS (Maleki *et al.*, 2014a). Class II provides lightweight insulation materials for space and commercial applications (Capadona *et al.*, 2006). Introducing cross-linking polymers into the structure enhances the strength of silica aerogels. Cross-linking can be achieved be modifying the structure of silica aerogel with functional groups such as di or tri isocyanate to form urethane groups or using amine groups to make crosslinking with polymers such as poly-functionalised epoxy, isocyanates and cyanoacrylate (Shahzamani *et al.*, 2016).

Modifying aerogel's structure by amine groups is reported to introduce the hydrophobicity and to introduce organic groups to native silica structure, which gives flexibility to silica aerogel. Li *et al.* (2017b) utilised 3-aminopropyltriethoxysilane (APTES) to introduce hydrophobicity and to strengthen the structure of the silica aerogel via reacting those groups with isocyanates (hexamethylene diisocyanate (HDI), see Figure 1. 12).

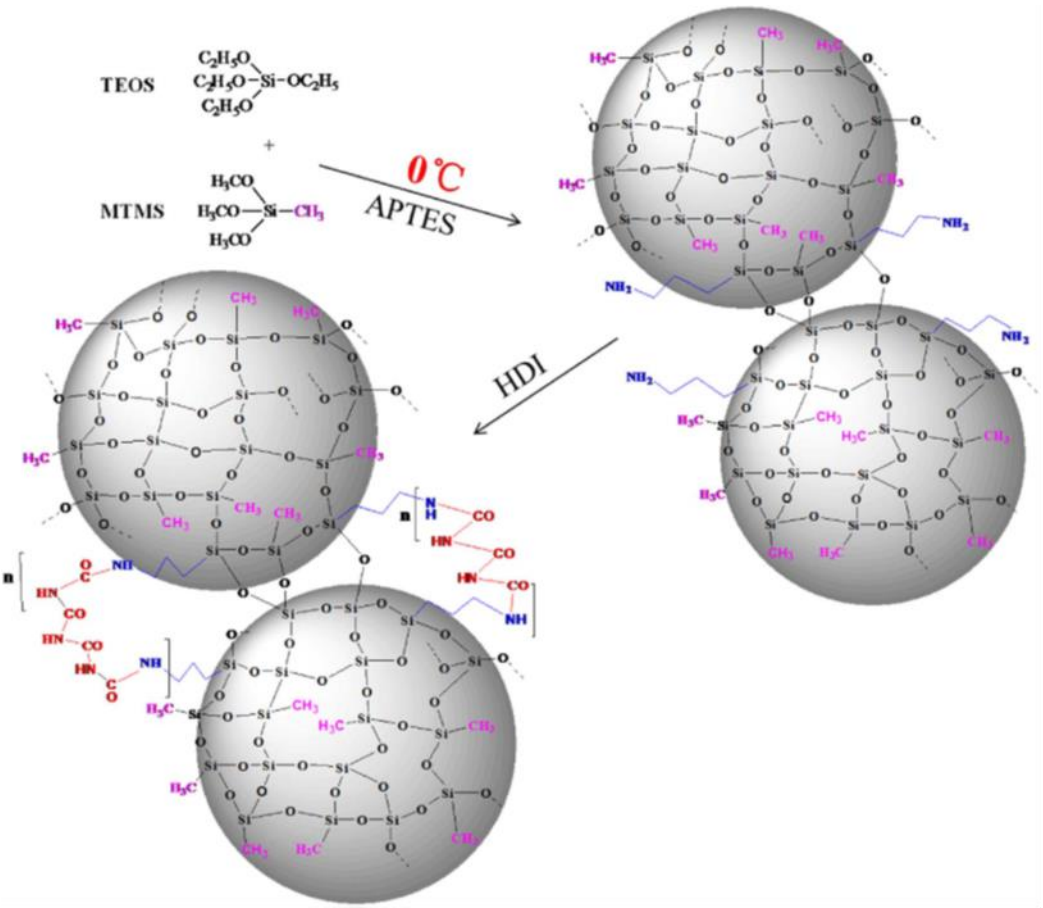

Figure 1. 12. In-situ amine modification, hydrophobisation and isocyanate cross-linking of silica aerogels. Where (APTES) is 3-aminopropyltriethoxysilane and (HDI) is hexamethylene diisocyanate (Li *et al.*, 2017b).

Wu *et al.* (2018) investigated the synthesis for robust and more hydrophobic silica aerogels by using in situ synthesis hybridisation method of propyltriethoxysilane (PTES) with tetraethylorthosilicate (TEOS) by sol-gel process.

Reinforcement by secondary materials

Synthesis of silica aerogels by the sol-gel process enables amending and improving native properties of silica aerogel networks. Some common silica aerogel additives are nanoparticles, fibres or nanofibers (Lamy-Mendes *et al.*, 2018). Reinforcement with fibres or mats is a common solution to tackle the drawback of scaling up silica aerogel. Recently, tremendous efforts on fibres reinforcement of silica aerogels were devoted to produce appropriate composite materials for industrial applications. For instance, glass-fibres is reported by Ul Haq *et al.* (2017) to be used for reinforcing silica aerogels derived from MTMS and from TEOS precursors and dried by the freeze drying method to produce hydrophobic and hydrophilic silica aerogels composites. While Li *et al.* (2017a) prepared glass fibres reinforced TEOS-based silica aerogel composites via ambient pressure drying method for fire resistance. Also, microglass fibres are used to reinforce silica aerogels (Jiang *et al.*, 2017b).

On the other hand, reinforcement with organic fibres have been reported in the literature too. For example, polyacrylonitrile fibres are utilised to improve the mechanical properties of silica aerogels and to produce lightweight hydrophobic silica aerogel composites for oil absorption applications (Shi *et al.*, 2017). Polyester fibres are also used for reinforcing silica aerogel composites for vacuum insulation panels (VIPs) production (Li *et al.*, 2016). Furthermore, Aramid fibres (He *et al.*, 2017), carbon fibres (Slosarczyk, 2017b), graphene oxide (Dervin *et al.*, 2017) and cellulose fibres (Jaxel *et al.*, 2017) are devoted to enhance the mechanical properties of silica aerogels.

In order to obtain the desired properties, it is important to insure the homogeneous distribution of fibres inside the aerogel. This can be achieved through control of the gelation stage by preventing the fibres sedimentation. A summary of reported fibres used to enhance the mechanical properties of silica aerogels are presented in the schematic diagram in Figure 1. 13 (Slosarczyk, 2017a).

In the past few years, aerogel blankets (fibres, silica aerogels, opacifiers and optional binders) have been developed as effective materials for thermal insulation in aerospace applications. In general, the synthesis is based on organic or inorganic porous fibre blankets that are soaked in the silica sol during sol-gel process and then dried via supercritical or ambient pressure drying

method (Hoseini *et al.*, 2016a; Berthon-Fabry *et al.*, 2017; Lakatos, 2017b; Lakatos, 2017a; Lee *et al.*, 2018).

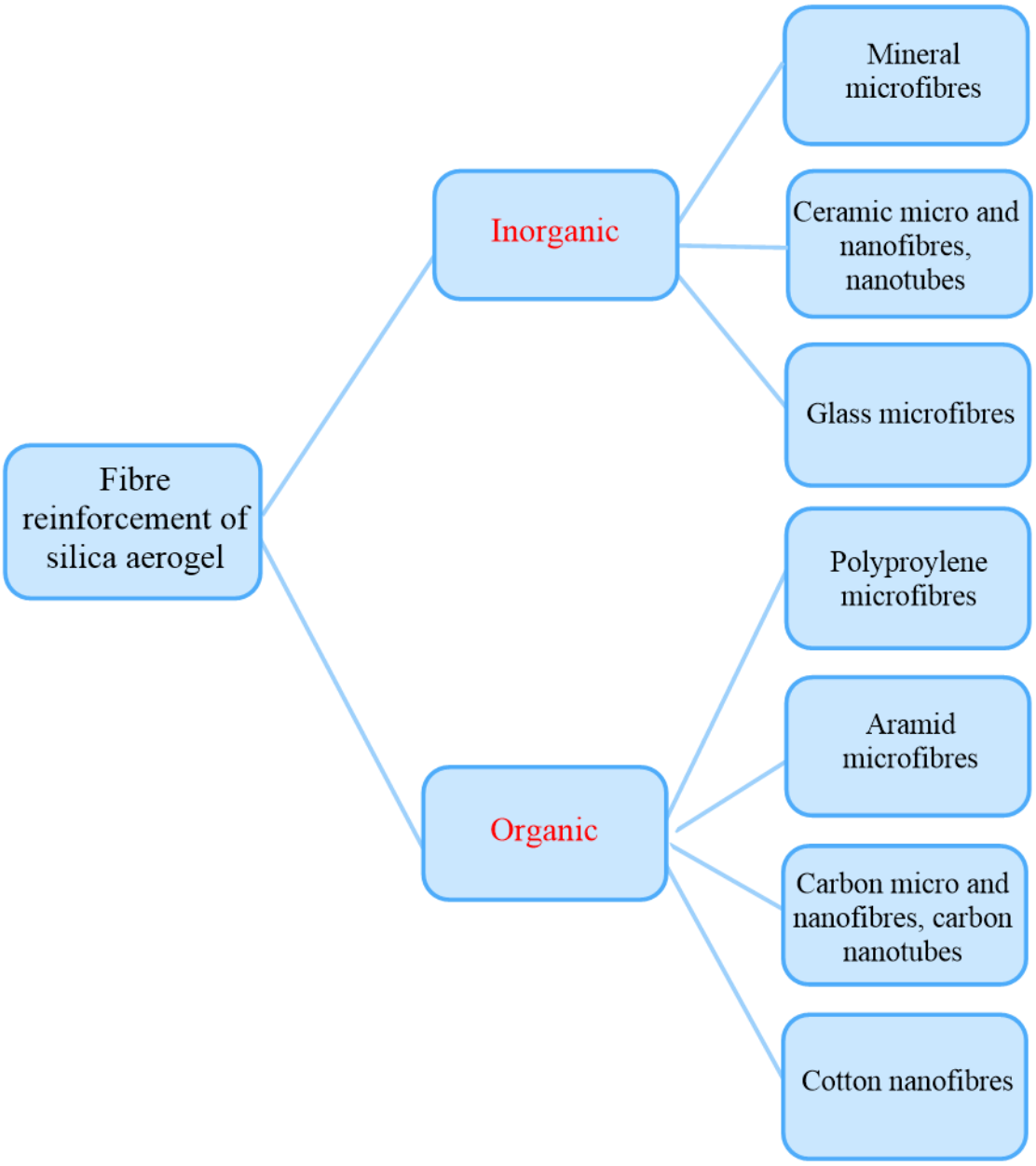

Figure 1. 13. Reinforcing fibres of silica aerogels nanocomposites (Slosarczyk, 2017a).

Due to its mechanical stability and low thermal conductivity (0.017-0.04 W m^{-1} K^{-1}), the aerogel's blanket structure provides a solution for the improvement of the mechanical properties of silica aerogels and a reduction of the heat transfer through original fibres mat. An additional advantage of incorporating aerogel is filling the gaps between fibres, which reduces the further gas conducting (Hoseini *et al.*, 2016b). Reinforcement fibres are coated with silica aerogel particles as can be seen in Figure 1. 14 in case of silica aerogels reinforced with glass fibres (Yang *et al.*, 2017).

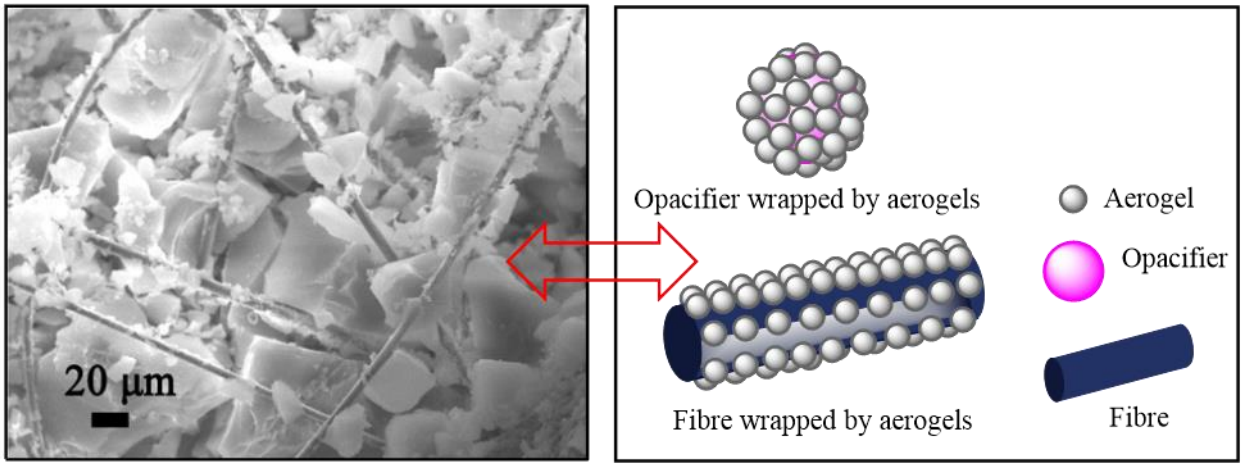

Figure 1. 14. Real scanning electron microscopy image of silica aerogels with glass fibres and assumed physical structure of silica aerogels with glass fibres (Yang *et al.*, 2017).

1.6 Aerogels applications

Currently there is a consensus among scientists about the outstanding properties of aerogels, which enables the material to be used for a wide range of applications. It can be used in roofs, on windows, as solar collectors or sound insulators. This section highlights the most recent research and applications of aerogels.

1.6.1. Thermal insulation

In the last few decades and as a result of increased greenhouse emission, tremendous effort has been carried out on optimising transportation systems such as cars, trains and aviation. Today, it is necessary to optimise the energy consumption of HVAC system (heating, ventilation and air conditioning) of buildings. To do that, it is important to increase the isolation efficiency. Reducing the heat loss through thermal insulation can be carried out by increasing the thickness of the insulation materials. However, that solution is accompanied with additional space consumption (Koebel *et al.*, 2012).

With the continuous increase in construction of commercial and residential buildings, it is necessary to employ high performance thermal insulation materials in order to reduce both the consumption of energy and the space that is occupied by the conventional insulators. In addition, usage of superinsulation materials in HVAC systems of building is a facile solution to tackle the increase in emission of the greenhouse gases (Hoseini *et al.*, 2016b). Figure 1. 15 illustrates the relationship between the performance and the cost of the insulation materials (Koebel *et al.*, 2012).

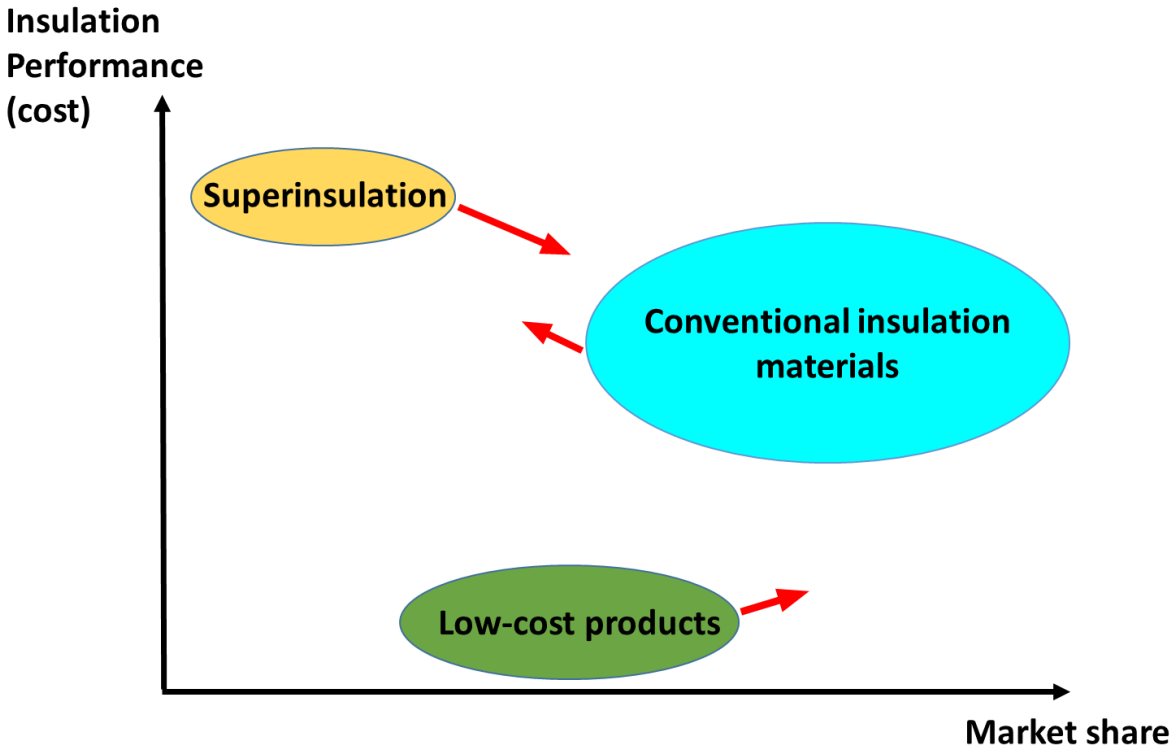

Figure 1. 15. Market share displayed by cost/performance: high-performance (superinsulation) and low-cost products have smaller market shares. The red arrows symbolize the expected development of each segment in the future (Koebel *et al.*, 2012).

The recent development for the synthesis of silica aerogels and their composites at ambient pressure indicates a promising super insulative material could potentially be produced for the superinsulation materials in building sector. For example, aerogel blankets have shown many benefits such as effective insulation properties, lightweight and space saver while the incorporation of aerogels in glazing systems is under development (Berardi, 2018).

Despite the promising thermal properties of silica aerogel composites, the thermal insulation market is still dominated by conventional insulators due to their lower costs. The thermal efficiency of insulative materials is commonly described by a factor of thermal transmittance which is also known as the U-value. The U-value for a surface of a designed construction material is defined as the rate of heat transfer in watts per square meter for each degree difference in temperature of air between the outdoor and indoor of construction (Selves *et al.*, 2013). Therefore, in order to calculate the U-value for a simple construction, the U-value is found to be the reciprocal of the total thermal resistance (R-value),

$$U = \frac{1}{R} (\mathrm{W/m^2\,K}) \qquad (1.4)$$

where total thermal resistance R is

$$R = R_{si} + R_1 + R_2 + R_3 + R_a + R_{so} \quad (1.5)$$

where R_{si} and R_{so} are the thermal resistances of the inner and outer surfaces of layer, respectively. R_1, R_2 and R_3 are the thermal resistances of elements. R_a is the thermal resistance of an air space or cavity. The thermal resistance can be calculated from the following formula:

$$R = \frac{t}{\lambda} \text{ m}^2\text{K/W} \quad (1.6)$$

where t is the thickness of the material and λ is the thermal conductivity (Selves *et al.*, 2013).

For example, in the UK, the insulation thickness for modern houses must achieve a U-value of 0.3 W m^{-2} K^{-1}. To reach that value, using conventional insulation materials, a thick layer of insulation is required. Figure 1. 16 illustrates the cost gap between the conventional insulation and superinsulation. However, (Cuce *et al.*, 2014) reported that by 2050, the predicted manufacturing cost of silica aerogels is to be below £500 per m^3. It is a clear fact that in order to compete with conventional insulative materials, an intensive effort needs to be done on manufacturing cost of aerogels to be more cost effective (Cuce *et al.*, 2014).

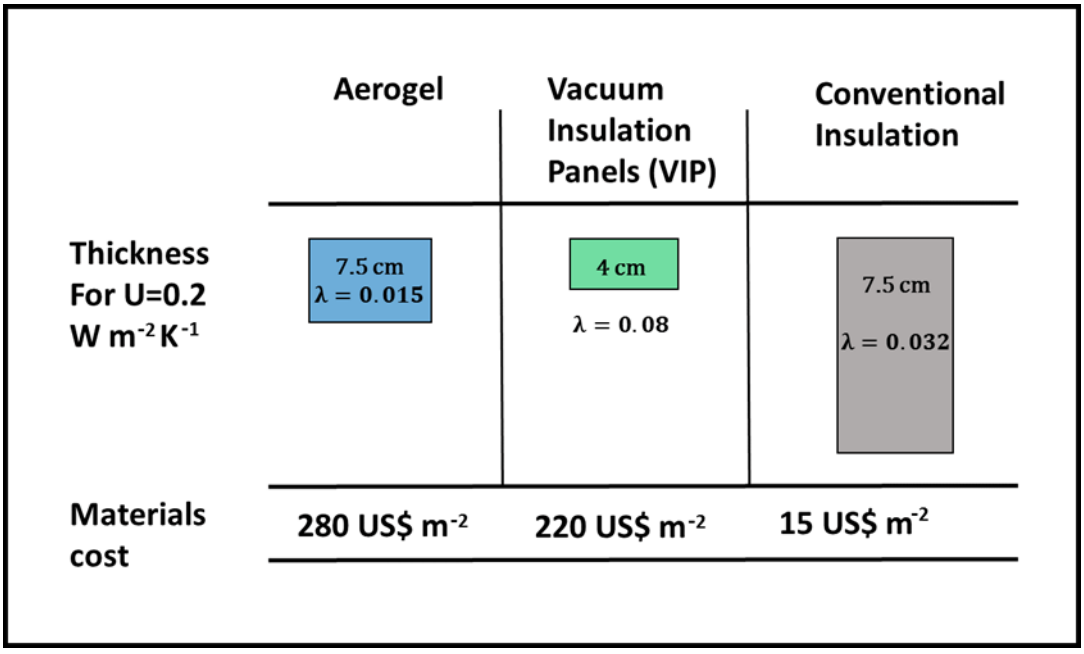

Figure 1. 16. Comparison between superinsulation and conventional insulation in terms of costs and space savings (Cuce *et al.*, 2014).

1.6.2. Silica aerogels as support to catalysts

The open porous structure and high surface area properties of aerogels among nanostructure materials empower the effective hosting of nanoparticles. In addition, the open porous structure of aerogels enables an effective mass transfer of gas- phase or reactant molecules to reach the active sites. All those properties in addition to good thermal stability makes aerogels attractive hosting materials for catalytic applications (Amiri *et al.*, 2016).

Because of the thermal stability of SiO_2 and Al_2O_3, they were used more than other materials as catalysts supports (Zheng *et al.*, 2015; Zhao *et al.*, 2017). Amiri and Moghaddas (2015) synthesised copper-silica aerogels catalysts for hydrogen production from methanol reforming by cogelation of copper and sodium silicate precursors followed by ambient pressure drying method. Li *et al.* (2013) utilised silica aerogels to support Ni nanoparticles as a catalyst for a partial oxidation of methane. In addition, silica aerogels are used with Fe and Mo bimetallic nanoparticles to make a porous nanocomposite catalyst in synthesis multi wall carbon nanotubes by chemical vapour deposition method (Marras *et al.*, 2015). While, Han *et al.* (2015) employed silica aerogels synthesised by ambient pressure drying method to support Ni nanoparticles for carbon dioxide hydration reaction. Alumina aerogels are also employed to support catalyst nanoparticles. Zhao *et al.* (2017) synthesised Ni nanoparticles confined in alumina aerogel and silicon carbide (SiC) in order to promote catalysis of dry reforming of methane (DRM). The high stability of mesoporous alumina aerogels prevents Ni nanoparticles from sintering and allows the SiC decoration for better catalytic performance.

1.6.3. Other applications of aerogels

Recently, aerogels have been widely used in many applications. One promising usage of aerogels is to minimise anthropogenic emission of greenhouse gases. Modifying aerogel with amine groups is a facile way for CO_2 capture (Kong *et al.*, 2016). For example, silica aerogels which are modified using 3-aminopropyltriethoxysilane (APTES) (Kong *et al.*, 2016), tetraethylenepentamine (TEPA) and polyethyleneimine (PEI) (Sanz *et al.*, 2013) are employed for CO_2 capture. Air pollution also involves vapours of organics, which are emitted by vehicle exhausts and industries. Activated carbon and silica aerogels indicate the possibility to be excellent sorbent candidates to adsorb organic vapours (Maleki, 2016). Water remediation is another important application of aerogels. Graphene oxide based-aerogels are reported to have adsorption capacity of 220 mg g^{-1} in one hour and as high as 397 mg g^{-1} at equilibrium for adsorption of indigo disulphonate dye (Pan *et al.*, 2018). In addition, incorporation of graphene

in SiO_2 aerogels promote the hydrophobic properties and develops the selectivity towards oil sorbent from water (Mi *et al.*, 2018). In pharmaceutical applications, the high porosity and surface area of aerogels provide a good solution to overcome the drawbacks in drug delivery that are related to both toxicity and water solubility. Depending on the affinity and stability properties of the drug in the solvent, it is possible to load the drug at any stage of aerogel synthesis while the release of the drug will depend on the nature of the aerogel (Maleki *et al.*, 2016). Aerogels are also used as an efficient material for solar energy harvesting (Fu *et al.*, 2017). Recently, graphene oxide and graphene aerogels have been receiving a lot of attention in solar stream generation which is used to generate solar vapour because of their large surface area, porosity, and high light absorbance. Those unique properties enlarged their evaporation efficiency (Fu *et al.*, 2017; Fu *et al.*, 2018).

1.7 Research objectives and motivations

Currently, scientists are spending a great deal of effort on the development of aerogels and getting the benefits from their distinctive properties is always faced with the manufacturing costs and environmental and safety issues. Therefore, in an attempt to cut off the manufacturing cost and to reduce the produced chemical waste of ambient pressure drying method, a novel approach has been developed by Xiao Han and Lidija Šiller in our nanoscale science and nanotechnology group at Newcastle university, based on drying silica aerogels synthesised from TEOS precursor and dried at ambient pressure using sodium bicarbonate solution rather than organic solvents (Han and Šiller, 2015). However, the mechanical properties of silica aerogels which are prepared by this novel method still have to be improved. In addition, in order to prove the general validity of the novel approach, the proposed approach has to be applied to other precursors.

The current proposed PhD work is an attempt to reach the following goals:

Fibre-reinforced silica aerogels

One of the most promising applications of silica aerogels is replacing the currently used conventional insolation materials with super-insulators. Reinforcement with different kinds of fibres is the best way to tackle the drawback in mechanical properties of silica aerogels and to produce reinforced-silica aerogels composites for thermal applications. The aim of this part of the thesis is to produce low cost, lightweight and environmentally friendly super-thermal insulation panels, which can be used for a variety of applications. Fabrication of silica aerogel blankets and fibre-reinforced silica aerogel composites using short ceramic fibres are the main

focus of this part of the thesis. In addition, an investigation into the mechanical and thermal properties of silica aerogels composites had to be performed. The characterisation of both types of fibre reinforcement aerogel composites are presented in chapter 3 of this thesis.

Extending the novel approach

The capability of the novel approach to become a facile low cost and environmentally friendly method for the synthesis of aerogels had to be proved further. To fulfil that, the approach needs to be extended and applied to other precursors. Therefore, the credibility of the approach was investigated on the synthesis of silica aerogels from water glass precursor, which is the cheapest and most promising precursors to produce low cost silica aerogels. In addition, an alumina precursor was utilised to produce aerogels using the novel approach. The results and characterisations of synthesised water glass-based silica aerogels and dawsonite aerogels are presented in chapter 4 and chapter 5 of this thesis, respectively.

Synthesis of multi-layered silica aerogels

The novel approach was originally inspired by the drying process of a damselfly's wings. Damselfly wings are lightweight, relatively strong and they consist of very thin porous layers. The structure of these wings inspired us to synthesise multi-layered silica aerogel films. The novel approach has been applied for that purpose. Synthesis and characterisations of the multi-layered silica aerogels are presented in detail in chapter 6 of this thesis.

Immobilisation of Nickle Nanowires (NiNWs) in silica aerogels

An early study of embedded nickel nanoparticles in silica aerogels was carried out by Han *et al.* (2015). That study focused on supporting NiNPs by silica aerogel and investigating the catalytic activity of embedded NiNPs for carbon dioxide hydration reaction in aqueous solution (Han *et al.*, 2015). However, it is important to investigate different types of nanostructures of nickel in addition to the investigation of the catalytic activity in the gaseous phase. Therefore, the main aim of this part (all characterisation and experiments are presented in chapter 7 of this thesis) of thesis was to synthesise and investigate the catalytic activity of immobilised nickel nanowires (NiNWs) in silica aerogels in gaseous phase for carbon dioxide hydration reaction by using dynamic vapour sorption analysis (DVS) technology.

1.8 Conclusion

Chapter 1 focuses on summarising different techniques used to synthesise aerogel as well as potential applications of silica aerogels prepared via the sol-gel process. This chapter also describes the main three common drying methods (supercritical drying, freeze-drying and ambient pressure drying methods) to produce aerogels. In addition, we present the recently proposed sodium bicarbonate based-ambient pressure drying approach which is developed by Han and Šiller (Han and Šiller, 2015) to synthesise silica aerogels from TEOS precursor. In addition, this chapter highlights some promising applications of aerogels. Furthermore, this review outlines aims, and objects of the research presented in the next chapters of this PhD thesis.

References

Aegerter, M.A., Leventis, N. and Koebel, M.M. (2011) *Aerogels Handbook*. Springer.

Amiri, T.Y. and Moghaddas, J. (2015) 'Cogeled copper-silica aerogel as a catalyst in hydrogen production from methanol steam reforming', *International Journal of Hydrogen Energy*, 40(3), pp. 1472-1480.

Amiri, T.Y., Moghaddas, J. and Khajeh, S.R. (2016) 'Silica aerogel-supported copper catalyst prepared via ambient pressure drying process', *Journal of Sol-Gel Science and Technology*, 77(3), pp. 627-635.

Bangi, U.K.H., Park, C.S., Baek, S. and Park, H.H. (2012) 'Improvement in optical and physical properties of TEOS based aerogels using acetonitrile via ambient pressure drying', *Ceramics International*, 38(8), pp. 6883-6888.

Berardi, U. (2018) 'Aerogel-enhanced systems for building energy retrofits: Insights from a case study', *Energy and Buildings*, 159, pp. 370-381.

Berthon-Fabry, S., Hildenbrand, C., Ilbizian, P., Jones, E. and Tavera, S. (2017) 'Evaluation of lightweight and flexible insulating aerogel blankets based on Resorcinol-Formaldehyde-Silica for space applications', *European Polymer Journal*, 93, pp. 403-416.

Bhagat, S.D., Oh, C.S., Kim, Y.H., Ahn, Y.S. and Yeo, J.G. (2007) 'Methyltrimethoxysilane based monolithic silica aerogels via ambient pressure drying', *Microporous and Mesoporous Materials*, 100(1-3), pp. 350-355.

Blaszczynski, T., Slosarczyk, A. and Morawski, M. (2013) 'Synthesis of silica aerogel by supercritical drying method', in Juozapaitis, A., Vainiunas, P. and Zavadskas, E.K. (eds.) *Modern Building Materials, Structures and Techniques*. Amsterdam: Elsevier Science Bv, pp. 200-206.

Brinker, C.J. (1988) 'Hydrolysis And Condensation Of Silicates- Effects On Structure', *Journal of Non-Crystalline Solids*, 100(1-3), pp. 31-50.

Capadona, L.A., Meador, M.A.B., Alunni, A., Fabrizio, E.F., Vassilaras, P. and Leventis, N. (2006) 'Flexible, low-density polymer crosslinked silica aerogels', *Polymer*, 47(16), pp. 5754-5761.

Chen, Q., Wang, S. and Li, Z. (2012) 'Fabrication and characterization of aluminum silicate fiber-reinforced hollow mesoporous silica microspheres composites', *Microporous and Mesoporous Materials*, 152, pp. 104-109.

Cuce, E., Cuce, P.M., Wood, C.J. and Riffat, S.B. (2014) 'Toward aerogel based thermal superinsulation in buildings: A comprehensive review', *Renewable & Sustainable Energy Reviews*, 34, pp. 273-299.

Deng, Z.S., Wang, J., Wu, A.M., Shen, J. and Zhou, B. (1998) 'High strength SiO_2 aerogel insulation', *Journal of Non-Crystalline Solids*, 225(1), pp. 101-104.

Dervin, S., Lang, Y., Perova, T., Hinder, S.H. and Pillai, S.C. (2017) 'Graphene oxide reinforced high surface area silica aerogels', *Journal of Non-Crystalline Solids*, 465, pp. 31-38.

Dourbash, A., Buratti, C., Belloni, E. and Motahari, S. (2017) 'Preparation and characterization of polyurethane/silica aerogel nanocomposite materials', *Journal of Applied Polymer Science*, 134(8), p. 13.

Ehgartner, C.R., Grandl, S., Feinle, A. and Husing, N. (2017) 'Flexible organofunctional aerogels', *Dalton Transactions*, 46(27), pp. 8809-8817.

Einarsrud, M.A., Nilsen, E., Rigacci, A., Pajonk, G.M., Buathier, S., Valette, D., Durant, M., Chevalier, B., Nitz, P. and Ehrburger-Dolle, F. (2001) 'Strengthening of silica gels and aerogels by washing and aging processes', *Journal of Non-Crystalline Solids*, 285(1-3), pp. 1-7.

Feng, J.D., Le, D.Y., Nguyen, S.T., Nien, V.T.C., Jewell, D. and Duong, H.M. (2016) 'Silica-cellulose hybrid aerogels for thermal and acoustic insulation. applications', *Colloids and Surfaces a-Physicochemical and Engineering Aspects*, 506, pp. 298-305.

Fu, Y., Wang, G., Mei, T., Li, J.H., Wang, J.Y. and Wang, X.B. (2017) 'Accessible graphene aerogel for efficiently harvesting solar energy', *Acs Sustainable Chemistry & Engineering*, 5(6), pp. 4665-4671.

Fu, Y., Wang, G., Ming, X., Liu, X.H., Hou, B.F., Mei, T., Li, J.H., Wang, J.Y. and Wang, X.B. (2018) 'Oxygen plasma treated graphene aerogel as a solar absorber for rapid and efficient solar steam generation', *Carbon*, 130, pp. 250-256.

Gurav, J.L., Jung, I.K., Park, H.H., Kang, E.S. and Nadargi, D.Y. (2010) 'Silica aerogel: synthesis and applications', *Journal of Nanomaterials*, pp. 1-11.

Gurav, J.L., Rao, A.V., Rao, A.P., Nadargi, D.Y. and Bhagat, S.D. (2009) 'Physical properties of sodium silicate based silica aerogels prepared by single step sol-gel process dried at ambient pressure', *Journal of Alloys and Compounds*, 476(1-2), pp. 397-402.

Haereid, S., Anderson, J., Einarsrud, M.A., Hua, D.W. and Smith, D.M. (1995) 'Thermal and temporal aging of TMOS-based aerogel precursors in water', *Journal of Non-Crystalline Solids*, 185(3), pp. 221-226.

Han, X., Hassan, K.T., Harvey, A., Kulijer, D., Oila, A., Hunt, M.R.C. and Šiller, L. (2018) 'Bioinspired synthesis of monolithic and layered aerogels', *Advanced Materials*, p. 1706294 (1 of 7).

Han, X. and Šiller, L. (2015) 'Aerogel synthesis', P221149GB/DW(WO2016132117 A1).

Han, X., Williamson, F., Bhaduri, G.A., Harvey, A. and Šiller, L. (2015) 'Synthesis and characterisation of ambient pressure dried composites of silica aerogel matrix and embedded nickel nanoparticles', *J. Supercrit. Fluids* 106, pp. 140-144.

Hayase, G., Kanamori, K., Kazuki, K., Hanada, T. and Iop (2011) 'Synthesis of new flexible aerogels from MTMS/DMDMS via ambient pressure drying', *3rd International Congress on Ceramics*. pp. 1-5. Available at: <Go to ISI>://WOS:000299436300013.

Hayase, G., Kugimiya, K., Ogawa, M., Kodera, Y., Kanamori, K. and Nakanishi, K. (2014) 'The thermal conductivity of polymethylsilsesquioxane aerogels and xerogels with varied pore sizes for practical application as thermal superinsulators', *Journal of Materials Chemistry A*, 2(18), pp. 6525-6531.

He, F., Zhao, H.L., Qu, X.H., Zhang, C.J. and Qiu, W.H. (2009) 'Modified aging process for silica aerogel', *Journal of Materials Processing Technology*, 209(3), pp. 1621-1626.

He, S., Sun, G.X., Cheng, X.D., Dai, H.M. and Chen, X.F. (2017) 'Nanoporous SiO_2 grafted aramid fibers with low thermal conductivity', *Composites Science and Technology*, 146, pp. 91-98.

Hegde, N.D. and Rao, A.V. (2007) 'Physical properties of methyltrimethoxysilane based elastic silica aerogels prepared by the two-stage sol-gel process', *Journal of Materials Science*, 42(16), pp. 6965-6971.

Hoseini, A., Malekian, A. and Bahrami, M. (2016a) 'Deformation and thermal resistance study of aerogel blanket insulation material under uniaxial compression', *Energy and Buildings*, 130, pp. 228-237.

Hoseini, A., McCague, C., Andisheh-Tadbir, M. and Bahrami, M. (2016b) 'Aerogel blankets: From mathematical modeling to material characterization and experimental analysis', *International Journal of Heat and Mass Transfer*, 93, pp. 1124-1131.

Iswar, S., Malfait, W.J., Balog, S., Winnefeld, F., Lattuada, M. and Koebel, M.M. (2017) 'Effect of aging on silica aerogel properties', *Microporous and Mesoporous Materials*, 241, pp. 293-302.

Jaxel, J., Markevicius, G., Rigacci, A. and Budtova, T. (2017) 'Thermal superinsulating silica aerogels reinforced with short man-made cellulose fibers', *Composites Part a-Applied Science and Manufacturing*, 103, pp. 113-121.

Jiang, L., Kato, K., Mayumi, K., Yokoyama, H. and Ito, K. (2017a) 'One-pot synthesis and characterization of polyrotaxane-silica hybrid aerogel', *Acs Macro Letters*, 6(3), pp. 281-286.

Jiang, Y.G., Feng, J.Z. and Feng, J. (2017b) 'Synthesis and characterization of ambient-dried microglass fibers/silica aerogel nanocomposites with low thermal conductivity', *Journal of Sol-Gel Science and Technology*, 83(1), pp. 64-71.

Kim, H. and Popov, B.N. (2002) 'Characterization of hydrous ruthenium oxide/carbon nanocomposite supercapacitors prepared by a colloidal method', *Journal of Power Sources*, 104(1), pp. 52-61.

Kistler, S.S. (1931) 'Coherent expanded aerogels and jellies', *Nature*, 127, p. 741.

Koebel, M., Rigacci, A. and Achard, P. (2012) 'Aerogel-based thermal superinsulation: an overview', *Journal of Sol-Gel Science and Technology*, 63(3), pp. 315-339.

Kong, Y., Jiang, G.D., Wu, Y., Cui, S. and Shen, X.D. (2016) 'Amine hybrid aerogel for high-efficiency CO_2 capture: Effect of amine loading and CO_2 concentration', *Chemical Engineering Journal*, 306, pp. 362-368.

Kumar, A., Rana, A., Sharma, G., Sharma, S., Naushad, M., Mola, G.T., Dhiman, P. and Stadler, F.J. (2018) 'Aerogels and metal-organic frameworks for environmental remediation and energy production', *Environmental Chemistry Letters*, 16(3), pp. 797-820.

Lakatos, A. (2017a) 'Comprehensive thermal transmittance investigations carried out on opaque aerogel insulation blanket', *Materials and Structures*, 50(1), p. 12.

Lakatos, A. (2017b) 'Investigation of the moisture induced degradation of the thermal properties of aerogel blankets: Measurements, calculations, simulations', *Energy and Buildings*, 139, pp. 506-516.

Lamy-Mendes, A., Silva, R.F. and Duraes, L. (2018) 'Advances in carbon nanostructure-silica aerogel composites: a review', *Journal of Materials Chemistry A*, 6(4), pp. 1340-1369.

Lee, K.J., Choe, Y.J., Kim, Y.H., Lee, J.K. and Hwang, H.J. (2018) 'Fabrication of silica aerogel composite blankets from an aqueous silica aerogel slurry', *Ceramics International*, 44(2), pp. 2204-2208.

Leventis, N. (2007) 'Three-dimensional core-shell superstructures: Mechanically strong aerogels', *Accounts of Chemical Research*, 40(9), pp. 874-884.

Leventis, N., Sotiriou-Leventis, C., Zhang, G.H. and Rawashdeh, A.M.M. (2002) 'Nanoengineering strong silica aerogels', *Nano Letters*, 2(9), pp. 957-960.

Li, C.C., Cheng, X.D., Li, Z., Pan, Y.L., Huang, Y.J. and Gong, L.L. (2017a) 'Mechanical, thermal and flammability properties of glass fiber film/silica aerogel composites', *Journal of Non-Crystalline Solids*, 457, pp. 52-59.

Li, C.D., Li, B.B., Pan, N., Chen, Z.F., Saeed, M.U., Xu, T.Z. and Yang, Y. (2016) 'Thermo-physical properties of polyester fiber reinforced fumed silica/hollow glass microsphere composite core and resulted vacuum insulation panel', *Energy and Buildings*, 125, pp. 298-309.

Li, Q., Hou, Y.H., Dong, L.Y., Huang, M.X., Weng, W.Z., Xia, W.S. and Wan, H.L. (2013) 'Catalytic behaviors and stability of aerogel silica-supported Ni catalysts for the partial oxidation of methane into synthesis gas', *Acta Physico-Chimica Sinica*, 29(10), pp. 2245-2254.

Li, S.Q., Ren, H.B., Zhu, J.Y., Bi, Y.T., Xu, Y.W. and Zhang, L. (2017b) 'Facile fabrication of superhydrophobic, mechanically strong multifunctional silica-based aerogels at benign temperature', *Journal of Non-Crystalline Solids*, 473, pp. 59-63.

Lin, Y.F. and Kuo, J.W. (2016) 'Mesoporous bis(trimethoxysilyl)hexane (BTMSH)/tetraethyl orthosilicate (TEOS)-based hybrid silica aerogel membranes for CO_2 capture', *Chemical Engineering Journal*, 300, pp. 29-35.

Liu, H., Xia, X.L., Ai, Q., Xie, X.Q. and Sun, C. (2017) 'Experimental investigations on temperature-dependent effective thermal conductivity of nanoporous silica aerogel composite', *Experimental Thermal and Fluid Science*, 84, pp. 67-77.

Lu, X., Arduinischuster, M.C., Kuhn, J., Nilsson, O., Fricke, J. and Pekala, R.W. (1992) 'Thermal-conductivity of monolithic organic aerogels', *Science*, 255(5047), pp. 971-972.

Maleki, H. (2016) 'Recent advances in aerogels for environmental remediation applications: A review', *Chemical Engineering Journal*, 300, pp. 98-118.

Maleki, H., Duraes, L., Garcia-Gonzalez, C.A., del Gaudio, P., Portugal, A. and Mahmoudi, M. (2016) 'Synthesis and biomedical applications of aerogels: Possibilities and challenges', *Advances in Colloid and Interface Science*, 236, pp. 1-27.

Maleki, H., Duraes, L. and Portugal, A. (2014a) 'An overview on silica aerogels synthesis and different mechanical reinforcing strategies', *Journal of Non-Crystalline Solids*, 385, pp. 55-74.

Maleki, H., Duraes, L. and Portugal, A. (2014b) 'Synthesis of lightweight polymer-reinforced silica aerogels with improved mechanical and thermal insulation properties for space applications', *Microporous and Mesoporous Materials*, 197, pp. 116-129.

Marras, C., Loche, D., Corrias, A., Konya, Z. and Casula, M.F. (2015) 'Bimetallic Fe/Mo-SiO_2 aerogel catalysts for catalytic carbon vapour deposition production of carbon nanotubes', *Journal of Sol-Gel Science and Technology*, 73(2), pp. 379-388.

Mazraeh-shahi, Z.T., Shoushtari, A.M., Abdouss, M. and Bahramian, A.R. (2013) 'Relationship analysis of processing parameters with micro and macro structure of silica aerogel dried at ambient pressure', *Journal of Non-Crystalline Solids*, 376, pp. 30-37.

Meador, M.A.B., Fabrizio, E.F., Ilhan, F., Dass, A., Zhang, G.H., Vassilaras, P., Johnston, J.C. and Leventis, N. (2005) 'Cross-linking amine-modified silica aerogels with epoxies: Mechanically strong lightweight porous materials', *Chemistry of Materials*, 17(5), pp. 1085-1098.

Mi, H.Y., Jing, X., Huang, H.X., Peng, X.F. and Turng, L.S. (2018) 'Superhydrophobic Graphene/Cellulose/Silica Aerogel with Hierarchical Structure as Superabsorbers for High Efficiency Selective Oil Absorption and Recovery', *Industrial & Engineering Chemistry Research*, 57(5), pp. 1745-1755.

Pan, L.P., Liu, S.L., Oderinde, O., Li, K.W., Yao, F. and Fu, G.D. (2018) 'Facile fabrication of graphene-based aerogel with rare earth metal oxide for water purification', *Applied Surface Science*, 427, pp. 779-786.

Pan, Y.L., He, S., Gong, L.L., Cheng, X.D., Li, C.C., Li, Z., Liu, Z. and Zhang, H.P. (2017) 'Low thermal-conductivity and high thermal stable silica aerogel based on MTMS/Water-glass co-precursor prepared by freeze drying', *Materials & Design*, 113, pp. 246-253.

Prakash, S.S., Brinker, C.J., Hurd, A.J. and Rao, S.M. (1995) 'Silica aerogel films prepared at ambient- pressure by using surface derivatization to induce reversible drying shrinkage', *Nature*, 374(6521), pp. 439-443.

Rajanna, S.K., Vinjamur, M. and Mukhopadhyay, M. (2015) 'Mechanism for formation of hollow and granular silica aerogel microspheres from rice husk ash for drug delivery', *Journal of Non-Crystalline Solids*, 429, pp. 226-231.

Randall, J.P., Meador, M.A.B. and Jana, S.C. (2011) 'Tailoring mechanical properties of aerogels for aerospace applications', *ACS Applied Materials & Interfaces*, 3(3), pp. 613-626.

Rao, A.V., Nilsen, E. and Einarsrud, M.A. (2001) 'Effect of precursors, methylation agents and solvents on the physicochemical properties of silica aerogels prepared by atmospheric pressure drying method', *Journal of Non-Crystalline Solids*, 296(3), pp. 165-171.

Reichenauer, G. (2004) 'Thermal aging of silica gels in water', *Journal of Non-Crystalline Solids*, 350, pp. 189-195.

Rolison, D.R. and Dunn, B. (2001) 'Electrically conductive oxide aerogels: new materials in electrochemistry', *Journal of Materials Chemistry*, 11(4), pp. 963-980.

Sanchez, C. and Ribot, F. (1994) 'Design of hybrid organic-inorganic materials synthesized via sol-gel chemistry ', *New Journal of Chemistry*, 18(10), pp. 1007-1047.

Sanz, R., Calleja, G., Arencibia, A. and Sanz-Perez, E.S. (2013) 'Development of high efficiency adsorbents for CO_2 capture based on a double-functionalization method of grafting and impregnation', *Journal of Materials Chemistry A*, 1(6), pp. 1956-1962.

Sarawade, P.B., Kim, J.-K., Hilonga, A. and Kim, H.T. (2010) 'Production of low-density sodium silicate-based hydrophobic silica aerogel beads by a novel fast gelation process and ambient pressure drying process', *Solid State Sciences*, 12(5), pp. 911-918.

Sarawade, P.B., Kim, J.-K., Hilonga, A., Quang, D.V., Jeon, S.J. and Kim, H.T. (2011) 'Synthesis of sodium silicate-based hydrophilic silica aerogel beads with superior properties: Effect of heat-treatment', *Journal of Non-Crystalline Solids*, 357(10), pp. 2156-2162.

Schwertfeger F., F.D., Schmidt M., (1998) 'Hydrophobic waterglass based aerogels without solvent exchange or supercritical drying', *Journal of Non-Crystalline Solids*, 225, pp. 24-29.

Selves, N., Shanahan, J. and Sproul, C. (2013) *Profiled sheet roofing and cladding: A guide to good practice*. Routledge.

Shahzamani, M., Bagheri, R. and Masoomi, M. (2016) 'Synthesis of silica-polybutadiene hybrid aerogels: The effects of reaction conditions on physical and mechanical properties', *Journal of Non-Crystalline Solids*, 452, pp. 325-335.

Shao, Z.D., Luo, F.Z., Cheng, X. and Zhang, Y. (2013) 'Superhydrophobic sodium silicate based silica aerogel prepared by ambient pressure drying', *Materials Chemistry and Physics*, 141(1), pp. 570-575.

Shi, F., Wang, L. and Liu, J. (2006) 'Synthesis and characterization of silica aerogels by a novel fast ambient pressure drying process', *Materials Letters*, 60(29-30), pp. 3718-3722.

Shi, M.J., Tang, C.G., Yang, X.D., Zhou, J.L., Jia, F., Han, Y.X. and Li, Z.Y. (2017) 'Superhydrophobic silica aerogels reinforced with polyacrylonitrile fibers for adsorbing oil from water and oil mixtures', *RSC Advances*, 7(7), pp. 4039-4045.

Slosarczyk, A. (2017a) 'Recent advances in research on the synthetic fiber based silica aerogel nanocomposites', *Nanomaterials*, 7(2), p. 15.

Slosarczyk, A. (2017b) 'Synthesis and characterization of silica aerogel-based nanocomposites with carbon fibers and carbon nanotubes in hybrid system', *Journal of Sol-Gel Science and Technology*, 84(1), pp. 16-22.

Smith, D.M., Scherer, G.W. and Anderson, J.M. (1995) 'Shrinkage during drying of silica-gel', *Journal of Non-Crystalline Solids*, 188(3), pp. 191-206.

Smitha, S., Shajesh, P. and Warrier, K.G.K. (2011) 'Investigations on the effect of experimental parameters on the porosity features of silica aerogels synthesized at ambient drying conditions', *Materials Chemistry and Physics*, 131(1-2), pp. 507-511.

Sone, M., Chang, T.M. and Uchiyama, H. (eds.) (2013) *Advanced topics on crystal growth*. Ed. InTech.

Sorensen, L., Strouse, G.F. and Stiegman, A.E. (2006) 'Fabrication of stable low-density silica aerogels, containing luminescent ZnS capped CdSe quantum dots', *Advanced Materials*, 18(15), p. 1965.

Stergar, J. and Maver, U. (2016) 'Review of aerogel-based materials in biomedical applications', *Journal of Sol-Gel Science and Technology*, 77(3), pp. 738-752.

Toivonen, M.S., Kaskela, A., Rojas, O.J., Kauppinen, E.I. and Ikkala, O. (2015) 'Ambient-dried cellulose nanofibril aerogel membranes with high tensile strength and their use for aerosol collection and templates for transparent, flexible devices', *Advanced Functional Materials*, 25(42), pp. 6618-6626.

Ul Haq, E., Zaidi, S.F.A., Zubair, M., Karim, M.R.A., Padmanabhan, S.K. and Licciulli, A. (2017) 'Hydrophobic silica aerogel glass-fibre composite with higher strength and thermal insulation based on methyltrimethoxysilane (MTMS) precursor', *Energy and Buildings*, 151, pp. 494-500.

Ulker, Z., Erucar, I., Keskin, S. and Erkey, C. (2013) 'Novel nanostructured composites of silica aerogels with a metal organic framework', *Microporous and Mesoporous Materials*, 170, pp. 352-358.

Wan, W.C., Zhang, R.Y., Ma, M.Z. and Zhou, Y. (2018) 'Monolithic aerogel photocatalysts: a review', *Journal of Materials Chemistry A*, 6(3), pp. 754-775.

Wang, C.T., Wu, C.L., Chen, I.C. and Huang, Y.H. (2005) 'Humidity sensors based on silica nanoparticle aerogel thin films', *Sensors and Actuators B-Chemical*, 107(1), pp. 402-410.

Wu, Z., Zhang, L., Li, J., Zhao, X.L. and Yang, C.H. (2018) 'Organic-inorganic hybridization for the synthesis of robust in situ hydrophobic polypropylsilsesquioxane aerogels with fast oil absorption properties', *RSC Advances*, 8(11), pp. 5695-5701.

Yamada, T., Zhou, H.S., Uchida, H., Tomita, M., Ueno, Y., Ichino, T., Honma, I., Asai, K. and Katsube, T. (2002) 'Surface photovoltage NO gas sensor with properties dependent on the structure of the self-ordered mesoporous silicate film', *Advanced Materials*, 14(11), pp. 812-815.

Yang, H., Kong, X., Zhang, Y., Wu, C. and Cao, E. (2011) 'Mechanical properties of polymer-modified silica aerogels dried under ambient pressure', *Journal of Non-Crystalline Solids*, 357(19-20), pp. 3447-3453.

Yang, J.M., Wu, H.J., Huang, G.S., Liang, Y.Y. and Liao, Y.D. (2017) 'Modeling and coupling effect evaluation of thermal conductivity of ternary opacifier/fiber/aerogel composites for super-thermal insulation', *Materials & Design*, 133, pp. 224-236.

Yim, T.J., Kim, S.Y. and Yoo, K.P. (2002) 'Fabrication and thermophysical characterization of nano-porous silica-polyurethane hybrid aerogel by sol-gel processing and Supercritical solvent drying technique', *Korean Journal of Chemical Engineering*, 19(1), pp. 159-166.

Zhang, F., Ren, H., Dou, J., Tong, G.L. and Deng, Y.L. (2017) 'Cellulose nanofibril based-aerogel microreactors: a high efficiency and easy recoverable W/O/W membrane separation system', *Scientific Reports*, 7, pp. 1-7.

Zhang, G.H., Dass, A., Rawashdeh, A.M.M., Thomas, J., Counsil, J.A., Sotiriou-Leventis, C., Fabrizio, E.F., Ilhan, F., Vassilaras, P., Scheiman, D.A., McCorkle, L., Palczer, A., Johnston, J.C., Meador, M.A. and Leventis, N. (2004) 'Isocyanate-crosslinked silica aerogel monoliths: preparation and characterization', *Journal of Non-Crystalline Solids*, 350, pp. 152-164.

Zhao, X.Y., Cao, Y., Li, H.R., Zhang, J.P., Shi, L.Y. and Zhang, D.S. (2017) 'Sc promoted and aerogel confined Ni catalysts for coking-resistant dry reforming of methane', *RSC Advances*, 7(8), pp. 4735-4745.

Zheng, X.G., Tan, S.Y., Dong, L.C., Li, S.B. and Chen, H.M. (2015) 'Silica-coated $LaNiO_3$ nanoparticles for non-thermal plasma assisted dry reforming of methane: Experimental and kinetic studies', *Chemical Engineering Journal*, 265, pp. 147-156.

Zuo, L.Z., Zhang, Y.F., Zhang, L.S., Miao, Y.E., Fan, W. and Liu, T.X. (2015) 'Polymer/carbon-based hybrid aerogels:Preparation, properties and applications', *Materials*, 8(10), pp. 6806-6848.

Chapter 2 Experimental Methods

This chapter describes the synthesis methods and principles behind the experimental techniques that are used during characterisation of fibre reinforced silica aerogels composites, water glass-based silica aerogels, dawsonite, nickel nanowires immobilised on silica aerogels and multi-layered silica aerogel films. A transmission electron microscope (TEM) and scanning electron microscope (SEM) are used to investigate the microstructures and morphologies of aerogels and aerogel composites. X-Ray diffraction was used to quantify the structures of the synthesised aerogels. The surface areas and pore size distributions were determined from nitrogen adsorption-desorption isotherms by using Brunauer-Emmett-Teller (BET) method and Barrett-Joyner-Halenda (BJH) methods, respectively. Uniaxial compression tests were utilised to investigate the mechanical properties of fibre-reinforced silica aerogel and multi-layers silica aerogels. A hot disk method was used to measure the thermal conductivity of silica aerogels and their composites. Dynamic vapour sorption (DVS) is employed to investigate the gas sorption kinetics and catalytic activity for nickel nanowires and nickel nanoparticles immobilised on silica aerogels for CO_2 hydration reaction (CHR) in gaseous phase. All techniques are discussed in detail.

2.1 Materials and methods

2.1.1 Fibre reinforced silica aerogel composites synthesised by the novel ambient pressure drying method

All materials that are used in the synthesis of reinforced silica aerogels are used with no further treatment. Tetraethoxysilane (98%; TEOS), chlorotrimethylsilane (≥98%; TMCS), sodium-bicarbonate (99.7-100.3 %), ammonium hydroxide (≥99.99%) and ammonium fluoride (≥98%) were purchased from Sigma Aldrich. Ethanol (99.99%; EtOH) is supplied by Fisher Scientific. Ceramic short fibres (T/3740/48 Triton™ Kaowool Epsilon Ceramic Fibre, Pure) were provided by Fisher Chemical. Ceramic blanket (Superwool 607 Max) is purchased from Bath Potters' Supplies.

2.1.1.a Silica gel preparation

The sol-gel process was used to synthesise silica gels by hydrolysis of TEOS precursor in ethanol. Two beakers were prepared for use in the experiment. The first one contains a mixture of TEOS and ethanol. The second one contains a mixture of ethanol, water and catalyst (the catalyst is a mixture of ammonium hydroxide (28-30%), ammonium fluoride (≥98%) and deionised water of molar ratio 1:8:111, respectively). The molar ration of TEOS: ethanol: water was 2:38:33, respectively. For example, in typical synthesis of AB5 and CSSA samples, the first beaker contained 7.2 ml of TEOS and 16 ml of ethanol and the second beaker contained of 16 ml, 10.25 ml and 1.25 ml of ethanol, water and catalyst, respectively. The mixture of both beakers was stirred and dissolved at room temperature and then the content of beaker two was added and mixed with beaker one, while beaker one was constantly stirred. The mixed of solvents was poured on ceramic blanket (CFB) and ceramic short fibres (CSF). The gelation process was accomplished within 3 to 5 minutes and transparent gel was obtained. Figure 2. 1 shows a diagram of the synthesis and drying processes by ambient pressure drying method of both CBSA and CSSA.

Table 2. 1. Synthesised samples of ceramic fibre blankets (CFB) and Ceramic short fibres (CSF)-silica aerogels composites.

Sample	CFB	AE	AB1	AB2	AB3	AB4	AB5
SiO_2 wt.%	0	100	23	26	28	30	34
CF wt.%	100	0	77	74	72	70	66
Sample	CSF	SA1	SA2	SA3	SA4	SA5	
SiO_2 wt.%	0	98.4	96.2	94.8	92.5	88.8	
CF wt.%	100	1.62	3.8	5.2	7.5	11.2	

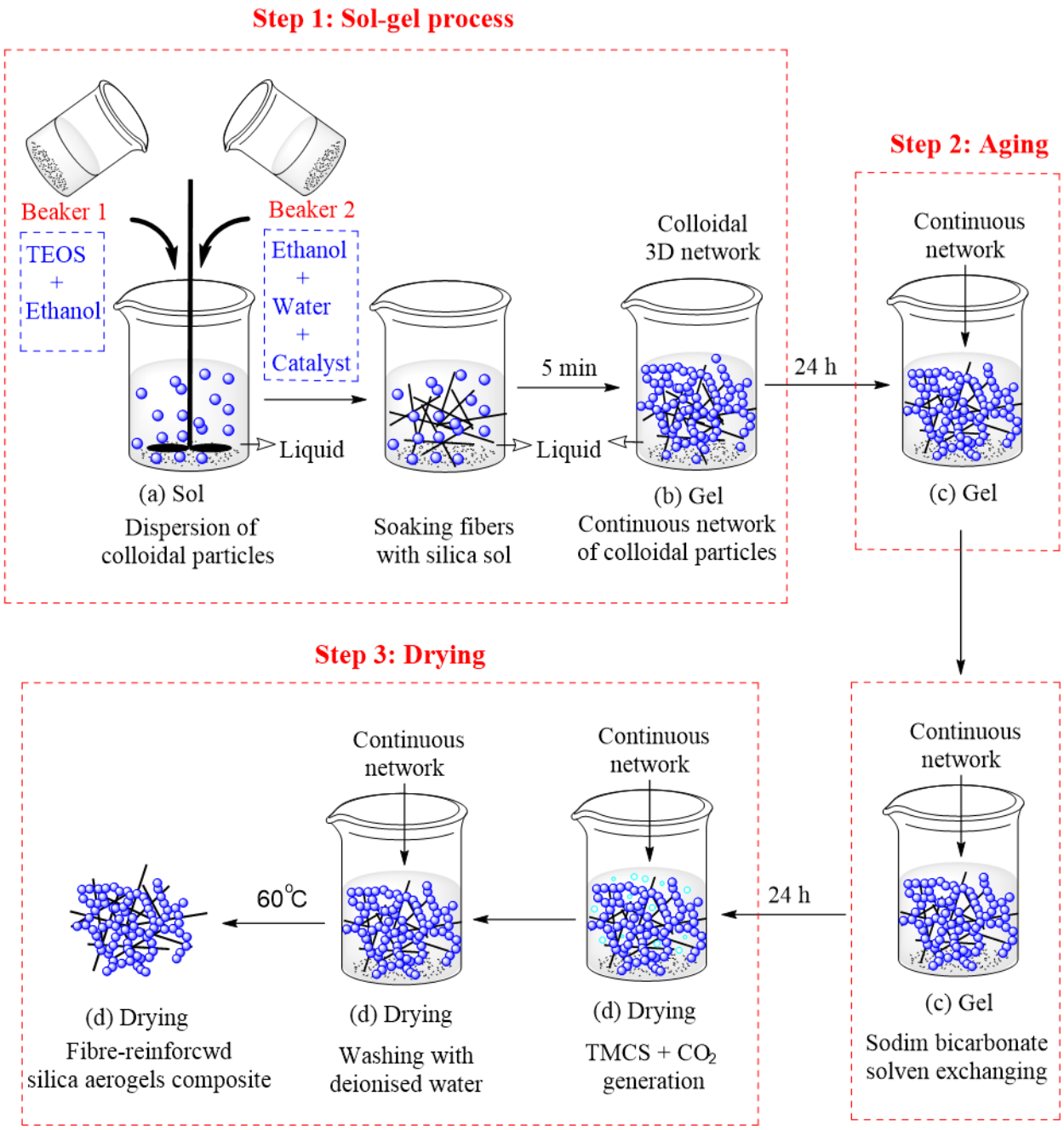

Figure 2. 1. Schematic diagram of synthesis of CSSA and CBSA by bicarbonate ambient pressure drying method.

2.1.2 Synthesis of silica aerogels from sodium silicate precursor using the bicarbonate ambient pressure drying method

Silica hydrogels were synthesised by the sol-gel method then dried by the novel APD (Han and Šiller, 2015). Water glass (sodium silicate, 338443 Sigma-Aldrich: Na_2O ~10.6%, SiO_2 ~26.5%) was diluted with deionised water at different volume ratios (1:3, 1:3.5, 1:4, 1:4.5 and 1:5). Two treatment processes are used during the synthesis of wet the gels. The first process

included ion exchange by using a strongly acidic cation exchange resin (Amberlite® IR 120 hydrogen form: 39389-20-3, supplied by Sigma-Aldrich). Figure 2. 2 shows a diagram of the synthesis of silica aerogels from water glass precursor.

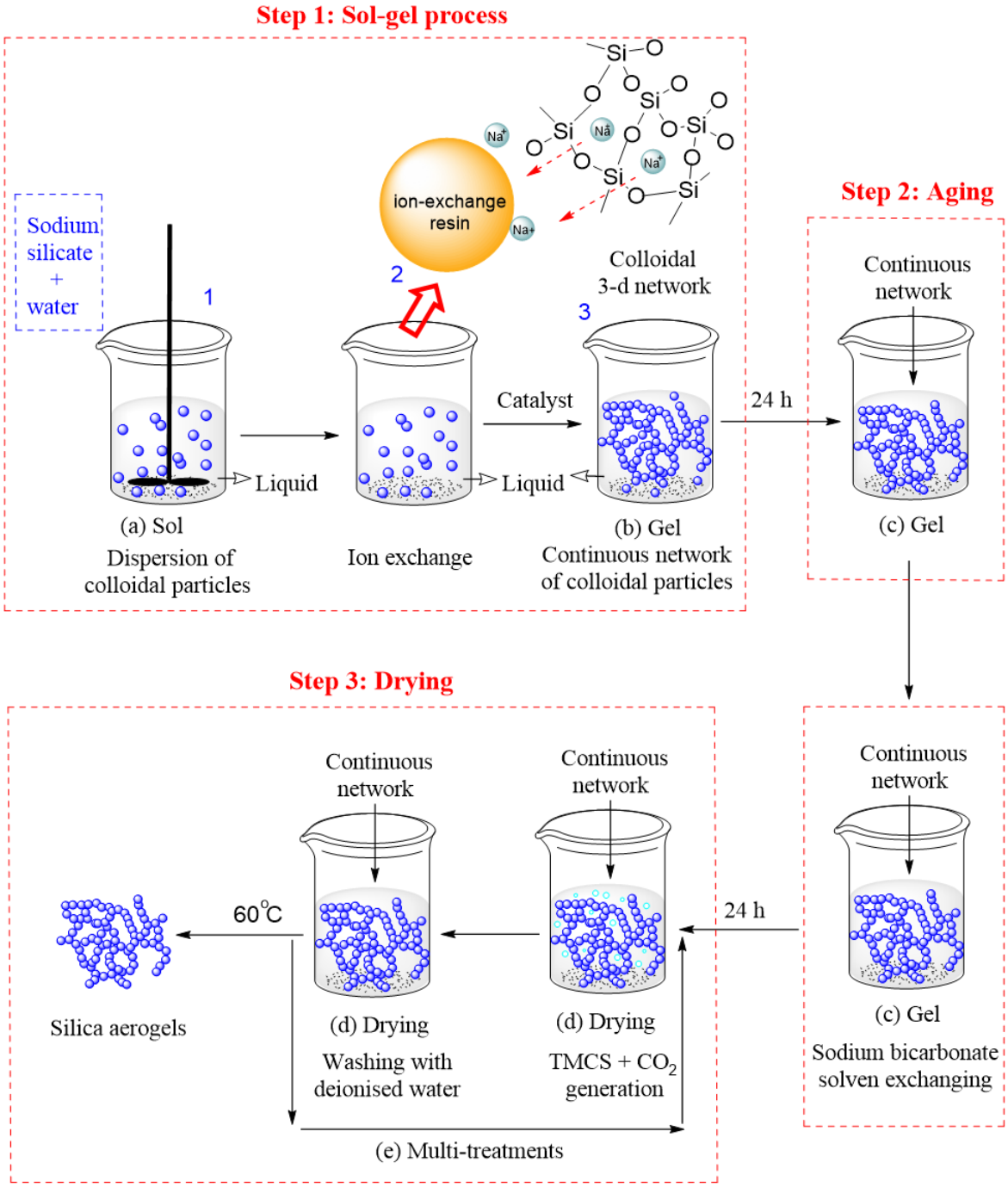

Figure 2. 2. (a) Schematic for the synthesis of silica aerogels from water glass precursor via novel ambient pressure drying method, (b) multi surface modification process to obtain monolithic silica aerogels.

2.1.3 Synthesis of dawsonite aerogels via using novel ambient pressure drying method

All materials used during experiments conducted in Chapter 5 are supplied by Sigma-Aldrich with no further purification. Synthesis of dawsonite aerogels involved three main steps: preparation of the alcogel; treatment with sodium bicarbonate and TMCS and solvent displacement; removal of trapped solvent from the pores by APD. The sol was prepared by mixing aluminum tri-sec butoxide (≥ 97%), deionised water (resistivity of 18 $M\Omega.cm^{-1}$), ethyl acetoacetate (≥ 99%) and ethanol (99.99%, supplied by Fisher Scientific) in a molar ratio of 1:0.6:0.58:16, for 45 min at 60°C. Hydrolysis and condensation reactions were carried out by mixing the sol with a mixture of methanol (≥ 99.9%), DI water, acetic acid (≥ 99.7%), and N, N–dimethylformamide (DMF, ≥ 99.8%) in a weight ratio Sol:MeOH:H_2O:DMF of 1:0.2:0.003:0.03. 1 ml of acetic acid was added for each 30 ml of mixture while stirring for 30 mins at room temperature. The resulting homogeneous sol was transferred to airtight boxes and kept for 7 days at room temperature to complete gelation. After gelation was completed, the gel was then treated and dried by our approach. Figure 2. 3 displays a diagram of the synthesis steps of dawsonite aerogel by using our novel approach (Han *et al.*, 2018).

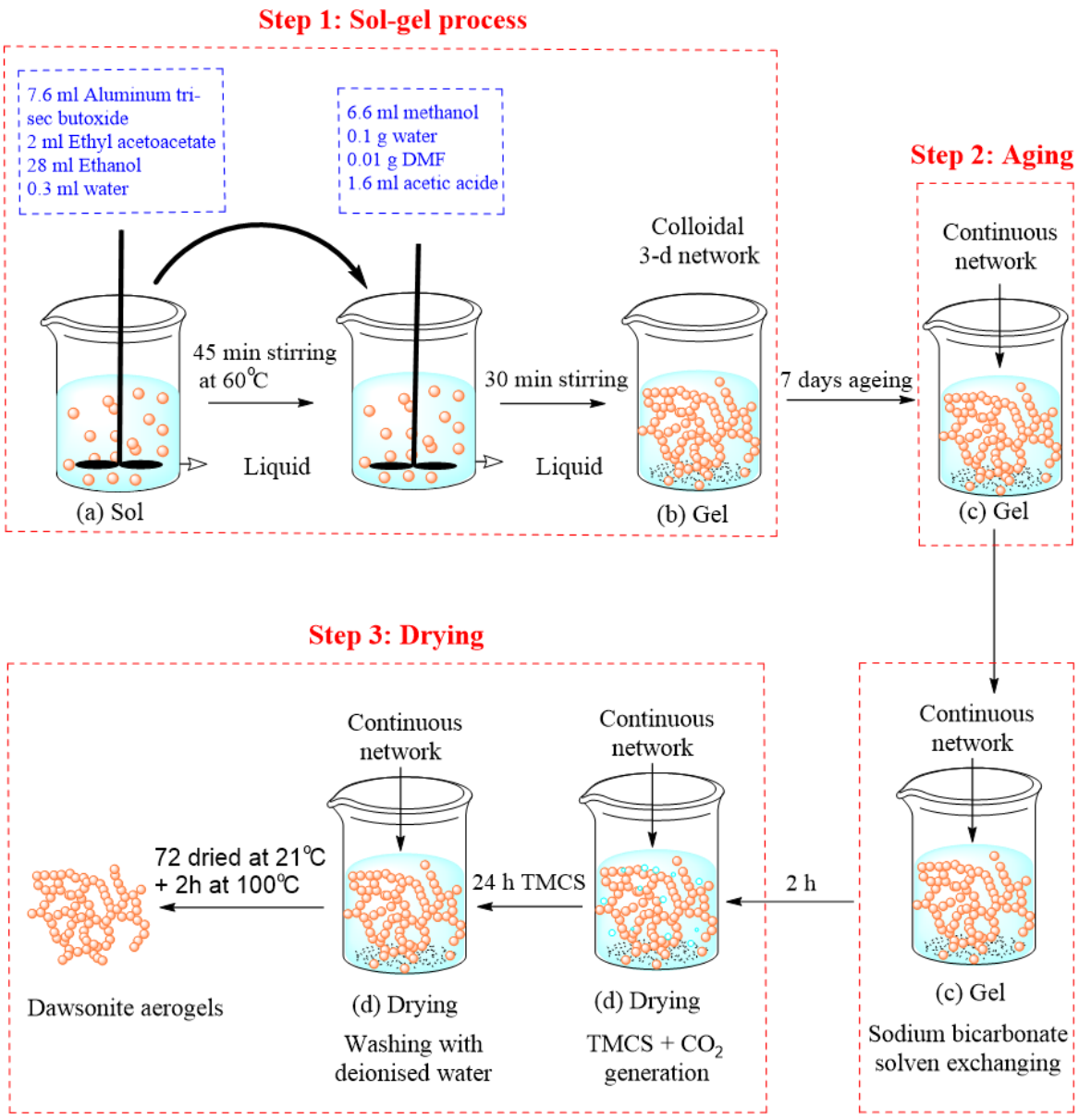

Figure 2. 3. Schematic diagram of the synthesis steps of dawsonite aerogels via using novel ambient pressure drying approach.

2.1.4 Synthesis of multi-layered silica aerogel films via novel ambient pressure drying approach

Multi-layered silica aerogel films were synthesised and characterised in chapter 6 of this thesis from tetraethoxysilane (TEOS) precursor using the same method and molar ratios detailed of describing silica gel preparation with TEOS precursor in section (2.1.1), above. Briefly (Han *et al.*, 2018), cling film was pulled tight over a petri dish to create a flat surface and the silica sol dripped on the film by pipette. The drying mechanism of aerogels using the bicarbonate based ambient pressure drying method is illustrated in Figure 1. 11 in chapter 1.

2.1.5 Synthesis and immobilised nickel nanowires on silica aerogels

All chemicals that were used to synthesis the materials of chapter 7's experiments were used as received from Sigma-Aldrich without further purification. Nickel chloride hexahydrate ($NiCl_2 \cdot 6H_2O$) and hydrazine hydrate ($N_2H_4 \cdot H_2O$; 80 wt %), Ethylene glycol anhydrous (EG) (99.8%), sodium hydroxide (≥98%), hexane (≥97.0%), tetramethylorthosilicate (TEOS), (98% ammonium hydroxide (28-30%) and ammonium fluoride (≥98%) were supplied by Sigma-Aldrich. Ethanol (99.99%) was purchased from Fisher Scientific. Nickel nanoparticles purchased from Nano Technologies (Korea). CO_2 (99 %) was bought from BOC. Deionised water of resistivity 18 $M\Omega.cm^{-1}$ was used for preparation of solutions and washing.

Synthesis of nickel nanowires (NiNWs)

Nickel nanowires were synthesized following solvothermal process as reported by Chen *et al.* (2015) with modification. Typically, 137 mg of $NiCl_2 \cdot 6H_2O$ was first added to 60 ml of ethylene glycol (EG) in a round bottom flask. After $NiCl_2 \cdot 6H_2O$ had fully dissolved in EG, 5 ml of 1M NaOH and 2.3 ml of $N_2H_4 \cdot H_2O$ was then added into this solution. This solution was then kept in a water bath at 60 ^{0}C for 3 hours, the solution turned black indicating synthesis of Ni nanowires. These nickel nanowires were then dried in an oven at 60 °C for 8 hours. It was observed that when these nanowires were suspended in DI water, the pH of the suspension was acidic. It was suspected that the low pH could be due to the presence of residual reactants at the nanowire surface. Therefore, in order to remove these residuals, the nanowires were washed with 6M NaOH solution followed with DI water until the nanowire suspension had near neutral pH. Typically, 30 mg of NiNWs were mixed with 20 mL of 6 M NaOH and sonicated for 3 min. NaOH solution was refreshed and the process was repeated five times. A high-power magnet was used to separate NiNWs from the solution. In order to remove any excess NaOH from the samples, additional post-washing with DI water was introduced. NiNWs were dispersed in 20 ml of DI water followed by sonication for 3 min. DI water was then refreshed and the process was repeated 20 times. Finally, NiNWs were washed by ethanol five times before drying at 60 °C for 8 hours.

Immobilisation of nickel nanowires (NiNWs) on silica aerogels

The sol-gel process was used to synthesise silica aerogel. Immobilisation of NiNWs (see Figure 2. 4) and NiNPs (for comparison) were carried out according to process proposed by Han *et al.* (2015). NiNWs were dispersed during the sol stage prior to gelation. Silica aerogels samples with 0, 400, 500 and 700 ppm of NiNWs (S, N1, N2 and N3 in Table 7. 1 chapter 7,

respectively) were synthesized (Figure 7. 2 a and b). For the procedure, the desired amount of NiNWs were suspended in 5 ml of DI water using a sonic horn (Sonopuls, Bandelin) for 2 minutes. The hydrolysis of TEOS in ethanol and deionised water was used to prepare the silica gel with a molar ratio of 2:38:33 of TEOS: ethanol: water, respectively.

To accelerate the gelation process, a 1 ml mixture of ammonium hydroxide, ammonium fluoride and DI water in a molar ratio 1:8:111 was used as a catalyst. Subsequently, the mixture was stirred for 3 minutes and poured in a plastic mould for gelation. When gelation was complete, the mould was removed, and the gel was soaked in ethanol for aging. After 24 hours, the ethanol solvent was replaced by hexane. The hexane was refreshed every 24 hours for three days. Finally, the gel was dried at room temperature for 24 hours. After which the gel was transferred to an oven for 8 hours at 60 °C, after which the temperature was increase to 100 °C for a further 2 hours, see Figure 2. 4.

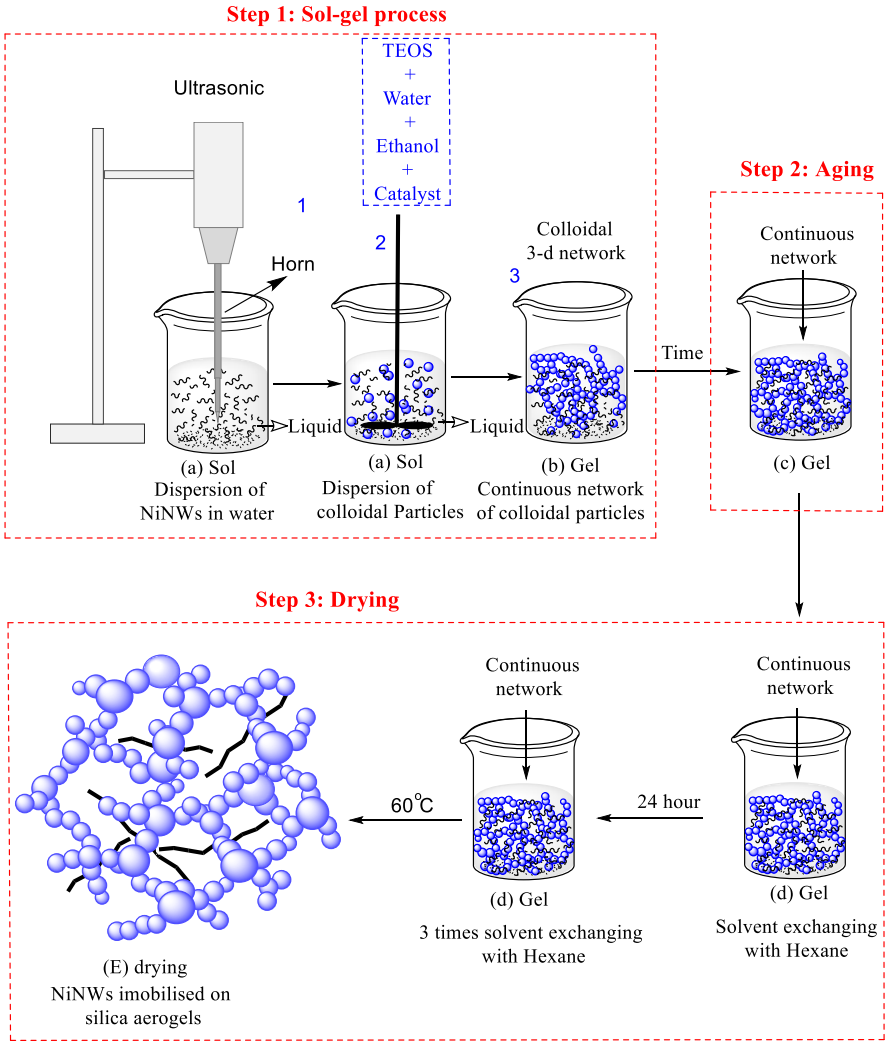

Figure 2. 4. Schematic diagram of the immobilising process of NiNWs on silica aerogels.

2.2 Characterisation and techniques

Background of electron microscopy

Electron microscopy works on the principle of bombarding a specimen with highly energetic primary electrons. The bombardment of these electrons causes unique interactions which depend upon the atoms present within the specimen. A wide range of charged particles and photons are generated as a result of that collision. Those interactions can be divided into elastic and inelastic interactions. Elastic scattering results from electrons deflection without loss of energy either by the specimen's atomic nucleus or by the outer shell electrons of similar energies. Inelastic scattering causes transferring a substantial energy from the primary electrons beam to the atoms of specimen (Stokes, 2008). Figure 2. 5 illustrates a diagram of the emitted particles and photons which result from interactions between primary electron beams and the specimen (Watt, 1997).

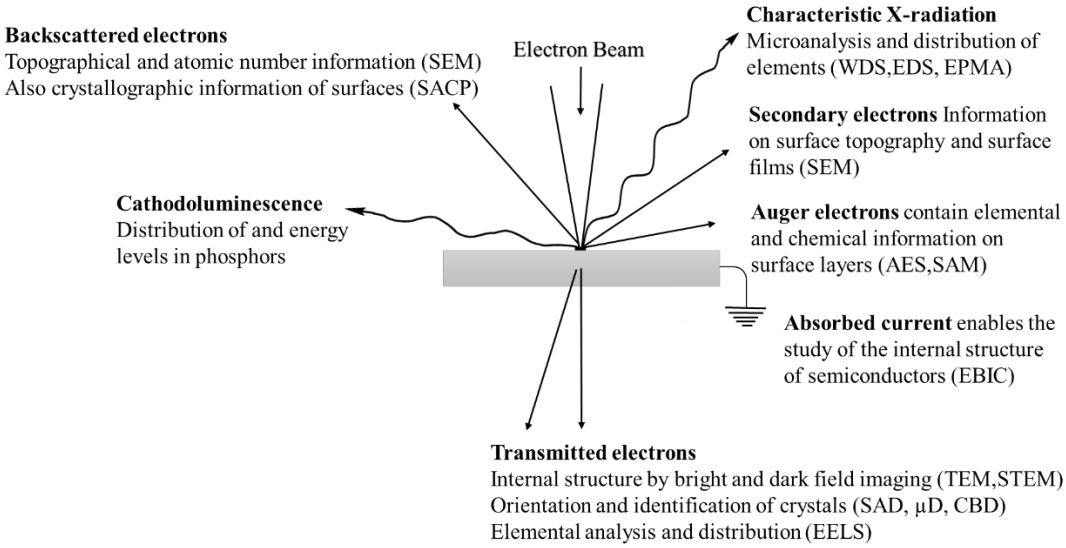

Figure 2. 5. Schematic representation of the wealth of information resulting from the interaction between the electron beam and the specimen in an electron microscope (Watt, 1997).

Backscattered electrons. Backscattered electrons (BSEs) are the primary electrons that have undergone a single or multiple scattering (scattered with an angle higher than 90°) after colliding with the atoms of the solid. Elastic scattering is caused by electrons deflecting and ejecting from a specimen's atomic nucleus with a wide angle and energy of approximately 50 eV (Zhou and Wang, 2006; Egerton, 2016). It may have energy from that of the primary electrons beam down to SE (Figure 2. 6) (Stokes, 2008). On an average 10-15 % of the primary electrons beams are backscattered and hold approximately 60-80 % of their initial energy (Zhou and Wang, 2006).

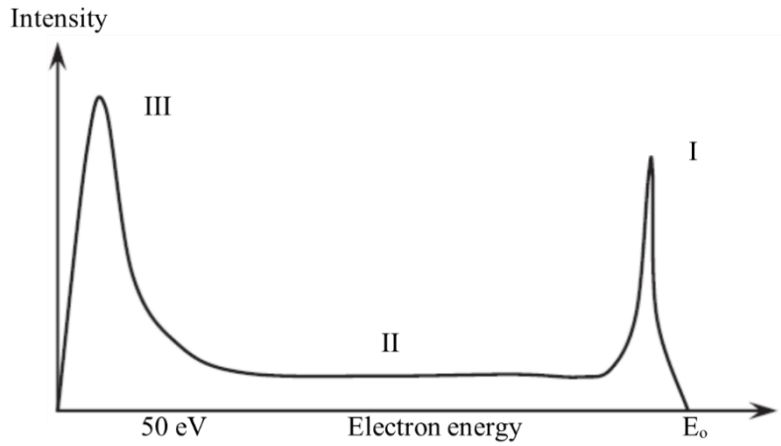

Figure 2. 6. Approximate energies of electrons signals for a given primary beam energy. Region I and II are backscattered electrons contributions. Region III refer to the secondary electron contribution (Stokes, 2008).

The ratio between the number of emitted backscattered electrons (n_{BSE}) and the number of primary electrons (n_{PE}) or their currents, which have bombarded a sample, is known as BSE coefficient η.

$$\eta = \frac{\eta_{BSE}}{\eta_{PE}} = \frac{i_{BSE}}{i_{PE}} \quad (2.1)$$

The value of η is found to be proportional with the atomic number Z and provides an important contrast which enables to distinguish the different materials (Stokes, 2008).

Secondary electrons. Secondary electrons (SEs) are low energy electrons (less than 50 eV, majority < 10 eV (Stokes, 2008)) emitted from a solid as a result of inelastic collision. The outermost electrons are detached from the atoms leaving ionized atoms with a positive charge. Those electrons are immediately captured after their emission by the nearest ionised atoms. Some of the generated SE receive sufficient energy allowing them to escape from the surface (Watt, 1997; Goldstein *et al.*, 2003; Stokes, 2008). SE can be subdivided into two categories (Figure 2. 7). First category is the SE that are excited after penetration by primary electrons in the solid target. Those are beneficial in high-resolution scanning microscopy and provide information about the surface of the sample. While the second are the SE that are generated by the backscattered electrons; this type adds a noise to the signal. (Wells *et al.*, 1974).

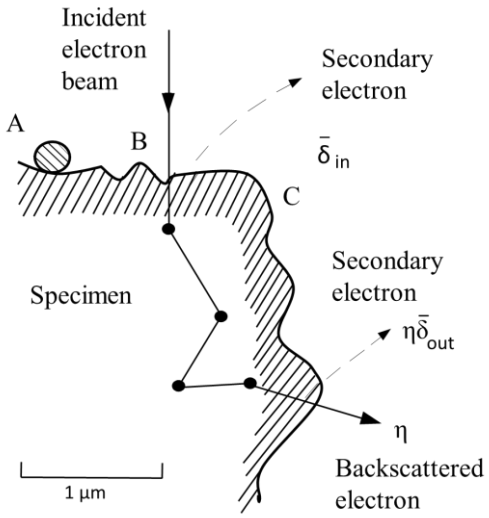

Figure 2. 7. Secondary electron emission from a solid target (Wells *et al.*, 1974).

A ratio of the number of emitted secondary electrons n_{SE} to the number of bombarded primary electrons n_{PE} on sample or their equivalent current i is known as SEs coefficient δ.

$$\delta = \frac{\eta_{SE}}{\eta_{PE}} = \frac{i_{SE}}{i_{PE}} \tag{2.2}$$

The SE coefficient is insensitive to the atomic number and their typical value is ~ 0.1. Due to their low energies, the SEs travel for a few nanometres and can therefore provide information about the surface of the specimen (used in SEM) (Stokes, 2008).

X-ray photons. If a specimen is subjected to bombardment by a primary electron beam, the electron of the atom will be knocked out leaving a vacancy and the remaining atom shifts to its excited state. Later, the atom tends to relax by filling the empty electron state with an electron from a higher energy orbital and releasing the excess energy in the form of a secondary photon effect. If the knocked electron was from the inner shell of the atom (see Figure 2. 8), the amount of released energy is huge which could be emitted in the form of an X-ray (Goodhew and Humphreys, 1997). X-rays are classified as electromagnetic waves with wavelengths shorter than visible light by two to five orders. X-rays can be emitted due to the atom being bombarded with electrons, α-particles or irradiate by higher energy gamma rays (Watt, 1997).

Auger electrons. Auger electron injection is an alternative process to X-ray emission (Figure 2. 8a) when the excited atom follows the relaxation process. Auger electron ejection is a three electrons contribution process. The first electron is the elected SE which leaves a hole (in the case of Figure 2. 8 in a K level) in the inner shell energy level. The process is followed by filling the hole by the second electron from higher energy levels (an L_1 level in the case of Figure 2. 8a) and the final electron (Auger electron) is also ejected from $L_{2,3}$ levels (Goodhew and Humphreys, 1997; Wolstenholme, 2015).

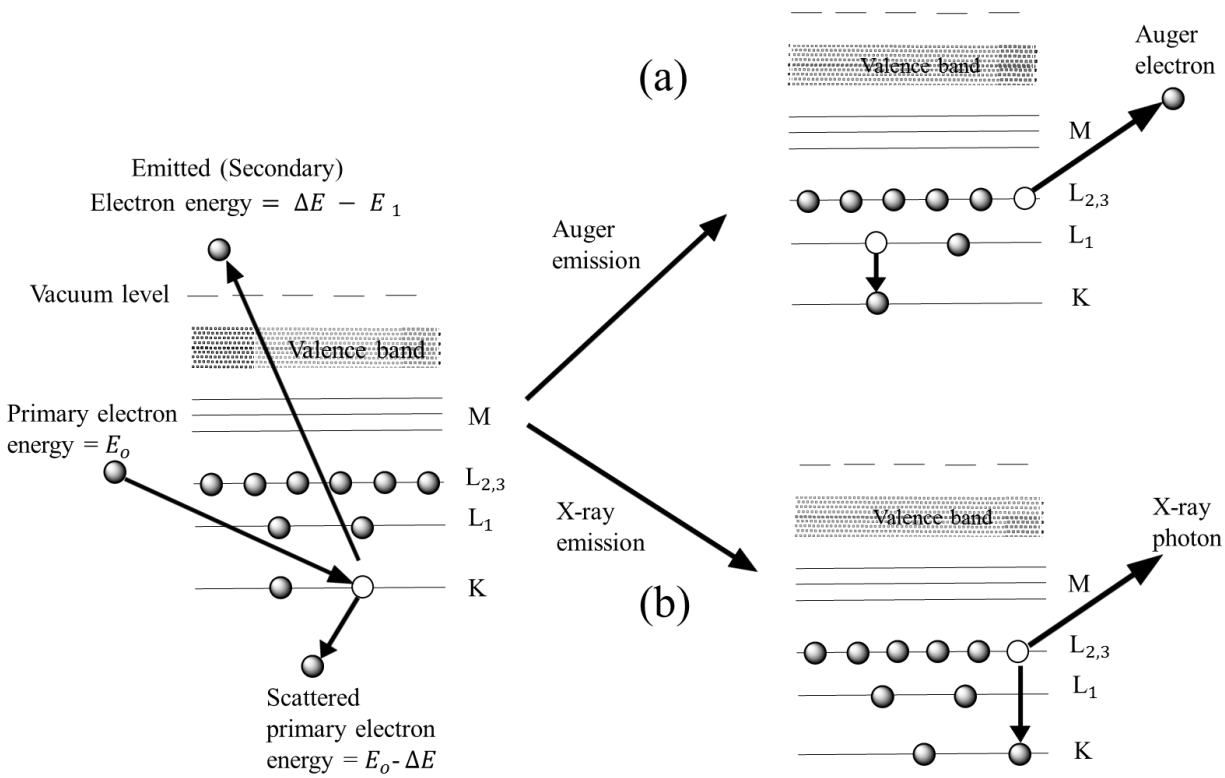

Figure 2. 8. Mechanism of the auger effect induced by X-rays (Wolstenholme, 2015).

2.2.1 Physics of electron microscopy

The basic principles of electron microscopy is backed to the early 20th century when Louis de Broglie proposed the relation that connects an electron's wavelength and Einstein's description of photon,

$$\lambda = h/p = \frac{h}{mv} \qquad (2.3)$$

where h is the Plank constant (6.626×10^{-34}), p and m are the momentum and the mass of electron, respectively. It was observed that electrons, which are emitted from a heated filament into vacuum chamber and potentially accelerated to 50 V, have a speed of $v \approx 4.2 \times 10^6$ m/s and $\lambda \approx 0.17$ nm, and they experience energetic diffraction when passed through an array of atoms at the crystal surface. If the acceleration potential is raised to 50 kV, the electron's wavelength is ~ 0.005 nm and such high energetic electrons can penetrate several microns into the solid. When the specimen is thin enough, it is possible for passing electrons to form a transmission electron diffraction pattern (Egerton, 2016). Figure 2. 9 demonstrates the different electron scattering effects for an incident electrons beam by a thin sample (Zuo and Spence, 2017).

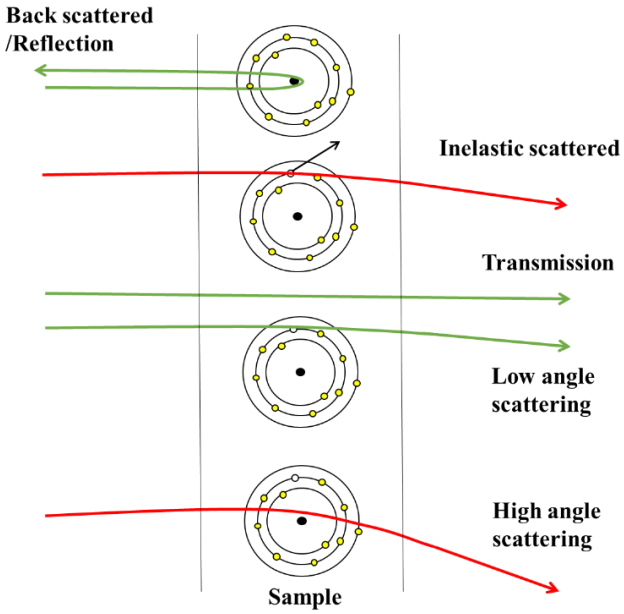

Figure 2. 9. Electron scattering by a thin sample (Zuo and Spence, 2017).

The resolution, obtained using electrons, is better than that of a light microscope (Egerton, 2016; Zuo and Spence, 2017). The resolution of a microscope d_{min} is limited by diffraction and it is obtained from Rayleigh formula (Zuo and Spence, 2017) :

$$d_{min} = 0.61\frac{\lambda}{nsin\theta} \qquad (2.4)$$

where λ is the wavelength of light or electron, θ is half of the acceptance angle of the lens and the term $nsin\theta$ is the lens numerical aperture (NA). For electrons under vacuum n = 1 and d_{min} is equal to 2.3 Å at 10 kV, λ = 0.037 Å and θ = 10 mrad.

2.2.2 Transmission electron microscope structure

Basic transmission electron microscopes have a similar mode of operation as an optical microscope unless electrons and electrons magnetic lens are used instead of light and glass lens for optical wavelength.

Generally, TEM (Figure 2. 10 illustrates the geometry of basic TEM (Zuo and Spence, 2017)) is consisting of the electron gun which generates electron beams, condenser lenses which focus the electrons toward a specimen, objective lenses which focus electrons into intermediate image, projector lenses for further enlargement of the image and finally the fluorescent screen (Watt, 1997).

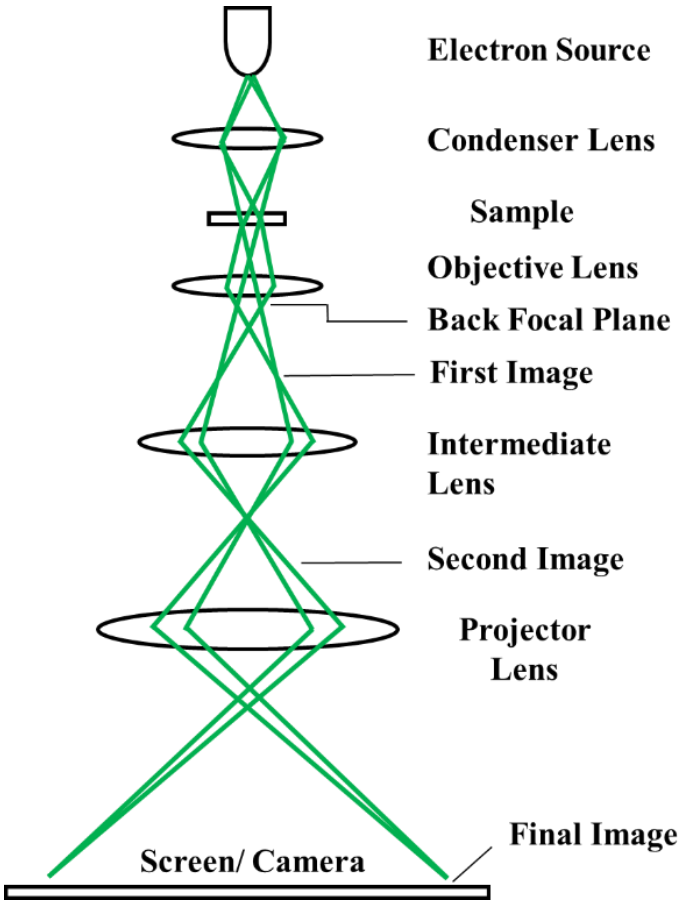

Figure 2. 10. Geometric optic of a basic Transmission Electron Microscope (Zuo and Spence, 2017).

Electron gun

Two types of electron guns are typically used to provide the electrons: thermionic and field emission guns (FEGs). The most common electron gun used in TEM is the thermionic gun. The current of electrons is emitted from a filament which is commonly made from tungsten (W) or lanthanum hexaboride (LaB_6) or cerium hexaboride (CeB_6) crystals (Luo, 2016).

Figure 2. 11.a illustrates the thermionic emission where E is the energy of an electron, E_F is the Fermi energy and ϕ is the work function.

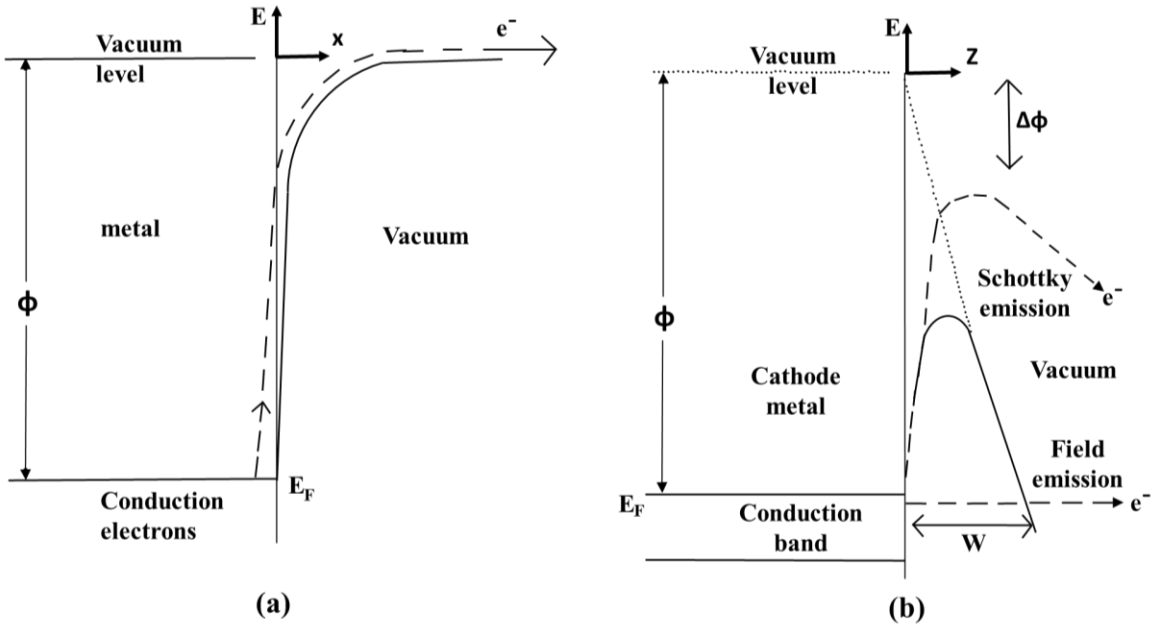

Figure 2. 11. a) thermionic emission of electrons (dashed line) when no electric field is applied into metal, b) field and Schottky emission of electrons (Egerton, 2016).

The amplitude of vibration for nuclei of cathode's atoms increases with the raising of the temperature and therefore some electrons from conductive band can escape after holding energies above the vacuum level. Richardson law describes the rate of electron emission at the cathode (Egerton, 2016).

$$J_e = AT^2 e^{\frac{\phi}{kT}} \qquad (2.5)$$

where J_e is the current density in A/m^2, A is the Richardson constant ($\approx 10^6$ A m^{-2} K^{-2}), T (in K) is the absolute temperature and k is the Boltzmann constant (1.38×10^{-23} J/K).

Despite its high work function ($\phi = 4.5$ eV), tungsten's high melting point allows the (material / cathode) to sustain temperatures up to 2500-3000 K under a vacuum which promotes electron emission by lowering exponent ϕ/kT in Eq. (2.5). Employing materials with a low work function (LaB_6; $\phi = 2.7$ eV) is an alternative strategy to the use of high temperatures. However, LaB_6 crystals need a better vacuum (pressure $< 10^{-4}$ Pa) than tungsten in order to not react with the residual oxygen.

On the other side, the potential barrier, which keeps electrons inside the cathode, can be lowered by an amount of $\Delta\phi$ (consequently increasing the thermionic emission) via applying an electrostatic field. That is a so-called Schottky effect (illustrated in Figure 2. 11b). Therefore, J_e could be enlarged by a factor of exp ($\Delta\phi$/kT), typically factor of 10 (Egerton, 2016).

Although thermionic guns are inexpensive and require a relatively low vacuum, their use is restricted because of many disadvantages such as a short lifetime, a low brightness and they consume large energy. Modern electron microscopes used FEGs. In FEGs, the electron source

is a very sharp tip, which is usually made from a single tungsten crystal. Field emission is the process by which electrons escape toward anode by a quantum-mechanical tunnelling when an electrostatic field at a cathode becomes high enough to lower the width of the potential barrier (Figure 2. 11b) (Zhou and Wang, 2006; Egerton, 2016).

Condenser lens

TEM magnification must be high enough ($M=10^5$) in order to produce a highly magnified image on the fluorescent screen. However, sometimes a large area of the specimen needs to be investigated which requires low magnification of 2000. Therefore, condenser lenses that have at least two electron lenses are used. The condenser lenses (see Figure 2. 10) are located above the specimen and their function is to provide the ability to control the illumination strength in the specimen plane. For a high resolution, double condenser lenses are used to reduce the diameter of the focused electron beam to micrometre size or less. The function of the first condenser lens (C1) is to control the beam size where the second lens (C2) controls the beam intensity (Watt, 1997; Luo, 2016).

Objective lens and objective aperture

This is the most important lens which is employed to form the first intermediate image and diffraction pattern of the specimen (Goodhew and Humphreys, 1997). The produced image is magnified by $M \approx 50\text{-}100$. In TEM, the location of the specimen is close to the objective lens (centre in the gap of pole-piece). The gap is adjusted according to the application for example in a high resolution TEM, the pole-piece is configured to have a smaller gap in order to obtain higher resolution images. The function of the objective aperture, which is located just below the specimen, is to conduct a regular imaging (Luo, 2016).

Intermediate lens

Also called a first projector lens, its purpose is to magnify the images and to transform the imaging mode to the diffraction mode and vice versa. It operates over a wide range of focal lengths.

Projector lens or second projector lens

The function of the projector lens is to provide further magnification of the image, which was formed by the intermediate lens. The magnification is controlled by modifying the strength of

one or both lenses. The great focus depth of the projector lens provides a focus image for a long distance.

Fluorescent screen and camera

A visible image is formed after an electron image falls on a coated screen with a phosphorescent powder. The screen could be damaged if the intensity of image mode or diffraction spot is too strong. A film camera or CCD camera can be used for recording under high vacuum. By using a CCD camera, recording of TEM data can be done on a digital film (Watt, 1997; Luo, 2016).

2.2.3 Scanning electron microscopy (SEM)

The capability of imaging by SEM depends on collecting the emitted backscattered electron (BSEs) and secondary electrons (SEs) (Zhou and Wang, 2006). SEM consists of two major parts (see Figure 2. 12). The first part consists of the electron gun and two or more lenses. This component is well-known as an electron column. The electrons, which are generated and accelerated by the electron gun with a typical energy range of 0.1-30 keV, travel through an evacuated tube (vacuum of 10^{-4} Pa) and are de-magnified by the lenses into a small electron spot on the specimen (spot size >10 nm). Sweeping the electron beam across the specimen is carried out by a couple of pairs of electromagnetic deflection coils. Therefore, the magnification can be controlled by adjusting the coils. The second part is the control console, which consists of the viewing screen (the cathode ray tube (CRT) and the computer keyboard). The standard Everhart-Thornley detector (E-T), illustrated in Figure 2. 13, is utilised to collect SEs and BSEs. The operation of E-T detector depends on converting the energetic electrons (~10 keV) into light when it strikes the scintillator. This light is guided to the photomultiplier by a light-pipe. The light is converted back into electrons at the output of the photomultiplier with a typical gain of 10^5-10^6.

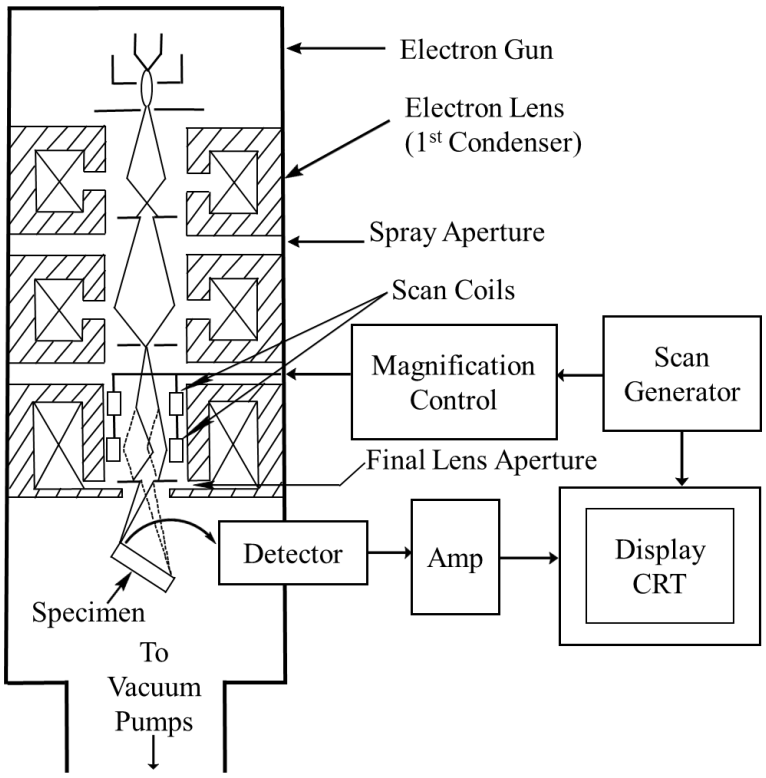

Figure 2. 12. Schematic of SEM spectroscopy parts (Goldstein *et al.*, 2003).

Originally, most BSEs have sufficient energy to enable direct excitation of the scintillator.

To collect both SEs and low energies BSEs, a positive potential of 10 to 12 kV is applied on the scintillator in order to accelerate those electrons to generate a light in the scintillator. However, when a negative bias is applied to the E-T detector, SEs are rejected and only BSEs are detected. The captured electrons are amplified for display on CRT (Thornton, 1968; Goldstein *et al.*, 2003).

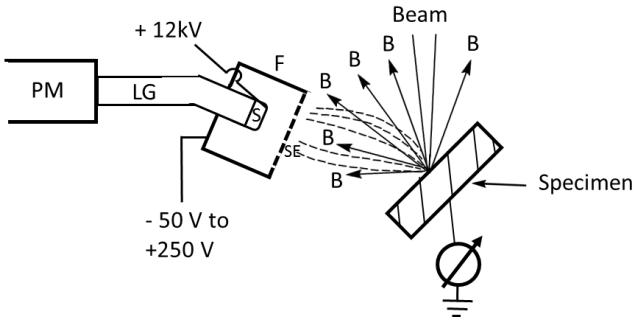

Figure 2. 13. Schematic diagram of the standard Everhart-Thornley detector: B, backscattered electrons; SE, secondary electrons; F, faraday cage (bias range -50 V to + 250 V); Scintillator with thin metallic coating; high bias (+ 12 kV) supply to the scintillator coating; LG, light guide; PM, photomultiplier (Goldstein *et al.*, 2003).

2.2.4 X-ray diffraction (XRD)

X-rays are electromagnetic waves in the energy range from 100 eV to 10 MeV and with wavelengths much shorter than visible light (typically order of 1 Å). To produce X-rays, a high voltage should be applied between the cathode (electron emitting filament) and the anode electrode (a metallic target). Upon collision with the target, the electrons rapidly slow down losing their energies and generating continuous X-rays with various wavelengths (Dinnebier and Billinge, 2008; Waseda *et al.*, 2011).

X-ray diffraction is a non-destructive experimental technique, which is used to study the crystallography of solids and powdered materials. XRD analysis is sensitive to the surface reflectivity and because an X-ray beam has a shallow penetration, the density and surface roughness of the tested materials affects their scattering. When the X-ray beam incidents on a specimen's surface, it is diffracted with different angles. However, at some incident angles (the constructive interference), the scattered waves from objects are reflected with a path length of the order of wavelength λ as illustrated in Figure 2. 14. Therefore, some of the scattered waves are in the same phase.

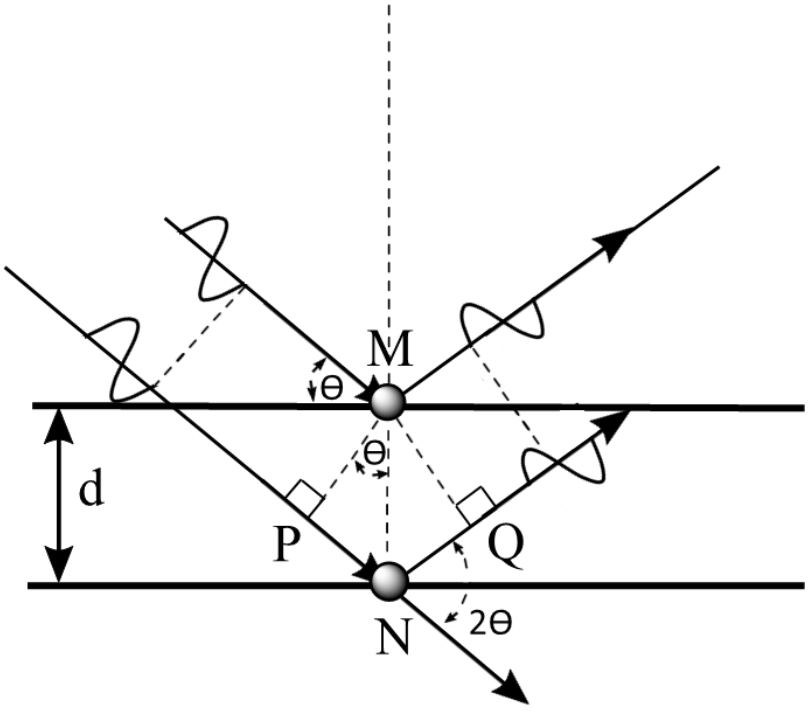

Figure 2. 14. Diffraction of X-ray from the planes of crystal (Dinnebier and Billinge, 2008).

W.L. Bragg (1912) described diffraction of X-rays in term of refractivity from a set of lattice planes. Bragg's analysis considered lattice planes behaviour like a mirror reflecting X-rays and because of the deep penetration of X-rays inside the material, additional reflections occur in parallel planes. In Figure 2. 14, the second wave travels a longer distance before and after

reflection ($\Delta = PN + NQ$) and the constructive interference occurs only when Δ is a multiple of the wave length

$$\Delta = n\lambda \quad (2.6)$$

$n = 0, \pm1, \pm2, \ldots$

Therefore, Bragg's equation can be written as;

$$n\lambda = 2d \sin\theta \quad (2.7)$$

where d is the distance between the planes, θ is the incident angle (Lifshin, 1999; Dinnebier and Billinge, 2008; Quinn and Yi, 2018).

In this thesis, X-ray diffraction analysis is carried out in Newcastle University using Panalytical X'Pert Pro multipurpose diffractometer with a wavelength of 0.15418 nm of Cu-Kα X-ray. X-ray was utilised to investigate the structure of the samples and to quantify the crystal structure of dawsonite in chapter 5 and the weight percentage of the NiNPs and NiNWs in chapter 7. The quantification test was determined by mixing an 80% of the sample with a 20% of standard sample (alumina) to quantify the amorphous and the crystalline structures.

2.2.5 Surface area and pore size analysis

Adsorption of solids

In general, the surface energy for a clean solid surface is relatively high. Adsorbing gases such as oxygen, nitrogen and carbon monoxide are the processes by which the solid can release the excess surface energy. Depending on the interaction between the solid and gas, adsorption can be classified into a physical or a chemical adsorption process. Physical adsorption processes involve only nonspecific van der Waals forces while in chemical adsorption there is a chemical bonding. Solid-vapour adsorption is an exothermic process in which increasing the temperature of the system decreases the amount of adsorbed gas by solid.

Physical adsorption is a reversible process and equilibrium is instantaneously accomplished in the absence of capillary condensation and a competitive adsorption. Generally, physical adsorption is a multilayer process (see Figure 2. 15) in which the solid surface area does not restrict the number of adsorbed molecules. Unlike physical adsorption, chemisorption is an irreversible process and is limited to form a monomolecular adsorbed layer (Lowell and Shields, 1984; Myers, 1999).

In the context of physisorption, it is important to define the pores. The pores according to their size can be classified into three types:

i) Macropores: the width of the pores is exceeding about 50 nm.

ii) Mesopores: the width of the pores is between 2 nm and 50 nm.

iii) Micropores: the width of the pores is not exceeding 2 nm.

Physical adsorption phenomenon is the base of BET (Brunauer, Emmet and Teller) theory for surface area determination of porous materials. If such materials are in equilibrium with a certain surrounded gas, at the internal and external surfaces pore, a certain amount of the surrounding gas is physically adsorbed at a certain temperature and a relative vapour pressure P/P_0 (Fagerlund, 1973).

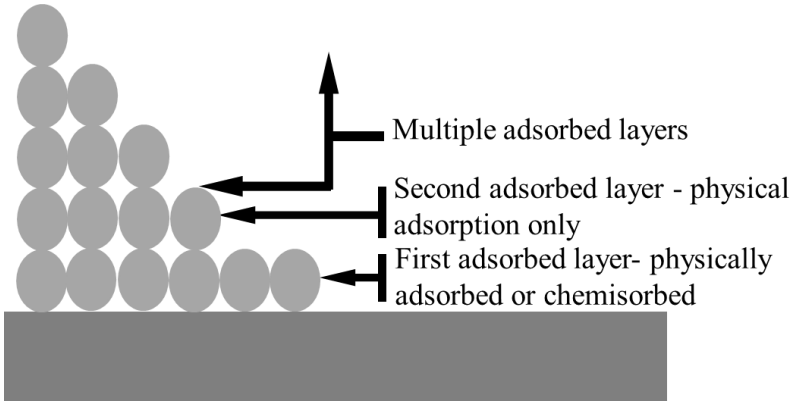

Figure 2. 15. Multilayers adsorption on a solid surface (Myers, 1999).

2.2.4.1 Classification of adsorption isotherms

Brunauer, Deming, Deming and Teller proposed after an intensive study of literature the classification of adsorption isotherm curves. The classification divides isotherms into five main types and all adsorption isotherms must fit into one of them (Lowell and Shields, 1984). Later deBoer developed the sixth isotherm and it was supplemented by Gregg and Sing (Condon, 2006). Each isotherm in Figure 2. 16 reflects some unique conditions.

Type I isotherm. This type is limited to a few molecular layers and it is characterised as either a chemical isotherm or a physical isotherm or a microporous solid such as some activated carbons, zeolites and certain porous oxides.

Type II isotherm. This type is a monolayer-multilayer adsorption isotherm and has the inflection point (point B in Figure 2. 16) that occurs almost near the completion of the monolayer or the start of the secondary layer, caused by multiplayer adsorption. By increasing the relative pressure, layer by layer are completed until they reach saturation. However, this type is characteristic for nonporous and macroporous materials or powders with diameters exceeding micropores. In addition, such materials should have a high adsorption energy (Sing *et al.*, 1985; Thommes *et al.*, 2015).

Type III isotherm. This is not a common isotherm. It is characteristic of nonporous materials or macroporous materials that have a low adsorption energy (Sing *et al.*, 1985; Thommes *et al.*, 2015).

Type IV isotherm. This type of isotherms contains a hysteresis loop characteristic to mesoporous adsorbents that have a high adsorption energy. The initial part of this type is similar to type II for a monolayer-multilayer adsorption. Furthermore, the range of pores radius of such adsorbent are ~ 1.5-100 nm.

Type V isotherm. Type V is an uncommon isotherm and is close in shape to a type III isotherm due to a small interaction between the adsorbate and adsorbent. This type of isotherms can be seen by the adsorption of water by mesoporous or microporous adsorbents (Thommes *et al.*, 2015).

Type VI isotherm. Several possibilities could be attributed to this type of isotherm. The most likely is a multilayer adsorption of nonporous material. Another possibility is a varying pore size (Lowell and Shields, 1984; Sing *et al.*, 1985).

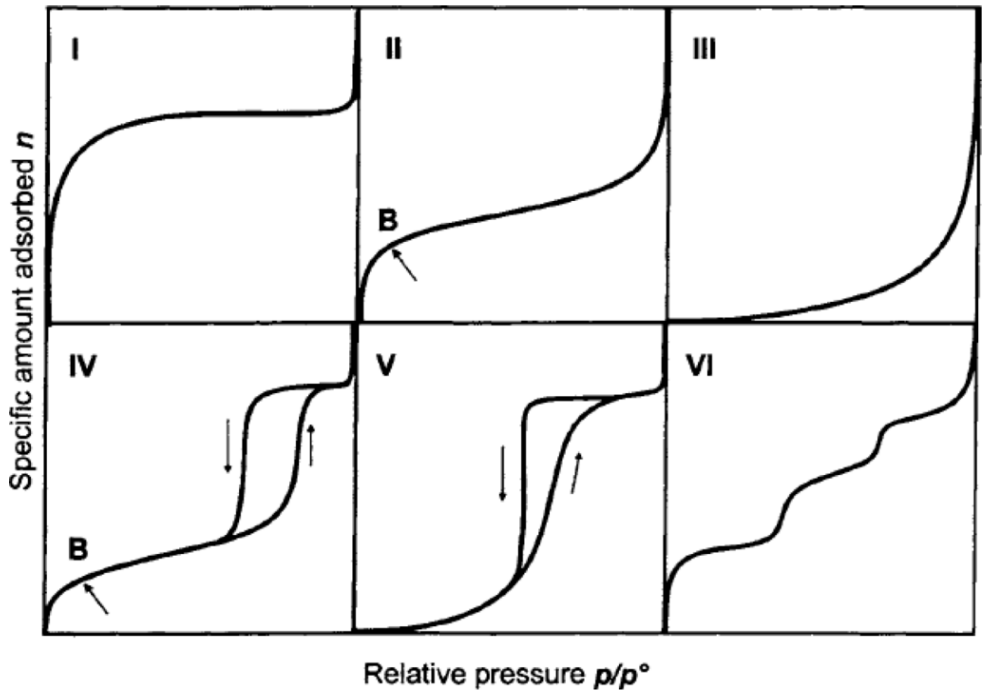

Figure 2. 16. Types of physical adsorption isotherms (Sing *et al.*, 1985).

2.2.4.2 Langmuir Theory

In chemisorption, the adsorbed molecules can form only one bonding layer with the surface of the adsorbent and that makes chemisorption exhibit a type I isotherm. The bonding between the adsorbed molecules and the adsorbent surface depends on adsorbent surface structure and the size of adsorbate molecules. As molecules are unable to compact among each other, spaces

form between the molecules causing a lower molecule capacity to occur on the substance's surface. This creates a difficulty in measuring the surface area as the measured value would be lower than the true value (Lowell and Shields, 1984).

Langmuir described adsorption as a dynamic process in which the rate of adsorption is equal to the rate of desorption. Using the kinetic theory of gas, Langmuir describes the type I isotherm by assuming that the adsorption is limited to the monolayer (Flood, 1967; Lowell and Shields, 1984). Therefore, the number of striking molecules N to the unit area per unit time is given by (Lowell and Shields, 1984):

$$N = \frac{\overline{N}P}{(2\pi\overline{M}RT)^{1/2}} \tag{2.8}$$

where $\overline{N}$, P, $\overline{M}$, R, and T are Avogadro's number, the adsorbate pressure, the adsorbate molecular weight, the gas constant and the absolute temperature, respectively. Then the number of collisions per square centimetre per second at the bare surface (with no adsorbed molecules) can be written as:

$$N' = k\mathrm{P}\theta_0 \tag{2.9}$$

where θ_0 is the fraction of bare surface and k is a constant $\left(\overline{N}/(2\pi\overline{M}\,RT)^{1/2}\right)$. Consequently, the number of adhered molecules to each square centimetre is

$$N_{ads} = kP\theta_0 A_1 \tag{2.10}$$

where A_1 is the condensation coefficient.

The rate of desorption from each square centimetre of the surface of sample is given by

$$N_{des} = N_m\theta_1 v_1 e^{-E/RT} \tag{2.11}$$

where N_m, θ_1, v_1 and E are the number of adsorbed molecules in square centimetres of a completed monolayer, fraction of surface occupied by adsorbed molecules, frequency of vibration of the normal adsorbate of the surface and the energy of adsorption, respectively. Equation (2.11) describes the rate at which molecules leave the surface of adsorbent at each square centimetre.

At equilibrium the rate of adsorption is equal to the rate of desorption, therefore:

$$N_m\theta_1 v_1 e^{-E/RT} = kP\theta_0 A_1 \tag{2.12}$$

$\theta_0 = 1 - \theta_1$, then

$$\theta_1 = \frac{kPA_1}{N_m v_1 e^{-E/RT} + kPA_1} \quad (2.13)$$

If the adsorption energy E is constant, the surface is energetically uniform,

$$K = \frac{kA_1}{N_m v_1 e^{-E/RT}} \quad (2.14)$$

therefore, Eq. (2.13) can be written as:

$$\theta_1 = \frac{KP}{1+KP} \quad (2.15)$$

Considering a one layer of coverage, we can write

$$\theta_1 = \frac{N}{N_m} = \frac{W}{W_m} \quad (2.16)$$

where N is the number of adsorbed molecules in the uncompleted monolayer and N_m is the number of molecules in completed monolayer. W and W_m are the weight adsorbed and the weight adsorbed of the completed monolayer, respectively. Substituting W/W_m in Eq. (2.15) gives:

$$\frac{P}{W} = \frac{1}{KW_m} + \frac{P}{W_m} \quad (2.16)$$

Eq. (2.16) is the Langmuir equation for type I isotherms. K and W_m can be calculated by plotting P/W versus P, to give a straight line, where their slope is $1/W_m$ and the intercept is $1/KW_m$.

Once W_m is known, the surface area, S_t, can be estimated from the following equation:

$$S_t = N_m A = \frac{W_m \bar{N} A}{\bar{M}} \quad (2.17)$$

where A is the cross-section area.

2.2.4.3 The Brunauer, Emmett and Teller (BET) theory

The Langmuir equation describes the chemisorption of a type I of isotherm. However, it fails to deal with a physical sorption and other types of isotherms. At a low relative pressure during a physical adsorption process, sites of higher energies are firstly covered. These high energetic sites are within narrow pores and between the vertical and horizontal edges of surface steps. As the adsorbate's pressure increases, the surface of the adsorbent is gradually coated by the adsorbed molecules and the probability of adsorbing molecules to the previously bonded molecules increases.

In 1938, Brunauer, Emmett and Teller generalised Langmuir's theory to multilayer adsorption. Brunauer, Emmett and Teller (BET) theory has proposed a state of dynamic equilibrium between the uppermost molecules of adsorbed stacks and the vapour. Therefore, whether one or more layers of adsorbate cover the surface, a dynamic equilibrium exists between the vapour and the upper layer and the number of molecules remains constant in each layer (Lowell and Shields, 1984).

The equilibrium between the vapour and adsorbate in the first layer can be described by using the Langmuir's theory and equation (2.12). Generalising Eq. (2.12) for *n*th layer one obtains

$$N_m \theta_n v_n e^{-E_n/RT} = kP\theta_{n-1}A_n \qquad (2.18)$$

BET theory assumes *v*, *E* and *A* in Eq. (2.18) remaines constant for the second and higher layers. This assumption is valid when the layers are away from the surface and all layers are equivalent to the liquid state. Therefore, Eq. (2.18) can be written as

$$N_m \theta_n v e^{-L/RT} = kP\theta_{n-1}A \qquad (2.19)$$

where *L* is the heat of liquefaction.

$$\frac{\theta_1}{\theta_0} = \frac{kPA_1}{N_m v_1 e^{-E_1/RT}} = \alpha \qquad (2.20a)$$

$$\frac{\theta_2}{\theta_1} = \frac{kPA}{N_m v e^{-L/RT}} = \beta \qquad (2.20b)$$

and generally

$$\frac{\theta_n}{\theta_{n-1}} = \frac{kPA}{N_m v e^{-L/RT}} = \beta \qquad (2.20d)$$

then

$$\theta_n = n_{n-1}\beta = \alpha\beta^{n-1}\theta_0 \qquad (2.21)$$

At equilibrium, the total number of adsorbed molecules is

$$N = N_m\theta_1 + 2N_m\theta_2 + \cdots + nN_m\theta_n = N_m(\theta_1 + 2\theta_2 + \cdots + n\theta_n) \qquad (2.22)$$

Substitution of Eq. (2.20a-d) in Eq. (2.22)

$$\frac{N}{N_m} = \alpha\theta_0 + 2\alpha\beta\theta_0 + 3\alpha\beta^2\theta_0 + \cdots + n\alpha\beta^{n-1}\theta_0$$

$$= \alpha\theta_0(1 + 2\beta + 3\beta^2 + \cdots + n\beta^{n-1}) \qquad (2.23)$$

since α and β are assumed to be constants,

$$\alpha = C\beta \tag{2.24}$$

from Eq. (2.20a) and Eq. (2.20b), C can be defined as

$$C = \frac{A_1 v_2}{A_2 v_1} e^{\frac{(E1-L)}{RT}} \tag{2.25}$$

Substitution of Eq. (2.24) in Eq. (2.23) yields to:

$$\frac{N}{N_m} = C\theta_0(\beta + 2\beta^2 + 3\beta^3 + \cdots + n\beta^n) \tag{2.26}$$

This summation can be written as $\beta/(1-\beta)^2$, therefore:

$$\frac{N}{N_m} = \frac{C\theta_0\beta}{(1-\beta)^2} \tag{2.27}$$

θ_0 can be defined as

$$\theta_0 = 1 - (\theta_1 + \theta_2 + \theta_3 + \cdots + \theta_n) = 1 - \sum_{n=1}^{\infty} \theta_n \tag{2.28}$$

Substitution of Eq. (2.28) in Eq. (2.27) and replacing θ_n and $C\beta$ from Eq. (2.21) and Eq. (2.24), yields to:

$$\frac{N}{N_m} = \frac{C\beta}{(1-\beta)^2}(1 - C\theta_0 \sum_{n=1}^{\infty} \beta^n \tag{2.29}$$

since

$$\sum_{n=1}^{\infty} \beta^n = \beta + \beta^2 + \beta^3 + \cdots + \beta^n = \frac{\beta}{1-\beta} \tag{2.30}$$

then

$$\frac{N}{N_m} = \frac{C\beta}{(1-\beta)^2}\left(1 - C\theta_0 \frac{\beta}{1-\beta}\right) \tag{2.31}$$

Substitution of Eq. (2.31) in Eq. (2.27) gives

$$\theta_0 = \frac{1}{1+\frac{C\beta}{1-\beta}} \tag{2.32}$$

Substitution of θ_0 in Eq. (2.27)

$$\frac{N}{N_m} = \frac{C\beta}{(1-\beta)(1-\beta+C\beta)} \tag{2.33}$$

$\frac{N}{N_m}$ becomes infinity if β is equal unity. Physically that situation occurs if the adsorbed molecules are condensed on the surface or $P/P_0 = 1$. Rearranging Eq. (2.20b) for $P = P_0$

$$1 = \frac{kAP_0}{N_m v e^{-\frac{L}{RT}}} \tag{2.34}$$

but from Eq. (2.20d)

$$\beta = \frac{kAP}{N_m v e^{-\frac{L}{RT}}}$$

then

$$\beta = \frac{P}{P_0} \tag{2.35}$$

Introducing of β from Eq. (2.35) into Eq. (2.33) gives

$$\frac{N}{N_m} = \frac{C\left(\frac{P}{P_0}\right)}{(1-P/P_0)[1-P/P_0+C(P/P_0)]} \tag{2.36}$$

Replacing the term N / N_m by W / W_m from Eq. (2.16) and rearranging Eq. (2.36), BET in final form becomes (Lowell and Shields, 1984):

$$\frac{1}{W[(P/P_0)-1]} = \frac{1}{W_m C} + \frac{C-1}{W_m C}\left(\frac{P}{P_0}\right) \tag{2.37}$$

Determination of the surface area from BET equation

Plotting $1/W[(P/P_0)-1]$ versus P/P_0 from BET equation (Eq. 2.37) provides a straight line if C is constant (see Figure 2. 17). C is constant for the majority of vapour adsorption isotherms in the very important region $0.05 \leq P/P_0 \leq 0.35$ (Flood, 1967; Lowell and Shields, 1984). The slope of the plot *s* and interception *i* are given by:

$$s = \frac{C-1}{W_m C}, \; i = \frac{1}{W_m C}$$

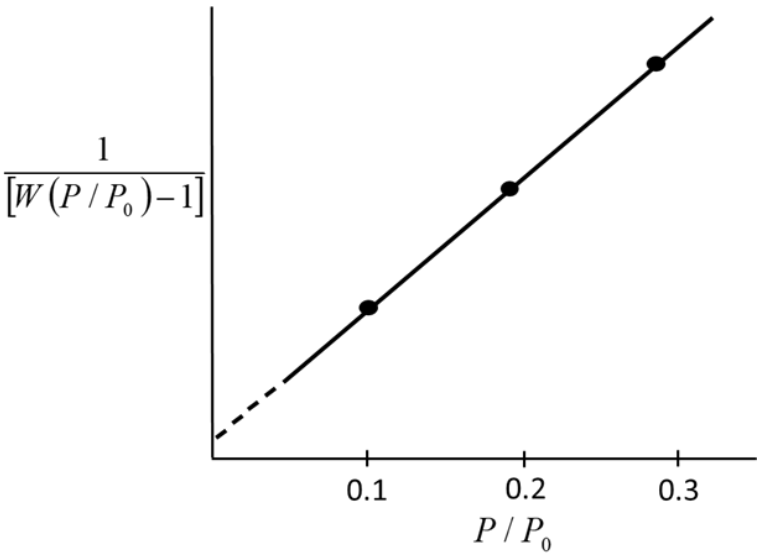

Figure 2. 17. Typical BET plot (Lowell and Shields, 1984).

therefore, *C* can be given as:

$$C = \frac{s}{i} + 1 \qquad (2.38)$$

The specific surface area can be calculated by dividing the total surface area S_t in Eq. (2.17) by the sample's weight.

2.2.4.4 Barret, Joyner and Halenda (BJH) theory and the pore size distribution

The common technique to determine pore size distribution of solid materials through the physical gas adsorption. Depending on the nature of the adsorbent material or the expected information, many adsorptive gases such as N_2, Ar, and CO_2 are utilised for that purpose. Applying N_2 adsorption at 77 K over a wide range of relative pressures (P/P_0) provides an information about micro-, meso-, and macro- porosity of the samples in the range of 0.5-200 nm (Groen *et al.*, 2003). Barrett *et al.* (1951) proposed a technique to estimate the pore volume and area for a range of pore sizes of relatively rough porous materials. Barrett *et al.* (1951) proposed their technique based on the Wheeler theory which can be expressed by the following equation:

$$V_s - V = \pi \int_{r_{Pn}}^{\infty} (r - t)^2 \, L(r) dr \qquad (2.39)$$

where V_s and V are the volume of *adsorbate* at saturation pressure P_o and pressure P, respectively. $L(r)\ dr$ represent the total length of pores in which the radii range are filled between r and $r+dr$. Where t is the multilayer's thickness at pressure P and r_{pn} is the critical

radius which is defined as the largest pore that is filled completely by condensed adsorbate molecules at any pressure.

Barrett *et al.* (1951) proposed to calculate the pore size distribution from the desorption isotherm and assumed that controlled equilibrium is reached by the contribution of two different mechanisms. The first mechanism occurs due to physical adsorption which causes layers of adsorbate molecules to form on the surface of the pore's walls and the second is caused by capillary condensation.

Barrett *et al.* (1951) assumed that the system consists of open-ended cylindrical pores (see Figure 2. 18) where to any change in the relative pressure (P/P_0), all pores of equal radius respond in a similar way. When $(P/P_0)_1$ is close to the saturation pressure, the liquid fills all the pores and evaporation occurs by lowering (P/P_0). Under equilibrium, the largest pore (see Figure 2. 18) of radius r_{p_1} has adsorbed a layer of thickness r_{k}. Therefore, the relation, which connects the volume of pore, V_{p_1}, and the volume of the inner capillary, V_{k}, can be written as:

$$V_{p_1} = \frac{V_{k_1} r_{p_1}^2}{r_{k_1}^2} \tag{2.40}$$

However, since V_{k_1} is not known, this equation is not valuable.

Desorbing of a measurable volume of adsorbate molecules (ΔV_1) lowers the relative pressure from $(P/P_0)_1$ to $(P/P_0)_2$. The reduction of (P/P_0) in the large pore is accompanied with both emptying of its capillary condensation and reducing the thickness of adsorbate molecules layer by Δt_1. Therefor Eq. (2.40) can be written as:

$$V_{p_1} = R_1 \Delta V_1 \tag{2.41}$$

where $R_1 = r_{p_1}^2/(r_{k_1} + \Delta t_1)^2$.

However, the problem arises when one applies the assumption on the second pore. Lowering the relative pressure from $(P/P_0)_2$ to $(P/P_0)_3$ will cause a complication when determining the volume. In fact, the reduction of the liquid's volume is a contribution of the second pore and the second thinning of adsorbate molecules layer of the first pore. Therefore, one can write

$$V_{p_2} = R_2\left(\Delta V_2 - V_{\Delta t_2}\right) \tag{2.42}$$

where $R_2 = r_{p_2}^2/(r_{k_2} + \Delta t_2)^2$, and $V_{\Delta t_2}$ is the volume of the second thinning.

From figure 2.18, one can write:

$$V_{\Delta t_2} = \pi L_1 \left(r_{k_1} + \Delta t_1 + \Delta t_2\right)^2 - \pi L_1 \left(r_{k_1} + \Delta t_1\right)^2 \qquad (2.43)$$

L_1 is the pore length of the first pore.

However, a practical calculation of $V_{\Delta t_2}$ from Eq. (2.43) becomes more sophisticated as the number of involved pores increased.

Another definition for $V_{\Delta t_2}$ is

$$V_{\Delta t_2} = \Delta t_2 A_{c_1} \qquad (2.44)$$

where A_{c_1} is the average area from which the adsorbate molecules are desorbed.

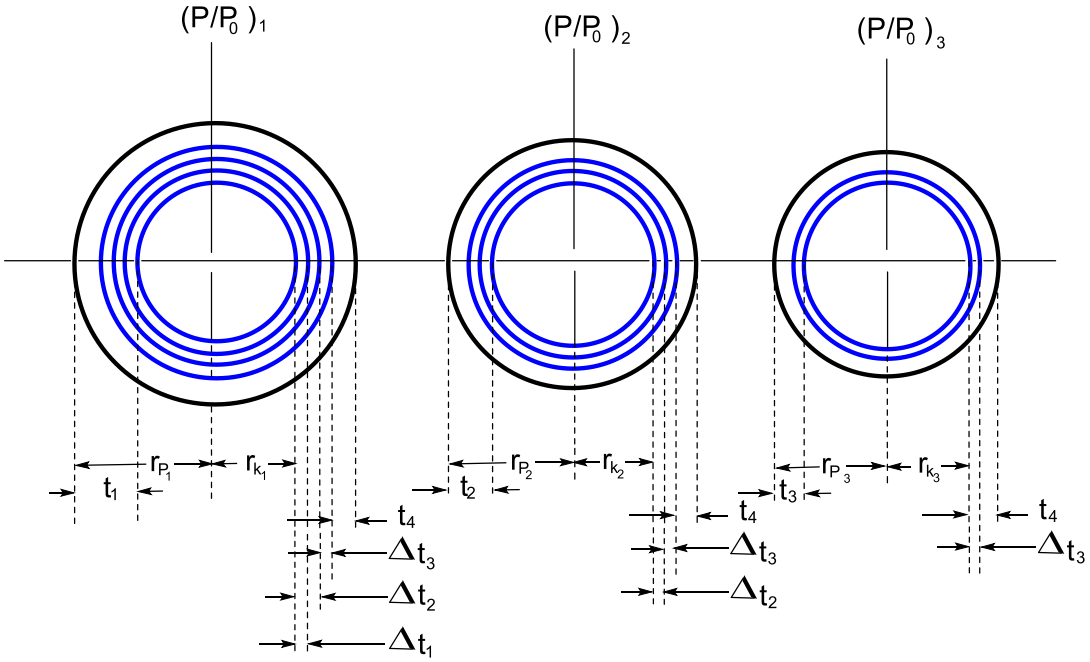

Figure 2. 18. Schematic of the assumption for desorption mechanism for three different pores (Barrett *et al.*, 1951).

Eq. (2.44) can be generalised to

$$V_{\Delta t_n} = \Delta t_n \sum_{j=1}^{n-1} A_{c_j} \qquad (2.44a)$$

The summation in Eq. (2.44a) represents the summation of the average area for unfilled pores. However, it does not include the pore for which the condensate molecules layers were emptied off during *nth* desorption.

By generalising and substituting Eq. (2.44a) into Eq. (2.42), one can get the porous model

$$V_{P_n} = R_n \Delta V_n - R_n \Delta t_n \sum_{j=1}^{n-1} A_{c_j} \qquad (2.45)$$

In an empty pore, any decrease in P/P_0 is accompanied with a change in the quantity of A_c which makes Eq. (2.45) unsatisfactory. That makes $\sum A_c$ during desorption an unknown quantity.

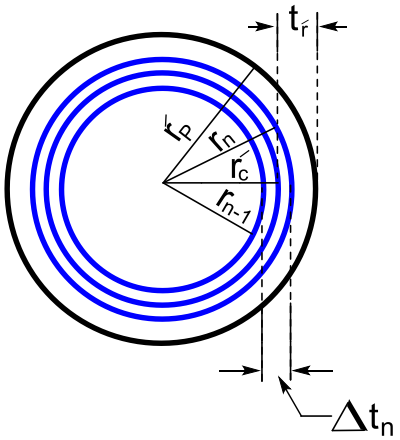

Figure 2. 19. The relation between $V\Delta t$ and r_p at nth step of desorption (Barrett *et al.*, 1951).

Since the capillaries are coaxial with pores and the area of each pore ($A_P = 2V_P/r_P$) is a constant quantity, with the successive decrease in P/P_0, Eq. (2.45) becomes satisfactory to calculate the pore volume, if $\sum A_c$ is calculated with respect to $\sum A_p$. To find that relationship, Figure 2. 19 assumed that each capillary that is emptied from condensate molecules layers has an average radius $\acute{r}_p$ between that measured during higher and lower values of P/P_0.

In Figure 2. 19, r_{n-1} and r_n are the capillary's radius before and after desorption and $\acute{r}_c$ is their average value. During desorption of Δt_n, the average area of the capillary is equal to $A_p \times (\acute{r}_c / \acute{r}_p)$. If $t_{\acute{r}}$ is the thickness of the adsorbed molecular layer then $\acute{r}_c = \acute{r}_p - t_{\acute{r}}$ can substitute A_c in Eq. (2.45) in the last term and one gets:

$$V_{\mathrm{P_n}} = R_n \Delta V_{\mathrm{n}} - R_n \Delta t_{\mathrm{n}} \sum_{j=1}^{n-1} c_j A_{P_j} \qquad (2.46)$$

where $c = (\acute{r}_p - t_{\acute{r}}) / \acute{r}_p$.

Equation (2.46) is the basis for the practical calculation of the pore size distribution. It is built on only two basic assumptions: (1) pores have a cylindrical shape, and (2) the mechanisms that retain the adsorbed molecular layers in equilibrium with the vapour phase are the physical adsorption and the capillary condensation.

It is necessary to know that r_k is calculated by using Kelvin equation (Barrett *et al.*, 1951).

$$\mathrm{Log}(P/P_0) = \frac{-2\sigma V}{8.316 \times 10^7 \times 2.303\, T r_k} = \frac{-4.14}{r_k} \qquad (2.47)$$

where σ is the surface tension of liquid nitrogen, V is liquid nitrogen's molar volume, r_k is the capillary radius in centimetres and T is the absolute temperature.

The surface area, pore size distribution and N_2 adsorption-desorption curves are presented in this thesis in chapters 3-7 and were calculated using Brunauer, Emmet and Teller (BET) and Barrett–Joyner–Halenda (BJH) methods. Nitrogen adsorption-desorption analysis SURFER (Thermo Scientific) is utilised to perform the analysis (see Figure 2. 20).

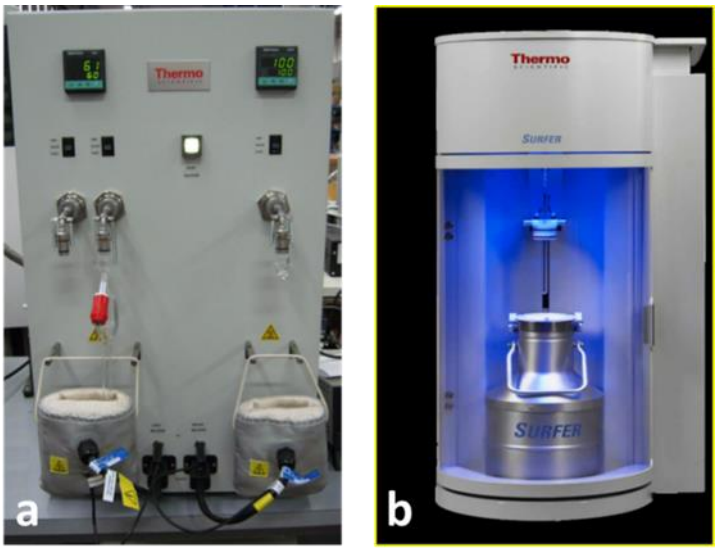

Figure 2. 20. SURFER (Thermo Scientific) main parts. a-External degasser unit b- Surfer cabinet.

All samples were degassed under a vacuum and heated. The degassing stage was carried out in two steps. The first step was carried out on an empty glass burette at 120 °C for 15 minutes. The mass of the burette was recorded as m_1. After which about 100-200 mg of the investigated aerogels materials was dropped in the burette. The second step of degassing was performed at temperature of 200 °C for 8 hours. Subsequently, the mass of the materials and burette were recorded as m_2. The net mass of aerogels (m) was calculated by subtracting m_2 from m_1. The mass m was then entered to the software of the instrument. The degassed burette was then plugged in the analyser (see Figure 2. 20b) and the drawer, which is filled with liquid nitrogen, was automatically elevated to submerge the burette, in order to cool the sample temperature to 77 K during the analysis.

2.2.6 Mechanical properties and compression testing of materials

When an applied load is subjected to the external surface of a material, a reversible deformation arises as a response to that load. This is known as the elastic behaviour of the

material. The material behaves under loading in the elastic region of the stress-strain curve (see Figure 2. 21) according to Hooke's law.

$$\sigma_x = E\varepsilon_x \tag{2.48}$$

where σ is the stress, E is Young's modulus and ε is the strain.

Plastic deformation starts after elastic deformation at the point on stress/strain curve called the yield stress or yield point. Materials, depending on their behaviour under loading, are classified as either brittle or ductile. Brittle materials cannot withstand a large stress and they break in the elastic region, where ductile material can bear a relatively large stress.

Figure 2. 21 demonstrates a typical tensile stress-strain curve, which is obtained from subjecting a continuously increasing tensile uniaxial load on a specimen.

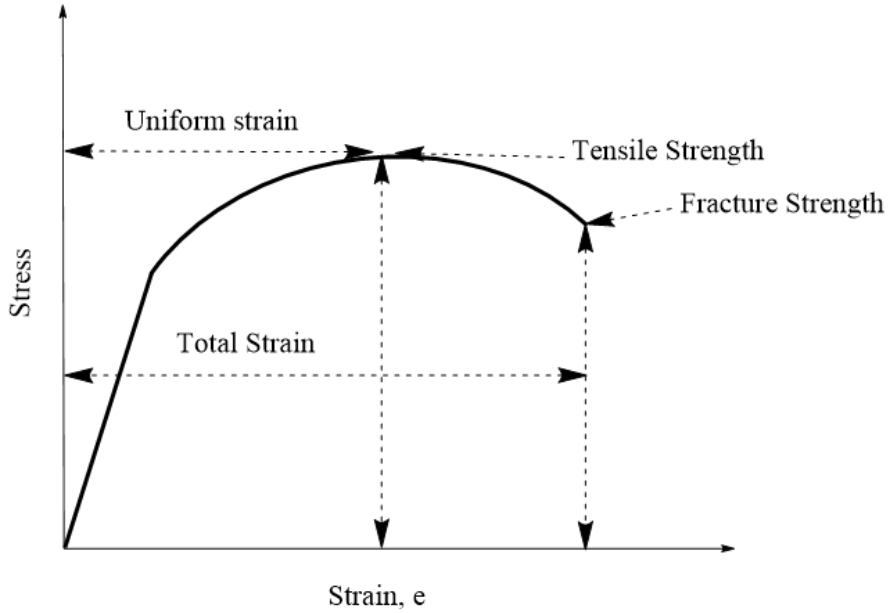

Figure 2. 21. Schematic diagram of stress-strain curve in a tensile test (Pelleg, 2013).

Another type of stress is the compressive stress (Figure 2. 22 shows typical compression stress-strain curve). Appling a compressive stress on a specimen generally reduces its size. Ductile materials show similar results in the compression and tensile tests, where brittle materials show a higher strength and a greater strain before the fracture in the compression test than in the tension test.

The difference between compression stress-strain curves and tensile curves is the absence of the necking phenomena. After reaching the ultimate tensile strength, the stress decreases until a fracture occurs. While in compression, the stress is continuing to rise until fracture (Figure 2. 22 shows typical compression stress-strain curve). A compression test is usually employed to measure the mechanical properties for a nonstandard material rather than the tension test

because the shape of the sample for a compression test is simpler than that for a tension. However, the feasibility of obtaining a reliable result from a nonstandard specimen is limited by taking the proper length (h) to diameter (d) specimen ratio. The ratio must be h/d < 2-3 (Pelleg, 2013).

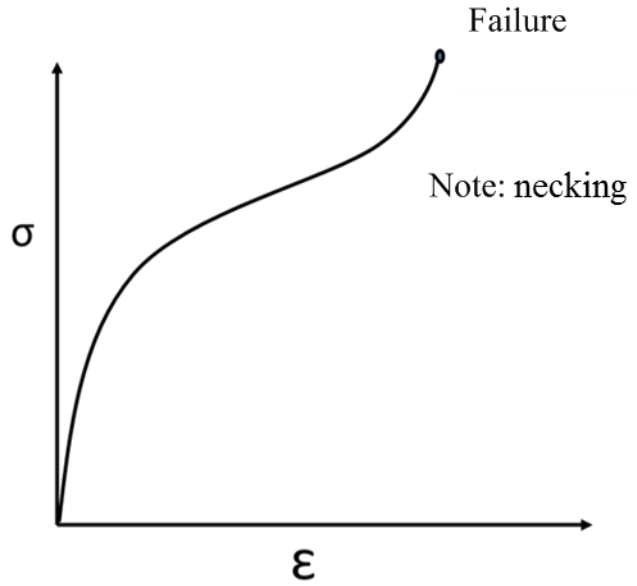

Figure 2. 22. Typical stress- strain curve in a compression test.(Pelleg, 2013)

In chapter 3 of this thesis, uniaxial compression tests were carried out with ASTM D695 by using a universal test machine (Tinius Olsen H25KS). In case of the ceramic blanket-silica aerogel composites (CBSA), the samples were cut in disk shapes of 20 mm diameter and thickness of 8 mm. The displacement's speed was controlled by 0.5 mm/min and the load cell was 5000 N for the loading-displacement evaluations. While for the short fibres reinforced-aerogel composites (CSSA), the samples were cut in a square shape of 4 mm x 4 mm x 8 mm and the load cell was 100 N with a displacement's speed of 0.5 mm/min.

2.2.7 Thermal conductivity measurement

Generally, the most common techniques that are used to measure the thermal conductivity for bulk materials can be classified into two major categories. The first classification is known as steady state methods and these include the comparative technique, radial heat flow method and parallel conductance method. Determination of the thermal conductivity in steady state methods is conducted by measuring the difference in temperature through a known distance of a sample under a steady state heat flow. The second classification is called transient techniques. The measurements are performed with a time dependent heat energy transfer through a sample.

The main transient techniques are the Pulsed power technique, the hot-wire method, the laser flash method and the transient plane source (TPS) method (also called Hot-disk method) (Zhao *et al.*, 2016).

The author of this thesis has conducted the hot-disk method (TPS 2500s) to measure the thermal conductivity of aerogel samples because this method provides quick and accurate measurement for small size samples.

Transient Plane source (TPS)

Transient plane source (TPS) is a practically instant and very precise technique that offers accurate thermal conductivity measurements in the range of 0.005-500 Wm^{-1} K^{-1} in a temperature range of -250 to 900 °C. In the TPS technique, a double spiral made of the electrical conductor, a thin pure nickel foil of 10 μm thickness, is employed as a transient plane sensor. Thin sheets of Kapton® are used as an insulator to retain the spiral. The determination of the thermal properties by the TPS method are performed when the heating sensor is sandwiched (see Figure 2. 23) between two samples of similar properties (Anis-ur-Rehman and Maqsood, 2003; Gustavsson *et al.*, 2006; Solorzano *et al.*, 2008).

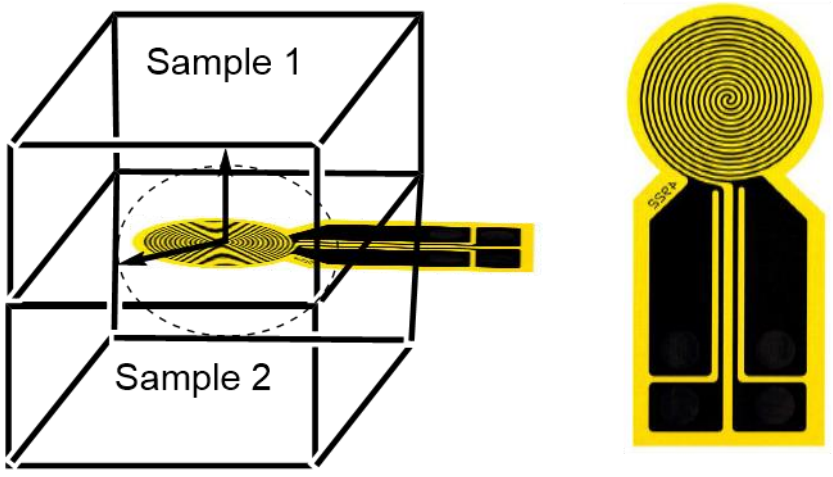

Figure 2. 23. Schematic diagram of the thermal conductivity measurement by TPS with Kapton® sensor shape (Solorzano *et al.*, 2008).

Theory

The principles of the plane source method was first proposed to measure the thermal conductivity of electrically insulating solid and liquid insulators by Gustafsson *et al.* (1979).

Later it was developed to determine the thermal conductivity of electrically conductive solids (Gustafsson *et al.*, 1986).

The TPS method is valid based on three assumptions:

(1) The heating source is composed of concentric equal spaced circles.

(2) The dimension of the tested sample is semi-infinite for the tested material.

(3) The sensor thickness is negligible.

In the TPS method, the function of sensor is to be a heat source and a temperature the sensor at the same time (Zhang *et al.*, 2017). Once a sufficient constant current is passed through the sensor (to increase the temperature by 1-2 K), the resistance will change associated with a corresponding drop in voltage over the sensor. Over a certain time, the heat flow between the sensor and the tested material can be obtained by recording the variation in the voltage and the current. Although there will be a small drop in the temperature, ΔT, over the layer of the Kapton (which is electrically insulating material), it will stay constant after a short initial period (Log and Gustafsson, 1995).

The relation between the resistance of the sensor $R(t)$ and the increase in temperature ΔT of the heating element can be expressed by:

$$R(t) = R_0\,(\,1\, + \alpha\Delta T) = \, R_0\,\left[\,1 + \,\alpha\Delta T_i + \,\alpha\overline{\Delta T(\tau)}\right] \tag{2.49}$$

where R_0 is the initial resistance of the heating element (nickel) at the beginning of the analysis, α is a temperature coefficient of resistance for a nickel foil, and $\overline{\Delta T(\tau)}$ is the average increase in temperature of the nickel element when there is perfect contact between the two halves of the specimen.

The average ($\overline{\Delta T(\tau)}$) can be obtained from the following relationship:

$$\overline{\Delta T(\tau)} = \frac{P_0}{\pi^{3/2}\, rk} D(\tau) \tag{2.50}$$

where P_0 is the sensor's heat liberation, k is the thermal conductivity of the tested material, r is the sensor's radius, $D(\tau)$ is the dimensionless time function, and τ is a variable defined as (Dixon *et al.*, 2000):

$$\tau = \frac{\sqrt{at}}{r} = \sqrt{\frac{t}{\Theta}} \tag{2.51}$$

where a is the specimen's thermal diffusivity, t is the time of measurement, and Θ ($\Theta \approx r^2/a$) is the measurement characteristic time.

By combining Eq. (2.50) with Eq. (2.49), one can get the following linear equation:

$$R(t) = R^* + CD(\tau) \tag{2.52}$$

where $R^* = R_0(1 + \alpha\Delta T_i)$, and $C = \frac{\alpha R_0 P_0}{\pi^{3/2} rk}$

According to Eq. (2.52) when Θ value is correct, plotting $R(t)$ versus $D(\tau)$ gives a straight line. After a transient recording, the thermal conductivity is determined by fitting the straight line of

Eq. (2.52) to the experimental data. Once fitting is completed, the thermal conductivity can be obtained from the slope of Eq. (2.52).

Figure 2. 24 and Figure 2.25 show the typical drift graph and transient graph for samples tested by the hot-disk method, respectively. The temperature drift must be randomly scattered across the horizontal axis and the temperature drift must be avoided to obtain accurate results. Therefore, the experiments must be performed in an environment with a stable temperature.

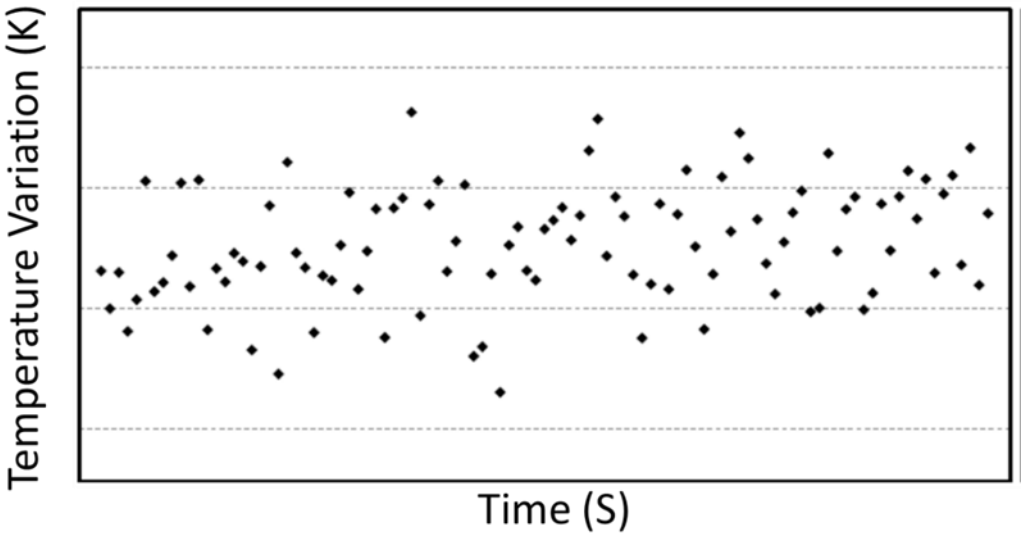

Figure 2. 24. An example of a drift graph.

The transient curve of increasing temperature should be continuous with no discontinuities or sudden jumps, alternatively the test must be repeated. The initial part of Figure 2. 25 which shows sharp increase in temperature is due to the contribution of the contact resistance between the sample and the contribution of the insulation material of the sensor. That part of the curve

and the end part of the curve (near boundary of the sample where data interfere with the air) must not be considered in the thermal conductivity calculation in order to obtain accurate results. A detailed example of the thermal conductivity measurement can be seen in appendix (A), chapter 9.

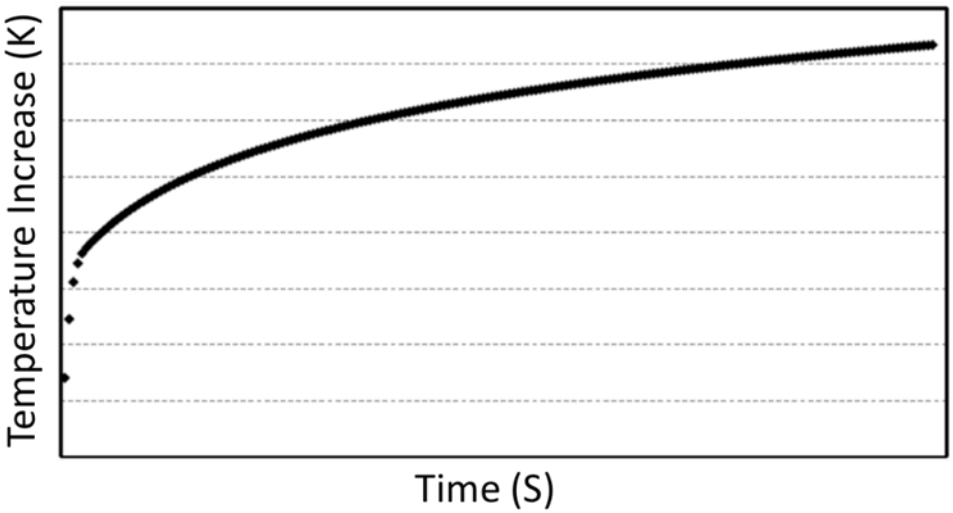

Figure 2. 25. Average increase of sensor temperature ($\Delta\bar{T}$) as a function of time during a typical hot disk measurement (Yi, 2005).

The author of this thesis has used a Hot-disk thermal constants analyser (TPS 2500 S) to determine the thermal conductivities of synthesised silica aerogels and reinforced silica aerogel composites in chapters 3 and 4. The hot disk sensor (C5465, radius of 3.189 mm) was held between two smooth and identical shaped pieces of the sample, which had a thickness of 6-10 mm. This analysis was carried out at range of temperatures, from 20 °C to 150 °C by oven. For accuracy, the temperature was increased by 10 °C each time and held for 30 minutes before taking each measurement. At each temperature, three measurements were carried out with an interval time of 10 mins between any two measurements.

2.2.8 Dynamic vapour sorption DVS

The term sorption is firstly utilised for food materials to describe the penetration and diffusion of the molecules into their network and later was generalised to include all types of polymeric materials. Sorption includes both adsorption and desorption processes and the formation of the cluster of adsorbates of water.

At a given temperature and humidity, the equilibrium of the sorption isotherm can be described by the following relationship (Guillard *et al.*, 2013):

$$Q_w = f(a_w) \tag{2.53}$$

where a_w is the ambient water activity, and Q_w is the water's concentration. Q_w can be obtained from the following relationship (Guillard *et al.*, 2013):

$$Q_w = \frac{M_w}{M_d} \tag{2.54}$$

where M_w is the sorbed water's mass at equilibrium and M_d is the dry matter mass.

At a given temperature, a_w can be obtained from (Guillard *et al.*, 2013)

$$a_w = \frac{P_w}{P_{w,0}} \tag{2.55}$$

where P_w is the water vapour pressure and $P_{w,0}$ is the water vapour pressure at its saturation state.

Models of water sorption are employed for many functions such as the predicting of sorption properties, analysing mechanisms of sorption and the interactions between water and materials.

Recently, a completed isotherm of water sorption (from 0-95% RH) can be obtained from a small sample in less than a week by utilising microbalance at controlled atmosphere and using automatic dynamic sorption methods (Guillard *et al.*, 2013).

The dynamic vapour sorption (DVS) system was designed by the company Surface Measurement Systems (illustrated in Figure 2. 26) to measure the amount and kinetics of solvent sorbed by a solid. This can be measured by recording the change in mass of the solid while varying the vapour concentration of sorbed solvent with the time (Sheokand *et al.*, 2014).

In chapter 7 of this thesis, sorption experiments were carried out in (Surface Measurement Systems Company) by using a DVS vacuum instrument. The schematic diagram of DVS is illustrated in Figure 2. 26. The instrument was used to investigate gas sorption kinetics and catalytic activity for a CO_2 hydration reaction (CHR) in gaseous phase of silica aerogel samples embedded with nickel nanowires and nickel nanoparticles. The mass data was recorded using ultra balance in dynamic mode, whereby both sorbate entry rate (upstream control by mass flow controllers) and sorbate exit rate (downstream control by butterfly valve) were controlled. During experiments, the pressure inside the chamber was controlled by a butterfly valve which has a regulated sorbate exit rate, whilst the mass flow controller delivered a gas at a constant flow rate.

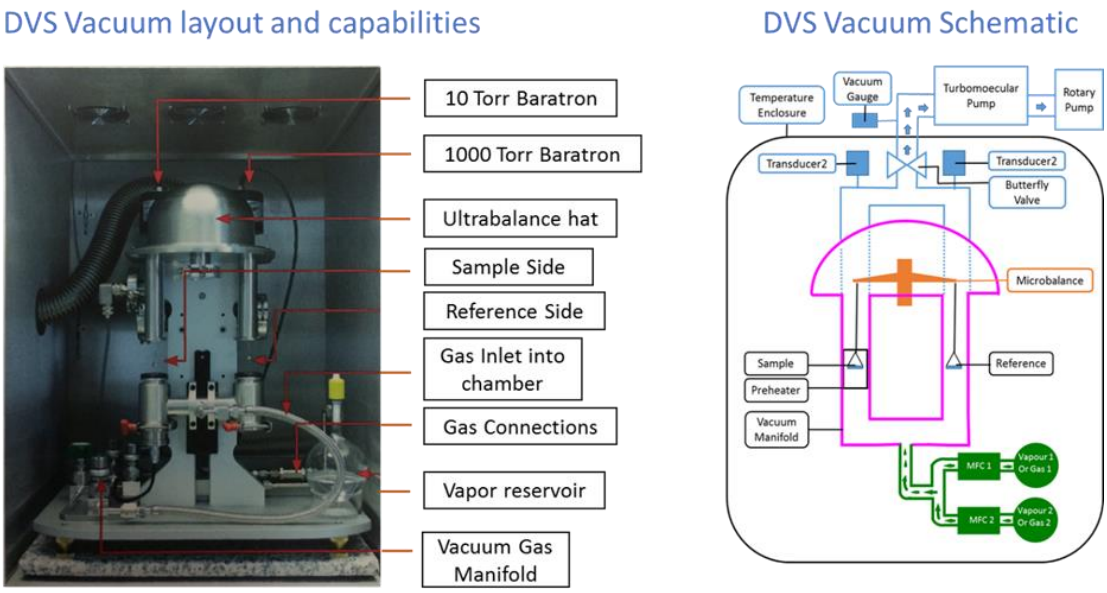

Figure 2. 26. A schematic for DVS Vacuum instrument with kind permission of Surface Measurement Systems.

Prior to the sorption analysis, the samples were *in-situ* degassed under a high vacuum and a temperature of 150 °C by using a heating rate of 5 °C in 120 mins. Upon the completion of the degassing stage, the samples were in-situ cooled down to 25 °C under high vacuum for 100 mins before starting the analysis. Sorption measurements were performed at 25 °C using a water vapour pressure (P_0) of 23.8 Torr and CO_2 of 760 Torr. The experiments were performed by measuring the mass change with time (dm/dt) by using criterion of 0.006%/min. Desorption branch were collected in a similar way.

2.3 Conclusion

The current chapter outlines synthesis methods of the materials presented in chapters 3-7. In addition, chapter 2 gives principles of operation of the techniques that are utilised in this thesis to characterise synthesised aerogels and their composites. Techniques such as TEM, SEM, XRD, BET, BJH, Hot-disk (TPS2500s) and DVS were described in detail.

References

Anis-ur-Rehman, M. and Maqsood, A. (2003) 'Measurement of thermal transport properties with an improved transient plane source technique', *International Journal of Thermophysics*, 24(3), pp. 867-883.

Barrett, E.P., Joyner, L.G. and Halenda, P.P. (1951) 'The determination of pore volume and area distributions in porous substances. I. computations from nitrogen isotherms', *Journal of the American Chemical Society*, 73(3), pp. 373-380.

Chen, L., Fang, M.L., Liu, C.Z., Liu, X.C. and Xing, S.X. (2015) 'Manipulating the nickel shape and catalytic performance: from spheres to chains to urchins', *Crystengcomm*, 17(47), pp. 4343-4348.

Condon, J.B. (2006) *Surface area and porosity determinations by physisorption measurements and theory*. Elsevier.

Dinnebier, R.E. and Billinge, S.J.L. (2008) *Powder diffraction theory and practic*. Cambridge : Royal Society of Chemistry.

Dixon, C., Strong, M.R. and Zhang, S.M. (2000) 'Transient plane source technique for measuring thermal properties of silicone materials used in electronic assemblies', *The International Journal of Microcircuits and Electronic Packaging*, 23(4).

Egerton, R.F. (2016) *Physical principles of electron microscopy*. Springer.

Fagerlund, G. (1973) 'Determination of specific surface by the BET method', *Materials and Structures*, 6(3), pp. 239-245.

Flood, E.A. (1967) *The solid-gas interface*. London: Edward Arnold Publishers Ltd.

Goldstein, J.I., Newbury, D.E., Echlin, P., Joy, D.C., Lyman, C.E., Lifshin, E., Sawyer, L. and Michael, J.R. (2003) *Scanning electron microscopy and X-ray microanalysis*. USA: Springer.

Goodhew, P.J. and Humphreys, F.J. (1997) *Electron microscopy and analysis*. Second edition edn. UK: Taylor & Francis.

Groen, J.C., Peffer, L.A.A. and Perez-Ramirez, J. (2003) 'Pore size determination in modified micro- and mesoporous materials. Pitfalls and limitations in gas adsorption data analysis', *Microporous and Mesoporous Materials*, 60(1-3), pp. 1-17.

Guillard, V., Bourlieu, C. and Gontard, N. (2013) *Food structureand and moisture transfer: A modeling approach*. Springer.

Gustafsson, S.E., Karawacki, E. and Chohan, M.A. (1986) 'Thermal transport studies of electrically conducting materials using the transient hot-strip technique', *Journal of Physics D-Applied Physics*, 19(5), pp. 727-735.

Gustafsson, S.E., Karawacki, E. and Khan, M.N. (1979) 'Transient hot-strip method for simul taneously measuring thermal-conductivity and thermal-diffusivity of solids and fluids', *Journal of Physics D-Applied Physics*, 12(9), pp. 1411-1421.

Gustavsson, M., Wang, H., Trejo, R.M., Lara-Curzio, E., Dinwiddie, R.B. and Gustafsson, S.E. (2006) 'On the use of the transient hot-strip method for measuring the thermal conductivity of high-conducting thin bars', *International Journal of Thermophysics*, 27(6), pp. 1816-1825.

Han, X., Hassan, K.T., Harvey, A., Kulijer, D., Oila, A., Hunt, M.R.C. and Siller, L. (2018) 'Bioinspired synthesis of monolithic and layered aerogels', *Advanced Materials*, 30(23).

Han, X. and Šiller, L. (2015) 'Aerogel synthesis', P221149GB/DW(WO2016132117 A1).

Han, X., Williamson, F., Bhaduri, G.A., Harvey, A. and Šiller, L. (2015) 'Synthesis and characterisation of ambient pressure dried composites of silica aerogel matrix and embedded nickel nanoparticles', *J. Supercrit. Fluids* 106, pp. 140-144.

Lifshin, E. (1999) *X-ray characterization of materials*. WILEY-VCH.

Log, T. and Gustafsson, S.E. (1995) 'Transient plan source (TPS) techniqu for measuring thermal transport properties of building materials ', *Fire and Materials*, 19(1), pp. 43-49.

Lowell, S. and Shields, J.E. (1984) *Powder surface area and porosity*. Chapman and Hall Ltd.

Luo, Z. (2016) *A practical guid to transmission electron microscopy*. Momentum Press®, LLC.

Myers, D. (1999) *Surfaces, interfaces, and colloids: priciples and applications*. John Wiley & Sons, Inc.

Pelleg, J. (2013) *Mechanical properties of materials*. springer.

Quinn, J.J. and Yi, K.-S. (2018) *Solid state physics: principle and modern applications*. Springer.

Sheokand, S., Modi, S.R. and Bansal, A.K. (2014) 'Dynamic vapor sorption as a tool for characterization and quantification of amorphous content in predominantly crystalline materials', *Journal of Pharmaceutical Sciences*, 103(11), pp. 3364-3376.

Sing, K.S.W., Everett, D.H., Haul, R.A.W., Moscou, L., Pierotti, R.A., Rouquerol, J. and Siemieniewska, T. (1985) 'Reporting physisorption data for gas/solid systems with spacial reference to determination of surface area and porosity ', *Pure and Applied Chemistry*, 57, pp. 603-619.

Solorzano, E., Reglero, J.A., Rodriguez-Perez, M.A., Lehmhus, D., Wichmann, M. and de Saja, J.A. (2008) 'An experimental study on the thermal conductivity of aluminium foams by

using the transient plane source method', *International Journal of Heat and Mass Transfer*, 51(25-26), pp. 6259-6267.

Stokes, D.J. (ed.) (2008) *Principles and practice of variable pressure/environmental scanning electron microscopy (VP-ESEM)*. UK: John Wiley & Sons, Ltd.

Thommes, M., Kaneko, K., Neimark, A.V., Olivier, J.P., Rodriguez-Reinoso, F., Rouquerol, J. and Sing, K.S.W. (2015) 'Physisorption of gases, with special reference to the evaluation of surface area and pore size distribution (IUPAC technical report)', *Pure Appl. Chem.* , 87(9-10), pp. 1051-1069.

Thornton, P.R. (1968) *Scanning electron microscopy application to matterials and device science*. Great Britain: Chapman and Hall Limited.

Waseda, Y., Matsubara, E. and Shinoda, K. (2011) *X-ray diffraction crystallography*. Springer.

Watt, I.M. (1997) *The principles and practice of electron microscopy* 2nd edition edn. UK: Cambridge University Press.

Wells, O.C., Boyde, A., Lifshin, E. and Rezanowich, A. (1974) 'Scanning electron microscopy'. USA: McGraw-Hill, Inc., p. 421.

Wolstenholme, J. (2015) *Auger electron spectroscopy practical application to materials analysis and characterization of surfaces, interfaces, and thin films*. Momentum Press®, LLC.

Yi, H. (2005) 'Rapid thermal conductivity measurement with a hot disk sensor - Part 2. Characterization of thermal greases', *Thermochimica Acta*, 436(1-2), pp. 130-134.

Zhang, H., Li, Y.M. and Tao, W.Q. (2017) 'Theoretical accuracy of anisotropic thermal conductivity determined by transient plane source method', *International Journal of Heat and Mass Transfer*, 108, pp. 1634-1644.

Zhao, D.L., Qian, X., Gu, X.K., Jajja, S.A. and Yang, R.G. (2016) 'Measurement techniques for thermal conductivity and interfacial thermal conductance of bulk and thin film materials', *Journal of Electronic Packaging*, 138(4), p. 19.

Zhou, W. and Wang, Z.L. (2006) *Scanning microscopy for nanotechnology*. Springer Science+Business Media, LLC.

Zuo, J.M. and Spence, J.C.H. (2017) *Advanced transmission electron microscopy imaging and diffraction in nanoscience*. Springer

Chapter 3 Fibre reinforced silica aerogels composites synthesised by bicarbonate ambient pressure drying method

This chapter details the reinforcement of silica aerogels by ceramic fibre blankets (CFB) and ceramic short fibres (CSF); these composites were synthesised using the ambient pressure drying method which utilises bicarbonate solvents and TMCS to reduce the production cost. The thermal conductivity of pure silica aerogel was found to be approximately (19 mW/m K). Reinforcing just by 11.2 wt % of CSF, the compressive strength of silica aerogels is increased ten times with a little decrease in the surface area and only a small increase in the thermal conductivity. Despite the small amount of the CSF (1.62-11.2 wt %), CSF reinforced silica aerogel composites (CSSA) exhibit low thermal conductivities of (21-28 mW/m K) while still exhibiting high surface areas (500-645 m2g-1). CFB reinforced silica aerogels composites (CBSA) were produced by introducing a small weight percentage of silica aerogels (23-34 wt %) to CFB. The composites had improved thermal insulation properties compared to pure CFB, with thermal conductivities in the range of 38-48 mW/m K. Both CBSA and CSSA composites could replace conventional insulation materials with an effective cost reduction.

3.1 Fibre reinforcement of silica aerogels

Preparation of ceramic blanket reinforced silica aerogels

Ceramic fibre blankets (CFB) with a size of 100 mm, 80 mm and 8 mm, were soaked in silica sol after mixing the contents of the two beakers. The gelation of the silica sol on ceramic fibres blanket was completed within 5 minutes. For ageing, silica gel-ceramic blanket composites are soaked in 150 ml of ethanol and covered for 24 h at room temperature and atmospheric pressure. Samples were synthesised for a range of silica aerogel weight percentages (see Table 3. 1, chapter 2) and named as AB1, AB2, AB3, AB4 and AB5.

Preparation of short ceramic fibre reinforced silica aerogels

Ceramic short fibres (CSF) were dispersed in DI water and then kept in sonication bath (Hilsonic) for 15 minutes. The solvents were prepared and mixed as mentioned in (2.1.1.a). Prior to the gelation stage, the sol was poured inside a plastic mould (size of 10 cm x 8 cm x 5 cm). Within 5 minutes the gel had been formed after which the gel was removed from the mould. Subsequently, the gel was soaked in ethanol solvent for 48h at room temperature and atmospheric pressure for the aging process. Samples were synthesised with different weight percentages (see Table 2. 1) of ceramic fibres and silica aerogel and named as SA1, SA2, SA3, SA4 and SA5.

Drying process

After aging the reinforced gels, sodium bicarbonate and surface modification treatment with TMCS was carried out as reported in Han *et al.* (2018). Briefly, the ethanol solvent was replaced with a mixture of sodium bicarbonate/deionised water solution (4.4 g for each 100 ml DI) and the gels were left for 24 hours under stirring. After that step, gels were removed and soaked in a trimethylchlorosilane (TMCS): ethanol mixture (1:20 volumetric ratio). Immediately after soaking, CO_2 gas bubbling could be observed and that continued for 24 h. Reinforced gels were then washed with DI water to ensure that no salt (sodium chloride) remained inside the pores. Subsequently, reinforced gels were soaked in ethanol solvent for 24 hours to replace the water in the pores with ethanol. The gel was dried at 60°C for 24 hour and 1 hour at 100°C to get reinforced silica aerogels composites.

3.2 **Results and Discussion**

In modern construction, efficient insulation materials must have lower thicknesses to mitigate problem of reduction of the space. However, conventional insulation materials are limited as a reduction in thickness lowers the effectiveness of the materials insulating properties. A solution is to use highly insulating materials with thermal conductivities lower than 25 mW/m K (Bouquerel *et al.*, 2012; Martinez *et al.*, 2016). Aerogels are a fascinating nanostructured material synthesised by replacing the solvent inside the pores of a wet gel with air while retaining the porous structure (Zhang *et al.*, 2017). Open cell pores give aerogel excellent heat insulation performance. Due to their unique properties such as high porosity, small pore size (2 to 50nm) and low solid conductivity of the silica skeleton, silica aerogels are considered among the best insulators. In addition to being known as the material having the smallest thermal

conductivity, silica aerogels offer a promising opportunity to produce a non-flammable insulator which is inert and transparent to solar light (Rolison and Dunn, 2001). At room temperature, silica aerogels have very low thermal conductivity in the range of 0.005-0.02 W/m K (Kistler, 1931; Lu *et al.*, 1992; Rolison and Dunn, 2001; Sorensen *et al.*, 2006; Hayase *et al.*, 2014; Jiang *et al.*, 2017; Liu *et al.*, 2017). However, wide spread commercialisation is inhibited by their poor mechanical properties, fragility even under a low stress, moisture sensitivity and high production cost. Therefore, different methods are pursued to reinforce silica aerogels to improve their mechanical properties, such as, cross-linking with polymers, incorporation of macro objects (fibres) or nanomaterials (nanoparticles, nanotubes) and the addition of fibrous scaffolds (Sai *et al.*, 2013; Zhao *et al.*, 2015a; Zhao *et al.*, 2015b). Recently, fibre reinforced silica aerogel composites have attracted attention in fabricating energy saving thermal insulators, such as aramid fibres (Li *et al.*, 2016), carbon nanotubes (Pinero *et al.*, 2018), cellulose fibres (Markevicius *et al.*, 2017; He *et al.*, 2018), glass fibres (Zhou *et al.*, 2018), silica nanowires (Tang *et al.*, 2017), and hydroxyapatite nanowires (Chen *et al.*, 2018). Silica aerogel-blanket panels have also been used for building insulation (Lee *et al.*, 2018; Nocentini *et al.*, 2018). Their commercial applications, however, are still not widespread because of the high production cost of aerogels (Lakatos, 2017). In the current work, we aim to investigate the capability of producing affordable superinsulation materials using the recently developed low cost ambient pressure drying method (Han and Šiller, 2015; Han *et al.*, 2018). The manufacturing cost of aerogels is lowered ~10 fold when compared to standard ambient pressure drying methods with organic solvents (Han *et al.*, 2018). Herein, silica aerogel composites are reinforced with two types of fibre reinforcement, ceramic fibres blanket (CFB) and ceramic short fibres (CSF), and the mechanical and thermal properties were investigated. The work explores way towards real manufacturing requirements with preferable properties.

Table 3.1 shows the weight percentage, the textural characteristics, thermal conductivities and the mechanical properties of silica aerogel composites.

Table 3. 1. Physical properties of silica aerogels, CBSA and CSSA composites synthesised by NAPD method.

Samples	SiO_2 wt%	CF wt.%	Surface area (m^2/g) [± 2 $m^2 g^{-1}$]	Average pore diameter(nm) [± 0.1nm]	Pore specific volume (cm^3/g) [± 0.02 $cm^3 g^{-1}$]	Compressive strength (MPa)[± 0.02 MPa]	Young's modulus (MPa) [± 0.001 MPa]	Th. conductivity (W/m.K) [± 0.002 W/m.K]
CFB	0	100	0.6	-	-	-	-	0.048
AE	100	0	585	6.4	0.9	0.1	1.11	0.019
AB1	23	77	83	10.3	0.3	3.1	0.043	0.049
AB2	26	74	86	6.5	0.18	6.6	0.06	0.047
AB3	28	72	93	7.1	0.19	10.3	0.068	0.043
AB4	30	70	109	6.8	0.26	11.2	0.066	0.039
AB5	34	66	117	7.9	0.23	11.4	0.096	0.038
CSF	0	100	0.21	-	-	-	--	
SA1	98.4	1.62	646	5.3	0.85	0.3	1.35	0.021
SA2	96.2	3.8	554	5.8	0.82	0.6	1.3	0.023
SA3	94.8	5.2	536	8.9	1.19	0.8	1.3	0.024
SA4	92.5	7.5	492	5.5	0.69	0.9	1.5	0.026
SA5	88.8	11.2	435	8.6	0.87	1.1	4.76	0.028

Figure 3. 1 a, b and c show the XRD patterns for CFB alone, washed ceramic fibres reinforced silica aerogel composites and unwashed ceramic fibre reinforced aerogel composites, respectively. A XRD analysis was carried out to ensure that all fibre reinforced silica aerogel samples are well prepared without any residual sodium chloride. Sodium chloride is generated before the silica gel is dried with bicarbonate and TMCS (Han *et al.*, 2018) (see Figure 1.11 chapter 1). The broad peaks around $2\theta = 20$ in all patterns are for amorphous silica. On the other hand, pattern C in Figure 3.1 shows the characteristic peaks for sodium chloride.

Figure 3. 2 and Figure 3. 3 show the nitrogen adsorption-desorption isotherms and corresponding pore size distribution curves of CBSA and CSSA composites, respectively. Surface area, pore size distribution, average diameter and the specific volume of composites are given in Table 3. 1.

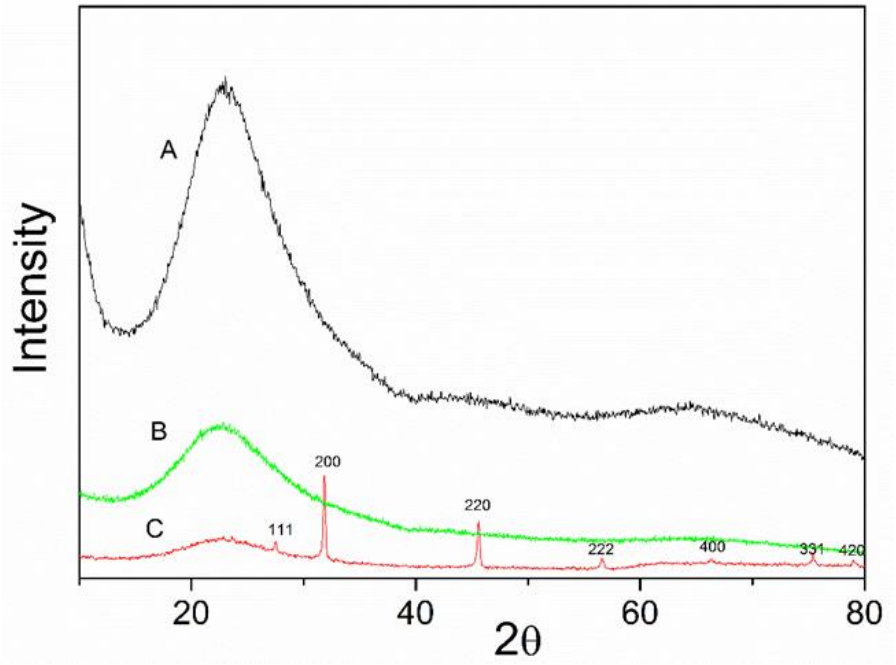

Figure 3. 1. X-ray diffraction pattern of ceramic fibres reinforced silica aerogels, (a) ceramic fibres (sample CFB), (b) washed ceramic fibre reinforced- silica aerogels (sample AB5 after washing with water), (c) unwashed ceramic fibre reinforced silica aerogels that contain sodium chloride salt (sample AB5 dried without washing with water).

For comparison, the surface area of pure silica aerogel (AE) produced by this low cost ambient pressure drying method, is also listed in Table 3. 1 and has a value of 582 m^2/g. The surface area of the AE sample is close to the value obtained by Malfait (2015), that used TEOS as a silica precursor and dried the gel using a standard ambient pressure drying method (by using hexane solvent during drying).

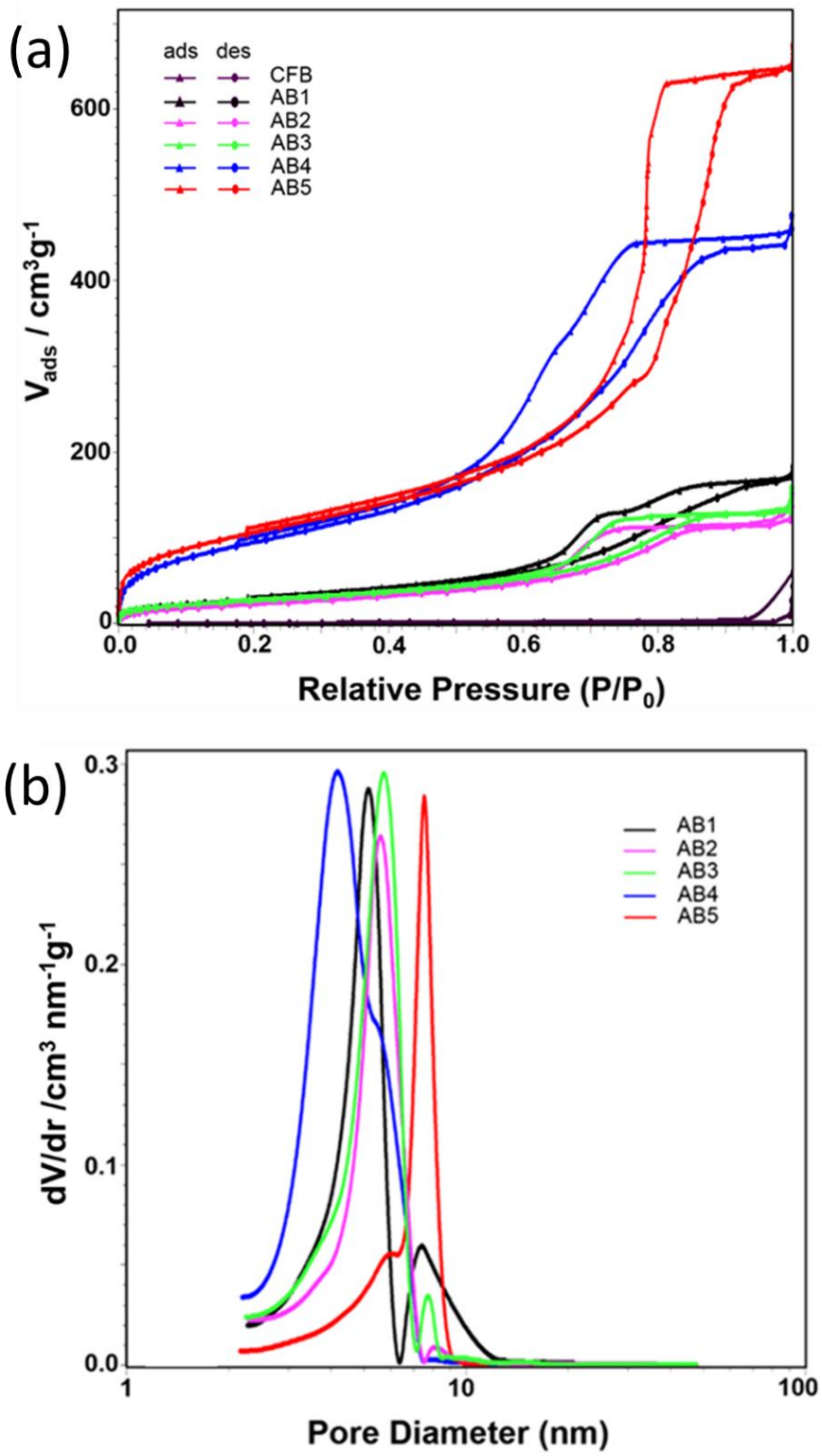

Figure 3. 2. (a) Nitrogen adsorption –desorption isotherms of ceramic blankets reinforced silica aerogels composites and (b) corresponding pore size distribution.

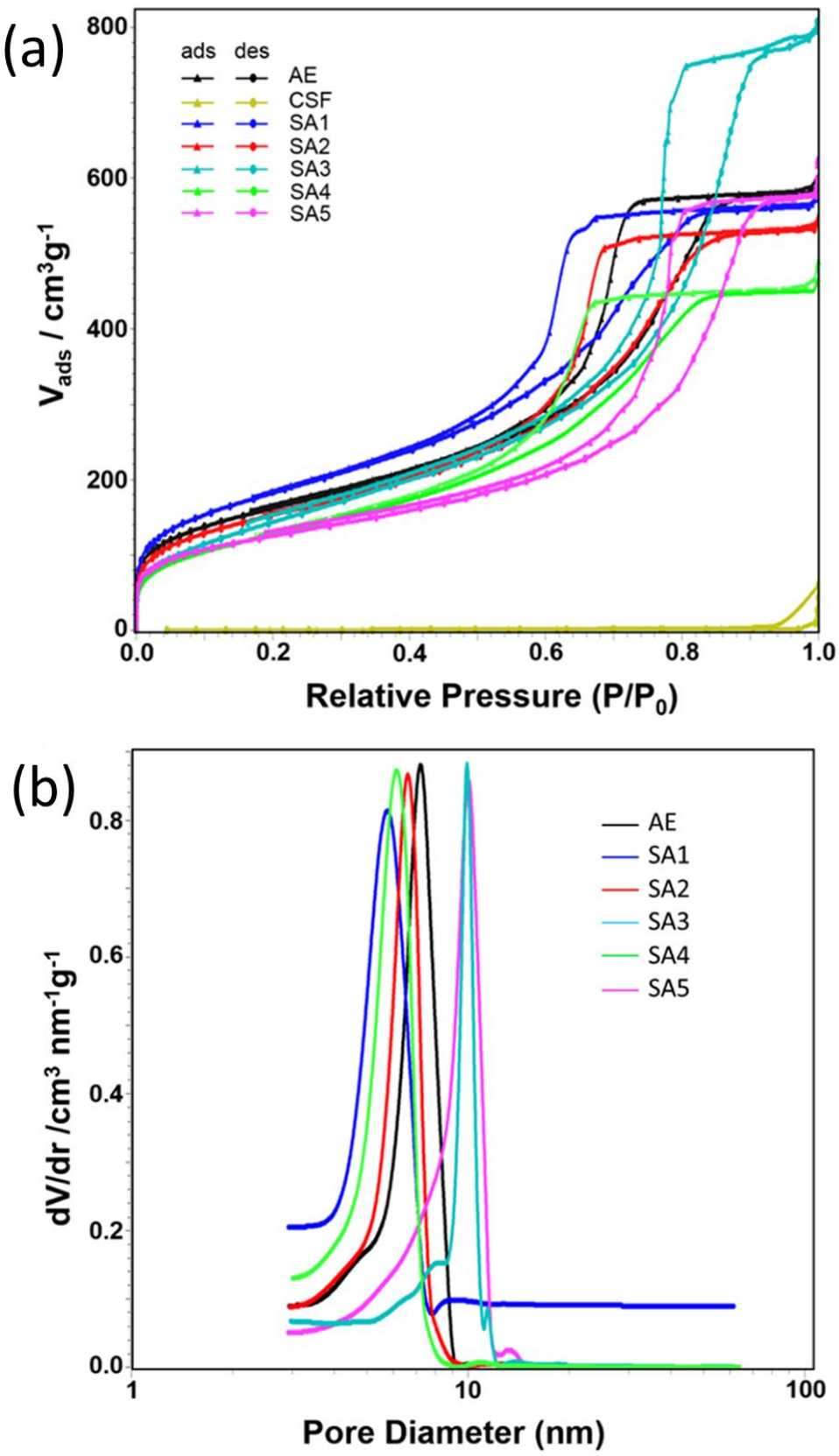

Figure 3. 3. (a) Nitrogen adsorption –desorption isotherms of ceramic short fibres reinforced silica aerogel composites and (b) corresponding pore size distribution.

Overall, the surface area of ceramic blanket reinforced silica aerogel composites is in the range from 83 m^2/g to 117 m^2/g (see values AB1-AB5 in Table 3. 1). The surface area for CBSA composites were low in comparison to that of AE. The surface area of the CFB was substantially enlarged by the addition of silica aerogels inside the blankets, as the surface area of non-modified CFB is only 0.6 m^2/g. the BJH method of analysis indicates narrow mesoporous ranges of pore size distributions. The average pore diameters vary from 6.5 nm to 10.3 nm for samples AB2 and AB1, respectively. Samples of CSSA composites exhibit high surface areas and small average pore diameters. As expected, (see Figure 3. 3), the surface area decreases with the increase of CFB content and vary from 500-645 m^2/g by added reinforcement with 0.11 wt. % and 1.62 wt. % of CSF, respectively. On the other hand, the pore diameters have a very narrow size range of 5.3-8.9 nm. In literature (Oh *et al.*, 2009), the surface area of silica aerogel- glass fibre composites synthesised via standard ambient pressure drying method (by using hexane solvent) were reported to be between 380-445 m^2/g and the pore size between 9.4-26 nm.

Accordingly, reinforced silica aerogels that are synthesised via our approach show a significant improvement over those reported previously (Oh *et al.*, 2009). All nitrogen adsorption- desorption isotherm curves match the characteristics of a type IV isotherm and a hysteresis loops type H2 according to IUPAC and are characteristic of mesoporous materials (Yang, 2011). Figure 3. 4 (a) and (b) show SEM images of fibres of CFB before and after they've been impregnated with silica aerogel, respectively. The clusters of silica aerogels inside CBSA composites (Figure 3. 4 b) are stacked and surround ceramic fibres. The image, seen in Figure 3. 4 (c), shows the silica aerogel reinforcement with short ceramic fibre (CSF), there is a better cohesion between the short fibres and silica aerogel. The sedimentation of silica aerogel formed on the surface of ceramic fibres is known to be due to Van deer Waals forces (Oh *et al.*, 2009). Furthermore, higher magnification of silica aerogels reinforced with CSF, Figure 3. 4 d image, detects some macropores in the silica aerogel structure. The diameters of the macropores are in the range of 1-7.5 μm. Higher magnification of silica aerogel composites with CSF samples, Figure 3. 4 e and f images illustrate SiO_2 secondary particles and the mesoporous structure of silica aerogels. The diameters of mesopores are distributed with the short size range of 3-15 nm. The average pore diameters, obtained with SEM imaging, matched those obtained from the BJH method of analysis. Figure 3.5 shows the typical stress-strain curves of a compression test for all CBSA composites. The overall shape of the curves are the same but the compressive strength values increase with the increase of the silica aerogel content inside the ceramic blanket. The increase is from 3.15 MPa for AB1 specimen to 11.2 MPa for AB5 specimen. However, a further increase in silica aerogel weight ratio does not significantly

change the compressive strength of the samples. This is because the fibres are supporting the main load. Stress-strain curves show a high fracture strain over 85% for sample AB5. Compression stress- strain curves are divided into three main regions. The linear region (Hook region, see inset in Figure 3.5) is observed when the strain is in the range between 0 to 0.05, the elastic modulus was measured at this point. The yield region (collapsed plateau) occurs where the strain is less than 0.3 and plastic hardening occurs. Finally, the densification region arises when the strain is over 0.3 to fracture (Hrubesh and Pekala, 1994; Siligardi *et al.*, 2017) .

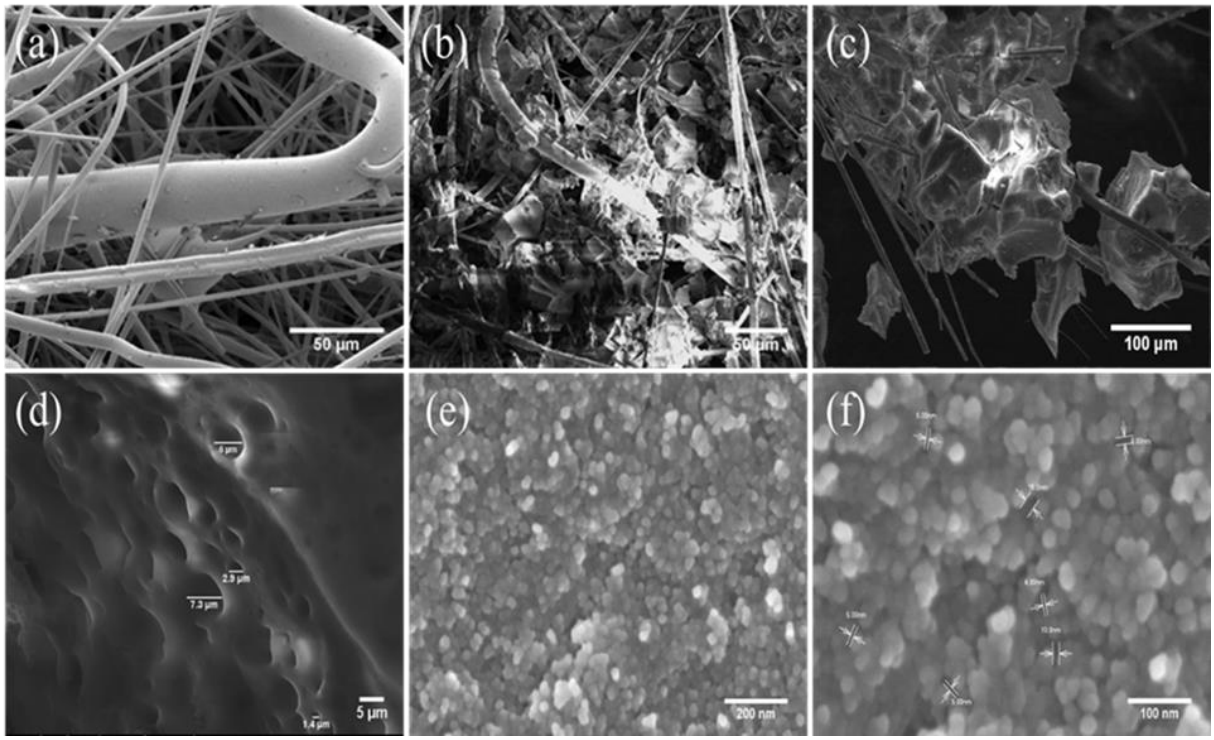

Figure 3. 4. SEM images of (a) ceramic blanket, (b) CBF reinforced silica aerogels, (c) CSF reinforced silica aerogels, (d) silica aerogel's macropores of sample (c), (e) further magnification of sample (c), detection of silica aerogel's mesopores, (f) further magnification of sample (c), detection of narrow size of silica aerogel's mesopores.

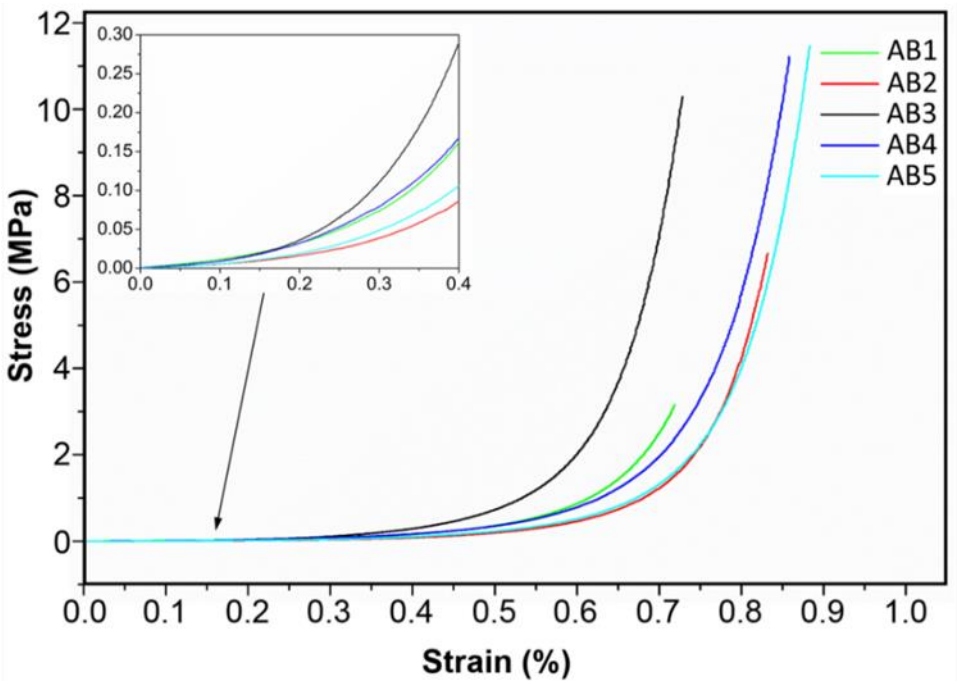

Figure 3.5. Compression stress-strain curves of ceramic blanket reinforced silica aerogel composites. The inset in figure shows the linear part of the curve from which Young modulus are calculated.

Because of silica aerogel's brittle nature, the aerogel's structure collapsed early meaning that the elastic region is very short. Similarly, compression stress- strain curves of pure silica aerogel and CSSA composites are presented in Figure 3. 6. The stress-strain compression curves are similar to that carried out by Yang (2011) for fibre reinforced- silica aerogels. The stress- strain curve of AE not only and showed a typical curve for brittle materials, but also that the fracture occurred after a short time of applying the compressive stress. The deformation area is small ~3% of strain axis and the compressive strength is only 0.12 MPa. Furthermore, the pure aerogel AE (blue curve in inset of Figure 3. 6) shows a very small elastic region then a high rough region due to successive cracks that are generated during load propagation in the material. Sample SA1 which had a low weight percentage of CSF showed a stress-strain curve quite similar to that of pure silica aerogel but with significantly higher compressive strength (see red curve in inset of Figure 3. 6).

However, CSSA composites with a larger loading of CSF (SA2 to SA5 curves in Figure 3. 6) show nonlinear compression stress-strain curves and the nonlinearity is more dominant as the percentage of fibres increases in the composites. Sample SA2 (pink curve in Figure 3. 6) shows an intermediate behaviour in compression regions, the yield stage is wide, and the densification stage is reached with a clear brake point. Further increase in the percentage of fibres, leads to an increase in the deformation in all CSSA composite. In the elastic region, all curves (see inset

Figure 3. 6) have the same mechanism of compression, the load bearing is carried out by the open pores of the silica aerogel.

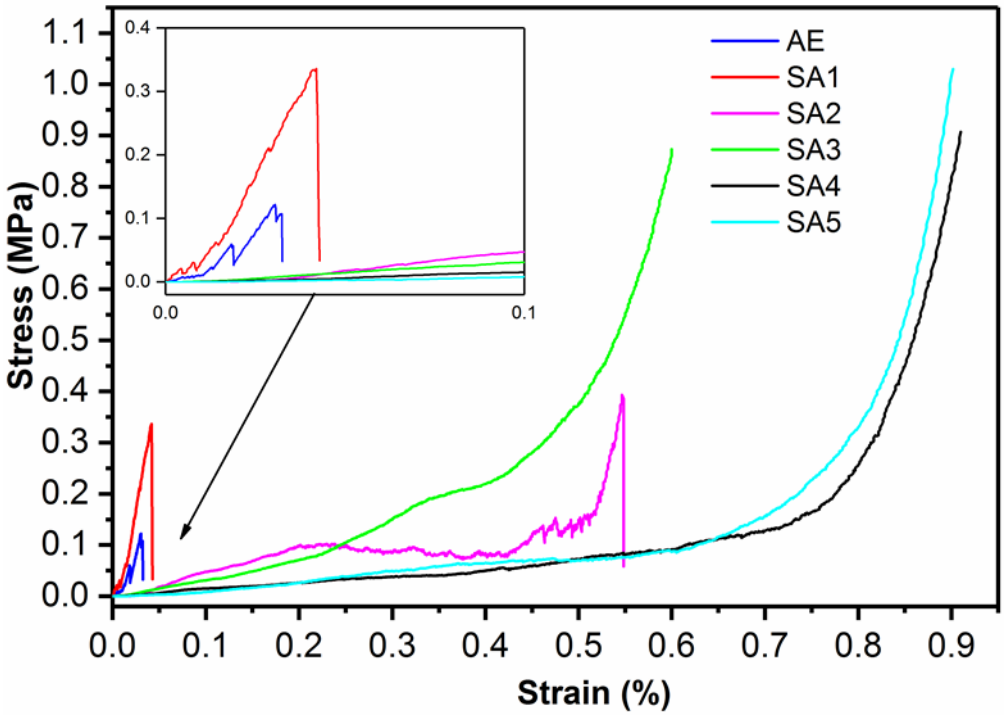

Figure 3. 6. Compression stress-strain curves of ceramic short fibres reinforced silica aerogel composites. The inset in figure shows linear part of curves from which Young modulus were calculated and with the brittle fracture for pure silica aerogels (AE) and SA1 sample, which contain a low weight fraction of short fibres (see a very abrupt drop signature of braking point of blue and red curves in inset).

Once composites reach the yield stage, the fibres become the responsible for bearing the load. Where, both aerogel and the fibres would be responsible upon the densification stage (Wang, 2006). Figure 3. 7 presents the summary of compressive strengths and Young's modulus for all CBSA and CSSA composites. The compressive strength and Young's modulus in CBSA were found to increase when the silica aerogel content was increased, this is due to silica aerogel initially occupying empty spaces in the ceramic blanket and improved adhesion of fibres. This is also observed clearly in SEM images (compare Figure 3. 4 a with b). A noticeable increase in compressive strength and Young's modulus of CSSA composites (Figure 3. 7 c and d) is observed when compared to that of pure silica aerogels. For example, the compressive strength is increased by ~ 10 times that of a pure silica aerogel (from 0.1 MPa to 1.1 MPa) when reinforced by 11 wt % of CSF and the Young's modulus increased from 1.11 MPa to 4.77 MPa.

Thermal stability of both types of silica aerogel composites were studied using TGA-DTA curves for AB5 and SA5 specimens (see Figure 3. 8). At the beginning of heat ramping for both

samples, an endothermic peak is observed at ~ 135 °C for AB5 (Figure 3. 9a) and ~153 °C for SA5 (Figure 3. 8b) which indicated the removal of adsorbed species. The weight loss was much higher for SA5 (7.47 wt. %), than for AB5 (0.88 wt. %). This is because of the larger amount of silica aerogels inside SA5 compared to that in AB5. In addition, the hydrophilic nature of the synthesised silica aerogels (Han *et al.*, 2018) leads to adsorption of moisture, as well as other adsorbed species after ~ 1 year exposed to atmospheric pressure. A sharp exothermic peak at 1005 °C for AB5 and at 1010 °C for SA5 has a relatively high weight loss (see Figure 3. 8 b, 2.47 wt. %) indicating the phase change in materials. This can be attributed to the crystallisation of the ceramic fibres, where SiO_2 is the major component (Siligardi *et al.*, 2017). This can be seen in Figure 3.8 c.

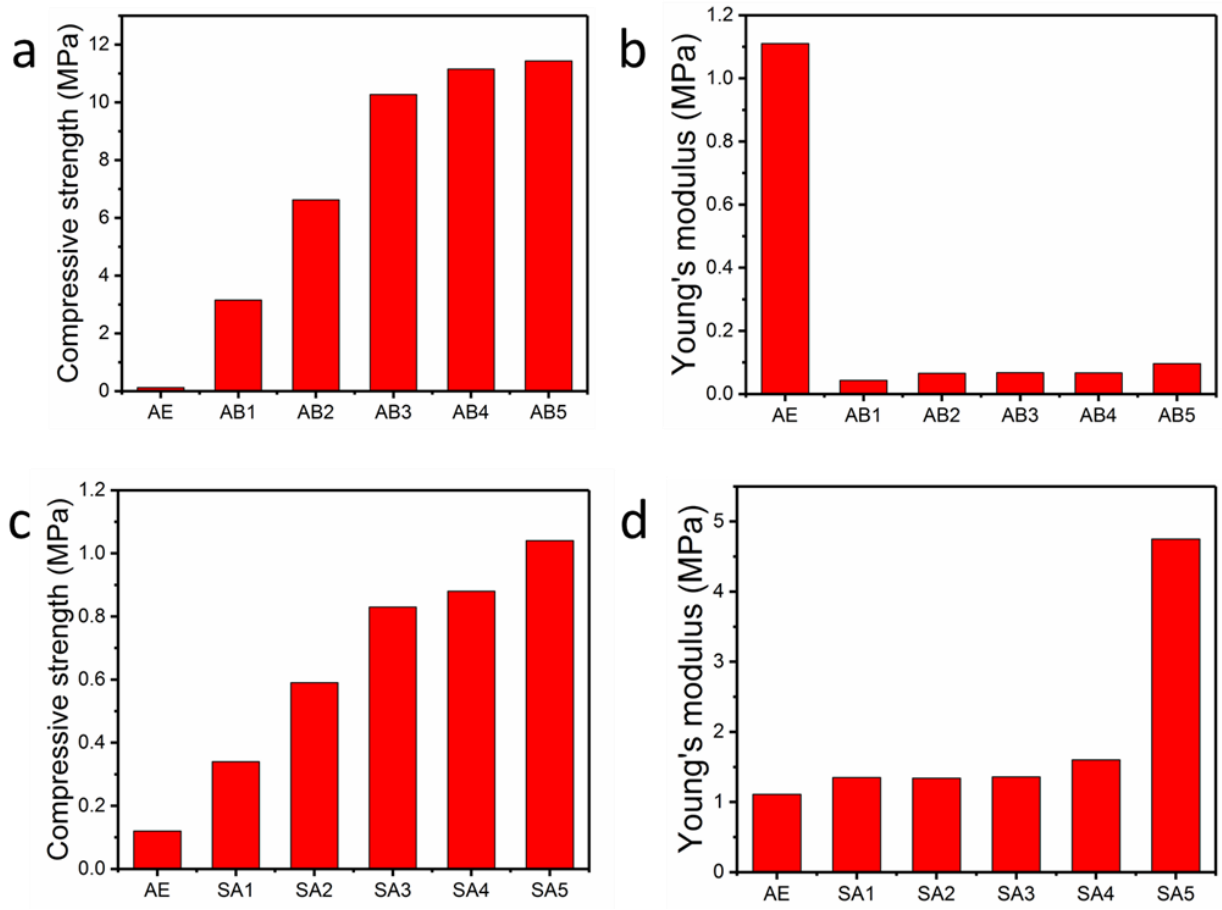

Figure 3. 7. a) and c) Compressive strength of CBSA and CSSA composites, respectively. b) and d) Young's modulus of CBSA and CSSA composites, respectively.

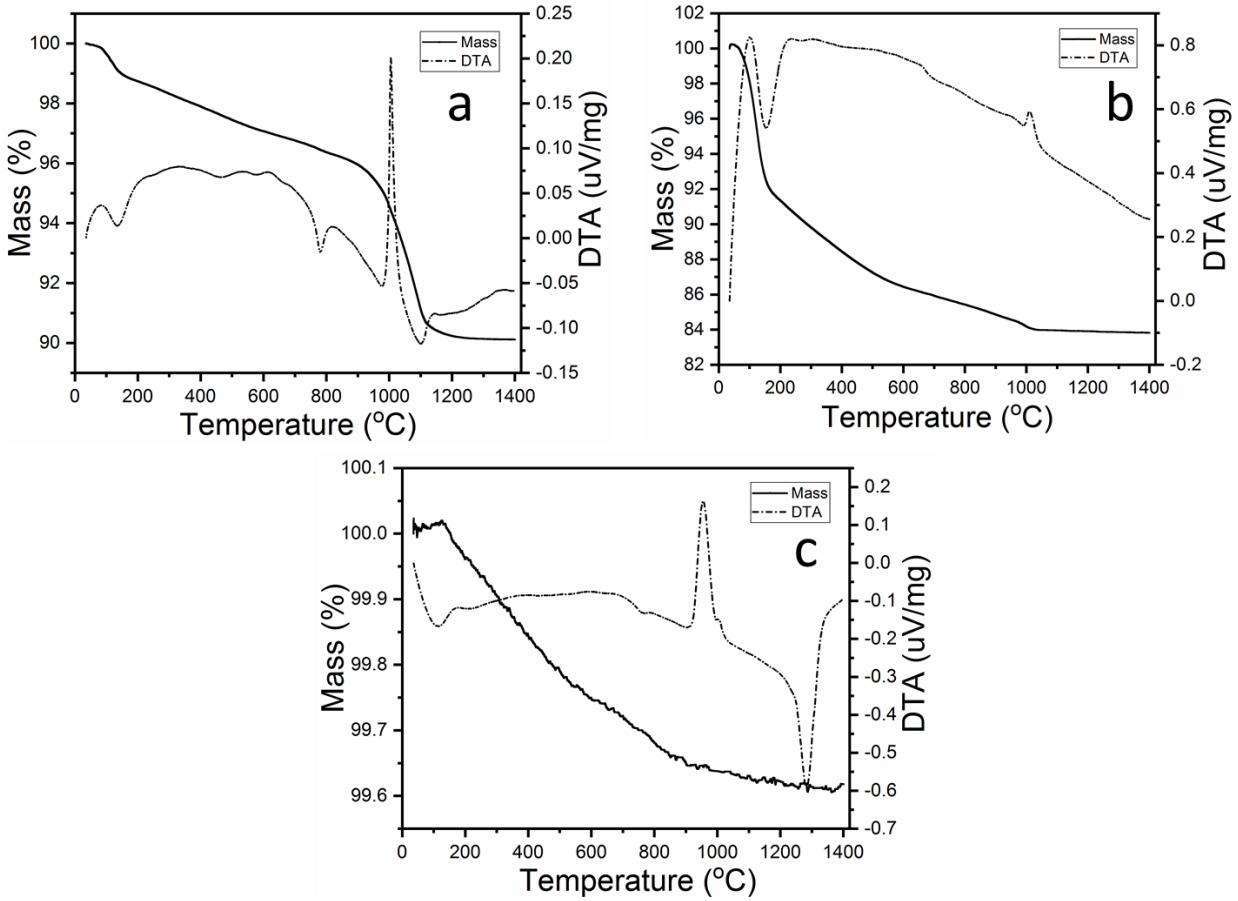

Figure 3. 8. TGA-DTA curves for (a) sample AB5, (b) sample SA5, and sample CFB.

Figure 3. 9 shows the change in thermal conductivities in the range of 295 K to 423 K for CBSA composites. Thermal conductivities of CBSA composites decrease with the increase of silica aerogel content. Although, at low percentage of silica aerogel (see AB1 and AB2 in Figure 3. 9) the thermal conductivity has slightly increased compared to pure CFB, but for other CBSA samples the thermal conductivity decreased with the increase in silica aerogels' weight percent. This initial increase of sample AB1 and AB2 might be because silica aerogel acted as a glue and caused a linking of fibres. Consequently, the thermal conduction by solid materials (mainly fibres) increased despite the fact that silica aerogels have low thermal conductivity. At room temperature, the thermal conductivity of CBSA composites decreased from 0.049 to 0.038 W/m K for the ceramic blanket when incorporating 0.34 wt % of silica aerogels which clearly indicated improvement in the thermal insulation. Figure 3. 10 shows the change in the thermal conductivity, in range of 295 K to 423 K, for pure silica aerogels and CSSA composites. The synthesis of silica aerogels by bicarbonate ambient pressure method produces silica aerogels with a low thermal conductivity of 0.019 W/m K at room temperature. Previously, it has been reported that the thermal conductivity, under the same conditions, of silica aerogels is between 0.01-0.03 W/m K and it would drop to 0.002 W/m K under evacuation (Hrubesh and Pekala,

1994; Yoldas *et al.*, 2000; Yuan *et al.*, 2012). Our synthesis method produced silica aerogels with excellent thermal insulation at room temperature. The narrow range of AE pore sizes used in this work, as indicated by BJH analysis in Table 3. 1, provides confirmation that this can lower thermal conductivity of aerogels and their composites (Feng *et al.*, 2011).

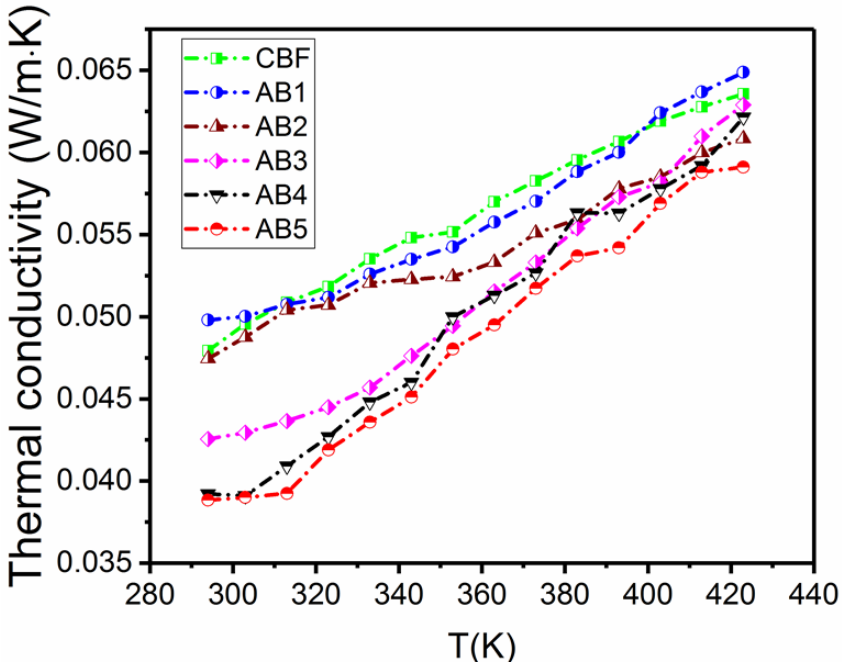

Figure 3. 9. Temperature dependence-thermal conductivity of CBSA composites.

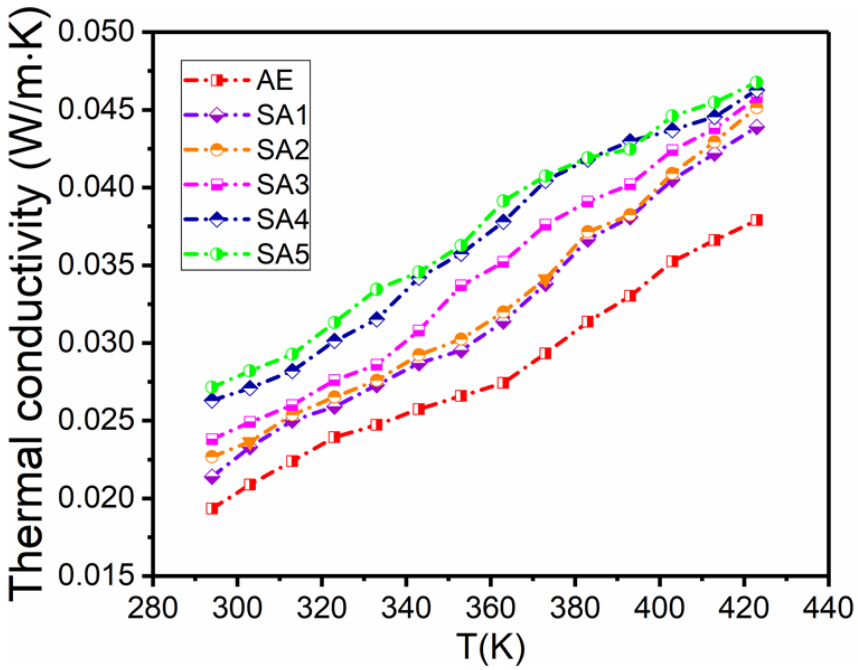

Figure 3. 10. Temperature dependence-thermal conductivity of CSSA composites.

In addition, the thermal conductivity of pure silica aerogels increases with an increase in temperature. This is attributed to an increase of radiative conduction at high temperatures

because silica aerogels are transparent to infrared radiation due to the small absorption coefficient of SiO_2 in this region (Zeng *et al.*, 1995). Thermal conductivity of CSSA composites also increased with the increase of the fibre's weight fraction. A higher fibre content in composites increased the solid's thermal conductivity because they act as a heat transfer pathway (Yuan *et al.*, 2012). As mentioned earlier, the reinforcement of silica aerogels with CSF improved the mechanical properties of the material and provided better thermal stability for silica aerogel composites at high temperature than that seen in pure silica aerogels. This could be attributed to the fact that ceramic fibres contain some metal oxides that could work as an opacifier material for radiative heat transport (Wang *et al.*, 1995). Also, results here agree with those reported by Zheng (2015), that inorganic fibres could improve aerogel's ability to shield heat radiation at high temperatures.

3.3 **Conclusion**

Mechanical and thermal properties of reinforced silica aerogels with ceramic blankets and ceramic short fibres synthesised using bicarbonate solutions with TMCS as reagent for CO_2 gas formation, within the gel as ambient pressure drying method, have been investigated as a possible insulation material. Pure silica aerogels are produced with a low thermal conductivity of 0.019 W/m K and high surface area of 584 m^2/g. Both methods of fibre reinforcement have been optimised and improved mechanical properties have been obtained. The thermal insulation of commercial ceramic blanket insulation materials was improved from 0.048 to 0.038 W/m K by the incorporation of 34 weight percent of silica aerogel. A small percentage of silica aerogels, in this cost-effective synthesis approach, drastically increased the thermal insulation properties of the commercial ceramic blanket. Reinforcement with short fibres (CSSA composites) exhibited a significant enhancement in the compressive strength, increasing tenfold with a little decrease in the surface area of ~14 % and an increase in thermal conductivity from 0.019 to 0.028 W/m K. The bicarbonate approach indicates that it is possible to produced superinsulation materials or improve the insulative properties of the conventional insulation materials with an affordable cost.

References

Bouquerel, M., Duforestel, T., Baillis, D. and Rusaouen, G. (2012) 'Heat transfer modeling in vacuum insulation panels containing nanoporous silicas-A review', *Energy and Buildings*, 54, pp. 320-336.

Chen, F., Zhang, J.X., Li, N., Zhang, C., Ji, B., Hu, L.H., Zhao, T.T., Wang, Z.Y. and Zhang, S.D. (2018) 'Heat insulating, fire retardant and flexible inorganic nanocomposite paper', *Materials & Design*, 144, pp. 281-289.

Feng, J.Z., Zhang, C.R., Feng, J., Jiang, Y.G. and Zhao, N. (2011) 'Carbon aerogel composites prepared by ambient drying and using oxidized polyacrylonitrile fibers as reinforcements', *Acs Applied Materials & Interfaces*, 3(12), pp. 4796-4803.

Han, X., Hassan, K.T., Harvey, A., Kulijer, D., Oila, A., Hunt, M.R.C. and Siller, L. (2018) 'Bioinspired synthesis of monolithic and layered aerogels', *Advanced Materials*, 30(23).

Han, X. and Šiller, L. (2015) 'Aerogel synthesis', P221149GB/DW(WO2016132117 A1).

Hayase, G., Kugimiya, K., Ogawa, M., Kodera, Y., Kanamori, K. and Nakanishi, K. (2014) 'The thermal conductivity of polymethylsilsesquioxane aerogels and xerogels with varied pore sizes for practical application as thermal superinsulators', *Journal of Materials Chemistry A*, 2(18), pp. 6525-6531.

He, J., Zhao, H.Y., Li, X.L., Su, D., Zhang, F.R., Ji, H.M. and Liu, R. (2018) 'Superelastic and superhydrophobic bacterial cellulose/silica aerogels with hierarchical cellular structure for oil absorption and recovery', *Journal of Hazardous Materials*, 346, pp. 199-207.

Hrubesh, L.W. and Pekala, R.W. (1994) 'Thermal-properties of organic and inorganic aerogels', *Journal of Materials Research*, 9(3), pp. 731-738.

Jiang, L., Kato, K., Mayumi, K., Yokoyama, H. and Ito, K. (2017) 'One-pot synthesis and characterization of polyrotaxane-silica hybrid aerogel', *Acs Macro Letters*, 6(3), pp. 281-286.

Kistler, S.S. (1931) 'Coherent Expanded Aerogels and Jellies', *Nature*, 127(3211), p. 741.

Lakatos, A. (2017) 'Comprehensive thermal transmittance investigations carried out on opaque aerogel insulation blanket', *Materials and Structures*, 50(1), p. 12.

Lee, K.J., Choe, Y.J., Kim, Y.H., Lee, J.K. and Hwang, H.J. (2018) 'Fabrication of silica aerogel composite blankets from an aqueous silica aerogel slurry', *Ceramics International*, 44(2), pp. 2204-2208.

Li, Z., Cheng, X.D., He, S., Shi, X.J., Gong, L.L. and Zhang, H.P. (2016) 'Aramid fibers reinforced silica aerogel composites with low thermal conductivity and improved mechanical performance', *Composites Part a-Applied Science and Manufacturing*, 84, pp. 316-325.

Liu, H., Xia, X.L., Ai, Q., Xie, X.Q. and Sun, C. (2017) 'Experimental investigations on temperature-dependent effective thermal conductivity of nanoporous silica aerogel composite', *Experimental Thermal and Fluid Science*, 84, pp. 67-77.

Lu, X., Arduinischuster, M.C., Kuhn, J., Nilsson, O., Fricke, J. and Pekala, R.W. (1992) 'Thermal Conductivity of Monolithic Organic Aerogels', *Science*, 255(5047), pp. 971-972.

Malfait, W.J., Zhao, S. Y. Verel, R., Iswar, S., Rentsch, D., Fener, R., Zhang, Y. C., Milow, B., Koebel, M. M. (2015) 'Surface chemistry of hydrophobic silica aerogels', *Chemistry of Materials*, 27(19), pp. 6737-6745.

Markevicius, G., Ladj, R., Niemeyer, P., Budtova, T. and Rigacci, A. (2017) 'Ambient-dried thermal superinsulating monolithic silica-based aerogels with short cellulosic fibers', *Journal of Materials Science*, 52(4), pp. 2210-2221.

Martinez, R.G., Goiti, E., Reichenauer, G., Zhao, S.Y., Koebel, M. and Barrio, A. (2016) 'Thermal assessment of ambient pressure dried silica aerogel composite boards at laboratory and field scale', *Energy and Buildings*, 128, pp. 111-118.

Nocentini, K., Achard, P. and Biwole, P. (2018) 'Hygro-thermal properties of silica aerogel blankets dried using microwave heating for building thermal insulation', *Energy and Buildings*, 158, pp. 14-22.

Oh, K.W., Kim, D.K. and Kim, S.H. (2009) 'Ultra-porous flexible PET/aerogel blanket for sound absorption and thermal insulation', *Fibers and Polymers*, 10(5), pp. 731-737.

Pinero, M., Mesa-Diaz, M.D., de los Santos, D., Reyes-Peces, M.V., Diaz-Fraile, J.A., de la Rosa-Fox, N., Esquivias, L. and Morales-Florez, V. (2018) 'Reinforced silica-carbon nanotube monolithic aerogels synthesised by rapid controlled gelation', *Journal of Sol-Gel Science and Technology*, 86(2), pp. 391-399.

Rolison, D.R. and Dunn, B. (2001) 'Electrically conductive oxide aerogels: new materials in electrochemistry', *Journal of Materials Chemistry*, 11(4), pp. 963-980.

Sai, H.Z., Xing, L., Xiang, J.H., Cui, L.J., Jiao, J.B., Zhao, C.L., Li, Z.Y. and Li, F. (2013) 'Flexible aerogels based on an interpenetrating network of bacterial cellulose and silica by a non-supercritical drying process', *Journal of Materials Chemistry A*, 1(27), pp. 7963-7970.

Siligardi, C., Miselli, P., Francia, E. and Gualtieri, M.L. (2017) 'Temperature-induced microstructural changes of fiber-reinforced silica aerogel (FRAB) and rock wool thermal insulation materials: A comparative study', *Energy and Buildings*, 138, pp. 80-87.

Sorensen, L., Strouse, G.F. and Stiegman, A.E. (2006) 'Fabrication of stable low-density silica aerogels, containing luminescent ZnS capped CdSe quantum dots', *Advanced Materials*, 18(15), pp. 1965.

Tang, X.B., Sun, A.H., Chu, C.Y., Yu, M.L., Ma, S., Cheng, Y.C., Guo, J.J. and Xu, G.J. (2017) 'A novel silica nanowire-silica composite aerogels dried at ambient pressure', *Materials & Design*, 115, pp. 415-421.

Wang, J., Kuhn, J. and Lu, X. (1995) 'Monolithic silica aerogel insulation doped with TiO_2 powder and ceramic fibers', *Journal of Non-Crystalline Solids*, 186, pp. 296-300.

Wang, X.D. (2006) *Base Research on the Application of Nanoporous SiO2 Aerogel based Thermal Insulation Composites, in National University of Defense Technology*. Changsha.

Yang, X.G., Sun, Y. T. ,Shi, D. Q. ,Liu, J. L. (2011) 'Experimental investigation on mechanical properties of a fiber-reinforced silica aerogel composite', *Materials Science and Engineering a-Structural Materials Properties Microstructure and Processing*, 528(13-14), pp. 4830-4836.

Yoldas, B.E., Annen, M.J. and Bostaph, J. (2000) 'Chemical engineering of aerogel morphology formed under nonsupercritical conditions for thermal insulation', *Chemistry of Materials*, 12(8), pp. 2475-2484.

Yuan, B., Ding, S., Wang, D., Wang, G. and Li, H. (2012) 'Heat insulation properties of silica aerogel/glass fiber composites fabricated by press forming', *Materials Letters*, 75, pp. 204-206.

Zeng, S.Q., Hunt, A. and Greif, R. (1995) 'Theoritical mobeling of carbon content to minimize heat-transfer in silica aerogel', *Journal of Non-Crystalline Solids*, 186, pp. 271-277.

Zhang, F., Ren, H., Dou, J., Tong, G.L. and Deng, Y.L. (2017) 'Cellulose nanofibril based-aerogel microreactors: A high efficiency and easy recoverable W/O/W membrane separation system', *Scientific Reports*, 7.

Zhao, S.Y., Malfait, W.J., Demilecamps, A., Zhang, Y.C., Brunner, S., Huber, L., Tingaut, P., Rigacci, A., Budtova, T. and Koebel, M.M. (2015a) 'Strong, thermally superinsulating biopolymer-silica aerogel hybrids by cogelation of silicic acid with pectin', *Angewandte Chemie-International Edition*, 54(48), pp. 14282-14286.

Zhao, S.Y., Zhang, Z., Sebe, G., Wu, R., Virtudazo, R.V.R., Tingaut, P. and Koebel, M.M. (2015b) 'Multiscale assembly of superinsulating silica aerogels within silylated nanocellulosic scaffolds: improved mechanical properties promoted by nanoscale chemical compatibilization', *Advanced Functional Materials*, 25(15), pp. 2326-2334.

Zheng, H.X., Shan, H. R., Bai, Y., Wang, X. F., Liu, L. F., Yu, J. Y., Ding, B. (2015) 'Assembly of silica aerogels within silica nanofibers: towards a super-insulating flexible hybrid aerogel membrane', *RSC Advances*, 5(111), pp. 91813-91820.

Zhou, T., Cheng, X.D., Pan, Y.L., Li, C.C., Gong, L.L. and Zhang, H.P. (2018) 'Mechanical performance and thermal stability of glass fiber reinforced silica aerogel composites based on co-precursor method by freeze drying', *Applied Surface Science*, 437, pp. 321-328.

Chapter 4 Synthesis and characterisation of sodium silicate-based silica aerogels by using bicarbonate ambient pressure drying method

The main challenge in silica aerogel synthesis is producing low cost and scalable silica aerogels. This chapter describes the synthesis of low cost and scalable silica aerogels from sodium silicate (water glass) precursor using novel ambient pressure drying approach. In addition, this chapter investigates the structural properties of silica aerogels in the case of using an ion exchange method to remove Na^+ or without using an ion exchange method. In both cases, washing with water was conducted to remove the generated sodium salts. XRD, BET, BJH, SEM, and a hot disk analysis are utilised to characterise the synthesised water glass-based silica aerogels.

4.1 Synthesis of silica aerogels from sodium silicate precursor

The gels are prepared by two methods. The first is cured out using ion exchange method. The silica sol had a pH in the range of 2 -3 after ion exchange. The sol was transferred to a beaker and stirred for 5 min. The second process was carried out without ionic exchange. For the gelation step, in the first process, the catalytic mixture of ammonium hydroxide and ammonium fluoride solutions (molar ratio was mentioned in 2.1.1.a) were used to modify the pH of the sol to a pH of 6. While in the second process, (5 M) HCl solution was used to obtain the gel. In both cases, silica sol was then transferred to a plastic mould for gelation. Gelation is completed within 15 mins, followed by the soaking of the hydrogel in deionised water for 24 hours for aging. The water was exchanged with sodium bicarbonate solution (4.4 g for each 100 ml water). The gel was treated with a mixture of 6 ml TMCS and 150 ml ethanol for 24 hours (Han *et al.*, 2018), soaked in ethanol for 8 hours to remove unreacted TMCS and residual HCl and then rinsed with water several times to remove the salt which is produced during the reaction between TMCS and sodium bicarbonate. Finally, the gel was soaked in ethanol for 24 hours with the ethanol refreshed every 12 hours and dried at 60 °C for 24 hours. To obtain monolithic silica aerogels, final addition of TMCS with ethanol was added to a wet gel (the wet-gel was soaked in TMCS and ethanol mixture for 24 hours followed by soaking in pure ethanol). Ethanol was exchanged two times and the gel dried at 60 °C for 24 hours and at 100 °C for 1 hour.

4.2 Results and Discussion

Sodium silicate Na_2SiO_3 (water glass) is used as a precursor to synthesis low cost silica aerogels. As mentioned earlier, in chapter 2 (section 2.1.2), water glass-based silica aerogels were synthesised in different volumetric ratios of water glass precursor and deionised water (see Table 4. 1) with and without the use of Amberlite® IR 120 hydrogen (Sigma-Aldrich) for sodium ion exchange. Sodium ions (Na^+) must be removed from the solution of sodium silicate precursor and water in order to improve the optical properties of silica aerogel (He *et al.*, 2015a). After soaking gels in sodium bicarbonate solution for 3 days, silica gels were treated with a mix of TMCS and ethanol. Sodium chloride is generated as a result of the reaction between HCl and sodium bicarbonate solution (see Figure 1. 10 in chapter 1) (Han *et al.*, 2018). Removing the trapped sodium salt inside pores of silica gels is a very important step because it introduces an opacity and a hydrophilicity to aerogels. The ion exchange method is reported to be used for removing Na^+ ions from water glass sol during synthesis of silica aerogels via ambient pressure drying method (Hwang *et al.*, 2008; He *et al.*, 2015b). Treating hydrogels with water vapour is also reported to remove Na^+ (Gurav *et al.*, 2009). In our synthesis approach, washing hydrogels with deionised water is an essential step of obtaining typical properties of the final silica aerogel product either or not an ion exchange method is used. Washing with water is used to remove the sodium salt from hydrogel prior to drying.

The aim behind using the ion exchange method or washing with only deionised water in this research is to investigate differences in silica aerogel properties such as surface area, pore sizes and pore diameters.

We have prepared a small-scale monolithic aerogel (Figure 4. 1 shows monolithic and fragments of water glass-based silica aerogel which are synthesised by using bicarbonate APD) indicating the potential of our process for a low-cost fabrication of larger freestanding aerogel materials.

Figure 4. 1. Silica aerogels synthesised from water glass precursor by using bicarbonate ambient pressure drying method (Han *et al.*, 2018), (a) water-glass based silica aerogels of 1:4.5 volumetric ration of water glass and deionised water, (b) monolithic silica aerogel of same volumetric ratio obtained by multi-treatment with TMCS-ethanol mixture (see synthesis process in section 2.2.2, chapter 2).

XRD pattern of a monoliths silica aerogel produced from a water glass (sodium silicate) precursor, which is prepared with volume ration of water glass: water 1:4.5 is demonstrated in Figure 4. 2. It is clear from the diffraction scan that water glass-derived aerogels have an amorphous structure with no NaCl by-products remained after washing the aerogel with water.

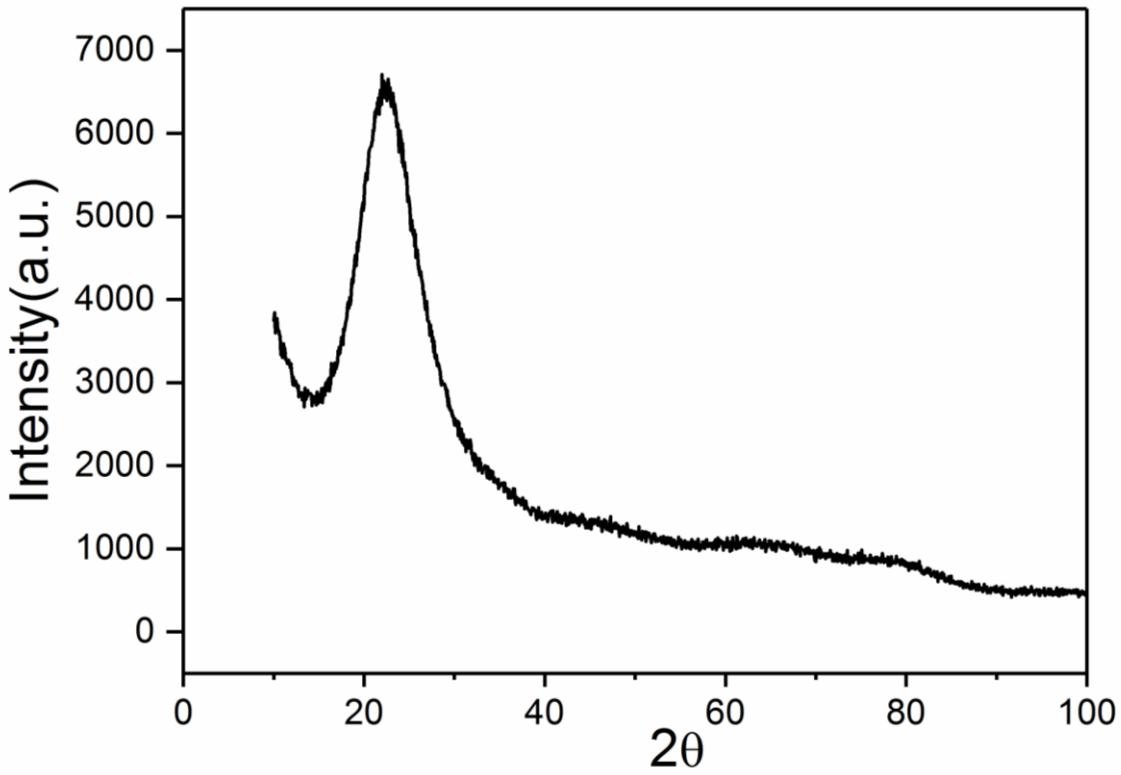

Figure 4. 2. XRD 2θ scan of a silica aerogel prepared using a water glass (sodium silicate) precursor by using bicarbonate APD method (Han *et al.*, 2018).

Table 4. 1. Volumetric ratio of water glass: deionised water with BET and BJH results for water glass-base silica aerogels.

Water glass: deionised water Vol. ratio	1:3	1:3.5	1:4	1:4.5	1:5
Water glass-based silica aerogel synthesis using Amberlite® IR 120 hydrogen					
Surface area (m^2/g) [± 5 m^2 g^{-1}]	524	604	677	703	611
Pore volume (cm^3/g) [± 0.02 cm^3 g^{-1}]	0.98	0.53	0.85	0.78	1.17
Average pore diameter (nm) [± 0.1 nm]	6.17	4	5.04	4.2	7.52
Water glass-based silica aerogel with no ionic exchange					
Surface area (m^2/g) [± 5 m^2 g^{-1}]	401	526	500	440	520
Pore volume (cm^3/g) [± 0.02 cm^3 g^{-1}]	2.06	1.33	1.6	1.49	1.56
Average pore diameter (nm) [± 0.1 nm]	18	11	24	14	16

Figure 4.3 shows the nitrogen adsorption desorption isotherms of synthesised water glass based-silica aerogels samples with different water volume in the case of using Amberlite® IR 120 hydrogen for an ion exchange method to remove Na^+ ions from the silica sol. The surface

area of an aerogel monolith (presented in Figure 4. 1b), obtained by the BET method, is for water-glass silica aerogel samples with a volume ratio of water glass: water of 1:4.5 found to be 703 m^2 g^{-1} (see Table 4. 1). The nitrogen adsorption- desorption isotherms (see Figure 4. 3) are a combination of type I (microporous) and type IV isotherms according to IUPAC classification. A type IV isotherm is characteristic to mesoporous structure of porous materials (Sing *et al.*, 1985; Thommes *et al.*, 2015). In the case of using the ion exchange method, the surface areas of all water glass silica aerogel samples were in the range of 524-703 m^2 g^{-1}. The specific surface area of water glass silica aerogels are in the range or are higher than reported surface areas for the typical synthesis of water glass silica aerogel samples synthesised using ion exchange method via standard ambient pressure drying method (Shi *et al.*, 2006; Hwang *et al.*, 2008).

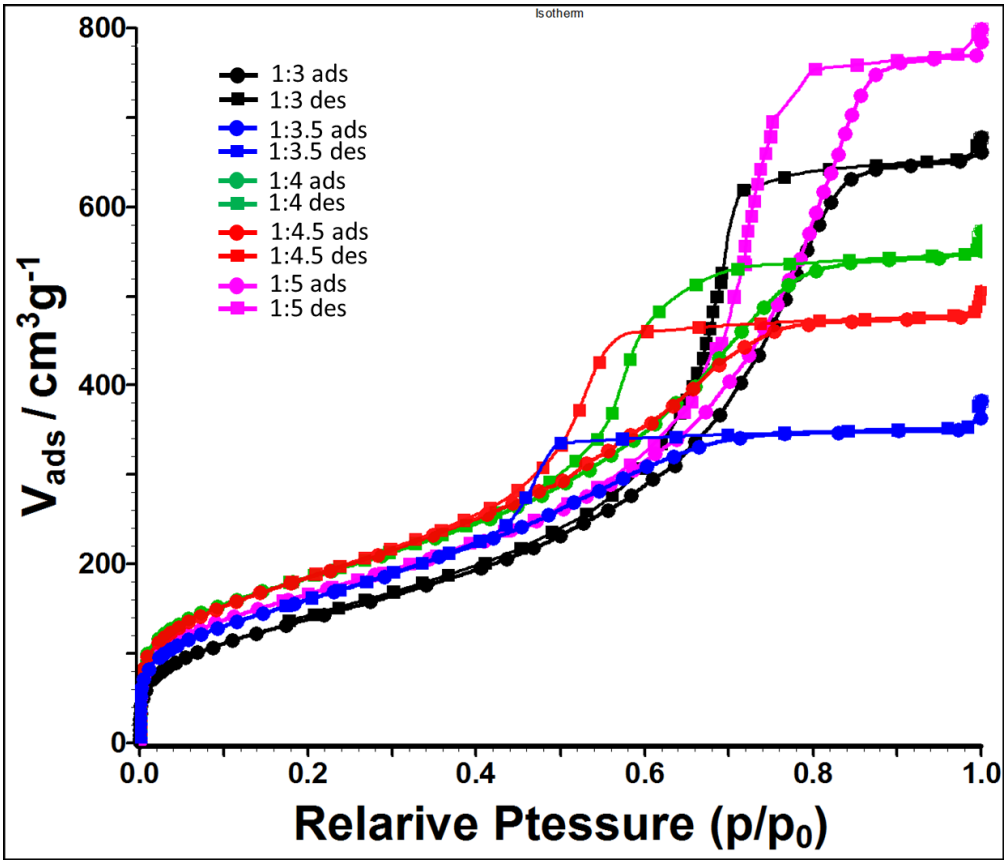

Figure 4. 3. Nitrogen adsorption-desorption isotherms of water glass based-silica aerogel samples with use of ion exchange method for different volume ratio of water glass: water. The adsorption isotherms are shown by filled circles, desorption isotherms are shown by filled squares.

The bulk density (ρ_b) of water glass silica aerogel sample, with a typical surface area, was measured using a microbalance of 10^{-6} g accuracy, in order to measure the mass of a known

volume of water glass silica aerogel and it was found to be 0.051 g/cm^3. ρ_s is the skeletal density of silica 2.65 g/cm^3. The porosity measured using the formula 4.1 was found to be 98.1%.

$$\% \text{ Porosity} = \left(1 - \frac{\rho_b}{\rho_s}\right) \times 100 \qquad (4.1)$$

Pore size distribution curves in Figure 4.4 are measured using the BJH method. The pore diameters are small and distributed from a few nanometres up to twenty nanometres. The average pore diameters were between 4-7.5 nm for all samples and an average pore diameter of 4.2 nm is determined with a specific pore volume of 1.2 cm^3 g^{-1} for the highest surface area sample (see orange colour, which is for volumetric ratio of 1:4.5 in Figure 4. 4).

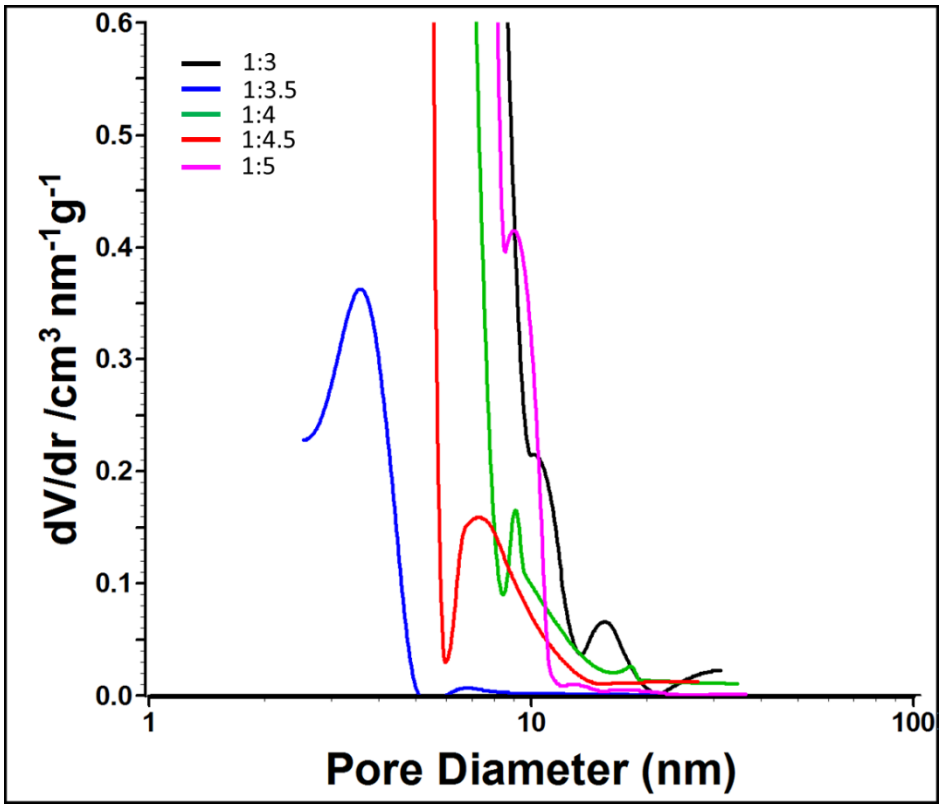

Figure 4. 4. Pore size distribution curves (BJH method) for water glass based-silica aerogels synthesised by using an ion exchange method for a different volume ratio of water glass: water.

Figure 4. 5 shows the nitrogen adsorption desorption isotherms of synthesised water glass based-silica aerogel samples of different water volumes without the use of the ion exchange method were silica gels were washed with deionised water before drying. According to a BET analysis, a water-glass silica aerogel sample with a volume ratio of water glass: water of 1:4 was found to have the highest specific surface area of 526 m^2 g^{-1}. The surface areas are between 401-526 m^2 g^{-1}, and for the same volume ratio they were lower than that obtained using the

amberlite (see Table 4. 1). However, surface areas are in the range of typical values for silica aerogels.

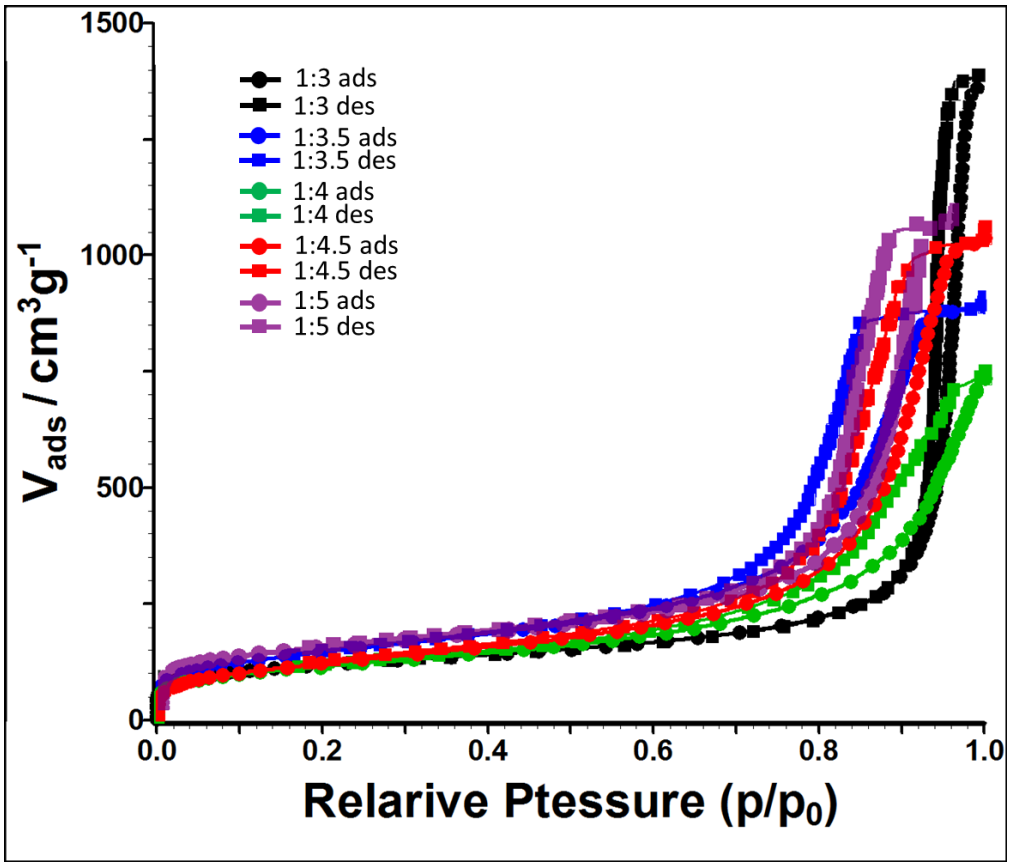

Figure 4. 5. Nitrogen adsorption-desorption isotherms of water glass based-silica aerogel samples washed with only DI water for different volume ratio of water glass: water. The adsorption isotherms are shown by filled circles, desorption isotherms are shown by filled squares.

Figure 4. 6 shows relative BJH pore size distribution curves of the same samples as seen in Figure 4. 5. The pore size distributions of those samples are distributed in a wide range of mesoporous diameters i.e. 10-50 nm. The average pore diameter and specific pore volume of water glass silica aerogel sample (with volume ratio 1:4) with highest surface area was 24 nm and 1.6 cm^3 g^{-1}, respectively. In general, it can be seen from Table 4. 1 that the average pore diameter and specific pore volume of water glass silica aerogels, which are synthesised without using an ion exchange method, are much higher than that obtained when the ion exchange method is used to remove Na^+ ions. The reason is the formation of sodium salt inside the gel structure, which later removed during washing with deionised water.

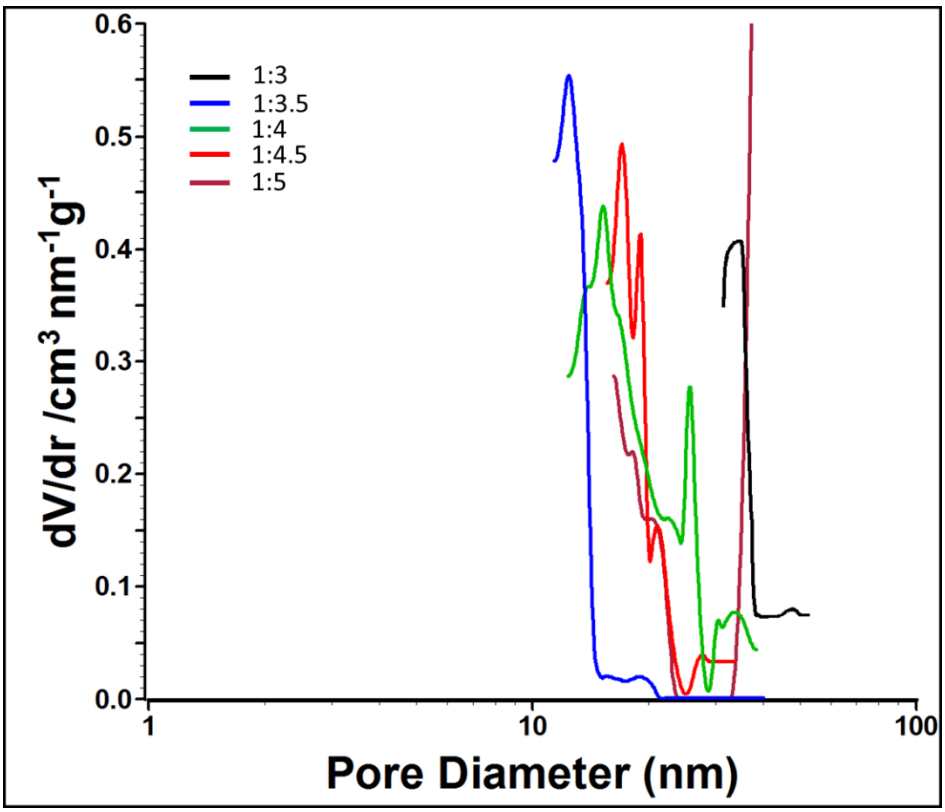

Figure 4. 6. Pore size distribution curves (BJH method) for water glass based-silica aerogels which are washed with only water for different volume ratio of water glass: water.

Figure 4.7 shows SEM micrographs for the highest surface area for both types of treatments of Na+ ions. SEM micrographs show the high porosity of both samples. Employing ion exchange during the synthesis of the water glass silica aerogels (Figure 4. 7 a) produces aerogels that have smaller pore diameters (less than 20 nm), while samples which are treated with washing with DI water only, produce silica aerogels with pore diameter from 20-50 nm and with some macropores (>50 nm). The microstructure results from SEM images agree well with the results obtained by the BJH method.

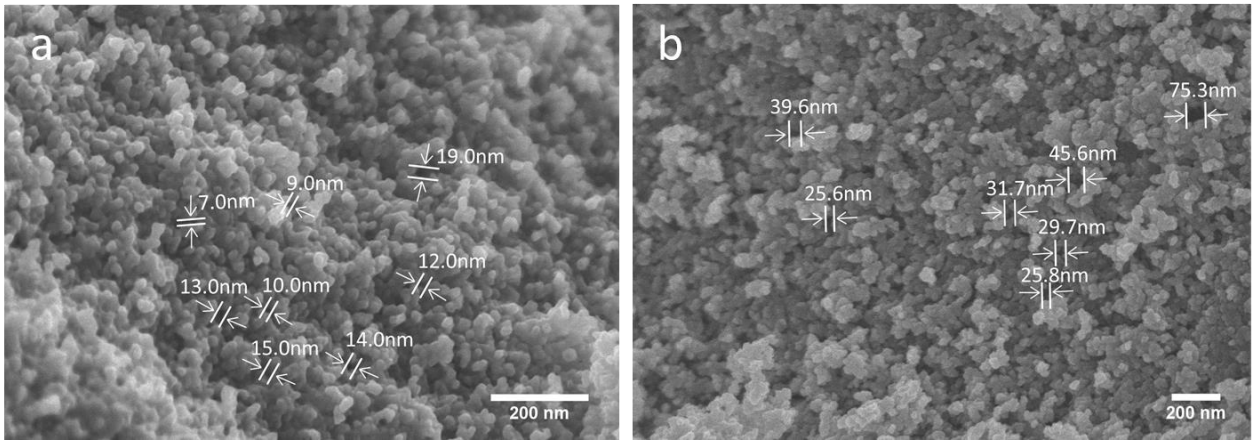

Figure 4. 7. SEM micrographs of water glass based silica aerogels for the highest surface area samples with including of typical pore diameters, (a) sample of volume ratio 1:4.5 with using of amberlite, (b) sample of volume ratio 1:4 washed with water only.

Figure 4. 8 shows the thermal conductivity results of the water glass silica aerogel sample with the highest surface area (703 m^2 g^{-1}). The thermal conductivity was measured from room temperature to 425 K, using a hot-disk technique. Each point on these curves is the mean of three independent measurements, and the time between the measurements was 10 minutes to allow the temperature to equilibrate. The thermal conductivity is found to increase monotonically as a function of temperature and at room temperature was found to be 0.016 W m^{-1} K^{-1}, demonstrating a good insulating performance equal to aerogels produced by conventional supercritical drying process (Fricke *et al.*, 1992).

In order to determine the viability of our APD approach for large-scale industrial production, the scalability has been considered too. The volume of aerogel which can be produced even within the laboratory context is scaled through appropriate increases in the quantities of reactants, and Figure 4. 9 shows an image of 350 cm^3 of salt washed aerogel granules produced in a single batch from a water glass precursor by ambient pressure drying using TMCS and bicarbonate solution.

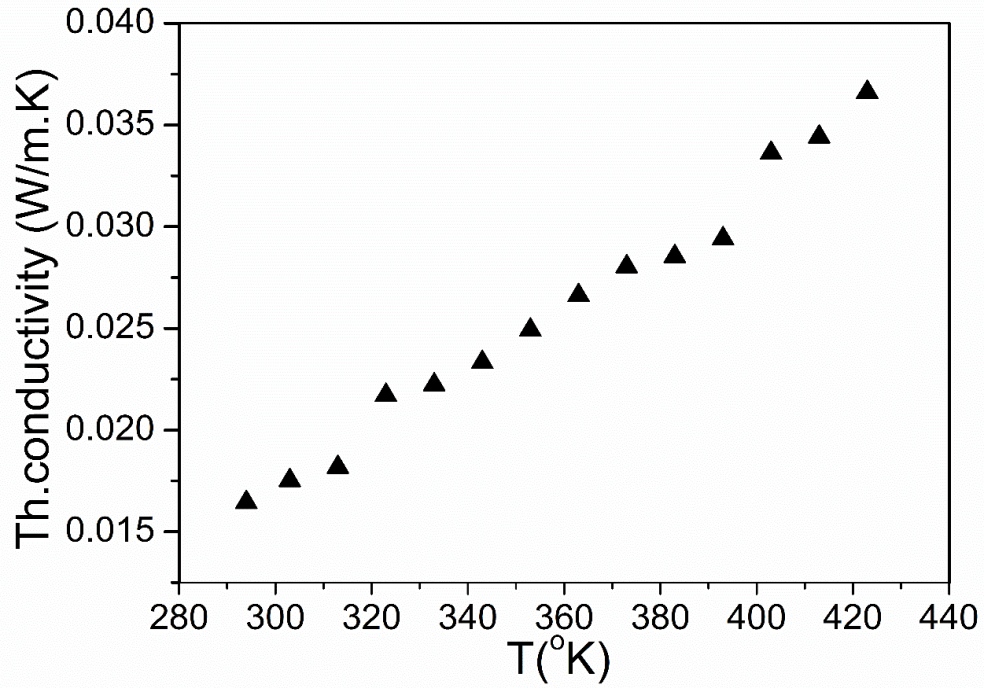

Figure 4. 8. Thermal conductivity of water glass-derived aerogel monoliths (volume ratio 1:4.5) measured over a range of temperature by the hot-disk technique.

Figure 4. 9. Scalability of the process: 350 cm^3 of salt washed aerogel granules produced in a single batch from a water glass precursor by ambient pressure drying using TMCS and bicarbonate solution.

4.3 Conclusion

Silica aerogel has been successfully synthesised from water glass precursor using sodium bicarbonate solution and TMCS. The obtained salt free silica aerogel, in the case of using ion exchange method to remove Na^+ ions from silica sol, was found to have a surface area of 703 $m^2\ g^{-1}$, an average pore diameter of 4.4 nm, a pore volume of 1.2 $cm^3\ g^{-1}$, a density of 0.051 g/cm^3, and a porosity of 98.1% (for silica aerogel sample of a volume ratio of water-glass: water of 1:4.5). While the best properties of the silica aerogel samples, that are synthesised without using ion exchange method, had surface an area of 526 $m^2\ g^{-1}$, an average pore diameter of 24 nm, and a pore volume of 1.6 $cm^3\ g^{-1}$ (for the silica aerogel sample of a volume ratio of water-glass: water of 1:4). The thermal conductivity of water glass-based silica aerogel sample with the highest surface area at room temperature is 0.016 $W\ m^{-1}\ K^{-1}$.

References

Fricke, J., Lu, X., Wang, P., Buttner, D. and Heinemann, U. (1992) 'Optimization of monolithic silica aerogel insulants ', *International Journal of Heat and Mass Transfer*, 35(9), pp. 2305-2309.

Gurav, J.L., Rao, A.V., Rao, A.P., Nadargi, D.Y. and Bhagat, S.D. (2009) 'Physical properties of sodium silicate based silica aerogels prepared by single step sol-gel process dried at ambient pressure', *Journal of Alloys and Compounds*, 476(1-2), pp. 397-402.

Han, X., Hassan, K.T., Harvey, A., Kulijer, D., Oila, A., Hunt, M.R.C. and Siller, L. (2018) 'Bioinspired synthesis of monolithic and layered aerogels', *Advanced Materials*, 30(23).

He, S., Huang, D.M., Bi, H.J., Li, Z., Yang, H. and Cheng, X.D. (2015a) 'Synthesis and characterization of silica aerogels dried under ambient pressure bed on water glass', *Journal of Non-Crystalline Solids*, 410, pp. 58-64.

He, S., Li, Z., Shi, X.J., Yang, H., Gong, L.L. and Cheng, X.D. (2015b) 'Rapid synthesis of sodium silicate based hydrophobic silica aerogel granules with large surface area', *Advanced Powder Technology*, 26(2), pp. 537-541.

Hwang, S.W., Kim, T.Y. and Hyun, S.H. (2008) 'Optimization of instantaneous solvent exchange/surface modification process for ambient synthesis of monolithic silica aerogels', *Journal of Colloid and Interface Science*, 322(1), pp. 224-230.

Shi, F., Wang, L.J. and Liu, J.X. (2006) 'Synthesis and characterization of silica aerogels by a novel fast ambient pressure drying process', *Materials Letters*, 60(29-30), pp. 3718-3722.

Sing, K.S.W., Everett, D.H., Haul, R.A.W., Moscou, L., Pierotti, R.A., Rouquerol, J. and Siemieniewska, T. (1985) 'Reporting physisorption data for gas/solid systems with spacial reference to determination of surface area and porosity ', *Pure and Applied Chemistry*, 57, pp. 603-619.

Thommes, M., Kaneko, K., Neimark, A.V., Olivier, J.P., Rodriguez-Reinoso, F., Rouquerol, J. and Sing, K.S.W. (2015) 'Physisorption of gases, with special reference to the evaluation of surface area and pore size distribution (IUPAC technical report)', *Pure Appl. Chem.* , 87(9-10), pp. 1051-1069.

Chapter 5 Synthesis and characterisation of alumina-based aerogel (dawsonite - sodium aluminium carbonate hydroxide) by using bicarbonate ambient pressure drying method.

The main purpose of this chapter is to prove that the new APD approach can be applied to different aerogel precursors. Aluminium sec-butoxide precursor (ASB) has been used to synthesise alumina aerogels by applying the new APD approach. This chapter presents results of characterisations such as XRD, FTIR, SEM, BET and BJH that were carried out on the synthesised material.

5.1 Synthesis of dawsonite aerogels using novel ambient pressure drying method

To demonstrate that the new APD approach is applicable to different aerogel compositions, we have also produced an alumina-based aerogel (dawsonite - sodium aluminium carbonate hydroxide) by the same method. Alumina-based aerogels are produced from an aluminium sec-butoxide precursor (ASB). The alumina gels were synthesised according to the method reported by Wu *et al.* (2010) with modifications. Many factors such as the type of alkoxide, water and alkoxide ratio, hydrolysis rate, type of catalyst used, pH of the mixture and the temperature of the reaction affect the final structure of the gel. Therefore, the form of the final alumina aerogels produced could be powder or monolithic, amorphous or crystalline (Poco *et al.*, 2001).

Wu *et al.* (2010) reported using a mixture of ASB, water, ethyl acetoacetate and ethanol in a molar ratio of 1:0.6:0.72:16, respectively to obtain the gel. However, following that molar ratio we could not reach the gelation state. Therefore, firstly, the molar ratio was modified by changing the percentage of ethyl acetoacetate because the presence of ethyl acetoacetate causes a reduction in the rate of hydrolysis of ASB (Pierre *et al.*, 1999) and has an influence on the structure of the dried alumina aerogels (Le Bihan *et al.*, 2002). The optimum molar ratio of gelation in our work was observed to be 1:0.6:0.58:16 during synthesis. The second modification was on the ageing time, to find the optimum time for the completing of the gelation stage. Therefore, the gels were aged in an airtight box for 1, 2, 3, 6, 7, and 10 days. The gelation was completed after 7 days as there was no need for additional time. The gel was soaked in sodium bicarbonate solution (4.4 g for each 100 ml water) while stirring for 2 h. CO_2 was generated within the aerogel by soaking the aerogels in an ethanol solution containing TMCS (14 ml TMCS in 100 ml ethanol) for 24 h at room temperature. The gel was rinsed with ethanol

to remove the unreacted TMCS, soaked with water and stirred for 8 h. Finally, the gel was immersed in ethanol for 24 h and dried at room temperature for 72 h followed by 100°C for 2 h under ambient pressure.

5.2 Results and discussion

Figure 5. 1 shows the granules of the dawsonite-sodium aluminium carbonate hydroxide aerogels.

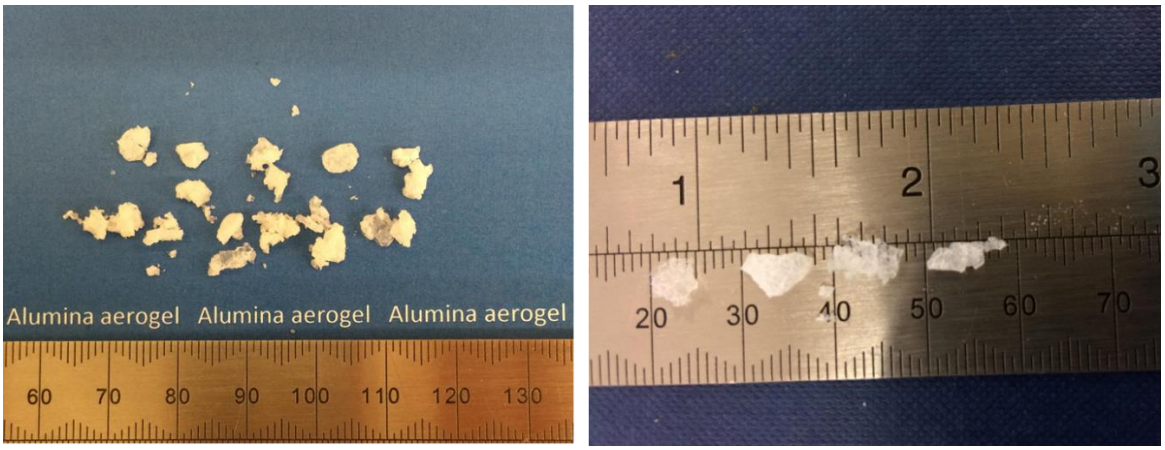

Figure 5. 1. Dawsonite - sodium aluminium carbonate hydroxide aerogel granules.

Figure 5. 2 presents scanning electron microscopy (SEM) images of alumina-based aerogel (dawsonite—sodium aluminium carbonate hydroxide). SEM images show the mesoporous structure of the dawsonite aerogels.

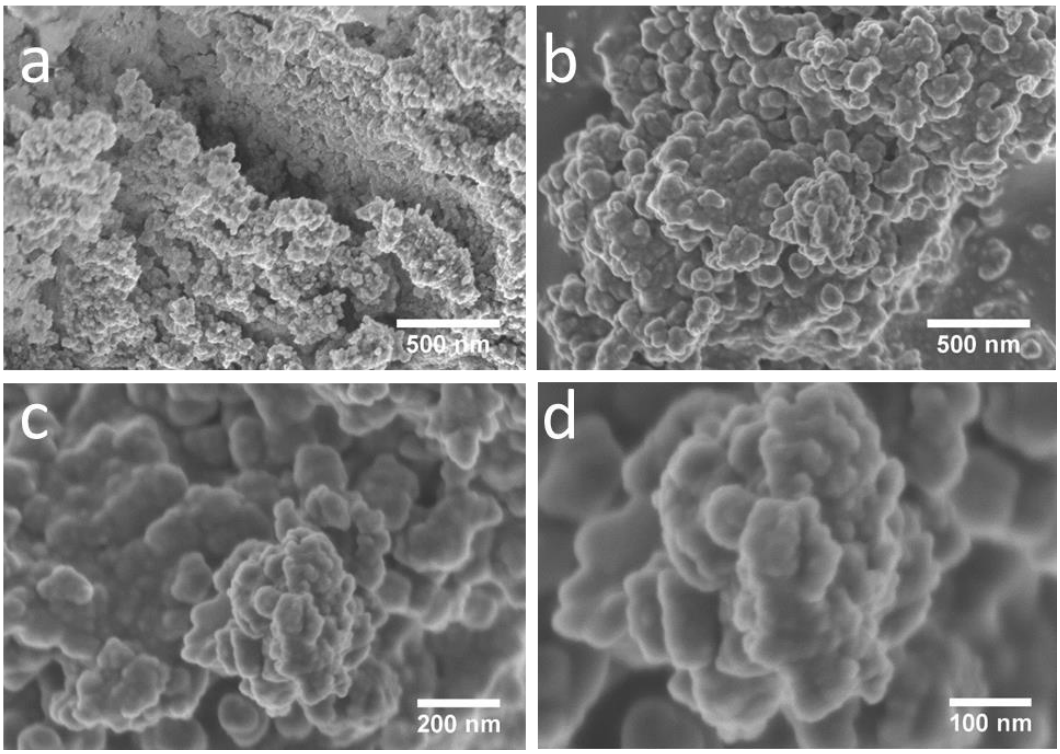

Figure 5. 2. SEM image of dawsonite ($NaAlCO_3(OH)_2$) aerogels synthesized with aluminium sec-butoxide and ambient pressure drying using bicarbonate solution and TMCS.

The samples were firstly characterised using x-ray diffraction technique. Figure 5. 3 shows an XRD pattern from a dawsonite aerogel. The peaks in the XRD scans from these aerogels match with crystalline sodium aluminium carbonate hydroxide (Benezeth *et al.*, 2007; Stoica *et al.*, 2009). The XRD pattern is in agreement with previous reports that dawsonite is accompanied by boehmite (AlOOH) (Benezeth *et al.*, 2007). The dawsonite fraction of the aerogel was determined as it was mentioned in chapter 2 section 2.2.3. The weight fraction of dawsonite was found to be 58 wt.% of the sample.

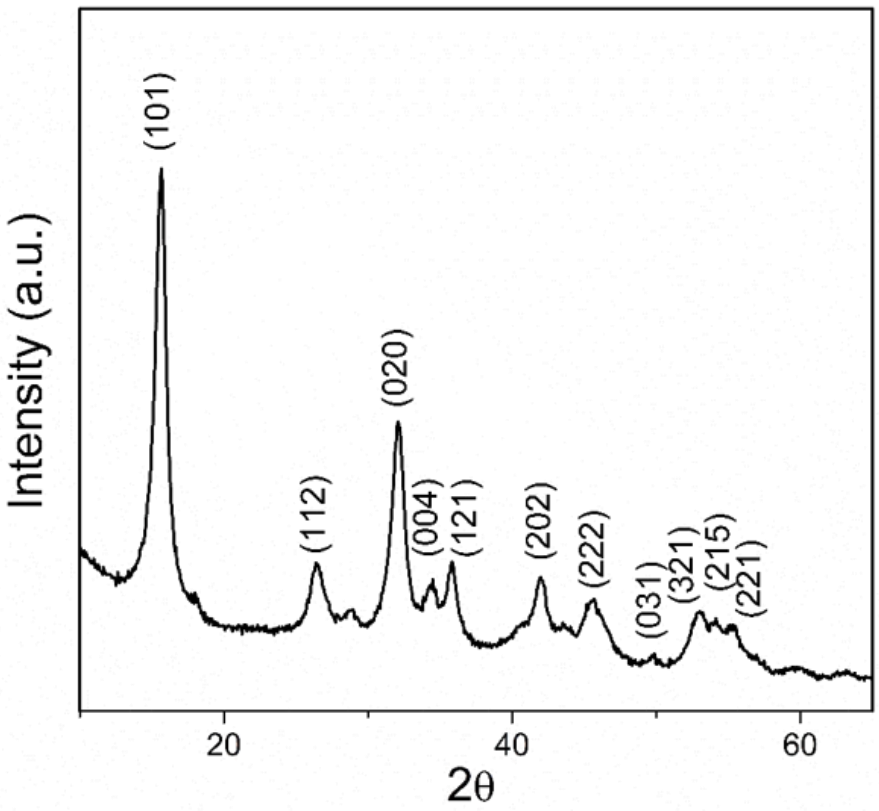

Figure 5. 3. XRD 2θ scan of a sodium aluminium carbonate hydroxide aerogel sample.

Figure 5. 4 presents a FTIR spectrum of a dawsonite aerogel. A number of distinct bands are observed, corresponding to the hydroxyl group (-OH), υ_{OH}, at 3270 cm^{-1} and δ_{OH} at 955.7 cm^{-1} and 927 cm^{-1}. The bands at 1549 cm^{-1}, 1390.8 cm^{-1}, 1096 cm^{-1} 845 cm^{1}, and at 730.7 cm^{-1} correspond to -CO_3, while the band at 671 cm^{-1} is the sodium aluminium carbonate hydroxide lattice vibration (Serna *et al.*, 1985; Stoica *et al.*, 2009; Chukanov, 2014). The FTIR spectra confirms the conclusions drawn from XRD regarding the composition of the aerogels.

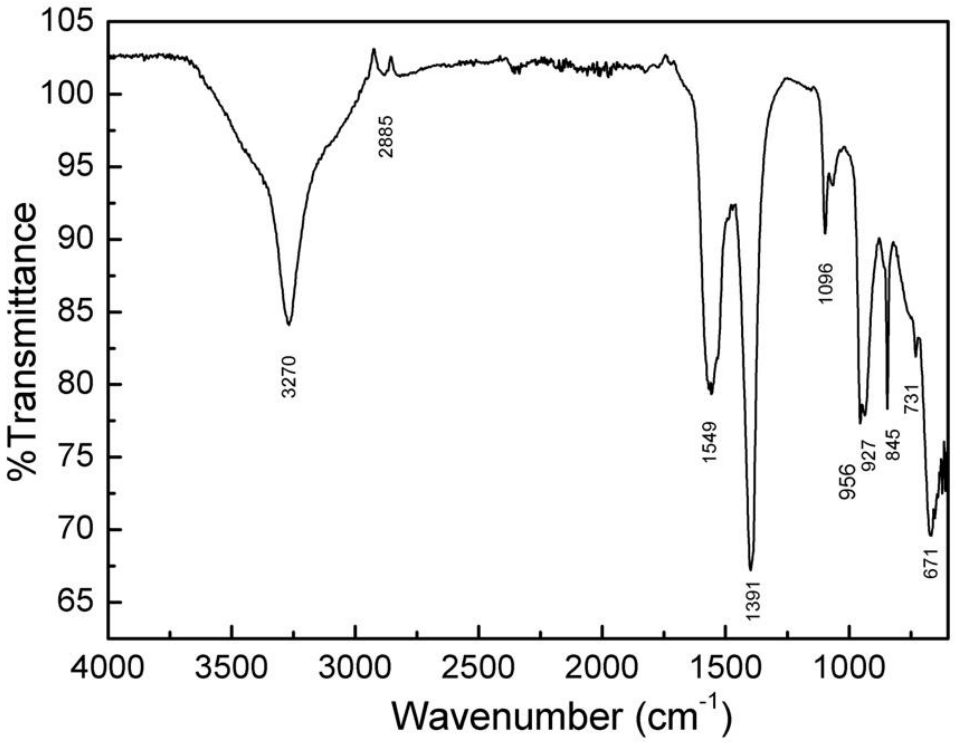

Figure 5. 4. FTIR spectrum of an as-synthesised Dawsonite aerogel.

The surface area and pore size distribution of the dawsonite aerogels were analysed by nitrogen adsorption/desorption isotherms using the BET and BJH methods. Figure 5. 5 shows the nitrogen adsorption-desorption curves. The analysis indicates that the dawsonite aerogels have a mesoporous structure with a surface area of 350 m^2 g^{-1}.

Figure 5. 6 shows the BJH analysis results of pore size distribution of the dawsonite aerogels which is taken from the desorption curve in Figure 5. 5. The results of BJH analysis shows that the pores are in a mesoporous range of pore size distribution, with an average pore diameter of 5.7 nm and pore specific volume of 0.54 cm^3 g^{-1}.

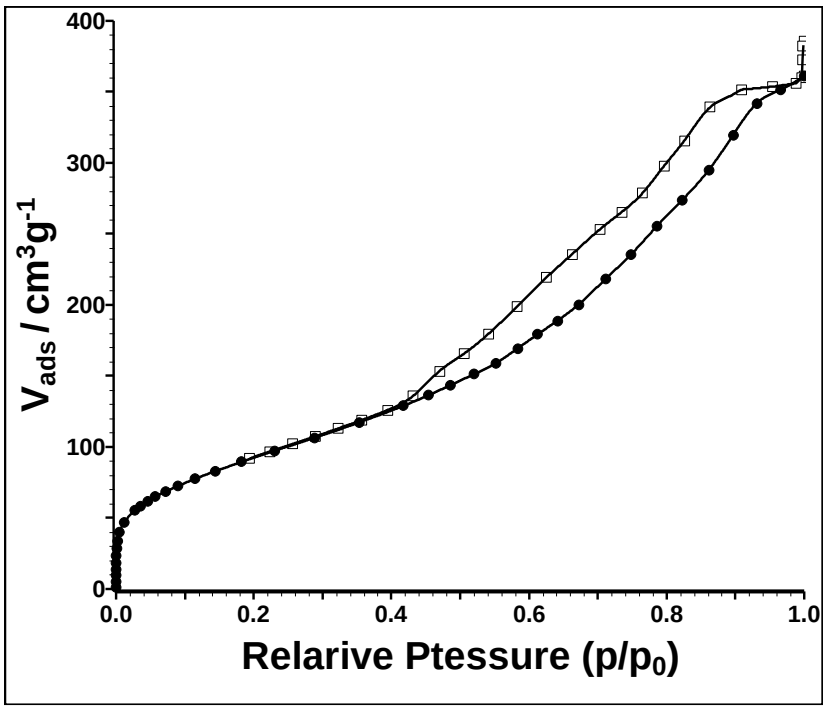

Figure 5. 5. N_2 adsorption-desorption isotherm curve of as-synthesised dawsonite aerogels. The adsorption isotherm is shown by the filled circles, the desorption isotherm is presented by the open squares.

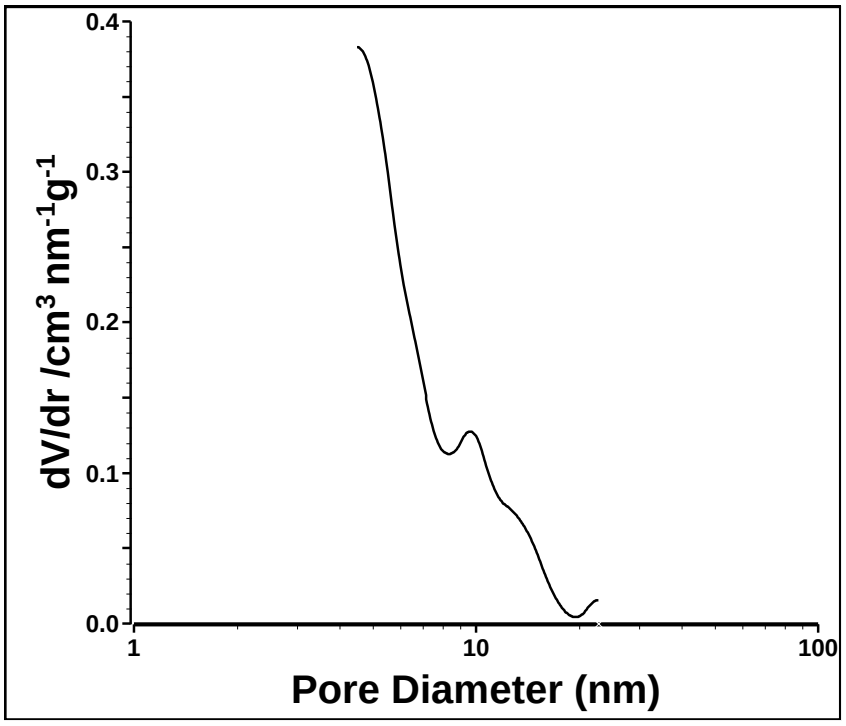

Figure 5. 6. Pore size distribution curve of as-synthesised dawsonite aerogels.

5.3 Conclusion

Alumina-based aerogels (dawsonite - sodium aluminium carbonate hydroxide) have been successfully synthesised using our novel ambient pressure drying approach with bicarbonate solution and TMCS. The as-synthesised dawsonite aerogel has a mesoporous structure and a surface area of 350 m^2 g^{-1} with an average pore diameter of 5.7 nm and pore specific volume of 0.54 cm^3 g^{-1}.

References

Benezeth, P., Palmer, D.A., Anovitz, L.M. and Horita, J. (2007) 'Dawsonite synthesis and reevaluation of its thermodynamic properties from solubility measurements: Implications for mineral trapping of CO_2', *Geochimica Et Cosmochimica Acta*, 71(18), pp. 4438-4455.

Chukanov, N.V. (2014) *Infrared spectra of mineral species*. Springer

Le Bihan, L., Dumeignil, F., Payen, E. and Grimblot, J. (2002) 'Chemistry of preparation of alumina aerogels in presence of a complexing agent', *Journal of Sol-Gel Science and Technology*, 24(2), pp. 113-120.

Pierre, A., Begag, R. and Pajonk, G. (1999) 'Structure and texture of alumina aerogel monoliths made by complexation with ethyl acetoacetate', *Journal of Materials Science*, 34(20), pp. 4937-4944.

Poco, J.F., Satcher, J.H. and Hrubesh, L.W. (2001) 'Synthesis of high porosity, monolithic alumina aerogels', *Journal of Non-Crystalline Solids*, 285(1-3), pp. 57-63.

Serna, C.J., Garciaramos, J.V. and Pena, M.J. (1985) 'Vibrational study of dawsonite type compounds $NAAL(OH)_2CO_3$, $KAL(OH)_2CO_3$, $NH_4AL(OH)_2CO_3$', *Spectrochimica Acta Part a-Molecular and Biomolecular Spectroscopy*, 41(5), pp. 697-702.

Stoica, G., Abello, S. and Perez-Ramirez, J. (2009) 'Na-dawsonite derived aluminates for DMC production by transesterification of ethylene carbonate', *Applied Catalysis a-General*, 365(2), pp. 252-260.

Wu, L.N., Huang, Y.D., Wang, Z.J., Liu, L. and Xu, H.F. (2010) 'Fabrication of hydrophobic alumina aerogel monoliths by surface modification and ambient pressure drying', *Applied Surface Science*, 256(20), pp. 5973-5977.

Chapter 6 Synthesis and characterisation of layered silica aerogels

This chapter presents bio-inspired synthesis of multi-layered silica aerogels to mimic the structure and thickness of the wings of the damselfly. The microstructure, surface area, pore size and mechanical properties of the multi-layered silica aerogel film of 0.3mm thickness were measured using SEM, BET, BJH and uniaxial compression analysis, respectively.

6.1 Synthesis of multi-layered silica aerogel films

To prepare uniform films, 1 ml of sol was spread using a glass rod. Once gelation of the first layer was completed, another layer of silica sol was dripped on the gel surface until gelation was completed. The process was repeated until the required number of layers was complete. After completing gelation, the cling film was placed inside the petri dish and the gel was soaked with ethanol for 8 hours. After ageing, ethanol was replaced by a mixture of deionised water and sodium bicarbonate for 8 hours. The gel was then soaked in a TMCS and ethanol mixture with a 16:100 volumetric ratio for 4 hours. Following this, the gel was rinsed with ethanol to remove unreacted TMCS. Finally, the gel film was dried at ambient pressure and room temperature for 12 hours, then at 100°C for 1 hour. Attempts to produce a single aerogel layer of the same overall thickness of the multi-layered aerogel samples, produced materials which were too brittle to successfully remove from the cling-film support.

6.2 Results and Discussion

Many material synthesis problems have been solved by biological systems as they provide inspiration for the design and production of man-made analogues (Meyers *et al.*, 2013; Tao *et al.*, 2015; Wegst *et al.*, 2015; Picot *et al.*, 2017). Lightweight and porous materials are key elements of many biological structures: for example, the wings of Odonata – dragonflies and damselflies – which are among the fastest and most agile flying insects,(Rajabi and Darvizeh, 2013; Appel *et al.*, 2015) consist of super-lightweight composites made of chitin microfibrils embedded in a protein matrix (resilin, an elastomeric protein) that have complex configurations at both macro and micro scale (Appel *et al.*, 2015). Typically, the wing weight is less than 2%

of a dragonfly's total body mass (Rajendran *et al.*, 2012). The SEM images, seen in Figure 6. 1 (a-c), of the wing of the damselfly Lestes virens (Odonata, Zygoptera: Lestidae), which are taken by Dr. L. Šiller and Dr. D. Kulijer, present a porous and layered structure similar to an aerogel-like material. It is clear that the thickness of the membrane varies across the wing and the wings are made from porous tactile multilayers (Han *et al.*, 2018).

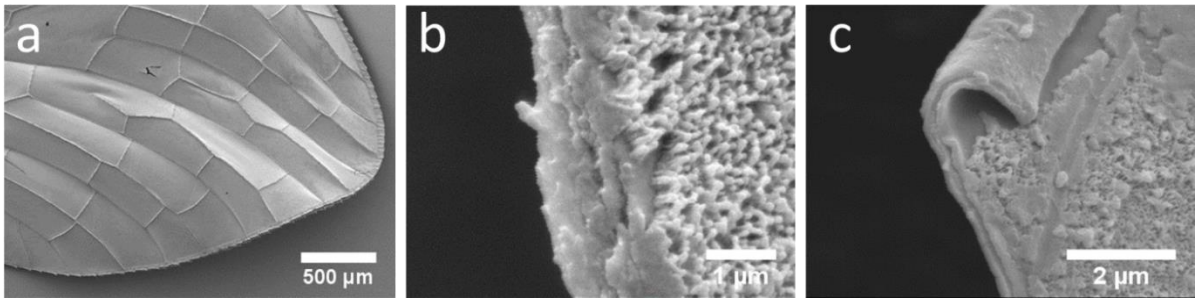

Figure 6. 1. SEM images of the membrane of the damselfly Lestes virens (Odonata, Zygoptera: Lestidae): (a) base of the wing; (b) multi-layered structure (5 layers are visible) of the base of the wing; (c) two layer structure of the end of the wing (Han *et al.*, 2018).

In the current work, the purpose of multi-layered aerogel synthesis is to show that we can obtain similar freestanding submillimetre structured aerogel layers to mimic the structure and thickness of the wings of the damselfly (compare Figure 6. 1c with Figure 6. 3 a, b). Normally it is known that laminated materials provide better toughness. Mechanical properties of non-layered free-standing silica aerogels are difficult to measure if they are under 0.5 mm thick.

Layered silica aerogels are prepared by the same novel AMD approach with bicarbonate solution and TMCS (see Figure 6. 2), enabling compositional variation through an aerogel monolith and providing a route by which large thickness monoliths may be built up. The synthesis of layered silica aerogels was mentioned in detail in chapter 2, section 2.1.4.

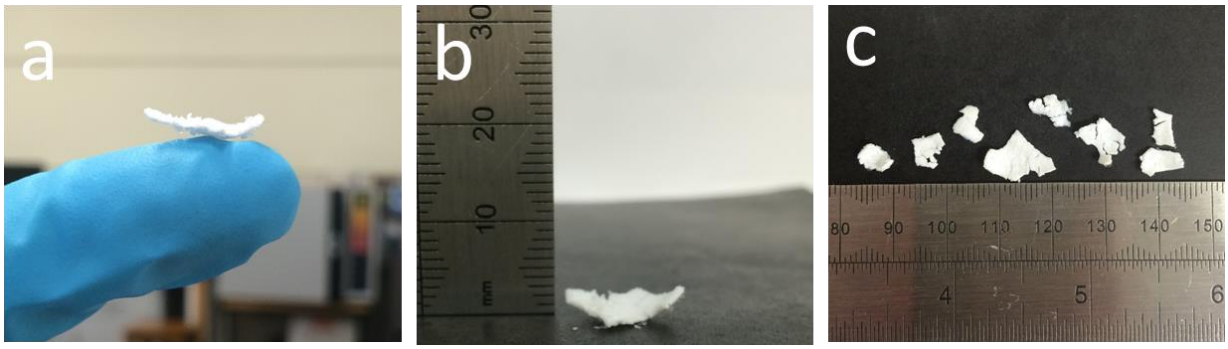

Figure 6. 2. Bioinspired wing-membrane-like multi-layered silica aerogels. (a-c), Photos of silica aerogels formed by the sodium bicarbonate solution based APD method using TEOS precursor.

Figure 6. 3 shows SEM images for multi-layered silica aerogel samples, which are displayed in Figure 6. 2. Figure 6. 3 (a, b) shows SEM micrographs of bilayer and triple layered aerogel material show similarity to the structure in figure 6.1c from Lestes virens. The interface between two layers is shown in Figure 6. 3c, the SEM image clearly shows the porosity and excellent tactility of the interface. SEM micrographs in Figure 6. 3 (d, e) show the nine layered structure of the silica aerogel where the thickness of each layer is between 16 to 35.6 µm. Further magnification shows the mesoporous structure of this layered silica aerogel (Figure 6. 3f). These layered aerogel structures display a remarkable similarity to the multi-layered structure of a damselfly's wings, as might be expected given the original inspiration for the APD approach presented here.

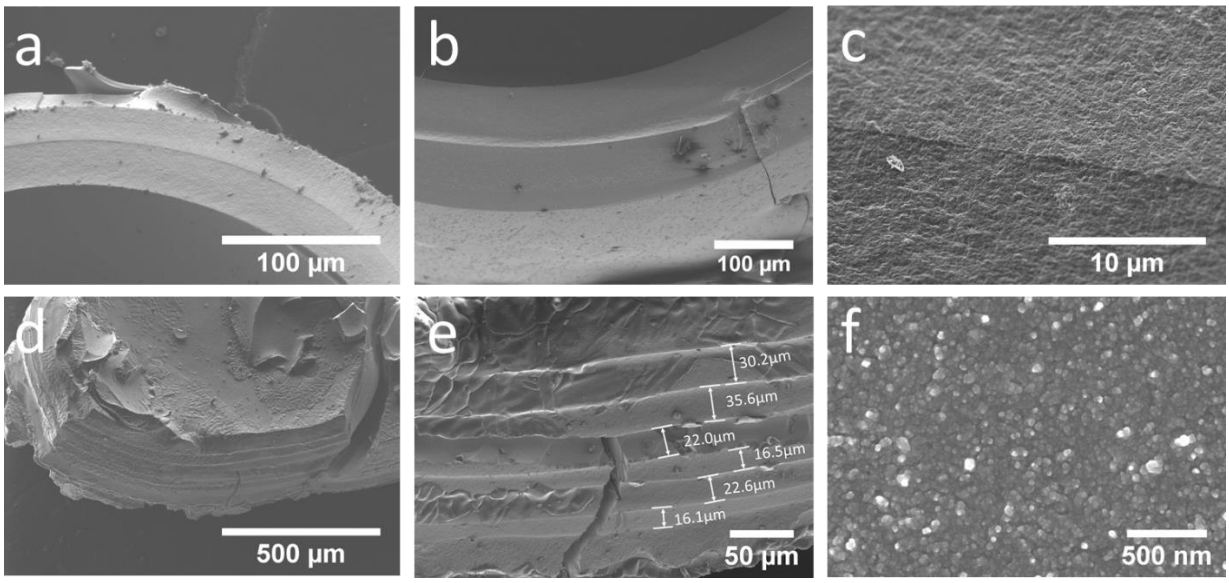

Figure 6. 3. SEM micrograph of Bioinspired wing-membrane-like multi-layered silica aerogels. (a) SEM micrograph of bilayer. (b) SEM micrograph of triple layers aerogel material. (c) SEM micrograph of the interface in the bilayer aerogel. (d-e) nine layers porous aerogel structures. (f) SEM micrograph of mesoporous structure.

Figure 6. 4 shows the nitrogen adsorption desorption curves for layered silica aerogel. From nitrogen adsorption-desorption isotherms and pore size distribution analysis (see Figure 6. 5), we find that the multi-layered silica aerogel films exhibit a surface area of 520 m^2 g^{-1}. The isotherm curves display type IV behaviour, indicating mesoporous structure (Thommes *et al.*, 2015). The pore size diameters are distributed in a cross a wide range of mesoporous diameters with an average pore diameter of 15.6 nm and a pore volume of 1.6 cm^3 g^{-1}.

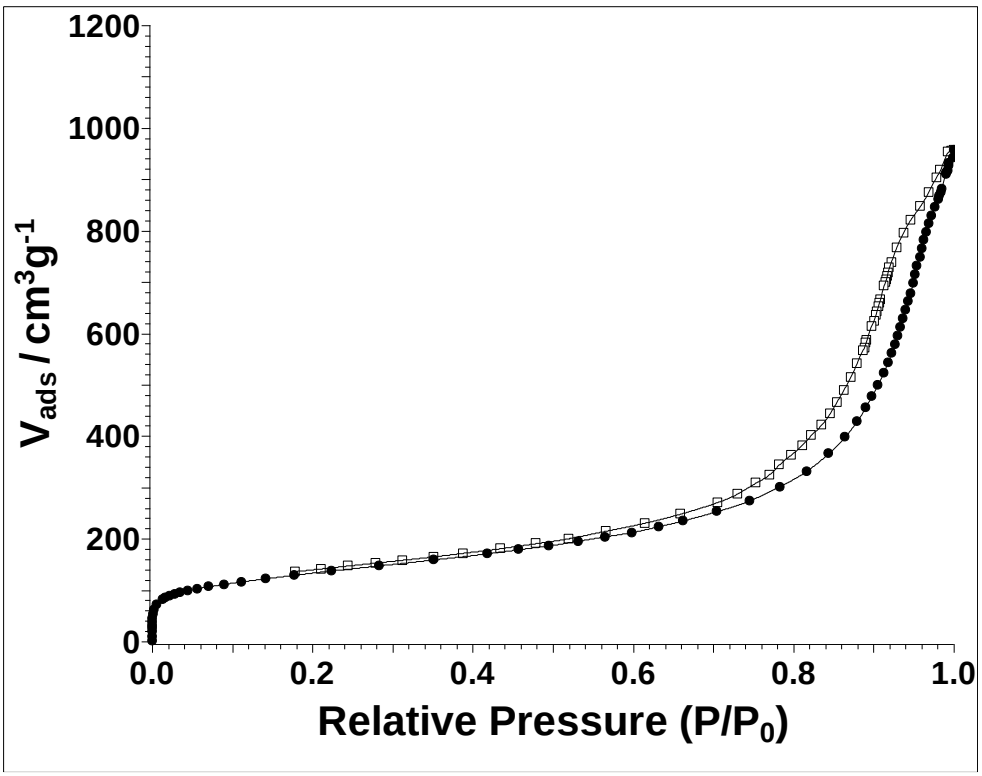

Figure 6. 4. N_2 adsorption-desorption isotherm for multi-layer silica aerogels. The adsorption isotherm is presented by the filled circles, desorption isotherm is presented by open squares.

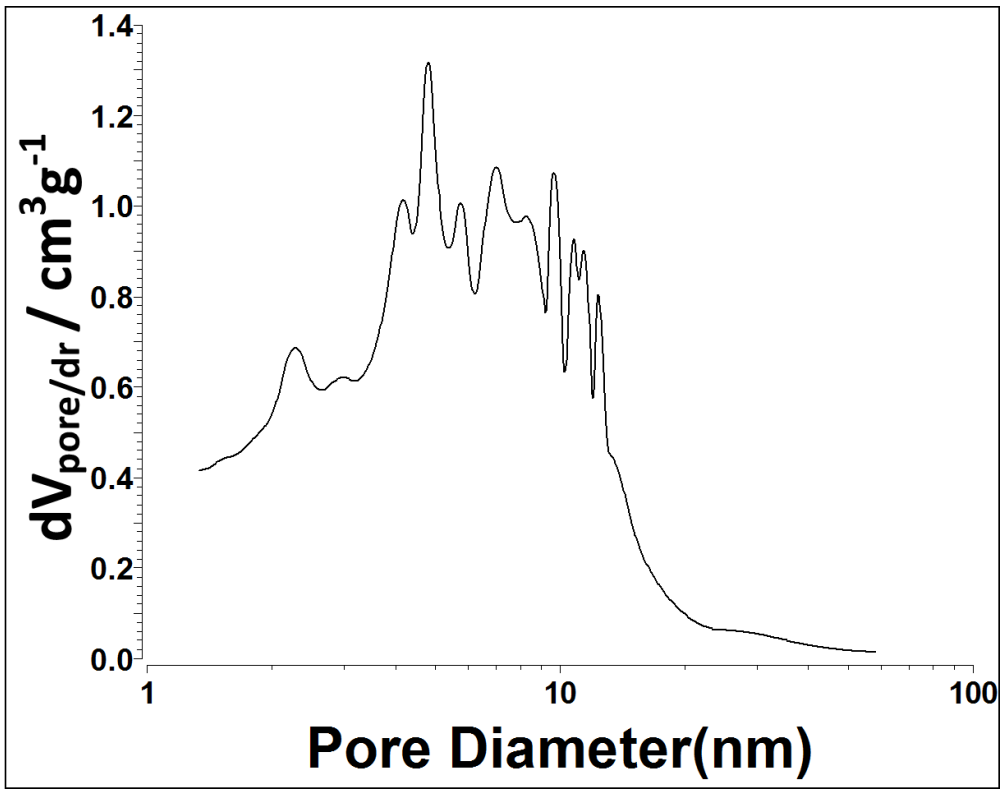

Figure 6. 5. Pore size distribution for multi-layer silica aerogels.

Layering the aerogel structure considerably increases aerogel durability – it was possible to produce free-standing aerogel with typical thicknesses of ~ 0.3 mm, whilst attempts to produce non-layered samples of similar thicknesses with the same composition and preparation approach failed as these more brittle samples broke up upon the most gentle of handling. These ultra-thin layered aerogel samples were sufficiently robust to allow for compression testing.

Compression tests were carried out on layered silica aerogels with an overall thickness, measured by SEM, to be approximately ~ 0.3 mm (see Figure 6. 6). Five samples were tested using a Tinius-Olsen mechanical testing frame at a crosshead speed of 0.5 mm min^{-1}. Typical stress-strain curves are shown in Figure 6. 7. The compression, the slope of the stress-strain curves, was used to calculate the compressive elastic modulus. The value obtained was $E_{layered}$ = 0.20 ± 0.07 GPa. The surface area needed for determination of moduli was determined with optical microscopy (as shown in Figure 6. 8).

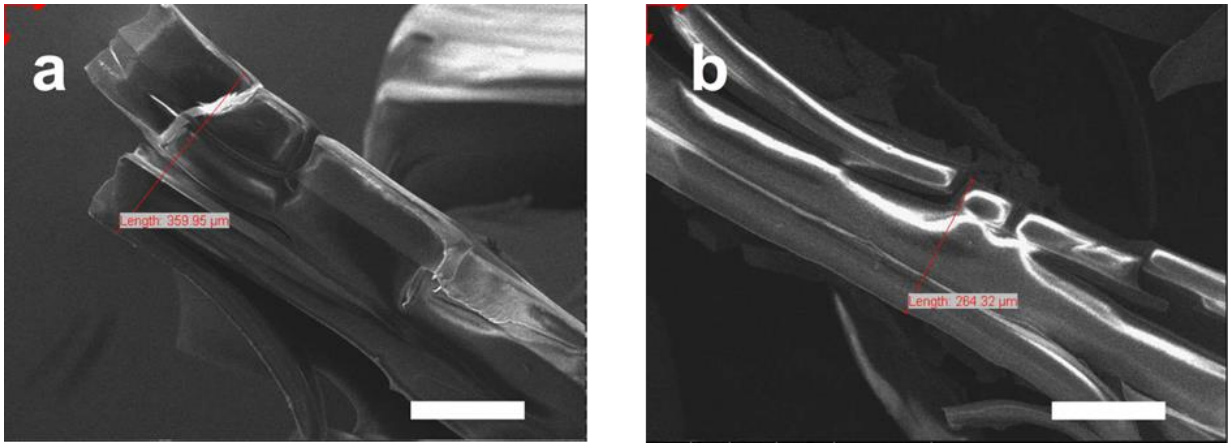

Figure 6. 6. *(*a-b*)*, thickness measurements of layered silica aerogels by scanning electron microscopy. Sample thickness was found to vary in the range ~ 250 – 350 nm**.** The scale bar is 200 nm.

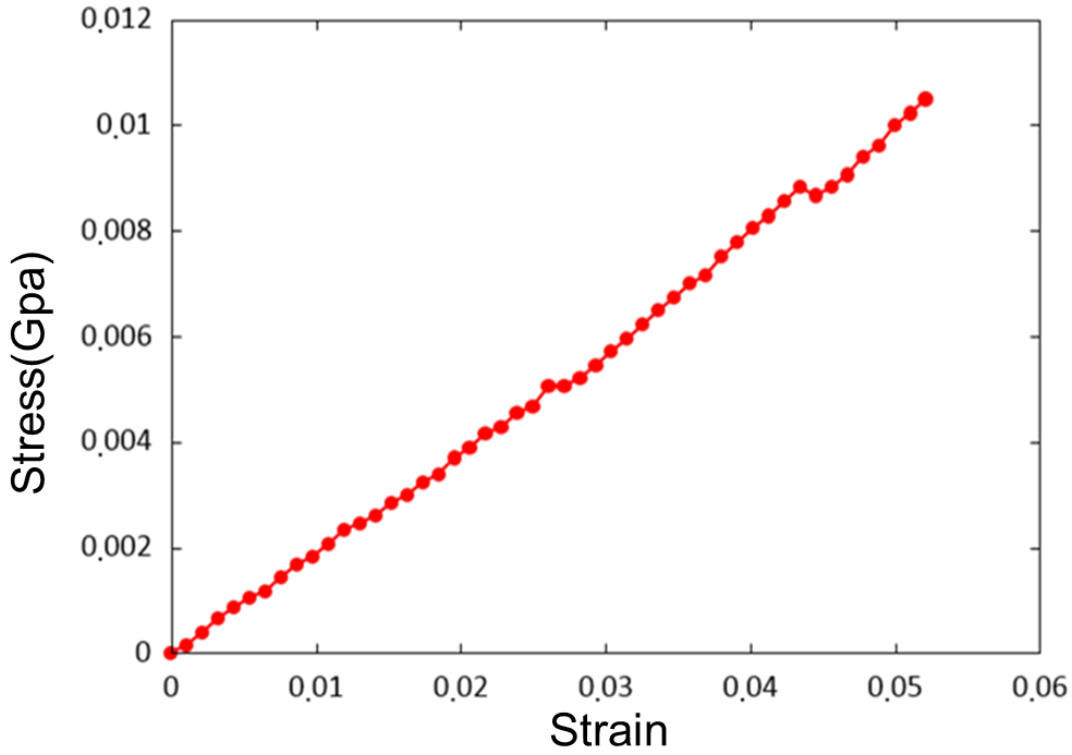

Figure 6. 7. Stress-strain curve for a typical layered silica aerogel.

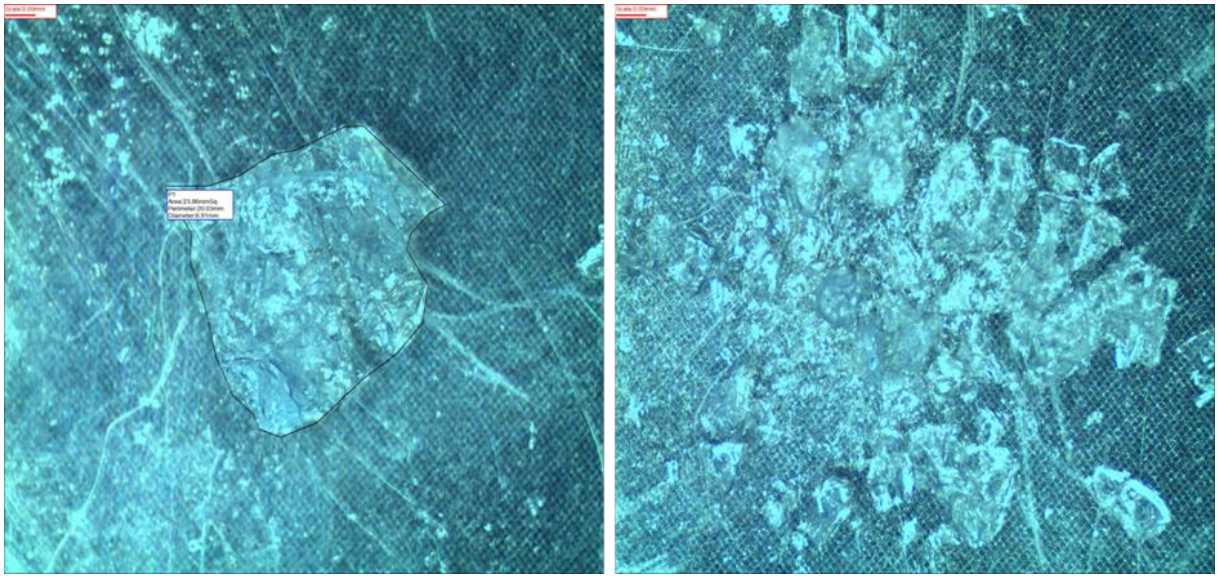

Figure 6. 8. Optical micrographs showing the surface area of a layered aerogel before (left) and after (right) compression testing.

Similar tests on monolithic aerogels of the same thickness, as the layered samples, were attempted but were found to be inconclusive. Without layering, aerogels of such small thickness were found to be too fragile to detach them from the support without complete breakage. The

mere fact that it was possible to extract the layered aerogel samples and perform stress tests indicate that they are much tougher than uniform monoliths.

6.3 Conclusion

An attempt to mimic the structure and thickness of the wings of the damselfly led to the synthesis of multi-layered silica aerogel films with a thickness of 0.3 mm. However, all attempts to synthesise the same thickness of silica aerogels without layering were found to be unsuccessful. Layering the aerogel structure considerably increases aerogel durability. Performing stress tests on such a small thickness of silica aerogel films indicate that they are much tougher than uniform monoliths. Silica aerogel films show high surface area and a porous structure.

References

Appel, E., Heepe, L., Lin, C.P. and Gorb, S.N. (2015) 'Ultrastructure of dragonfly wing veins: composite structure of fibrous material supplemented by resilin', *Journal of Anatomy*, 227(4), pp. 561-582.

Han, X., Hassan, K.T., Harvey, A., Kulijer, D., Oila, A., Hunt, M.R.C. and Siller, L. (2018) 'Bioinspired synthesis of monolithic and layered aerogels', *Advanced Materials*, 30(23).

Meyers, M.A., McKittrick, J. and Chen, P.Y. (2013) 'Structural biological materials: critical mechanics-materials connections', *Science*, 339(6121), pp. 773-779.

Picot, O.T., Rocha, V.G., Ferraro, C., Ni, N., D'Elia, E., Meille, S., Chevalier, J., Saunders, T., Peijs, T., Reece, M.J. and Saiz, E. (2017) 'Using graphene networks to build bioinspired self-monitoring ceramics', *Nature Communications*, 8.

Rajabi, H. and Darvizeh, A. (2013) 'Experimental investigations of the functional morphology of dragonfly wings', *Chinese Physics B*, 22(8), p. 8.

Rajendran, S., Karuppanan, K.K. and Pezhinkattil, R. (2012) 'Analysis on surface nanostructures present in hindwing of dragon fly (Sympetrum vulgatum) using atomic force microscopy', *Micron*, 43(12), pp. 1299-1303.

Tao, P., Shang, W., Song, C.Y., Shen, Q.C., Zhang, F.Y., Luo, Z., Yi, N., Zhang, D. and Deng, T. (2015) 'Bioinspired engineering of thermal materials', *Advanced Materials*, 27(3), pp. 428-463.

Thommes, M., Kaneko, K., Neimark, A.V., Olivier, J.P., Rodriguez-Reinoso, F., Rouquerol, J. and Sing, K.S.W. (2015) 'Physisorption of gases, with special reference to the evaluation of

surface area and pore size distribution (IUPAC technical report)', *Pure Appl. Chem.* , 87(9-10), pp. 1051-1069.

Wegst, U.G.K., Bai, H., Saiz, E., Tomsia, A.P. and Ritchie, R.O. (2015) 'Bioinspired structural materials', *Nature Materials*, 14(1), pp. 23-36.

Chapter 7 Synthesis and immobilised nickel nanowires on silica aerogels

The shape and size of nanomaterials is known to affect their catalytic behaviour. In this work, wavy nickel nanowires (NiNWs) and nickel nanoparticles (NiNPs) were immobilised in mesoporous silica (SiO_2) aerogels by the sol-gel method to compare their catalytic activity toward CO_2 hydration reaction (CHR). We measured the catalytic activity of pure NiNWs and NiNWs-SiO_2 aerogel composites toward the CO_2 hydration reaction (CHR) when submerged in water. A dynamic vapour sorption (DVS) analysis was performed at levels of 50% CO_2 and 50% H_2O vapour for SiO_2 aerogels, immobilised nickel nanoparticles (NiNPs) on silica aerogels and NiNWs-SiO_2 aerogels composites, in order to determine catalytic activity for CHR in gaseous phase. The results from the DVS analysis (gaseous phase) and CHR (aqueous phase) showed that NiNWs-SiO_2 aerogel composites are good heterogeneous catalysts for CHR in both gaseous and aqueous phases but they are less active than NiNPs-SiO_2 aerogel composites.

7.1 Synthesis of nickel nanowires (NiNWs)

Nickel nanowires were synthesized following solvothermal process as reported by Chen *et al.* (2015b) with modification. Typically, 137 mg of $NiCl_2 \cdot 6H_2O$ was first added to 60 ml of ethylene glycol (EG) in a round bottom flask. After $NiCl_2 \cdot 6H_2O$ had fully dissolved in EG, 5 ml of 1M NaOH and 2.3 ml of $N_2H_4 \cdot H_2O$ was then added into this solution. This solution was then kept in a water bath at 60 ^{0}C for 3 hours, the solution turned black indicating synthesis of Ni nanowires. These nickel nanowires were then dried in an oven at 60 °C for 8 hours. It was observed that when these nanowires were suspended in DI water, the pH of the suspension was acidic. It was suspected that the low pH could be due to the presence of residual reactants at the nanowire surface. Therefore, in order to remove these residuals, the nanowires were washed with 6M NaOH solution followed with DI water until the nanowire suspension had near neutral pH. Typically, 30 mg of NiNWs were mixed with 20 mL of 6 M NaOH and sonicated for 3 min. NaOH solution was refreshed and the process was repeated five times. A high-power magnet was used to separate NiNWs from the solution. In order to remove any excess NaOH from the samples, additional post-washing with DI water was introduced. NiNWs were dispersed in 20 ml of DI water followed by sonication for 3 min. DI water was then refreshed

and the process was repeated 20 times. Finally, NiNWs were washed by ethanol five times before drying at 60 °C for 8 hours.

7.2 Immobilisation of nickel nanowires (NiNWs) on silica aerogels

The sol-gel process was used to synthesise silica aerogel. Immobilisation of NiNWs (see Figure 2. 4) and NiNPs (for comparison) were carried out according to process proposed by Han *et al.* (2015). NiNWs were dispersed during the sol stage prior to gelation. Silica aerogels samples with 0, 400, 500 and 700 ppm of NiNWs (S, N1, N2 and N3 in Table 7. 1 chapter 7, respectively) were synthesized (Figure 7. 2 a and b). For the procedure, the desired amount of NiNWs were suspended in 5 ml of DI water using a sonic horn (Sonopuls, Bandelin) for 2 minutes. The hydrolysis of TEOS in ethanol and deionised water was used to prepare the silica gel with a molar ratio of 2:38:33 of TEOS: ethanol: water, respectively.

To accelerate the gelation process, a 1 ml mixture of ammonium hydroxide, ammonium fluoride and DI water in a molar ratio 1:8:111 was used as a catalyst. Subsequently, the mixture was stirred for 3 minutes and poured in a plastic mould for gelation. When gelation was complete, the mould was removed, and the gel was soaked in ethanol for aging. After 24 hours, the ethanol solvent was replaced by hexane. The hexane was refreshed every 24 hours for three days. Finally, the gel was dried at room temperature for 24 hours. After which the gel was transferred to an oven for 8 hours at 60 °C, after which the temperature was increase to 100 °C for a further 2 hours, see Figure 2. 4.

7.3 Results and discussion

Many technologies such as absorption, desorption, chemical looping combustion, membrane separation, hydrate-based separation and cryogenic distillation have been developed to isolate CO_2 from flue gas streams (Leung *et al.*, 2014). Another promising CCSU technology is removing the CO_2 by utilizing the CO_2 hydration reaction. However, in the absence of a catalyst the reaction is slow. A known catalyst for this reaction is carbonic anhydrase. The study of carbonic anhydrase led to the development of bio-inspired metal based catalysts to convert CO_2 into other chemical compounds such as the reduction of CO_2 into methanol or producing cyclic carbonates via coupling with oxiranes (Bandeira *et al.*, 2015). Šiller and Bhaduri at Newcastle University (UK) discovered experimentally that nickel nanoparticles (NiNPs) are inorganic heterogeneous catalysts which catalyses the CHR. (Bhaduri and Siller, 2013; Siller and Bahduri,

2013) proposed mechanism of CHR, in presence of NiNPs in the aqueous phase involves the formation of hydroxyl groups on the surface of NiNPs, which are then converted to bicarbonate groups through the nucleophilic attack of $CO_{2\,(aq)}$ molecules. Subsequently, bicarbonate ions are displaced by H_2O molecules which then dissociate, giving their proton to the solvent, whilst the remaining hydroxyl group forms on the surface of NiNPs (Bhaduri and Siller, 2013; Siller and Bahduri, 2013). In order to improve handling of NiNPs catalysts for potential scale up applications, it has been suggested a use of magnetic separator for recycle and reuse of NiNPs for CHR (Bhaduri and Siller, 2013) or NiNPs can be immobilised on mesoporous silica (SiO_2) aerogels (Han *et al.*, 2015). Often the difference in surface area and surface structure, due to different dimensionality of nanomaterials, could also affect their catalytic activity. Here, we study the difference in catalytic activity for CHR in a vapour phase when two different forms of nickel nanomaterials (NiNPs and NiNWs) are immobilised in silica aerogels, which has not been studied previously, as it was only known to enhance catalytic activity of NiNPs for CHR in aqueous solutions (Bhaduri *et al.*, 2015). The catalytic activity in a vapour phase by the co-sorption at high concentration levels of CO_2 and water was studied by adsorption-desorption kinetics and isotherms with a dynamic vapour sorption analyser (DVS Vacuum).

TEM images (see,

Figure 7. 1) show the wavy shape of the NiNWs, which are similar to that reported by Chen *et al.* (2015b). Wavy NiNWs have a non-uniform diameter (with the mean diameter ~ 400 nm) and ~4μm in length.

Figure 7. 1 c-d show the TEM images of NiNPs. The diameter of NiNPs in

Figure 7. 1d is ~ 125 nm. Where TEM images (e) and (f) in

Figure 7. 1 show the porous structure of 700 ppm NiNWs-silica aerogels composite. The photo images of NiNWs-SiO_2 aerogels composites (at 400, 500 and 700 ppm) are presented in Figure 7. 2b.

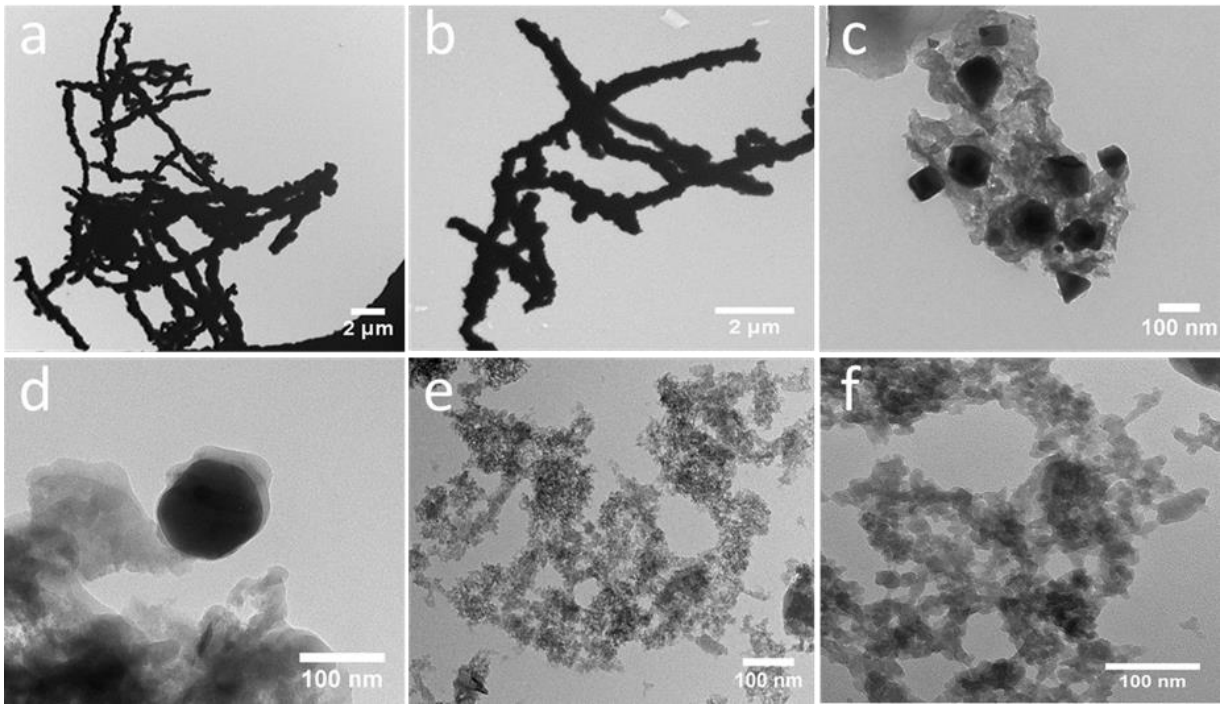

Figure 7. 1. Transmission electron microscopy (TEM) images, (a) and (b) of NiNWs, (c) and (d) are TEM images of NiNPs, (e) and (f) are TEM images of NiNWs-silica aerogels (sample N3).

Table 7. 1. Surface area and pore size and pore volume properties of NiNWs, NiNPs composites and NiNWs composites (pure nickel nanowires (N0), pure silica aerogel (S), 700 ppm of nickel nanoparticles in silica aerogel (Np), 400 ppm of nickel nanowires in silica aerogel (N1), 500 ppm of nickel nanowires in silica aerogel (N2) and 700 ppm of nickel nanowires in silica aerogel (N3).

Sample	NiNWs wt. %	NiNPs wt. %	Surface area (m^2/g) [± 5 m^2 g^{-1}]	Pore specific volume (cm^3/g) [± 0.02 cm^3 g^{-1}]	Average diameter (nm) [± 0.2 nm]
N0	100	-	9.3	-	-
S	-	-	509	1.48	17.3
Np	-	3.25	515	1.61	11.6
N1	0.5	-	421	1.8	30.16
N2	0.6	-	410	1.54	25.6
N3	1.25	-	470	1.22	23.64

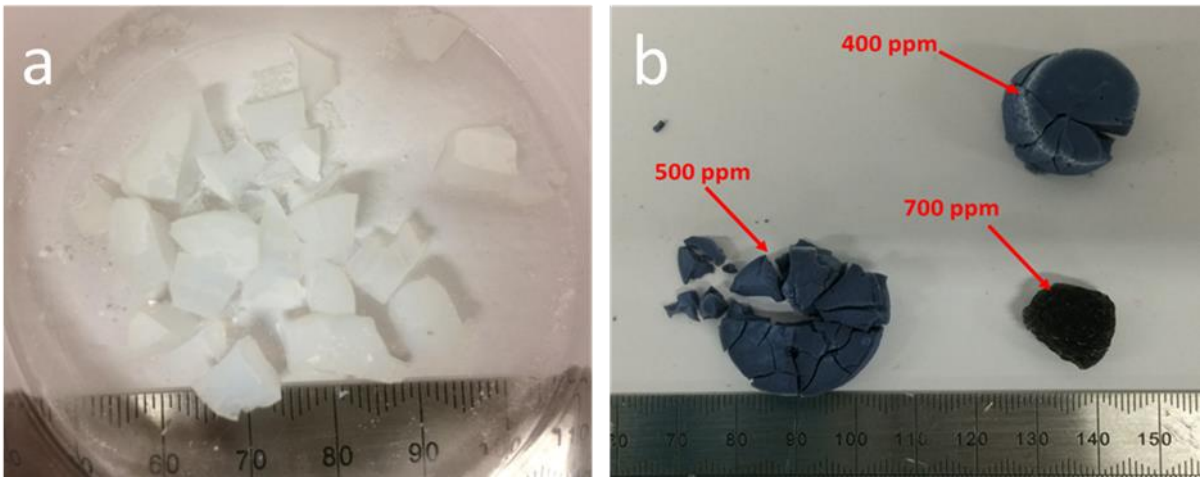

Figure 7. 2. (a) SiO_2 aerogels (b) Nickel nanowires (NiNWs) immobilised on SiO_2 aerogels synthesised with different nanowires concentrations.

The N_2 adsorption- desorption isotherm of pure NiNWs is shown in Figure 7. 3. The surface area of NiNWs was 9.3 m^2/g. N_2 adsorption - desorption isotherms of silica aerogels and NiNWs-SiO_2 aerogel composites (see, Figure 7. 4) show a type IV of isotherms and hysteresis loops of H1 type. According to IUPAC classification, a type IV isotherm indicates a mesoporous structure and H1 hysteresis loops are characteristic of materials that exhibit a narrow range of uniform mesopores (Sing *et al.*, 1985; Thommes *et al.*, 2015).

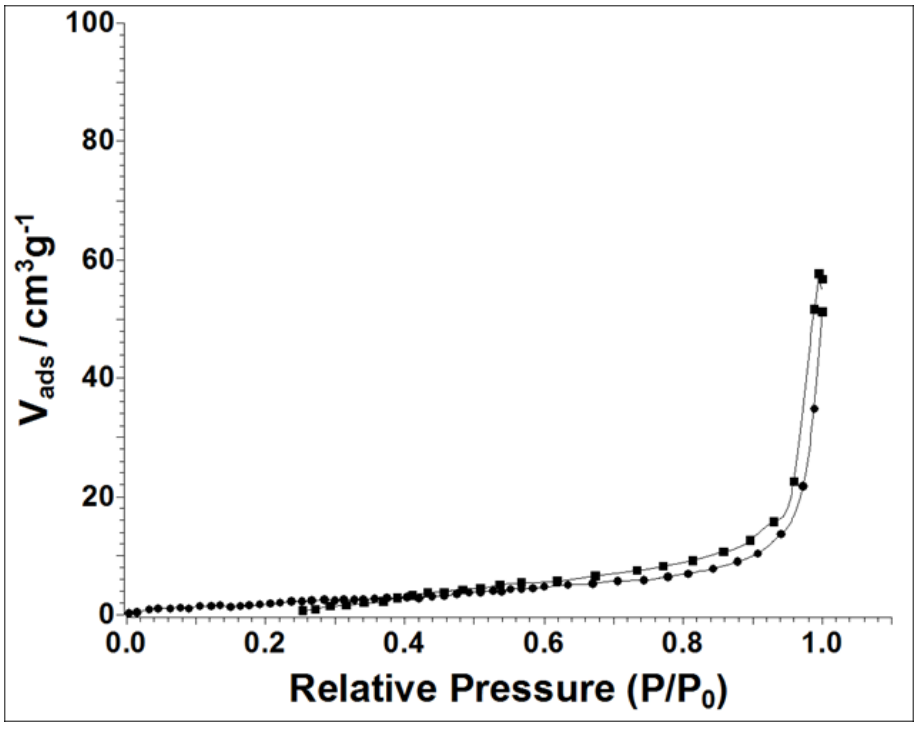

Figure 7. 3. Nitrogen adsorption–desorption isotherm of pure NiNWs, sample N0.

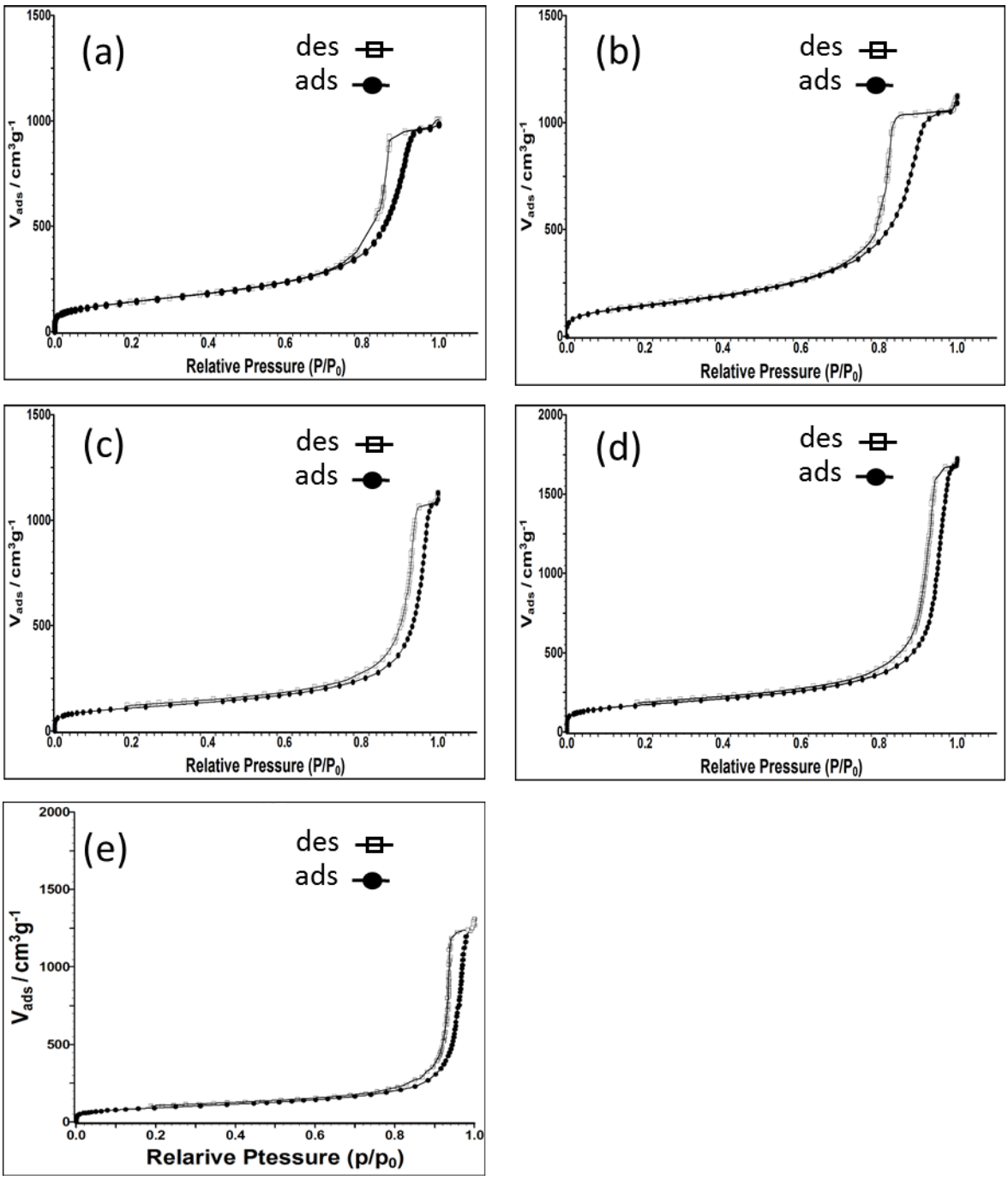

Figure 7. 4. Nitrogen adsorption–desorption isotherms, (a) pure silica aerogel (S), (b) 700 ppm of nickel nanoparticles in silica aerogel (Np), (c) 400 ppm of nickel nanowires in silica aerogel (N1), (d) 500 ppm of nickel nanowires in silica aerogel (N2) and (e) 700 ppm of nickel nanowires in silica aerogel (N3).

A summary of the surface area, pore volume and pore diameter data are listed in Table 7. 1. SiO_2 aerogel alone has a surface area of 509 m^2/g. While, the surface area for the 400 ppm, 500 ppm and 700 ppm NiNWs-SiO_2 aerogel composites were found to be 421 m^2/g, 410 m^2/g and 470 m^2/g, respectively. The pore size distribution curves are shown in Figure 7. 5. These are determined from N_2 desorption isotherms presented in Figure 7. 4 by The BHJ method. Most samples have mesoporous diameters with a broad pore size distribution. In addition, the pore

volume (see Table 7. 1) decreases with an increase of the NiNWs concentration inside silica aerogels. As expected, the pore specific volume for NiNWs in silica aerogel (N3) is smaller than that for NiNPs in silica aerogels (Np) (see Table 7. 1).

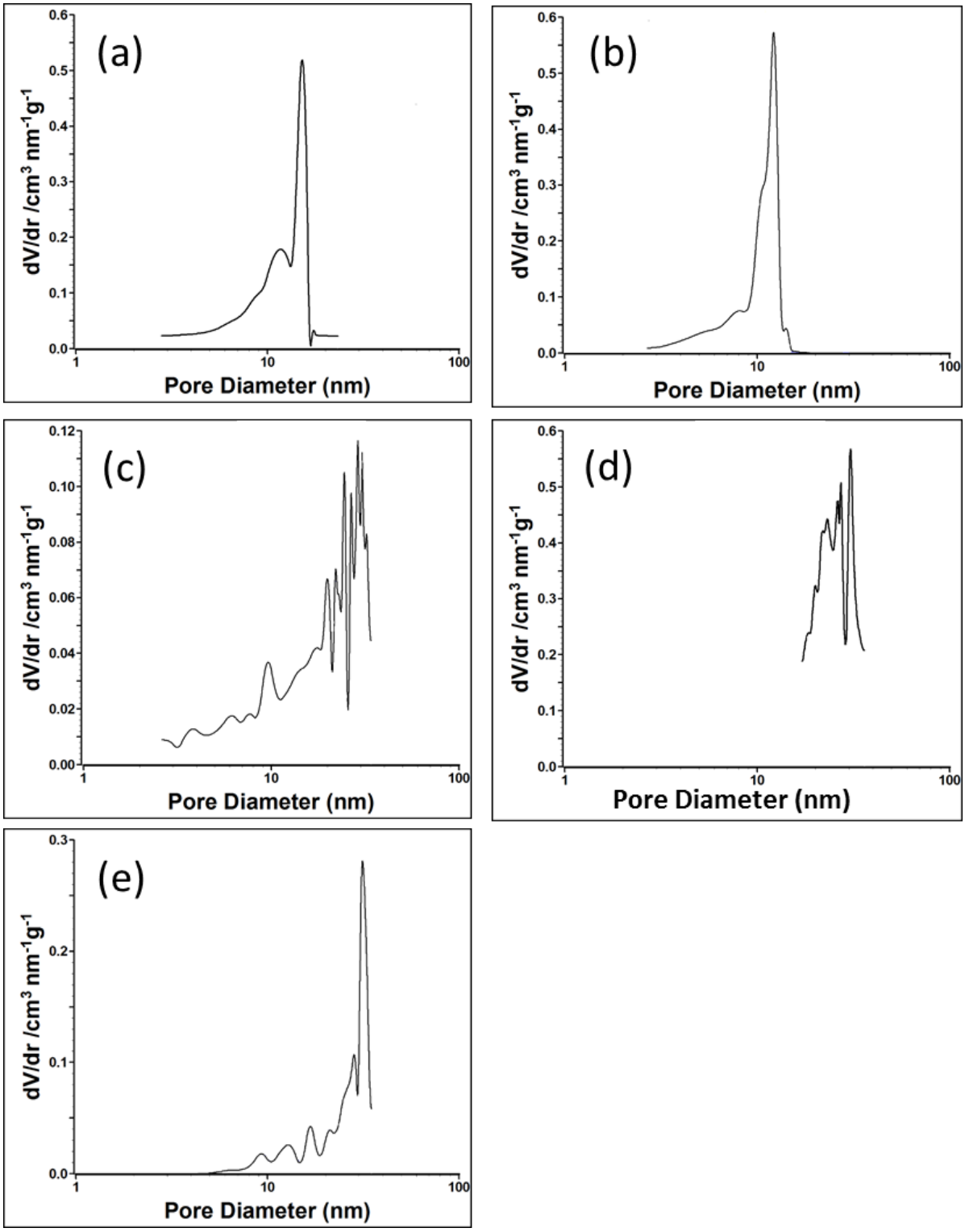

Figure 7. 5. Barrett–Joyner–Halenda (BJH) method of pore size distribution, (a) pure silica aerogel (S), (b) 700 ppm of nickel nanoparticles in silica aerogel (Np), (c) 400 ppm of nickel nanowires in silica aerogel (N1), (d) 500 ppm of nickel nanowires in silica aerogel (N2) and (e) 700 ppm of nickel nanowires in silica aerogel (N3).

Figure 7. 6 shows XRD patterns from NiNWs and NiNWs-SiO_2 aerogel composites. The border peak around 2θ = 20° in Figure 7. 6 is for amorphous silica (Amiri and Moghaddas, 2015). The three characteristic peaks observed at 2θ = 44.58°, 51.9° and 76.5° corresponds to the nickel with Miller indices (111), (200), and (220), respectively, indicating the pure face centre cube structure (fcc) of the NiNWs (Wang *et al.*, 2010). No other peaks suggesting oxidisation were recorded which means a high purity of synthesis take place (Wang *et al.*, 2010). The XRD pattern of NiNWs immobilised in silica aerogels was also observed in Figure 7. 6. The quantification of NiNWs and NiNPs weight percentages (wt. %) in silica aerogels are presented in Table 7. 1.

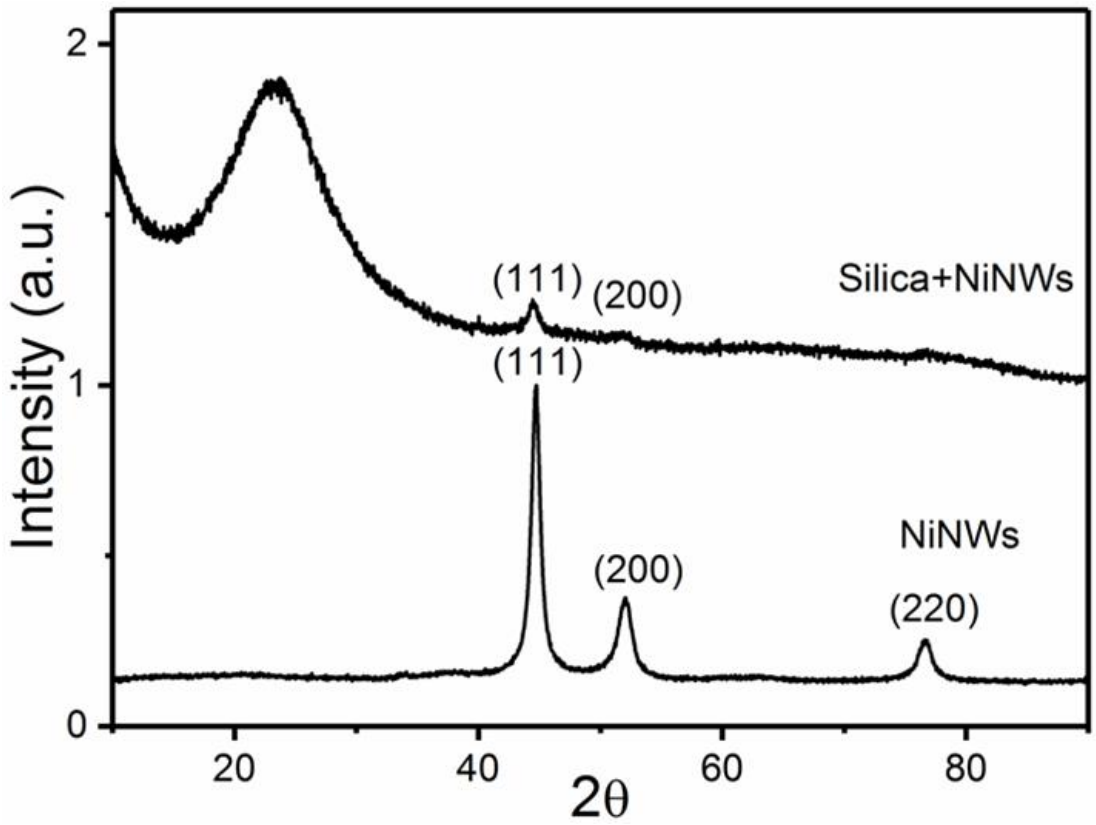

Figure 7. 6. X-ray diffraction (XRD) patterns of pure NiNWs and immobilised NiNWs on SiO_2 aerogels.

SEM images of NiNWs-SiO_2 aerogel composites (Figure 7. 7 a-f) confirm the mesoporous nature of the support as obtained by the BHJ analysis (Figure 7. 5). An estimation of the pore diameters from SEM images show that the majority of the pore diameters are in the range between 20-40 nm. However, some macropores (>50 nm) are observed for N3 sample. The presence of macropores in porous materials enhances the diffusion of gases through pores and therefore enhances CO_2 capture (Zelenak *et al.*, 2008; Drese *et al.*, 2009).

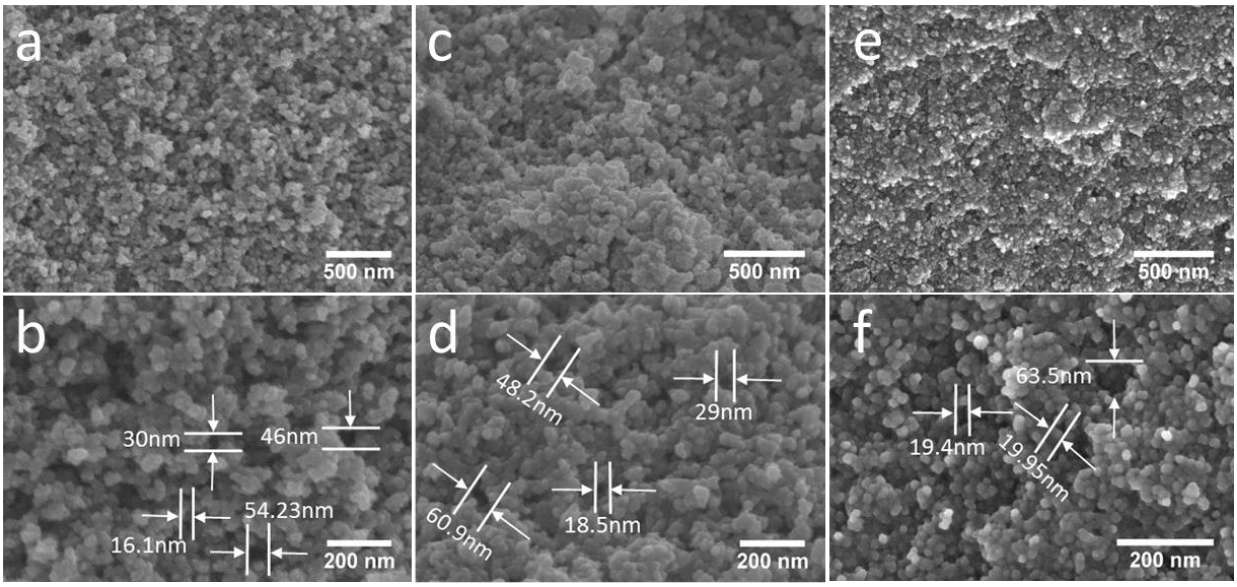

Figure 7. 7. SEM images at different magnifications and different concentrations of NiNWs immobilised on SiO_2 aerogels. (a and b) SEM images for N1, (c and d) SEM images for N2 and (e and f) SEM images for N3. (Denotation: 400 ppm of nickel nanowires in silica aerogel (N1), 500 ppm of nickel nanowires in silica aerogel (N2) and 700 ppm of nickel nanowires in silica aerogel (N3).

CO_2 dissolution

Figure 7. 8 shows CO_2 dissolution in DI water and in NiNWs suspensions. We plot the average values of the increase in saturation concentration of CO_2 dissolved in DI water and with suspended NiNWs in DI water as a function of the concentration of nanowires, taken at room temperature and atmospheric pressure. The maximum uptake of CO_2 is at NiNWs concentration of ~ 30 ppm. The amount of CO_2 dissolved in water without NiNWs was similar to that reported in literature (~39 mM) (Favre *et al.*, 2009). Therefore, further pH change analysis was performed in suspensions with a NiNWs concentration of ~30 ppm.

Catalytic and non-catalytic CHR

Figure 7. 8 shows pH changes during the bubbling of carbon dioxide through DI water, including silica aerogel supported or freely suspended NiNWs catalyst in a fluidized bed reactor. All experiments are taken at room temperature and atmospheric pressure. DI water was used as a control to observe the effectiveness of the catalysts towards the CHR. Silica aerogels alone do not catalyse the CHR (see grey and blue curves in Figure 7. 8). The three supported catalysts at different NiNWs concentration (N1, N2 and N3, see Table 7. 1) all show catalytic activity for CHR; however, they are less effective when compared to freely suspended NiNWs. We

observe enhancement in catalytic activity of NiNWs-SiO_2 aerogel composites as a function of NiNWs concentration i.e. $N_1<N_2<N_3$. This is due to CO_2's mass transfer limitations created by the small size of the pores in silica aerogel. Another reason for the loss in activity could be due to a loss of active sites on NiNWs, as freely suspended NiNWs have higher active surface area than immobilised NiNWs in silica aerogels.

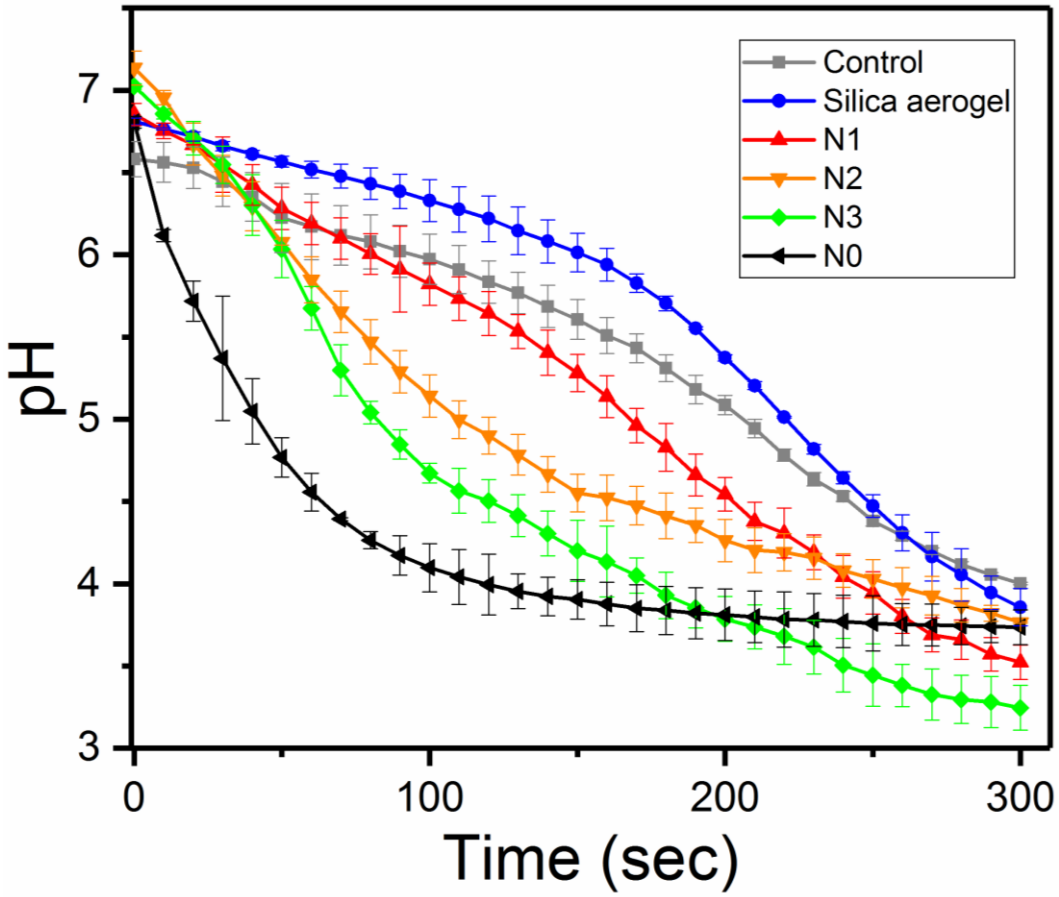

Figure 7. 8. pH changes during the bubbling of CO_2 through DI water (grey), NiNWs suspension (N0-black), SiO_2 aerogels suspension (blue), and Ni nanowire-SiO_2 aerogels composites at 400 ppm (N1-red), 500 ppm (N2-orange) and 700 ppm (N3-green). All experiments are performed at RT and atmospheric pressure.

Dynamic water vapour/CO_2 adsorption-desorption test

DVS was used to investigate catalytic activity of immobilised NiNWs on SiO_2 aerogels for CHR in vapour phase. The experiments were performed on 700 ppm NiNWs-SiO_2 aerogels, 700 ppm NiNPs-SiO_2 aerogels and pure SiO_2 aerogels at same experimental conditions. Adsorption-desorption curves were plotted based on mass equilibrium with time. Figure 7. 9 a-c show CO_2 uptake cycles of SiO_2 aerogels, 700 ppm NiNPs-SiO_2 aerogels and 700 ppm NiNWs-SiO_2 aerogels composites at 25 °C, respectively. Adsorption-desorption cycles (red

line) are presented by changes in mass with time while the blue line represents the relative pressure changes with time.

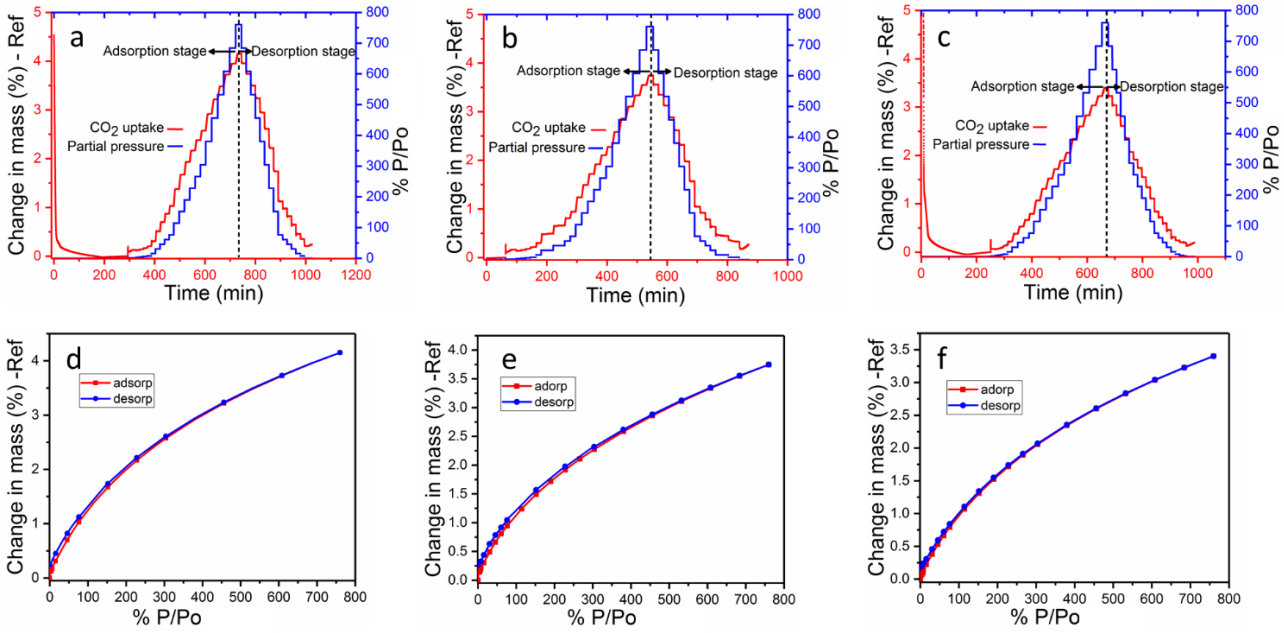

Figure 7. 9. Adsorption-desorption cycles and adsorption-desorption isotherms showing CO_2 sorption kinetics at 25 °C. (a) sorption kinetics for SiO_2 aerogels, (b) sorption kinetics for 700 ppm NiNPs-SiO_2 aerogel composites, (c) sorption kinetics for 700 ppm NiNWs-SiO_2 aerogel composites, (d) adsorption-desorption isotherm curves of SiO_2 aerogels, (e) adsorption-desorption isotherm curves of 700 ppm NiNPs-SiO_2 aerogel composites and (f) adsorption-desorption isotherm curves of 700 ppm NiNWs-SiO_2 aerogel composites.

All samples show the capability of CO_2 uptake. The adsorption capacities were 41.5 mg, 37.5 mg and 34 mg of CO_2 per gram of adsorbent at 25 °C for pure silica aerogels, NiNPs-SiO_2 aerogel composites and NiNWs-SiO_2 aerogel composites, respectively (see Table 7. 2). Pure silica aerogels exhibit a higher uptake capacity than NiNPs-SiO_2 and NiNWs-SiO_2 aerogel composites. However, the adsorption and desorption curves (Figure 7. 9 d-f) were almost identical meaning the process is approximately reversible (the desorption curve almost returns to same point as at the start of the analysis). Consequently, no hysteresis loops were associated with the adsorption-desorption isotherms indicating no tensile strength is applied to the pores (Al-Janabi *et al.*, 2015). Water vapour dynamic uptake curves (Figure 7. 10 a-c) of the investigated materials demonstrated a high interaction between water vapour molecules and the solid.

Table 7. 2. DVS adsorption capacity (Ads. C.) and retain mass (R.M.) of sorption gases

Sample	CO_2 Ads.C. mg/g	CO_2 R.M. mg/g	H_2O Ads.C. mg/g	H_2O R.M. mg/g	H_2O/CO_2 Ads.C. mg/g	H_2O/CO_2 R.M. mg/g
Silica aerogel	41.5	2.4	194.5	21	79.8	18
NiNWs	34	1.95	188	23	93	20
NiNPs	37.5	2.6	197.5	19.2	90	10

It is widely accepted that the water adsorption mechanism includes four steps; (1) water adsorption on surface functional groups; (2) formation of a cluster of water molecules through adsorption, due to the water molecules adsorbing on the previous adsorbed water molecules; (3) at a relative pressure (of approximately P/P_0=0.5) pore filling occurred and (4) when the pressure becomes high, the pores are completely filled and the plateau is reached (Brennan *et al.*, 2001; Chen *et al.*, 2015a). Relatively high-water vapour adsorption capacities at 25°C were recorded (194.5 mg, 197.5 mg and 188 mg of H_2O per gram of adsorbent, for pure silica aerogels, NiNPs-SiO_2 and NiNWs-SiO_2 aerogel composites, respectively; see Table 7. 2). Again, NiNWs-SiO_2 aerogel composites showed lower water adsorption capacity than pure silica aerogels or NiNPs-SiO_2 aerogel composites. It is likely that hydroxyl groups at SiO_2 aerogel surfaces via H-bonding interact with water vapour molecules and work as adsorption sites (Wei *et al.*, 2013). The formation of hysteresis loops (see Figure 7. 10 d-f) are due to capillary condensation and the formation of irreversible hydrate (capillary condensation is the dominated adsorption mechanism at high level of humidity loading (Li *et al.*, 2008)). The isotherms demonstrated as an open loop system (do not come back to zero) meaning some moisture is retained in the solid matrices. In particular, water is more strongly bonded to NiNWs-SiO_2 aerogel composites than NiNPs -SiO_2 aerogel composites. The retention mass for NiNWs was larger than for NiNPs, see column 4, Table 7. 2. Since NiNWs are wavy (see TEM images in

Figure 7. 1a-b), there is larger number of defect sites on step edges, which they will act as a stronger bonding sites for water molecules.

Comparing the uptake of CO_2 and water vapour for the different aerogel compositions, it was observed that NiNWs-SiO_2 aerogel composites show the highest uptake for water vapour when compared to CO_2 uptake (188/34=5.5 times higher). Figure 7. 11 shows the co-sorption cycles and isotherm behaviour for investigated samples at a gaseous volumetric mixture of 50/50 H_2O/CO_2. The desorption behaviour is similar to that observed for H_2O in Figure 7. 10.

Isotherms have an open loop hysteresis and samples retain liquids (see Table 7. 2, 6th column). Since there is a high level of humidity and CO_2 during loading, water vapour could condense and form carbonic acid (Li *et al.*, 2008).

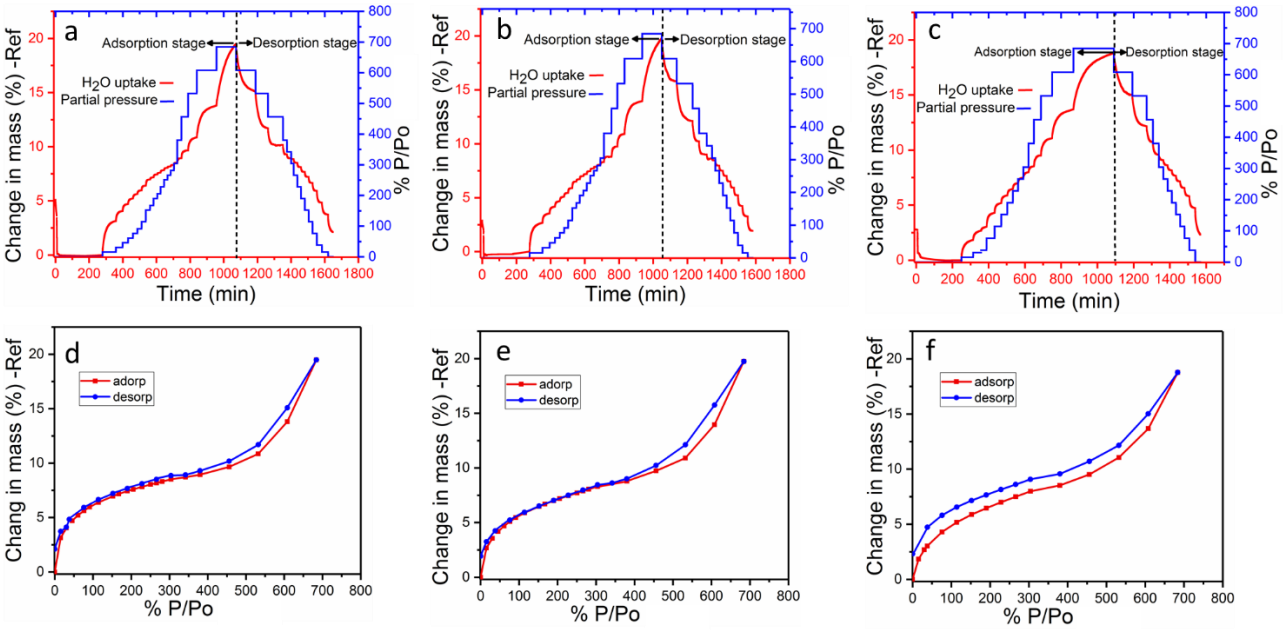

Figure 7. 10. Adsorption-desorption cycles and adsorption-desorption isotherms showing H_2O vapour sorption kinetics at 25 °C. (a) sorption kinetics for SiO_2 aerogels, (b) sorption kinetics for 700 ppm NiNPs-SiO_2 aerogel composites, (c) sorption kinetics for 700 ppm NiNWs-SiO_2 aerogel composites, (d) adsorption-desorption isotherm curves of SiO_2 aerogels, (e) adsorption-desorption isotherm curves of 700 ppm NiNPs-SiO_2 aerogel composites and (f) adsorption-desorption isotherm curves of 700 ppm NiNWs-SiO_2 aerogel composites.

NiNWs-SiO_2 aerogel composite (93 mg of H_2O/CO_2 /g-adsorbent) and NiNPs-SiO_2 aerogel composite (90 mg of H_2O/CO_2 /g-adsorbent) exhibited higher adsorption capacity than pure silica aerogels (79.8 mg of H_2O/CO_2 /g-adsorbent), see the 5th number column in Table 7. 2.

The slopes of the linear part of the adsorption curves in Figure 7. 12, the adsorption parts, for silica aerogel, NiNPs-silica aerogel composites and NiNWs silica aerogel composites are 0.088, 01196 and 0.105, respectively. This change could be or due to different catalytic activities or due to different pore size diameters that could influence the flow rate of vapour through material. However, we see in Table 7. 1 that the pore diameter of NiNWs – silica aerogel composites is much larger than for NiNPs – silica composites that can rule out this second possibility. In addition, because we have retention of water on NiNWs silica aerogel samples much larger than on NiNPs silica aerogels, this implies that the bonding of water molecules is stronger. Therefore, the changes in slope are due to changes in catalytic activities of NiNPs and NiNWs trapped in silica aerogels. The catalytic activity towards CO_2-H_2O co-adsorption is fastest on NiNPs-silica

aerogel composites, followed by NiNWs-silica aerogel composite and then followed by silica aerogels.

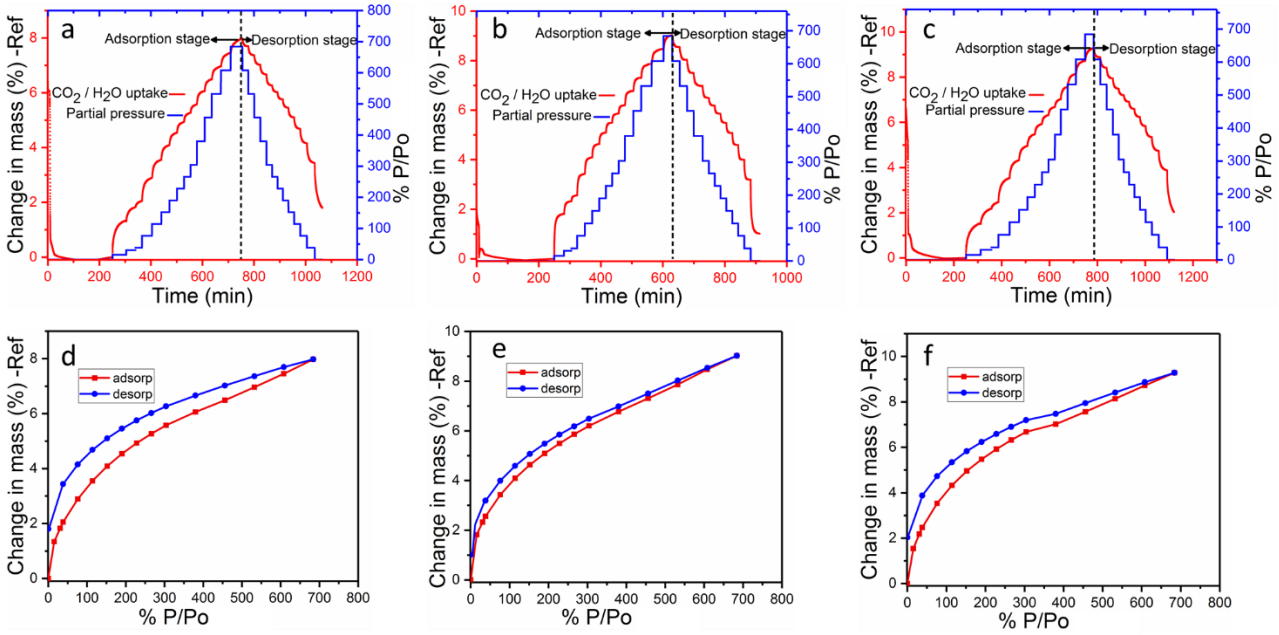

Figure 7. 11. Adsorption-desorption cycles and adsorption-desorption isotherm curves showing 50/50 H_2O/CO_2 sorption kinetics at 25 °C. (a) sorption kinetics for SiO_2 aerogels, (b) sorption kinetics for 700 ppm NiNPs-SiO_2 aerogel composites, (c) sorption kinetics for 700 ppm NiNWs-SiO_2 aerogel composites, (d) adsorption-desorption isotherm curves of SiO_2 aerogels, (e) adsorption-desorption isotherm curves of 700 ppm NiNPs-SiO_2 aerogel composites and (f) adsorption-desorption isotherm curves of 700 ppm NiNWs-SiO_2 aerogel composites.

The mechanism of adsorption-desorption of H_2O/CO_2 vapour mixture on Ni nanowires could be similar to previous experimental (Bhaduri and Siller, 2013; Siller and Bahduri, 2013) and theoretical work (Verma *et al.*, 2016) on NiNPs . Adsorption of CO_2 and H_2O molecules in the liquid phase are energetically favourable at Ni surface when compared to the gas phase (Verma *et al.*, 2016; Xu *et al.*, 2016). The adsorption free energy of H_2O complex that is formed on the Ni surface was found to decrease from 9.95 kcal/mol in vacuum to 5.4 kcal/mol in solvent state (Verma *et al.*, 2016). This H_2O dissociates into OH and H groups on the surface of the Ni cluster, with the activation barrier for deprotonation found to be lower in solvent state than in a vacuum (Verma *et al.*, 2016). When CO_2 molecules react with the surface of Ni, a bent intermediate $CO_2^{\delta-}$ is formed and this transformation from a linear to a bent structure is associated with a significant reduction in the activation energy barrier (Ding *et al.*, 2007). When adsorbed CO_2 molecules interact with hydroxyl groups to form a bent OH—CO_2 complex, the oxygen atom of the hydroxyl group can lose a proton to a CO_2 oxygen atom forming a Ni—HCO_3^-complex. As mentioned, due to high capillary condensation, water vapour tends to be condensed in mesoporous SiO_2 aerogels forming a liquid phase. The HCO_3^-complex would be released from

the surface of Ni either by another water vapour molecule or directly dissolved in the generated water phase.

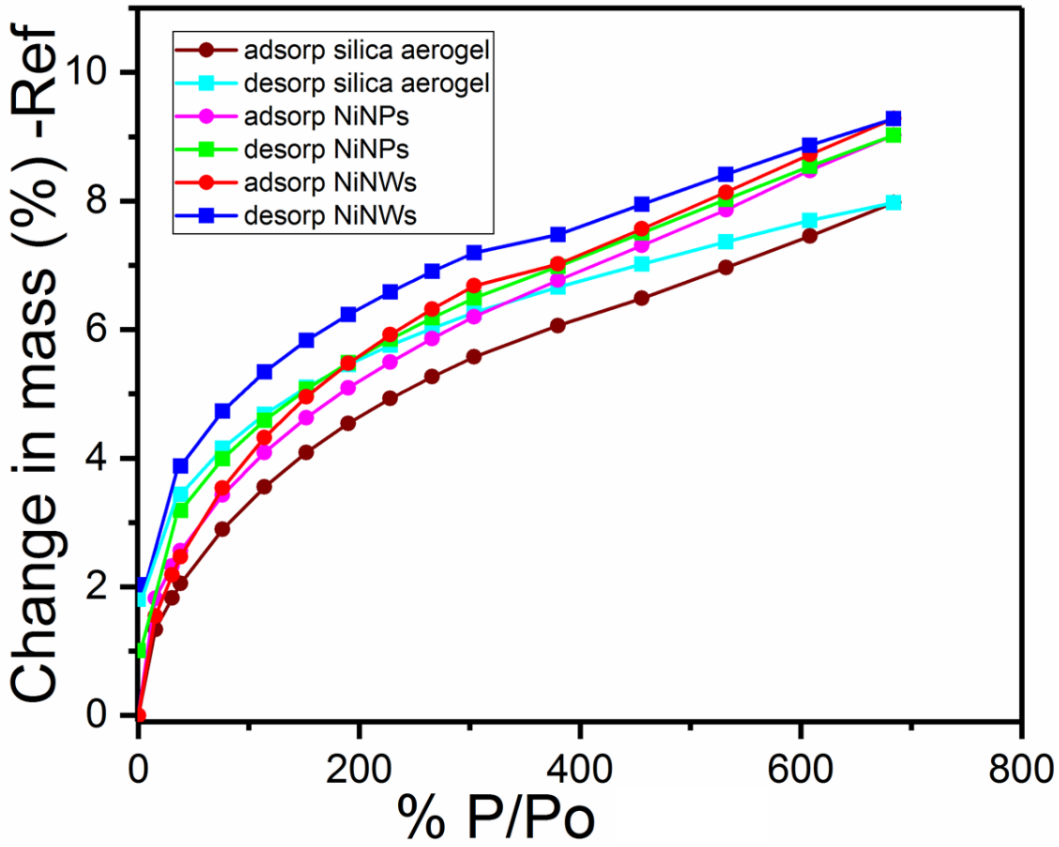

Figure 7. 12. Comparison of 50/50 H_2O/CO_2 adsorption (ads) and desorption isotherms (des) for 700 ppm NiNPs-SiO_2 aerogel composites (ads is in pink and des is in green), for 700 NiNWs-SiO_2 aerogel composites (ads is in red and des is in blue) and pure silica aerogels (ads in brown and des in turquoise). Data are taken at 25 °C.

7.4 Conclusion

The results of the catalytic activity analysis of wavy NiNWs and immobilised wavy NiNWs on silica aerogels for CHR that performed in aqueous phase at room temperature exhibit enhancement in the rate of dissolution of carbon dioxide. The rate of carbon dioxide dissolution in presence of supported NiNWs increased with the increase NiNWs concentration. The best catalytic efficiency was seen when testing the NiNWs-SiO_2 aerogel composites with a concentration of 700ppm NiNWs. The thermos gravimetric results that were obtained from the DVS showed that utilising NiNWs as a heterogeneous catalyst promoted the catalytic activity for CHR, agreeing with the results found in the aqueous catalytic activity testing. However, NiNPs on aerogel support are found to be better catalysts towards CHR than NiNWs aerogel composites.

References

Al-Janabi, N., Hill, P., Torrente-Murciano, L., Garforth, A., Gorgojo, P., Siperstein, F. and Fan, X.L. (2015) 'Mapping the Cu-BTC metal-organic framework (HKUST-1) stability envelope in the presence of water vapour for CO_2 adsorption from flue gases', *Chem. Eng. J.* , 281, pp. 669-677.

Amiri, T.Y. and Moghaddas, J. (2015) 'Cogeled copper-silica aerogel as a catalyst in hydrogen production from methanol steam reforming', *International Journal of Hydrogen Energy*, 40(3), pp. 1472-1480.

Bandeira, N.A.G., Garai, S., Muller, A. and Bo, C. (2015) 'The mechanism of CO_2 hydration: a porous metal oxide nanocapsule catalyst can mimic the biological carbonic anhydrase role', *Chemical Communications*, 51(85), pp. 15596-15599.

Bhaduri, G.A., Alamiry, M.A.H. and Siller, L. (2015) 'Nickel nanoparticles for enhancing carbon capture', *Journal of Nanomaterials*, p. 13.

Bhaduri, G.A. and Siller, L. (2013) 'Nickel nanoparticles catalyse reversible hydration of carbon dioxide for mineralization carbon capture and storage', *Catal. Sci. Technol.*, 3(5), pp. 1234-1239.

Brennan, J.K., Bandosz, T.J., Thomson, K.T. and Gubbins, K.E. (2001) 'Water in porous carbons', *Colloids Surf. A*, 187, pp. 539–568.

Chen, H.Y., Wang, W.L., Wei, X.L., Ding, J. and Yang, J.P. (2015a) 'Experimental and numerical study on water sorption over modified mesoporous silica', *Adsorption-Journal of the International Adsorption Society*, 21(1-2), pp. 67-75.

Chen, L., Fang, M.L., Liu, C.Z., Liu, X.C. and Xing, S.X. (2015b) 'Manipulating the nickel shape and catalytic performance: from spheres to chains to urchins', *Crystengcomm*, 17(47), pp. 4343-4348.

Ding, X., Pagan, V., Peressi, M. and Ancilotto, F. (2007) 'Modeling adsorption of CO_2 on Ni(110) surface', *Materials Science & Engineering C-Biomimetic and Supramolecular Systems*, 27(5-8), pp. 1355-1359.

Drese, J.H., Choi, S., Lively, R.P., Koros, W.J., Fauth, D.J., Gray, M.L. and Jones, C.W. (2009) 'Synthesis-structure-property relationships for hyperbranched aminosilica CO_2 adsorbents', *Advanced Functional Materials*, 19(23), pp. 3821-3832.

Favre, N., Christ, M.L. and Pierre, A.C. (2009) 'Biocatalytic capture of CO_2 with carbonic anhydrase and its transformation to solid carbonate', *Journal of Molecular Catalysis B-Enzymatic*, 60(3-4), pp. 163-170.

Han, X., Williamson, F., Bhaduri, G.A., Harvey, A. and Šiller, L. (2015) 'Synthesis and characterisation of ambient pressure dried composites of silica aerogel matrix and embedded nickel nanoparticles', *J. Supercrit. Fluids* 106, pp. 140-144.

Leung, D.Y.C., Caramanna, G. and Maroto-Valer, M.M. (2014) 'An overview of current status of carbon dioxide capture and storage technologies', *Renewable & Sustainable Energy Reviews*, 39, pp. 426-443.

Li, G., Xiao, P., Webley, P., Zhang, J., Singh, R. and Marshall, M. (2008) 'Capture of CO_2 from high humidity flue gas by vacuum swing adsorption with zeolite 13X', *Chem. Eng. Sci.*, 14, pp. 415-422.

Siller, L. and Bahduri, G.A. (2013) *Carbon capture*. GB132038.2 WO2013/171480 (A2).

Sing, K.S.W., Everett, D.H., Haul, R.A.W., Moscou, L., Pierotti, R.A., Rouquerol, J. and Siemieniewska, T. (1985) ' Reporting physisorption data for gas solid systems with special reference to the determination of surface-area and porosity (recommendations 1984)', *Pure and Applied Chemistry*, 57(4), pp. 603-619.

Thommes, M., Kaneko, K., Neimark, A.V., Olivier, J.P., Rodriguez-Reinoso, F., Rouquerol, J. and Sing, K.S.W. (2015) 'Physisorption of gases, with special reference to the evaluation of surface area and pore size distribution (IUPAC Technical Report)', *Pure and Applied Chemistry*, 87(9-10), pp. 1051-1069.

Verma, M., Kumar, K.B.S. and Deshpande, P.A. (2016) 'Computational insights into the activity of transition metals for biomimetic CO_2 hydration', *J. Phys. Chem. C*, 120(10), pp. 5577-5584.

Wang, J., Zhang, L.Y., Liu, P., Lan, T.M., Zhang, J., Wei, L.M., Kong, E.S.W., Jiang, C.H. and Zhang, Y.F. (2010) 'Preparation and growth mechanism of nickel nanowires under applied magnetic field', *Nano-Micro Letters*, 2, pp. 134-138.

Wei, X.L., Wang, W.L., Xiao, J., Zhang, L., Chen, H.Y. and Ding, J. (2013) 'Hierarchically porous aluminosilicates as the water vapor adsorbents for dehumidification', *Chem. Eng. J.* , 228, pp. 1133-1139.

Xu, H., Chu, W., Sun, W.J., Jiang, C.F. and Liu, Z.Q. (2016) 'DFT studies of Ni cluster on graphene surface: effect of CO_2 activation', *RSC Advances*, 6(99), pp. 96545-96553.

Zelenak, V., Badanicova, M., Halamova, D., Cejka, J., Zukal, A., Murafa, N. and Goerigk, G. (2008) 'Amine-modified ordered mesoporous silica: Effect of pore size on carbon dioxide capture', *Chem. Eng. J.* , 144(2), pp. 336-342.

Chapter 8 Conclusions and Future Work

This chapter summarize the conclusion of results of the work which is carried out in this thesis and suggests the areas that could be investigated in future.

8.1 Thesis conclusion

This thesis reports on investigations of the capability of bicarbonate ambient pressure drying approach to synthesise aerogels from different precursors. In addition, this thesis presents synthesis of efficient low-cost superinsulation silica aerogel composites and silica aerogel composites for CO_2 capture applications.

In chapter 3 of this thesis, bicarbonate ambient pressure drying approach is used to synthesise low cost silica aerogel thermal insulation materials. Ceramic blankets and ceramic short fibres are used for the reinforcement. The synthesised composites exhibit reasonable mechanical and thermal properties. Incorporation of 34 wt. % of silica aerogels in ceramic blankets reduces the thermal conductivity from 0.048 to 0.038 W/m K. While reinforcement with short ceramic fibres improves mechanical properties by tenfold of that for pure silica aerogels and produces thermal insulators with thermal conductivities of 0.019-0.028 W/m K.

Chapter 4 presents synthesis of silica aerogels from water glass precursor by using the bicarbonate approach (Han and Šiller, 2015). The salt free silica aerogels are synthesised by two ways depending on whether using or not the ion exchange method in order to remove Na^+ ions from silica sol. Using the ion exchange method during synthesis, it produced silica aerogels with surface area of 703 m^2g^{-1} when compared with 526 m^2g^{-1} when the water glass-based silica aerogels are carried out without using of the ion exchange method. The lowest thermal conductivity of the highest surface area sample is 0.016 W/m K.

Chapter 5 presents synthesis of alumina-based aerogels (dawsonite - sodium aluminium carbonate hydroxide) from an aluminium sec-butoxide precursor (ASB) by using the bicarbonate ambient drying pressure approach. The as-synthesised dawsonite aerogel has a mesoporous structure and a surface area of 350 m^2 g^{-1} with an average pore diameter of 5.7 nm and pore specific volume of 0.54 cm^3 g^{-1}.

In chapter 6, we present a bio-inspired synthesis of multi-layered silica aerogels to mimic the structure and thickness of the wings of the damselfly. This has led to synthesis of multi-layered silica aerogel films of thickness of 0.3 mm. Silica aerogel films show a high surface area and a porous structure. Layering of the silica aerogel structure increased the aerogel durability.

The catalytic activities for CO_2 hydration reaction (CHR) in gaseous phase of pure SiO_2 aerogels, NiNPs- SiO_2 composites and NiNWs-SiO_2 aerogels composites are investigated in chapter 7 by using the dynamic vapour sorption (DVS) technique. The analysis was performed with 50% CO_2 and 50% H_2O vapour. The thermo gravimetric results that are obtained from DVS showed that utilising the NiNWs as a heterogeneous catalyst, it promoted the catalytic activity for CHR. However, NiNPs-aerogel support is found to be a better catalyst towards CHR than NiNWs aerogel composites.

8.2 Future work

8.2.1 Epoxy-silica aerogel coatings

Nowadays, construction industries focus on the improvement of the energy savings. A number of research is dedicated on developing efficient thermal insulation properties of insulation materials and coatings in order to lower the space-cooling load. A great effort is conducted on producing thermal insulator paints that have a low thickness and a high efficiency in order to improve the thermal insulation of the roofs and ceilings of buildings. For example, epoxy resins are widely used as protective coatings in buildings and in many different applications because of their excellent adhesion, mechanical properties and chemical resistance in a different media (Akbarzade *et al.*, 2017). Introducing the micro- or nano-structural materials with excellent thermal properties into conventional adhesives lowers their thermal conductivities. Silica aerogels are the most promising inorganic additives that could be mixed with adhesives because of their excellent physical properties such as low thermal conductivity (0.013-0.04 W/m K), low density (0.003-0.1 g/cm^3), high porosity (>99%) and a high specific surface area (500-1200 m^2/g) (Vahtrus *et al.*, 2017). Therefore, many studies were reported on mixing of hydrophobic aerogels with epoxy resin to improve the mechanical, thermal and hydrophobic properties of epoxy-silica aerogel composites (Ge *et al.*, 2009; Maghsoudi and Motahari, 2018). However, direct mixing of epoxy with silica aerogel powders does not provide a satisfactory low thermal conductivity composites unless aerogel pores are not impregnated with polymer resin from the beginning of fabrication process (Kim *et al.*, 2015b). Therefore, Kim *et al.* (2015a) proposed a preparation method to prevent epoxy resin from filling aerogel pores and to preserve aerogel pores in final composite by using ethanol evaporation.

The aim of the future work is to develop thermal insulation properties of epoxy coatings by getting the benefit of incorporating a proper amount of silica aerogels which is synthesis via new low cost and environmental ambient pressure approach that is developed at Newcastle

university (Han and Šiller, 2015). We propose to use toluene solvent rather than ethanol for pore preserving because it is expected that toluene will provide an additional time for finishing polymerisation of the resin before evaporating. In addition, the high boiling point for toluene comparing to ethanol gives flexibility to do fabrication process at higher temperature than that when ethanol is used in order to prevent filling pores. The preliminary thermal conductivity results of our proposition show promised results when compared to pure epoxy resin (see Table 8. 1).

Table 8. 1. Thermal conductivity of Epoxy-silica aerogel composites.

Material	Silica aerogel (Vol. %)	Thermal conductivity (W/m K)	Sample thickness (mm)
Epoxy	0	0.227	12
Epoxy-Silica aerogel	13.5	0.176	12
Epoxy-Silica aerogel	40	0.154	7
Epoxy-Silica aerogel	58	0.104	9

In brief, silica aerogel powders are mixed with toluene solvent to fill pores of silica aerogels. Then the wet silica aerogel powders are left for ~ 5 minutes to evaporate the excessive toluene solvent prior to mix under stirring with epoxy solvents at 50 °C. After which the mixture is poured in a cylindrical mould for the solidification. Figure 8. 1 shows as prepared samples with different volumetric ratios of silica aerogels. The future work could concentrate on synthesis of epoxy samples that contain silica aerogels with additives such as milled glass fibres, with aim to reduce the manufacturing costs, improve mechanical properties and to maintain the thermal insulation properties of the epoxy paint.

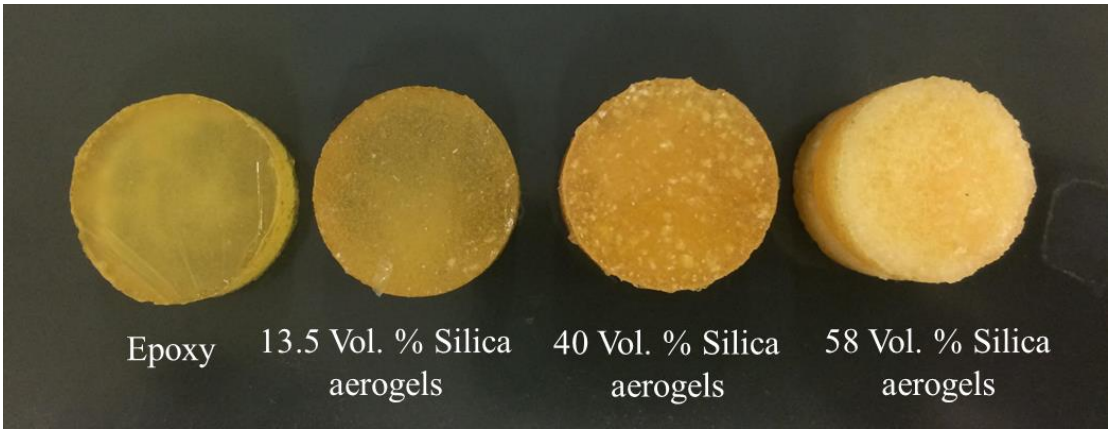

Figure 8. 1. Epoxy and silica aerogels-epoxy samples with a different volumetric ratio.

8.2.2 Amino-functionalisation of pure nickel nanoparticles-silica aerogels for CO_2 capture

The most effective technique to reduce emission of CO_2 is capturing of CO_2 emitted as a flue gas from power plants (Wang *et al.*, 2015). Amino-functionalised silica aerogels are widely investigated to be promising as excellent solid sorbents for CO_2 capture from a flue gas (Kong *et al.*, 2016; Chen *et al.*, 2017). The real flue gas contains a certain amount of water vapour (Wang *et al.*, 2015). The presence of water vapour can improve the CO_2 capture of solid amine sorbents (Huang *et al.*, 2003). Therefore, we propose here incorporation of nickel nanoparticles (NiNPs) with amine in post functionalised silica aerogel composites to investigate the catalytic activity of NiNPs toward the CO_2 capture. A preliminary study is carried out to amino-functionalised silica aerogels with NiNPs when immobilised on silica aerogels.

Synthesis of gels and the amine post-functionalisation of silica aerogel composites.

Synthesis of pure silica gels and immobilisation of nickel nanoparticles in silica gels were carried out as was described in chapter 2, section 2.1.5. Gels are then aged for 24 hours in ethanol before the amine functionalisation process. Synthesis of amine modified pure silica aerogels and NiNPs immobilised silica aerogels are carried out in the same way as it was reported by (Cui *et al.*, 2011). Briefly, after ageing of gels in ethanol for 24h, amine functionalisation is carried out by mixing 3-(Aminopropyl) triethoxysilane (AP) (≥98% Sigma-Aldrich) with ethanol with a volume ratio of (1:50 v/v) and the molar ratio of AP to TEOS was 1:2. Gels are then soaked in an AP/ethanol solution and stored for 6 days at 50 °C, for the AP functionalisation. After modification, the gels are washed with ethanol to remove unreacted AP and then ethanol solution was exchanged by the hexane. The hexane was refreshed every 24 h three times before drying the gels at room temperature and atmospheric pressure for 24 h, and then for 8h in oven at 60°C and finally at 100 °C for 2 h.

As the AP contains only one amine group, therefore longer organosilane groups of two or three amino groups could be further used to increase the efficiency of CO_2 capturing such as triethylenetetramine (TEPA) and polyethyleneimine (PEI). The preliminary experiments are carried out as follow: 5 g of methanol and 214 mg of PEI or TEPA are mixed at 50 °C. Then 497 mg of as prepared AP-silica aerogels (SA-AP) is soaked for 30 mins in the mixture at 50 °C then it is left for 20 hours before being washed with toluene and dried at room temperature for 24 hours. The aim of futher future work is to develop CO_2 solid sorbents by taking the advantages of the ability to functionalise silica aerogels with amine groups and at the same time, the catalytic activity of NiNPs for CO_2 in gaseous phase in presence of water vapour, as it has been concluded in this thesis. Therefore, the effect of amino-functionalising and immobilising

of NiNPs in silica aerogels for CO_2 separation and capture in presence of water vapour has been investigated by CO_2 adsorption isotherms at low partial pressure of CO_2 (see Figure 8. 2).

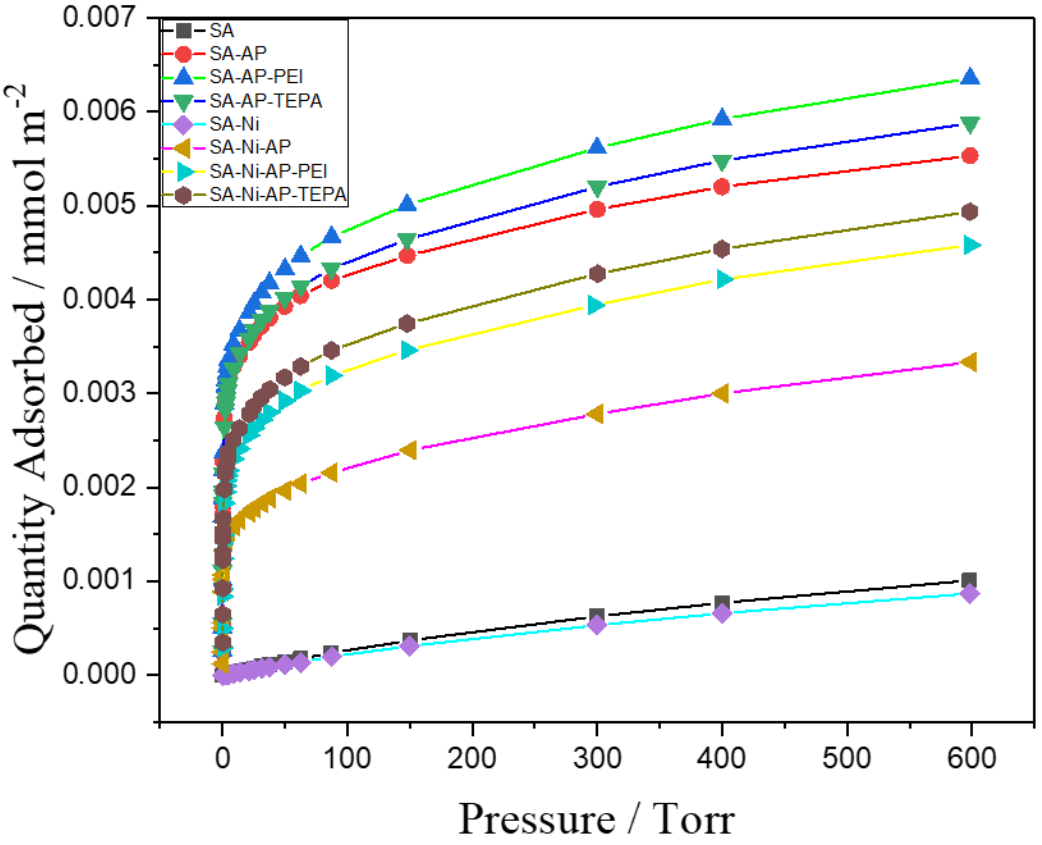

Figure 8. 2. CO_2 adsorption isotherms normalised for surface area of samples.

In addition, Raman spectra of samples are also recorded during CO_2 adsorption (see Figure 8. 3). Results of Figure 8. 2 and Figure 8. 3 reveal the increase of CO_2 adsorption capacity with the increase of amine functionalisation groups. However, presence of NiNPs in the samples show a slight decrease in CO_2 adsorption capacity (which is unexpected). However, in order to do a quantitative analysis, we need to measure the amount of amine groups in each sample, by using TGA technique before we draw a conclusion about NiNPs as additives to catalysis of the CO_2 adsorption. During preparation, AP may be reacted with NiNPs and consequently decreases the number of amine groups in aerogels compared to those samples with no NiNPs. Depending on TGA results, we could either further increase the percentage of amine functionalisation or use another loading mechanism such as functionalisation by co-condensation (Wormeyer *et al.*, 2012) by replacing 3-Aminopropyl) trimethoxysilane to the ammonia hydroxide (the catalyst used in the gelation). Further studies are needed to draw firm conclusions.

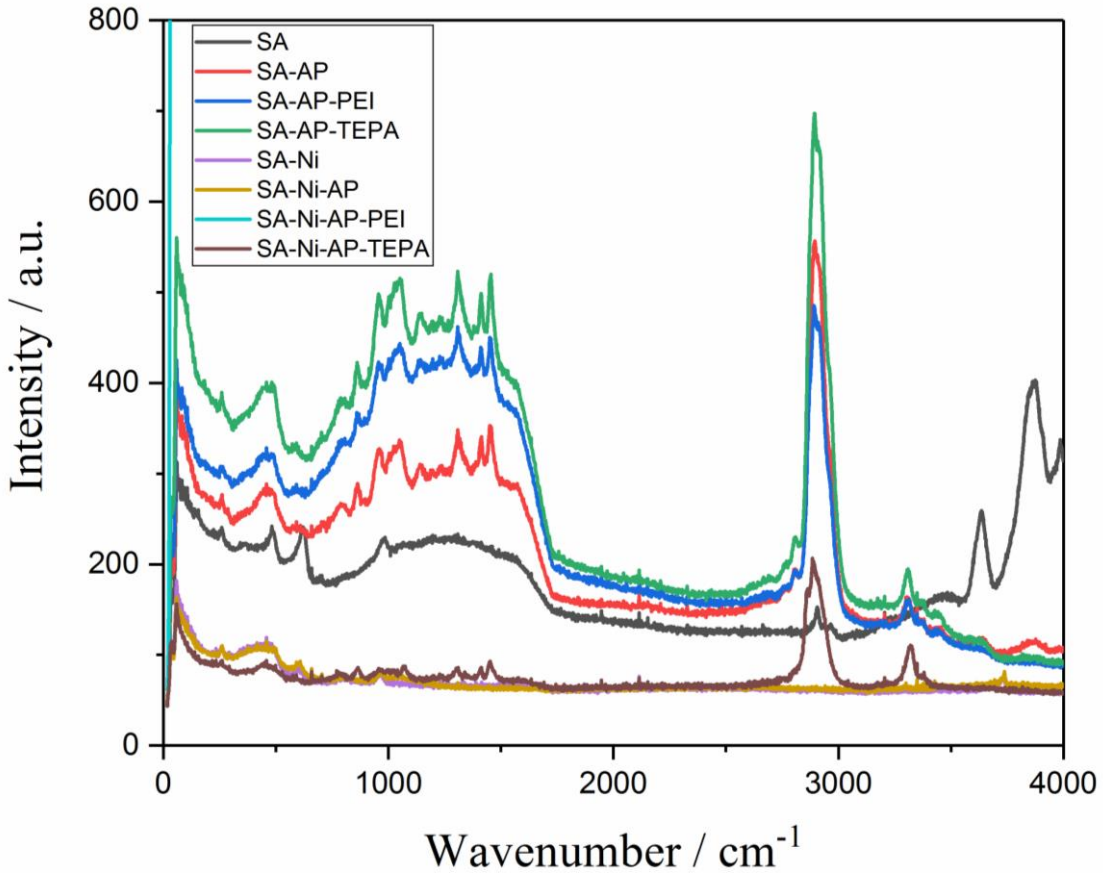

Figure 8. 3. Raman spectra of samples when follow CO_2 adsorption experiments above presented in Figure 8.2.

8.2.3 Graphene oxide encapsulated silica aerogels for metal ions remediation

Pollution of water by various toxic heavy metal ions and chemicals is a serious problem that affects people's health because of their toxicity and tendency to accumulate in human body (Yi *et al.*, 2018). Graphene oxide has been efficiently used either solely or with nanoparticles to remove the metal ions from the water (Salihi *et al.*, 2016; Wan *et al.*, 2018). Here as future work, we propose encapsulation of graphene oxide or graphene oxide-metal oxide nanoparticles (such as magnesium oxide nanoparticles) in silica aerogels for metal ions remediation such as Pb(II), Cd(II), Cu(II) Ni (II). The main aim of using silica aerogels is to support and to prevent accumulation of graphene oxide and nanoparticles. That will increase the sorption efficiency and help to recycle graphene oxide- metal oxide nanoparticles.

References

Akbarzade, K., Shishesaz, M.R., Danaee, I. and Zarei, D. (2017) 'The effect of nanoporous silica aerogel on corrosion protection properties of epoxy coatings on carbon steel', *Protection of Metals and Physical Chemistry of Surfaces*, 53(2), pp. 279-286.

Chen, C., Zhang, S., Row, K.H. and Ahn, W.S. (2017) 'Amine-silica composites for CO_2 capture: A short review', *Journal of Energy Chemistry*, 26(5), pp. 868-880.

Cui, S., Cheng, W.W., Shen, X.D., Fan, M.H., Russell, A., Wu, Z.W. and Yi, X.B. (2011) 'Mesoporous amine-modified SiO_2 aerogel: a potential CO_2 sorbent', *Energy & Environmental Science*, 4(6), pp. 2070-2074.

Ge, D.T., Yang, L.L., Li, Y. and Zhao, J.P. (2009) 'Hydrophobic and thermal insulation properties of silica aerogel/epoxy composite', *Journal of Non-Crystalline Solids*, 355(52-54), pp. 2610-2615.

Han, X. and Šiller, L. (2015) 'Aerogel synthesis', P221149GB/DW(WO2016132117 A1).

Huang, H.Y., Yang, R.T., Chinn, D. and Munson, C.L. (2003) 'Amine-grafted MCM-48 and silica xerogel as superior sorbents for acidic gas removal from natural gas', *Industrial & Engineering Chemistry Research*, 42(12), pp. 2427-2433.

Kim, H.M., Kim, H.S., Kim, S.Y. and Youn, J.R. (2015a) 'Silica aerogel/epoxy composites with preserved aerogel pores and low thermal conductivity', *E-Polymers*, 15(2), pp. 111-117.

Kim, H.M., Noh, Y.J., Yu, J., Kim, S.Y. and Youn, J.R. (2015b) 'Silica aerogel/polyvinyl alcohol (PVA) insulation composites with preserved aerogel pores using interfaces between the superhydrophobic aerogel and hydrophilic PVA solution', *Composites Part a-Applied Science and Manufacturing*, 75, pp. 39-45.

Kong, Y., Shen, X.D., Fan, M.H., Yang, M. and Cui, S. (2016) 'Dynamic capture of low-concentration CO2 on amine hybrid silsesquioxane aerogel', *Chemical Engineering Journal*, 283, pp. 1059-1068.

Maghsoudi, K. and Motahari, S. (2018) 'Mechanical, thermal, and hydrophobic properties of silica aerogel-epoxy composites', *Journal of Applied Polymer Science*, 135(3), p. 9.

Salihi, E.C., Wang, J.B., Coleman, D.J.L. and Šiller, L. (2016) 'Enhanced removal of nickel(II) ions from aqueous solutions by SDS-functionalized graphene oxide', *Separation Science and Technology*, 51(8), pp. 1317-1327.

Vahtrus, M., Oras, S., Antsov, M., Reedo, V., Maeorg, U., Lohmus, A., Saal, K. and Lohmus, R. (2017) 'Mechanical and thermal properties of epoxy composite thermal insulators filled with silica aerogel and hollow glass microspheres', *Proceedings of the Estonian Academy of Sciences*, 66(4), pp. 339-346.

Wan, S.L., Ding, W., Wang, Y.L., Wu, J.Y., Gu, Y.W. and He, F. (2018) 'Manganese oxide nanoparticles impregnated graphene oxide aggregates for cadmium and copper remediation', *Chemical Engineering Journal*, 350, pp. 1135-1143.

Wang, L., Yao, M.L., Hu, X., Hu, G.S., Lu, J.Q., Luo, M.F. and Fan, M.H. (2015) 'Amine-modified ordered mesoporous silica: The effect of pore size on CO_2 capture performance', *Applied Surface Science*, 324, pp. 286-292.

Wormeyer, K., Alnaief, M. and Smirnova, I. (2012) 'Amino functionalised silica-aerogels for CO_2-adsorption at low partial pressure', *Adsorption-Journal of the International Adsorption Society*, 18(3-4), pp. 163-171.

Yi, X.F., Sun, F.L., Han, Z.H., Han, F.H., He, J.R., Ou, M.R., Gu, J.J. and Xu, X.P. (2018) 'Graphene oxide encapsulated polyvinyl alcohol/sodium alginate hydrogel microspheres for Cu (II) and U (VI) removal', *Ecotoxicology and Environmental Safety*, 158, pp. 309-318.

Chapter 9 Appendix

9.1 Appendix A. Degassing process and surface area measurements with Surfer analyser

The main page of Surfer acquisition program (see Figure a. 1) contains the commands and dialog boxes to set parameters and to save the analysis. Prior to set samples for BET and BJH analysis, samples must be degassed. Degassing process starts with degassing of empty burette for 15 minutes at 120 °C to evaporate water adsorbed on the glass surface of the burette. Then the weight (m_1) of the empty degassed burette is measured by using a microbalance. The second step is degassing the sample of desired mass (0.1-0.2 g in our case according to the manufacture recommendations of materials of the surface area ≥ 30 m^2/g) for ≥ 8 hours at 200 °C. Figure a. 2 shows automatic temperature control page for degassing the samples.

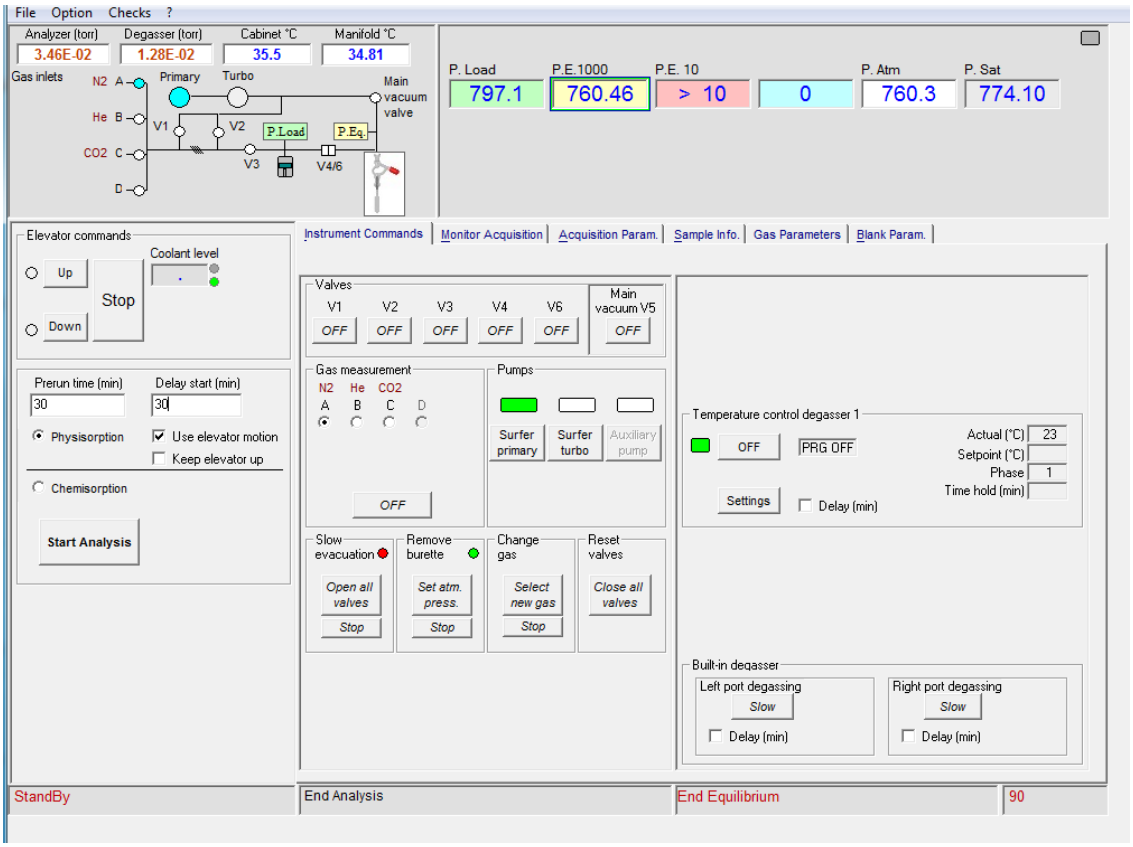

Figure a. 1. Surfer acquisition main page.

The next step after finishing degassing is to measure the mass of sample and burette (m_2). Therefore, the net mass of the degassed sample (m) can be calculated as below:

$$m = m_2 - m_1$$

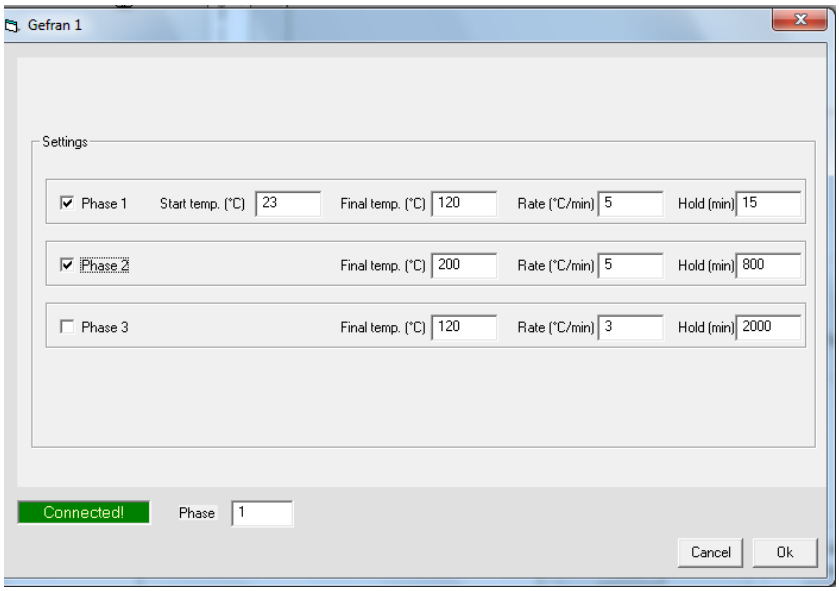

Figure a. 2. Automatic temperature control.

After finishing degassing of the sample, the burette is inserted in the Surfer acquisition. It must be insured that the adsorbate gas used is nitrogen (see gag measurement tab, main page, Figure a. 1) and the liquid nitrogen in the drawer (see Figure 2.20 b, chapter 2) is enough to fulfil the analysis. The next step is loading the method from the acquisition parameters tab of the main page (see Figure a. 1). For mesoporous material, it is recommended by the manufacturer company to used *METHOD MACROPORE and MESOPORE WITH 10 TORR TRANSD.mtd* (see Figure a. 3).

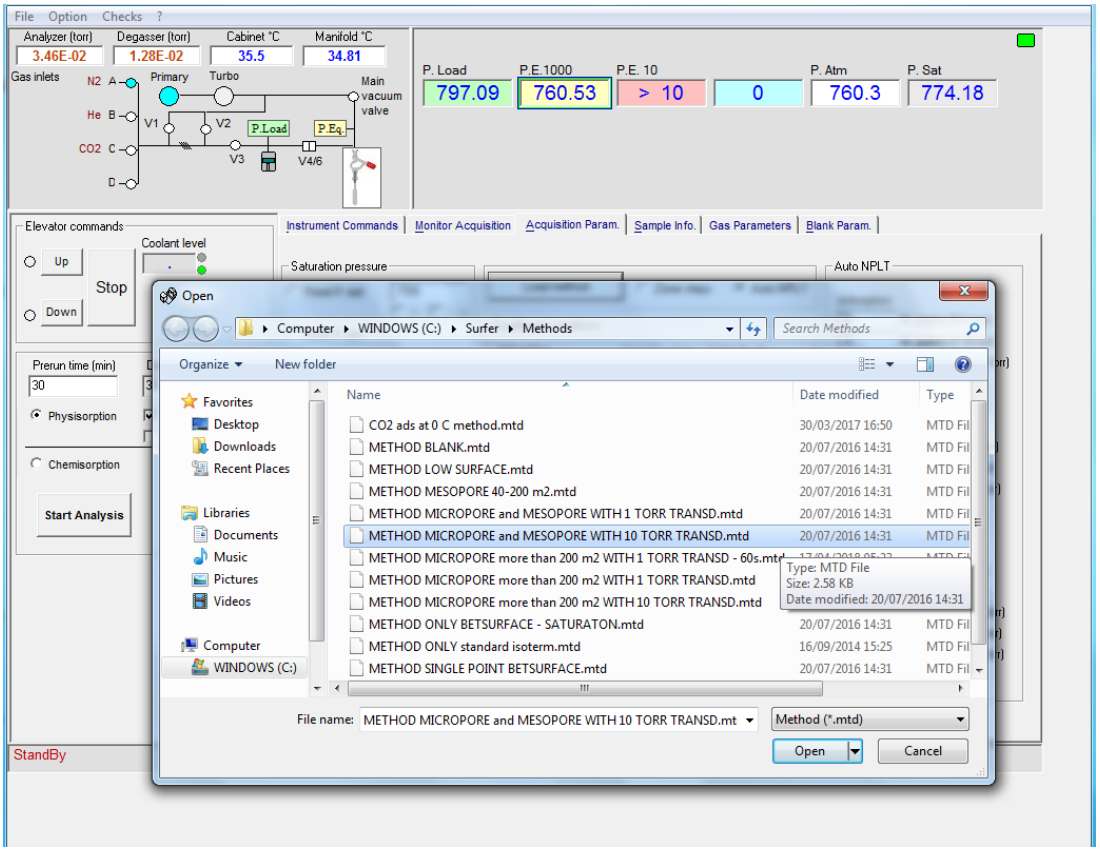

Figure a. 3. Load method from acquisition parameters tab.

Sample information such as the name, the date of operation, the sample mass (m) and the density of the sample are inserted by using the sample info tab to display the page of the sample information in Figure a. 4.

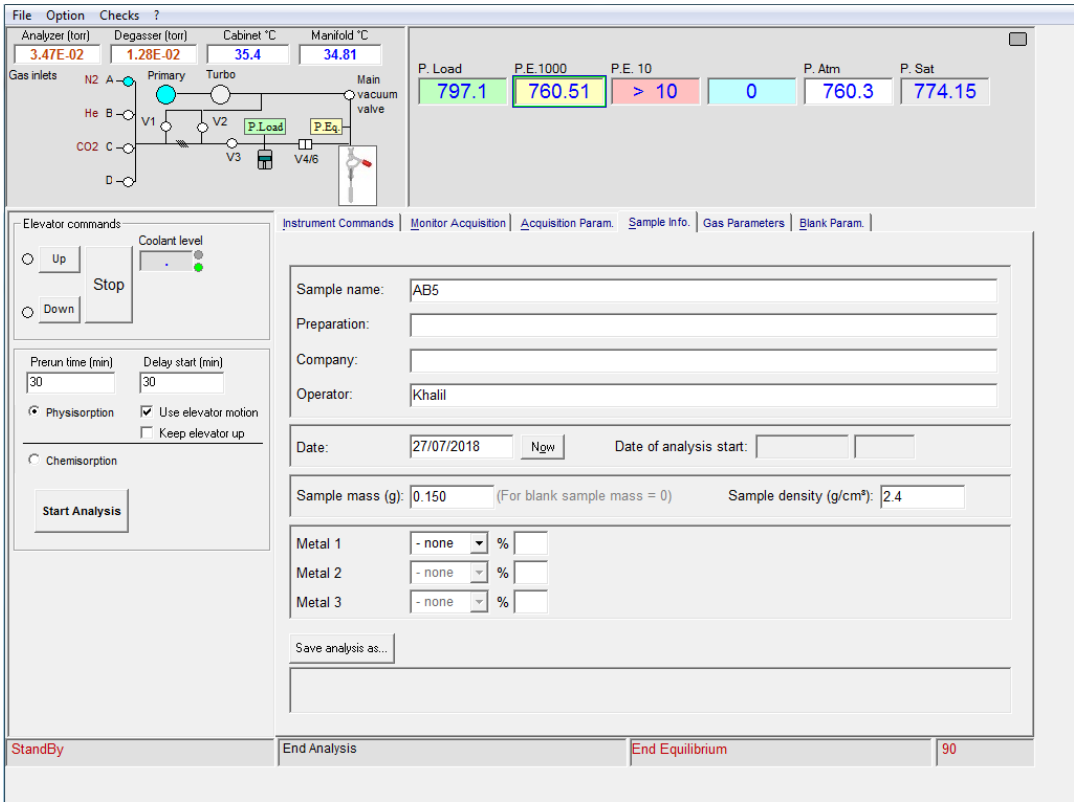

Figure a. 4. Sample info page.

The blank parameter of the burette must be loaded by using blank param. tab (see Figure a. 5). After finishing the setting of all parameters, it is recommended to set the pre-run time and the delay time at 30 mins for each (seen at the left side in main page of Figure a. 1).

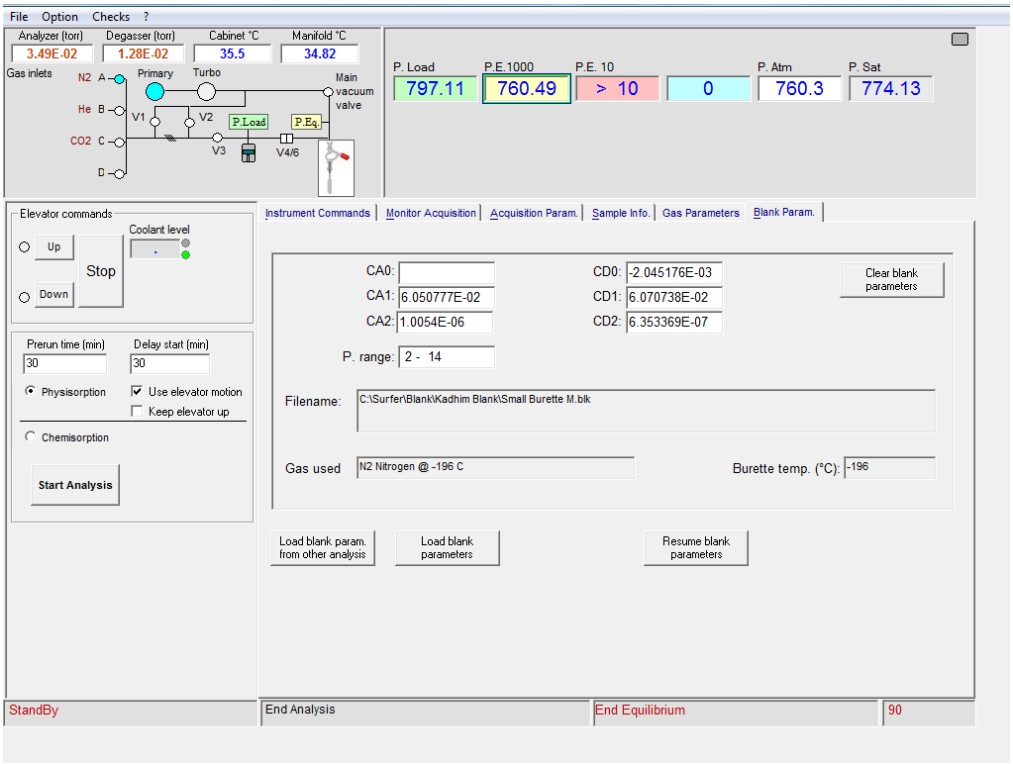

Figure a. 5. Blank parameters tab.

After insuring that all information and parameters are inserted, the file of the analysis is saved by using save analysis as tab in the sample info page (located at the bottom of the left side of sample info page, see Figure a. 4). Before starting the analysis, the system needs to be outgassed by pressing on all valves tab in the main page (Figure a. 1). Once degassing of the system is completed, the pressure of the system should reach E-03 torr (see analyser (torr), top left corner of the main page, see Figure a. 1) and when the burette stopcock is opened, the pressure must be in E-03 torr range as well. Then the turbo pump is used (by using Surfer turbo tab, Figure a. 1) to reach vacuum of E-06 torr. Once vacuum is reach E-06 torr, the analysis is started by pressing the start analysis tab.

9.2 Appendix B. Thermal conductivity measurement by the hot-disk

Measuring thermal conductivity for a material under investigation by using a hot-disk technique requires placing the sensor between the plane surfaces of two pieces of the sample. An accurate determination of thermal conductivity needs samples of thicknesses higher than the radius of the hot disk sensor because the theory of this technique assumes that the sensor must be located in an infinite material. In addition, the size of samples with low thermal conductivity must be increased because of the heat capacity of the sensor and the need to increase the measuring time (in all thermal conductivity measurement which are carried out in this thesis, the thickness of samples was double ≥ the radius of the sensor).

Selecting experimental parameters

As soon as we open the software, the window of the type of experiments is displayed (Figure b. 1). After clicking on Bulk (type I), the sample setup window will be displayed as shown in Figure b. 2

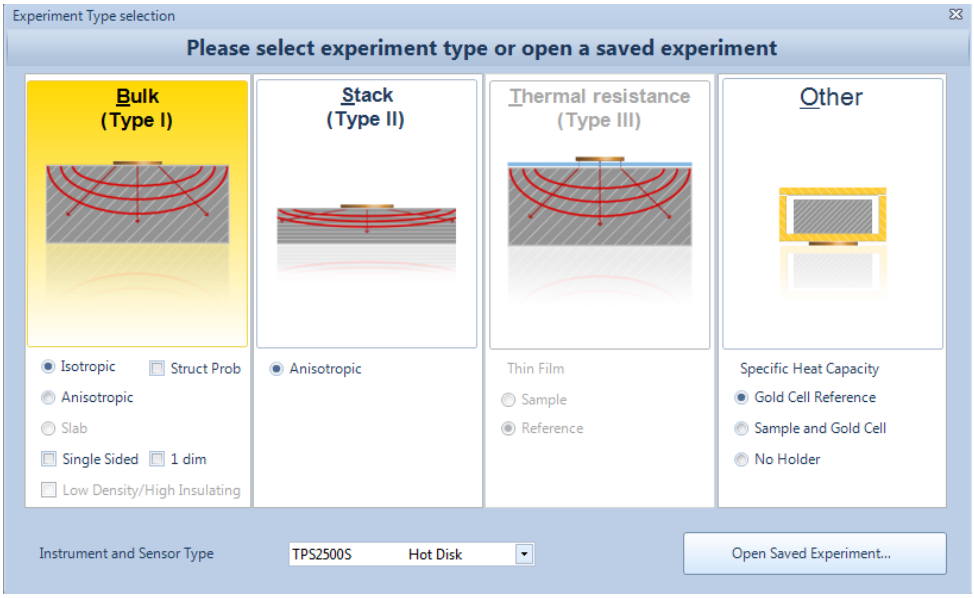

Figure b. 1. Experiment type selection dialog box.

In the setting window, the proper Kapton sensor must be carefully chosen (sensor C5465, radius of 3.189 mm was used for all samples in this thesis). In addition, the available depth is the thickness of one pieces of the sample where during transient recording, the thermal wave should not reach the outside boundaries of the sample. The measurement time and the heating power parameters are quite important and depend on the material itself and the radius of the

used sensor. In this work, the heating power and measurement time for a typical transient curve of silica aerogel and fibre reinforced composites (when Kapton sensor of 3.189 mm is used) are set to be 10 mW and 20 sec, respectively (see Figure b. 2).

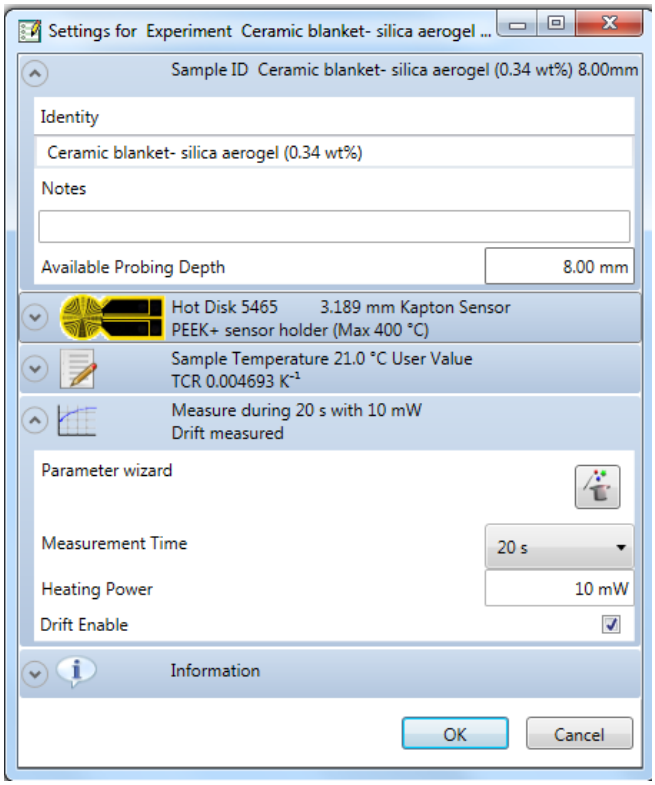

Figure b. 2. Experiment window, standard method. Experiment parameter of sample AB5 in Table 3.1, chapter 3.

The heat power is chosen to be 10 mW because thermal conductivity measurement of insulation materials required low heat power. While measuring time is measured from the following relation:

$$d_p = 2\sqrt{a.t}$$

Where d_p is the probing depth (in our case 8 mm), a is the thermal diffusivity (for our silica aerogel composites is ~ 1.76 mm/sec), and t is the measurement time. After setting up all parameters and starting the analysis, the transient recording is start and as soon as recording is finished, the drift graph (see Figure b. 3) and transient graph (see Figure b. 4) are displayed.

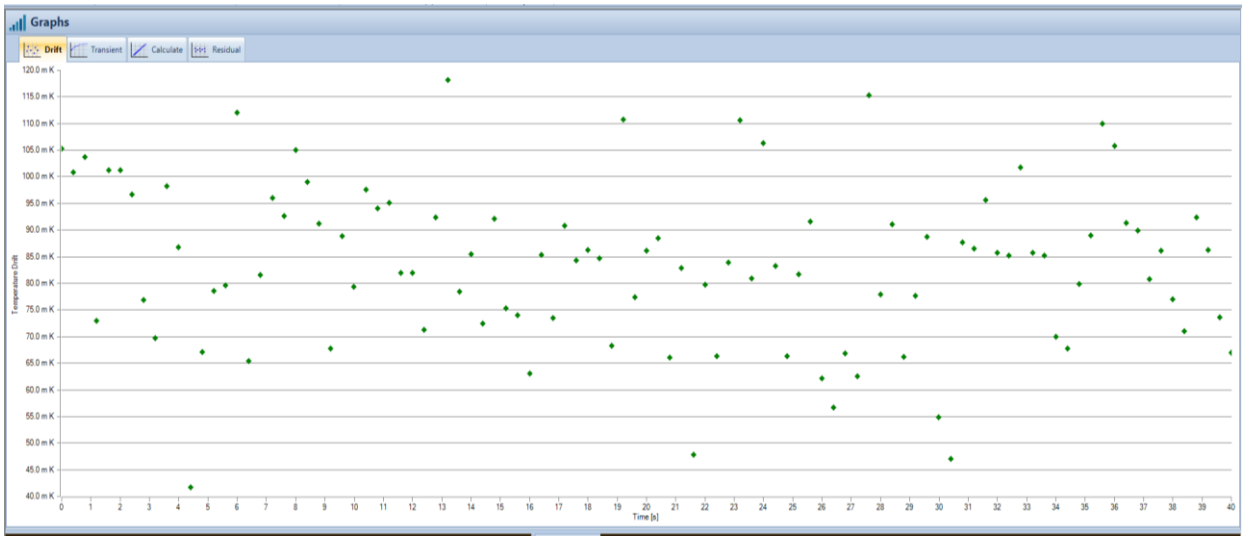

Figure b. 3. Temperature drift graph of sample AB5 in Table 3.1, chapter 3.

Figure b. 3 shows the typical drift graph for Sample AB5 where the distribution of the data is vibrated around the X-axis. If the there is any draft in temperature, the measurement must be repeated again.

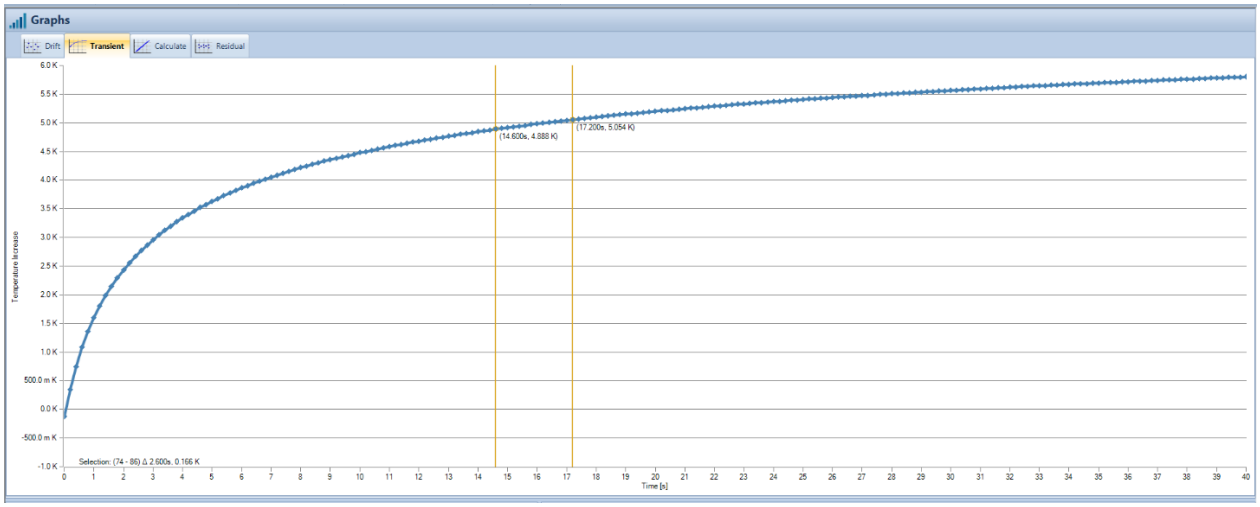

Figure b. 4. Transient measurement sample of AB5 in Table 3.1, chapter 3.

Figure b. 4 shows the transient graph of sample AB5. The transient curve should be continuous with no discontinuities or sudden jumps. As it can be seen in Figure b. 4 the initial and the final parts of the curve have not incorporated in the measurement to eliminate the contribution of the sensor and the environment. The highlighted area on the curve in Figure b. 4 is chosen so that the thermal conductivity measurement is calculated from a well distributed residual which should distributed randomly around the horizontal (see Figure b. 5).

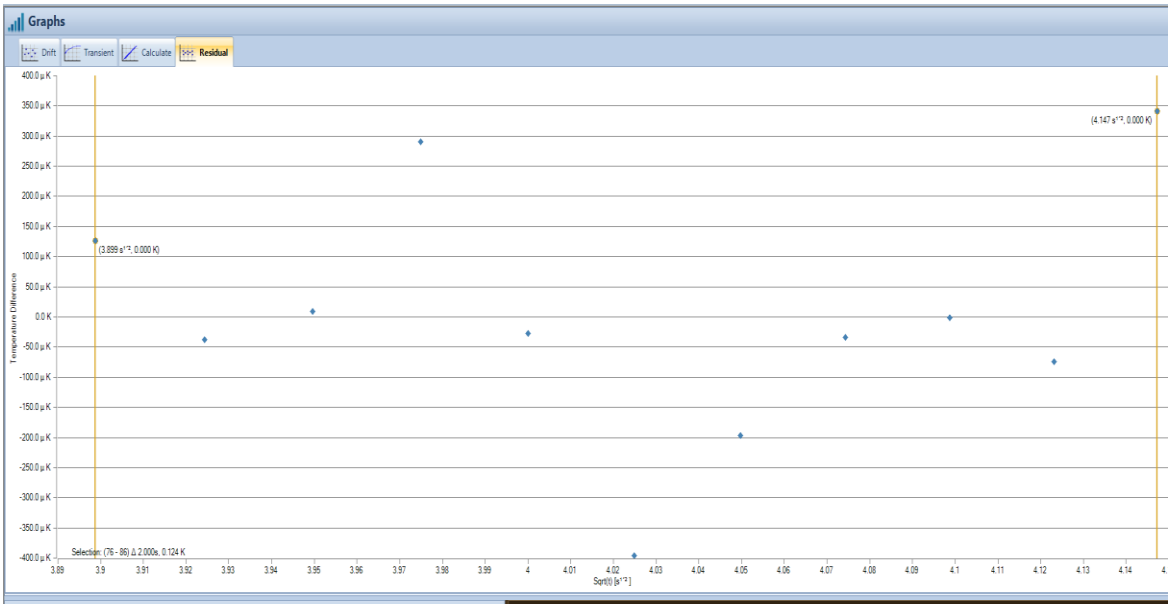

Figure b. 5. Residual of the selected area for thermal conductivity measurement of AB5 in Table 3.1, chapter 3.

Once we get good residual, the validity of data fitting can be considered. The calculation page (see Figure b. 6) shows a linear and a continuous graph as that in.

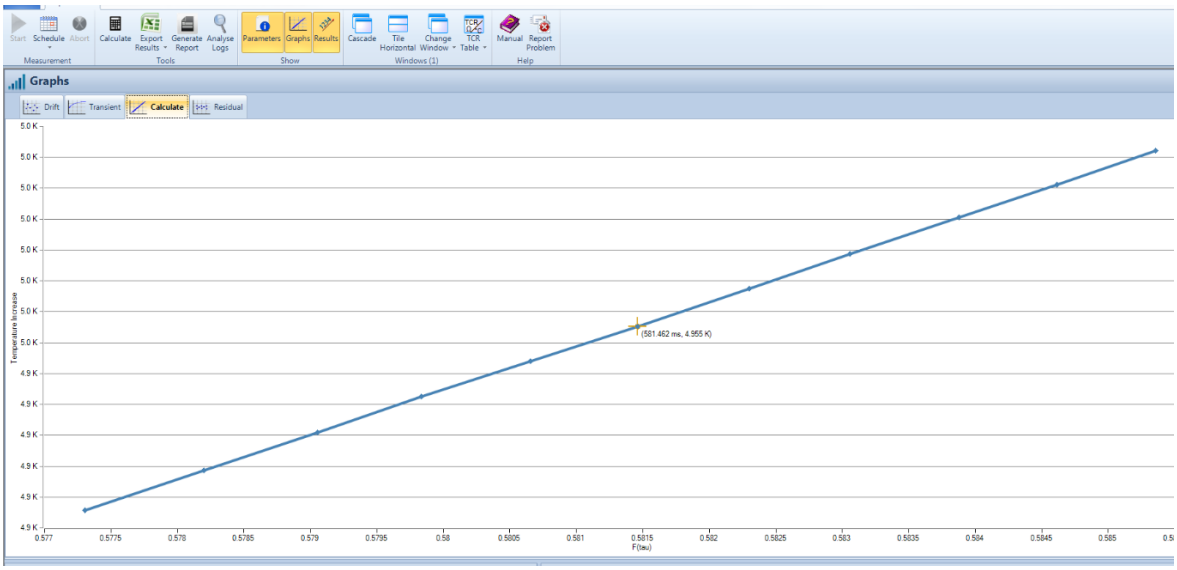

Figure b. 6. Linear curve of thermal conductivity calculation of AB5 sample.

9.3 Appendix C. List of publications

1. Khalil T. Hassan, Jiabin Wang, Xiao Han, Jon J Sharp, Gaurav A. Bhaduri, Vladimir Martis and Lidija Šiller, Catalytic Performance of Nickel Nanowires Immobilised in Silica Aerogels for CO_2 Hydration Reaction, ACS Omega, 4, Jan 2019.

2. Xiao Han, Khalil T. Hassan, Alan Harvey, Dejan Kulijer, Michael R.C. Hunt and Lidija Šiller, Bioinspired Synthesis of Monolithic and Layered Aerogels, Advanced Materials, 30 (23) June 2018.

3. Sherko Ghaderi, Khalil T. Hassan, Xiao Han, Jiabin Wang, Lidija Šiller, and Sarah H. Olsen, Thermoelectric characterization of nickel-nanowires and nanoparticles embedded in silica aerogels, AIP Advances 8(6), 065221 (2018).

4. Khalil T. Hassan, Xiao Han and Lidija Šiller, Optimisation of thermal and mechanical properties of ceramic fibres reinforced silica aerogels synthesised by ambient pressure drying method with bicarbonate solution, submitted to Energy and Buildings.

9.4 List of posters and oral presentation

1. 4th International Seminar on Aerogels, “Mapping catalytic performance of nickel nanowires immobilised in silica aerogels for CO_2 hydration reaction”, 2018 Hamburg, Germany on 24-26, September 2018, (oral presentation).

2. Northern Post-doctoral Researcher's Meeting 4, “Affordable superinsulation materials via novel ambient pressure drying method”, 22nd June 2018, Newcastle, UK.

3. 8th Chemical Nanoscience Symposium Newcastle, “Bioinspired Synthesis of monolithic and layered aerogels”, CNSN-8, 23rd March 2018, UK.

4. North East Energy Materials Symposium (Durham), “Feasibility of utilising nickel nanowires immobilised on silica aerogels for CO_2 capture “, 21st April 2017, UK (oral presentation).

5. Faraday Joint Interest Group Conference, “Low cost superinsulation materials via novel ambient pressure drying method”, 11-13 April 2017, Coventry, UK (oral presentation).

6. 7th Chemical Nanoscience Symposium, “Catalytic activity of nickel nanowires (NiNWs) immobilised on silica aerogels for CO_2 hydration reaction “, CNSN-7, 28th March 2017, Newcastle, UK.

7. 7th Chemical Nanoscience Symposium, “Thermoelectrically characterisation of nickel-nanoparticles embedded in silica aerogels”, CNSN-7, 28th March 2017, Newcastle, UK.

8. Third International Seminar on Aerogels,” Lightweight thermal insulation ceramic fibres reinforced silica aerogels materials synthesised via novel economical ambient pressure drying method”, Sophia Antipolis France 22–23 September 2016 (oral presentation).

9. 6th Chemical Nanoscience Symposium, “Enhancing the mechanical properties of silica aerogels by reinforcement with short ceramic fibres”, 17th March 2016, Newcastle, UK.

10. 5th Chemical Nanoscience Symposium," Structural and mechanical properties of silica aerogel/ceramic fibre blanket composites", 26th March 2015, Newcastle, UK.

9.5 List of academic awards:

1. Second prize of the Postgraduate Conference of Chemical Engineering and Advance Materials 26th May 2017
2. Poster award "Thermoelectrically characterisation of nickel-nanoparticles embedded in silica aerogels", CNSN-7, 28th March 2017, UK
3. Third prize of the Postgraduate Conference of Chemical Engineering and Advance Materials 2nd June 2016
4. Second prize of the Postgraduate Conference of Chemical Engineering and Advance Materials 28th March 2015